

Computational and experimental investigation of the mechanisms involved in cellular water transport and (cat)ion homeostasis

DISSERTATION

zur Erlangung des akademischen Grades
eines Doktors der Naturwissenschaften (Dr. rer. nat.)
am Fachbereich Mathematik und Informatik
der Freien Universität Berlin

eingereicht von

Dipl.-Bioinf. Martina Fröhlich

Mai 2012

Gutachter:

1. Prof. Dr. Martin Vingron
2. Prof. Dr. Dr. h.c. Edda Klipp

Tag der Disputation: 17. Oktober 2012

Ich widme diese Arbeit meinem Vater

Danksagung

Besonders bedanken möchte ich mich bei Prof. Dr. Dr. h.c. Edda Klipp für die Vergabe des Themas und die Betreuung der Arbeit. Ihre wertvollen Ratschläge sowie Ihre Unterstützung im Aufbau von Kontakten und Kollaborationen haben sehr zum Gelingen dieser Arbeit beigetragen.

Prof. Dr. Martin Vingron danke ich für die Betreuung im Rahmen der International Max Planck Research School (IMPRS).

Bei Prof. Dr. Peter M. T. Deen möchte ich mich für die Möglichkeit bedanken, in seinem Labor die für diese Arbeit nötigen Experimente durchzuführen.

Mein Dank gilt auch Prof. Dr. Maik Kschischo für die hilfreichen Diskussionen sowie seine Unterstützung im Rahmen des Translucent-2 Projektes.

Im Rahmen des Aquaporin-Projektes möchte ich mich bei Dr. Enno Klussmann, Andrea Geelhaar, Jenny Eichhorst und Dr. Burkhard Wiesner für die Durchführung der Experimente an primären Zellkulturen bedanken.

Mein Dank gilt auch Dr. Mark Knepper für die Bereitstellung von Antikörpern sowie für hilfreiche Diskussionen.

Bedanken möchte ich mich auch bei den Mitarbeitern der Arbeitsgruppe von Prof. Deen an der Radboud University in Nijmegen. Besonders erwähnen möchte ich hier Dr. Joris Robben, Dr. Grazia Tamma und Marica Radivojevic für die Unterstützung im Arbeiten mit Zellkulturen.

Zudem möchte ich noch allen Beteiligten des Marie Curie-Netzwerkes für Aquaglyceroporin-Forschung danken, besonders den Koordinatoren Prof. Dr. Stefan Hohmann und Dr. Karin Lindkvist für die Organisation der interessanten und lehrreichen Kurse. Sylwia Zoltowska, Dr. Gerhard Fischer, Dr. Camilo Aponte und Dr. Roy Steier danke ich für die außergewöhnlich nette und kollegiale Atmosphäre bei den Marie Curie-Treffen.

Im Rahmen des Translucent-2 Projektes möchte ich mich besonders bedanken bei Prof. Sergey und Dr. Svetlana Shabala, Dr. Jost Ludwig, Dr. Hella Lichtenberg-Fraté, Matthias Kahm, Daniel

Ganser und Dr. Samuel Gelis für die Bereitstellung der Daten und die gute Zusammenarbeit sowie bei Matthias Kahm für die intensiven Diskussionen.

Meiner ehemaligen Kollegin Dr. Susanne Gerber danke ich für die konstruktive Zusammenarbeit, ihre Freundschaft und die vielen aufmunternden Worte.

Fachliche Unterstützung bekam ich während meiner Arbeit von den Mitarbeitern der Arbeitsgruppe Theoretische Biophysik an der Humboldt-Universität zu Berlin. Besonders bedanken möchte ich mich bei Christian Waltermann, Christian Diener und Margit Heiske für ihre Hilfe bei mathematischen und thermodynamischen Fragen, bei Marvin Schulz für seine Unterstützung mit Tide, bei Dr. Szymon Stoma für die gemeinsame Arbeit am Spatio-Temporal Simulation Environment (STSE) sowie bei Adriana Supady und Katarzyna Tyck für die kollegiale Zusammenarbeit. Ivo Maintz und Sabine Wagnitz möchte ich für die administrative Unterstützung und das angenehme Arbeitsklima danken.

Bedanken möchte ich mich auch bei Dr. Hannes Luz und Dr. Kirsten Kelleher für die Organisation von regelmäßigen Treffen und Tagungen im Rahmen der IMPRS, welche die Zeit meiner Doktorarbeit sehr bereichert haben.

Während der Fertigstellung dieser Arbeit haben mich besonders Dr. Christoph Wierling, Dr. Matteo Barberis, Dr. Thomas Hahndorf und Guido Klingbeil durch Korrekturlesen der Arbeit und hilfreiche Kommentare unterstützt.

Meinen Freunden danke ich für ihre Unterstützung, Ruhe und Geduld, mit denen sie mir in den letzten Jahren zur Seite standen.

Mein größter Dank geht an meine Eltern, die mich während meines Studiums und während meiner Doktorarbeit auf jede erdenkliche Weise unterstützt haben.

Während der Durchführung dieser Arbeit wurde ich finanziert und unterstützt aus Mitteln der Deutschen Forschungsgemeinschaft (DFG, SFB 740 und IRTG, GRK1360), des Bundesministeriums für Bildung und Forschung (BMBF, DrugIPS), der Niederländischen Organisation für wissenschaftliche Forschung (NWO, 865.07.002), des Marie Curie Research Training Network Aquaglyceroporins (LSHG-CT-2006-035995-2), des ERANET Projektes SysMo Translucent-2, der Frauenförderung des Instituts für Biologie der Humboldt-Universität und der Max-Planck-Gesellschaft (IMPRS for Computational Biology and Scientific Computing).

Abstract

Membranes are more than simple barriers between cells and their environment. They must both protect the cells and enable the exchange of substances. This thesis analyzed two aspects of membrane transport: The transport of water and the transport of ions, in particular the transport of cations, across the cellular membrane.

To analyze mechanisms involved in water transport, mammalian kidney cells were chosen as model system. A combined approach based on biological experiments and mathematical modeling was used to investigate the intracellular signaling pathway regulating the membrane abundance of the water channel Aquaporin-2 (AQP2) in the kidney. Data from biological experiments with rat and canine kidney cells were used to estimate the model parameters, thereby enabling the generation of species-specific models. Deletion of model reactions and subsequent parameter estimation resulted in the generation of model variants. Ranking of the model variants led to the conclusion that the importance of certain cellular reactions varies between different species. Moreover, reactions which are crucial for the temporal behavior of the system were identified. Time-dependent sensitivity analysis was performed demonstrating that membrane-located AQP2 reacts most sensitively when changing the parameters directly involved in the translocation mechanism. Regarding potential medical applications, the model based on canine kidney cells was used to investigate individual and combinatorial treatments for different pathological conditions.

Due to the fact that many membrane transport systems are well conserved between yeast and higher organisms, the regulation of cation transport was addressed in the yeast *Saccharomyces cerevisiae*. The theory of linear nonequilibrium-thermodynamics was applied to build a model of cation homeostasis with its main focus on plasma membrane transporters. With this approach it is possible to model passive ion fluxes driven by the electrochemical potential differences but also primary or secondary active transport processes driven by the interplay of different ions (symport, antiport) or by ATP consumption (ATPases). Data for proton and potassium fluxes from MIFE and FLISE experiments (non-invasive techniques to measure transmembrane ion fluxes) were used to estimate the model parameters. The model was used to predict additional ion fluxes and identified chloride fluxes as potential candidates. The Trk1,2p and Pma1p dynamics were analyzed by *in silico* mutation and inhibition experiments. Furthermore, the behavior of cells undergoing multiple salt stresses was predicted showing a reduced activity for cells pretreated with higher KCl stimuli.

The present study illustrates the applicability of mathematical and thermodynamical modeling to cellular membrane transport processes. The predictions derived from the models are a valuable tool to guide future biological experiments.

Keywords: systems biology, parameter estimation, time-dependent sensitivity analysis, linear nonequilibrium-thermodynamics, aquaporin-2, body water homeostasis, cation homeostasis, yeast

Contents

Acknowledgements	v
Abbreviations	xiii
Global Introduction	3
I Mathematical Modeling of Aquaporin-2 Trafficking	7
1 Introduction	11
1.1 Biological Background	11
1.1.1 Regulation of body water homeostasis	11
1.1.2 The water channel Aquaporin-2	11
1.1.3 Signaling via vasopressin	13
1.1.4 AQP2: regulation via phosphorylation/dephosphorylation	15
1.2 Previous model approaches	15
1.3 Literature-based data sets	16
1.4 Clinical disorders in body water homeostasis	17
1.5 Aims and structure of this thesis part	20
2 Methods	21
2.1 Computational techniques	21
2.2 Experimental approaches	24
2.2.1 Cell surface biotinylation	24
3 Modeling of AQP2 trafficking in MDCK cells	27
3.1 A mathematical model of AQP2 trafficking in MDCK cells	27
3.2 Time course simulation and parameter estimation	29
3.3 Model variations and ranking - To reproduce the data either a negative feedback or degradation of the stimulus has to be included	29
3.4 Sensitivity analysis reveals importance of AQP2 endocytosis	32
3.5 Time-dependent sensitivity analysis	32
3.6 AQP2 translocation after dDAVP stimulation	34

3.7	Model predictions and comparison with recent data	35
3.7.1	Prediction of the dose response of vasopressin on AQP2 in the membrane	35
3.7.2	Prediction of the dose response of vasopressin on cAMP	37
3.8	Prediction of potential drug targets with Tide	37
3.9	Discussion	43
4	Modeling of AQP2 trafficking in rat IMCD primary cells	47
4.1	A mathematical model of AQP2 trafficking in IMCD cells	47
4.2	Time course simulation and parameter estimation	48
4.3	Model Variations and Ranking indicate only moderate importance of negative feedback	49
4.4	Sensitivity analysis reveals importance of both AQP2 exo- and endocytosis . .	51
4.5	Time-dependent sensitivity analysis	51
4.6	Model predictions and comparison with newly generated data indicate that regulated endocytosis might have a minor effect in primary rat IMCD cells	53
4.7	Discussion	58
4.7.1	Primary rat IMCD cell model	61
4.7.2	Comparison between MDCK and primary rat IMCD cells	64
II	Thermodynamic Model of the Cation Homeostasis in Yeast	69
5	Introduction	73
5.1	Yeast as a model organism	73
5.2	Cation homeostasis in <i>S. cerevisiae</i>	73
5.3	Aim and structure of this thesis part	74
5.4	Biological background	74
5.4.1	Membrane proteins influencing cation homeostasis	74
5.4.2	Energy storage in cells	77
5.5	Thermodynamical background	78
5.5.1	Thermodynamic systems	78
5.5.2	Equilibrium versus nonequilibrium thermodynamics	78
5.5.3	The laws of thermodynamics	79
5.5.4	Entropy and entropy production	80
5.5.5	The electrochemical potential	82
5.5.6	Linear non-equilibrium thermodynamics	84
5.5.7	The membrane potential	87
5.5.8	Representation of the different transporter types	89

6	Methods	93
6.1	Computational techniques	93
6.1.1	<i>k</i> -means clustering	93
6.1.2	Parameter estimation and <i>k</i> -means clustering - details	94
7	Results	95
7.1	A thermodynamic model of cation homeostasis	95
7.2	Application of the model to cellular cation transport	100
7.3	The model fitted to experimental data predicts chloride influx	100
7.4	A minimal set of membrane transport proteins is sufficient to reproduce the biological data	102
7.5	Prediction of the effect of knocking out PMA1p and coupled or uncoupled potassium transport	104
7.6	Analysis of potential mechanisms for Trk1,2 transport	107
7.7	Prediction of the effect of multiple KCl stimuli with the model	108
7.8	Application of the model to experimental data from FLISE experiments	108
8	Conclusion and discussion	113
9	Outlook	117
	Global Discussion and Outlook	121
	Appendix	123
1	<i>In silico</i> variation of the amount of AQP2	123
2	Dephosphorylation of AQP2 at position S261 in MDCK cells	123
3	Model fitting results for the IMCD cell model without negative feedback	124
4	Sensitivity analysis and time dependent sensitivity analysis applied to the IMCD cell model with the new AQP2 _{membrane} dataset produced by Klusmann et al.	124
5	Cation homeostasis model as implemented in COPASI	129
6	MIFE - additional results	129
	Bibliography	136
	List of Figures	150
	List of Tables	151
	List of publications	153
	CV	154

Contents

Zusammenfassung	155
Declaration	159

Abbreviations

<i>A</i>	Affinity of a chemical reaction
<i>A_p</i>	Affinity of an ATPase
<i>Act</i>	Activator concentration
α_i	Deviation of species <i>i</i> from its equilibrium value
AC	Adenylate cyclase
AQP2	Aquaporin-2
ATP	Adenosine triphosphate
AVP	Arginine vasopressin
cAMP	Cyclic AMP
CDI	Central diabetes insipidus
<i>C</i>	Molar concentration
COPASI	COMplex PATHway SIMulator [43]
dDAVP	(Deamino-Cys1, D-arg8)-vasopressin
<i>D</i>	Diffusion coefficient
Ena1	Yeast plasma membrane Na ⁺ -ATPase
<i>E</i>	Electric field
∂_{el}	Electrical conductivity
<i>F</i>	Faraday constant, $9.6485 \cdot 10^4$ C/mol
<i>G</i>	Gibbs free energy
GEF	Guanine nucleotide exchange factor
GPCR	G-protein coupled receptors
G-protein	GTP-binding protein
<i>G_S</i>	Stimulatory G-protein
IMCD	Inner medullary collecting duct
<i>Inh</i>	Inhibitor concentration
<i>J_i</i>	Flow of component <i>i</i>
<i>J_{i,eq}</i>	Flow of component <i>i</i> under equilibrium conditions ($X=0$)
<i>J_q</i>	Flow of heat
<i>J_S</i>	Flow of entropy
<i>J_{ch}</i>	Flow of a chemical reaction
<i>K</i>	Equilibrium constant for a chemical reaction
<i>k</i>	Boltzmann constant, $1.3806504 \cdot 10^{-23}$ J/K
<i>L_{ij}</i>	Phenomenological coefficient relating the <i>i</i> th flow to the <i>j</i> th force
<i>L_{ij}^k</i>	Phenomenological coefficient relating the <i>i</i> th flow through transporter of type <i>k</i> to the <i>j</i> th force
MDCK	Madin-Darby canine kidney
MIFE	Microelectrode ion flux measuring
μ_i	Chemical potential of component <i>i</i>

Abbreviations

μ_0	Standard chemical potential
$\tilde{\mu}_i$	Electrochemical potential of component i
μ_{gen}	Generalized mobility
μ_q	Electrical mobility
N	Number of particles
NDI	Nephrogenic diabetes insipidus
n_{ij}^k	Stoichiometry of transporter type k for i if coupled to j
Nha1	Yeast plasma membrane K^+/H^+ antiporter
Nsc1	Yeast non-specific cation channel
ODE	Ordinary differential equation
ω_i	Weight function in COPASI
p	Pressure
pbc	Proton buffer capacity
Pf	Osmotic water permeability
PKA	Protein kinase A
PKC	Protein kinase C
P_i	Permeability coefficient of component i
Pma1	Yeast plasma membrane H^+ -ATPase
φ	Electric potential
Ψ	Local dissipation function
Ψ	Dissipation function for the cell membrane
q	Charge of an ion
Q	Heat
R	Universal gas constant, $8.314472 \frac{J}{mol \cdot K}$
RC	Normalized response coefficients
σ	Entropy production density
SBGN	Systems Biology Graphical Notation
S	Entropy
$d_i S$	Entropy produced within a system
$d_e S$	Entropy exchanged with the environment of a system
T	Absolute temperature
t	Time
TPA	12-tetradecanoylphorbol-13-acetate
Trk1,2	Yeast K^+ uptake system
Tok1,2	Yeast K^+ channel
U	Internal energy
u_i	Molar mobility
V	Volume
V2R	Vasopressin V2 receptor
V_{in}	Intracellular volume
V_{out}	Extracellular volume
WT	Wild-type
W	Work
X	Amount of large negatively charged proteins

X_i Thermodynamic force acting on component i
 z_i Valence of a charged ion i

Global Introduction

Cellular water and cation homeostasis

Homeostasis (i.e. the maintenance of an equilibrium) of various substances, nutrients and fluids through membrane transport systems is essential for all living organisms. Of great importance are water and ion homeostasis. A living organism needs to regulate the amount of water it excretes, depending on the amount of water it takes up and the external environment (for example the temperature). Furthermore, ion homeostasis, especially cation homeostasis, plays an important role because some cations, like potassium, are necessary for processes like protein synthesis, enzyme activation, and osmotic regulation [119], whereas other cations such as sodium can be toxic if present at higher intracellular concentrations.

In case water or ion homeostasis is impaired (e.g. due to external factors or because the organism has lost the ability for regulation due to a disease), this can affect the organism dramatically. The impairment to regulate body water homeostasis can be lethal, or it can lead to severe diseases such as Nephrogenic diabetes insipidus (NDI) [88, 125]. The impairment to regulate ion homeostasis can lead to the inability to cope with changes in the environment such as salt stress, inhibition of protein synthesis and growth, or to cell death [3, 119].

For this reason it is of high importance to know, how those mechanisms function and how they can be influenced in case of a disease.

Systems biology and its areas of application

Biological systems are very complex and often not completely understood. There exists a tightly regulated interplay between genes, mRNAs, proteins, metabolites and also between physical properties like cell volume or osmotic pressure. Quite often, a complicated network of feedback loops connects the biological players. In many cases it is impossible to gain biological information for a specific compound because it is technically or ethically impossible (e.g. unavailability of mutants or cellular reporters, protein or RNA concentrations below detection limit).

To gain information about biological systems despite high complexity or reduced availability of data, systems biology combines two major approaches:

1. Experimentally (*in vivo*, *in vitro*),
2. Computationally (*in silico*).

A classical biological approach to gain knowledge about these processes is to systematically perturb or knockout systemic players and to study the hereby resulting consequences, e.g. on the protein or RNA level, or on the phenotype of an organism [2]. In systems biology, data resulting from those experiments together with literature-based knowledge is used to generate mathematical models.

Based on the availability of biological data for a study that aims to contribute to the resolution of certain open issues, different computational methods can be applied:

- Cellular networks and their analysis via Boolean or Bayesian modeling proves useful, when it comes to gene regulation [62, 97].

- Flux balance analysis and metabolic control theory are applicable to the analysis of metabolic networks [63, 97].
- Mathematical modeling via ordinary differential equations (ODEs) is often applied while analyzing signaling networks [63, 97].
- Stochastic modeling approaches are useful if only few particles of a certain substance (e.g. a transcription factor) are involved and the inherent noise of a system strongly affects its dynamics [149].
- Partial differential equations (PDEs) or spatial discretization can be applied in case spatial resolution and compartmentalization are important [52].
- Thermodynamic methods are a useful basis or addition for systems biological models, especially if thermodynamic forces like heat, pressure, or electrochemical potential differences are involved [23, 58].

The computational models can be used to simulate the biological system *in silico* and make hypotheses, which can then be verified or falsified in a biological experiment. The result of the experiment can be utilized to modify the computational model. The iterative cycle of modeling and experiment is the cornerstone of systems biology and serves to strengthen the knowledge of the system.

Systems biology applied to water and cation transport

Within the present thesis systems biological as well as thermodynamic approaches were applied to enlighten the processes involved in two major areas of membrane transport:

1. The regulation of body water homeostasis by intracellular signaling pathways.

The water channel aquaporin-2 (AQP2) is expressed in the principal cells of the collecting duct in the kidney. Upon a stimulus by the hormone arginine vasopressin (AVP) an intracellular signaling cascade is activated, which leads to the translocation of the water channel aquaporin-2 (AQP2) from intracellular vesicles to the apical plasma membrane. This results in an osmotically driven water flow from the pro-urine through the cell into the blood and leads to increased storage of water in the body. In this part the emphasis is on the intracellular signaling pathway that regulates AQP2 trafficking:

- a) Biological data collected from the literature were used to build mathematical models of the signaling pathway. The models were analyzed and used to enlighten the difference between two biological data sources, Madin-Darby canine kidney (MDCK) cells [20] and primary cultures of rat inner medulla collecting duct (IMCD) cells [133].
- b) The mathematical models were used to predict the effect of different input stimuli (i.e. different concentrations of AVP) on the amount of AQP2 at the membrane. These predictions were compared with wet lab experiments (done by myself with MDCK cells and by Klusmann *et al.* with IMCD cells) to analyze the validity of the model.
- c) Time dependent sensitivity analysis was performed to analyze the effect of small perturbations in the model parameters. The resulting information can be used for guided model verification and to identify potential drug targets.

- d) Possible medical uses for cases of reduced availability of either AVP or AQP2 were simulated *in silico* and the target identification tool TIDE [126] was used to identify potential drug targets for single and combinatorial treatments.

2. The regulation of yeast cation homeostasis.

Fungi live on animals, plants, and on their decaying products and can have beneficial or destructive effects. They are important for medical treatments by producing antibiotics like penicillin and cyclosporin, play an important role in food production (e.g. *Saccharomyces cerevisiae* is used during bread, wine, and beer production). On the other hand they can lead to severe diseases (e.g. *Candida* species can lead to superficial infections and sepsis [135]). Hence, what affects fungi has also a high influence on health, economy and ecology.

What makes the unicellular fungus yeast an even better study object is that it is easy to handle and that many ion transport proteins are highly conserved between yeast and higher organisms. Therefore, yeast was developed into an ideal model to study alkali metal cation transport and homeostasis. The early work in this field has been summarized in [24, 119]. The organism of choice for the present work was the yeast *Saccharomyces cerevisiae*. In this organism, transport of cations and cation homeostasis plays an important role because some ions, like potassium, are necessary for processes like protein synthesis and enzyme activation, whereas other cations such as sodium are rather toxic if present at higher concentrations. In this work a combined approach based on biological experiments and thermodynamic modeling was used to analyze how cation homeostasis is regulated by the flux of ions through the cellular plasma membrane driven by the electrochemical potential and the usage of ATP driven pumps.

The workflow was as follows:

- a) Data from MIFE and FLISE experiments (non-invasive approaches which can be used to calculate transmembrane fluxes) were used for model generation and parameter estimation.
- b) The model was used to predict the effect of different mutations and inhibitions, the cellular behavior to multiple salt stresses as well as potential additional ion fluxes.

Structure of this thesis

This general introduction will be followed by two parts: “**Mathematical Modeling of Aquaporin-2 Trafficking**” and “**Thermodynamic Model of the Cation Homeostasis in Yeast**”. Each part highlights one important aspect of the factors influencing the kinetic behavior of cellular membrane transport, cellular homeostasis as well as its perturbation. The first part focuses on the underlying signaling pathway modulating membrane transport proteins with the emphasis on the water channel AQP2. The major signaling pathway for AQP2 trafficking is known from literature. However, there is yet no cure for diseases like NDI and available treatments are rare and sometimes even dangerous. Within this thesis, the dynamic behavior of the system is analyzed *in silico* based on biological data, and potential intracellular drug targets were identified.

In the second part the effects acting on membrane transport proteins already active and located at the plasma membrane is analyzed, while focusing on the model system yeast. This is a powerful model system for this purpose, because the major transport proteins in yeast are already known from literature. Nevertheless, the exact mechanisms are still unclear. With a thermodynamic approach the collectivity of membrane transport proteins was modeled and applied to measurements of net ion fluxes. Thereupon,

information was drawn from the model's parameters on the kinetic behavior of individual membrane transport proteins, namely Trk1,2p and Pma1p. Model predictions were made and it was investigated, how the model is applicable to data from different wild-type strains.

Each part is subdivided into an introductory chapter including background information and aims of each project in more detail, and a methods section specific for each project. Furthermore, in each part the specific results will be presented, discussed and an outlook for further studies given. Finally, the major aspects that both projects have in common will be summarized and the applicability of the different biological model systems to cellular membrane transport and homeostasis will be discussed.

Part I

Mathematical Modeling of Aquaporin-2 Trafficking

The first part of this thesis presents kinetic models of the regulation and trafficking of the water channel Aquaporin-2. The focus in this part is on the intracellular signal transduction starting with a trigger by the hormone arginine vasopressin (AVP) and ending with the translocation of AQP2 to the apical plasma membrane and a resulting water flow through the cell.

Two different models were build, one based on data and knowledge from Madin-Darby canine kidney (MDCK) cells and one on data from primary cultures of rat inner medullary collecting duct (IMCD) cells.

The kinetic parameters of the MDCK and IMCD cell models were estimated with the use of literature-based data sets. To get further insight into the systems behavior the models were analyzed by

- generation and ranking of model variants,*
- time dependent sensitivity analysis.*

The models were used to make predictions about the abundance of AQP2 at the membrane over time and at different concentrations of vasopressin. Furthermore, the MDCK cell model was used to identify potential individual and combinatorial drug treatments at different pathological conditions.

Additional biological data were generated to verify the models' predictions concerning AQP2 at the membrane at different vasopressin concentrations. The experiments on MDCK cells were performed by myself in the laboratory of Prof. Peter Deen (Radboud University, Nijmegen, the Netherlands). Experiments on IMCD cells were performed by Klussmann, Geelhaar et al. (Max Delbrück Center, Berlin-Buch, Germany)

In the final pages of Part I, the results obtained from MDCK and IMCD cells will be discussed in the light of the comparability of data from different cell lines and the use for medically relevant predictions.

The project was conducted within the Marie Curie Research Training Network in Aquaglyceroporin research.

1 Introduction

The aim of the here presented study was to apply mathematical modeling to achieve more knowledge about Aquaporin-2 (AQP2) trafficking and regulation. In this introductory chapter the biological background will be introduced together with the clinical relevance of this project. To allow a better understanding of the following work, the general aspects of the regulation of body water homeostasis will be summarized, followed by an introduction into AQP2 regulation and signaling via the hormone arginine vasopressin (AVP). Since G-protein coupled receptors are involved in this process, they will be described in more detail together with the regulation through their desensitization.

AQP2 is mainly regulated via phosphorylation or dephosphorylation at specific phosphorylation sites. Because one side project focused on this type of regulation, a short introduction into AQP2 phosphorylation will be given.

Previous model approaches performed on the field of AQP2 regulation will be outlined together with the data sets from the literature which were used for model generation and parameter estimation.

Finally, the clinical relevance of the project will be pointed out and the aims and structure of this thesis part will be specified.

1.1 Biological Background

1.1.1 Regulation of body water homeostasis

The kidneys are responsible for blood filtration and regulation of water and electrolyte homeostasis. During the day, an enormous amount of blood is filtered by the kidneys, resulting in approximately 140 L pro-urine per day [125]. A majority of the water (approximately 90% [14]) is constitutively reabsorbed via the water channel aquaporin-1 in the proximal tubule and descending limb of Henle's loop, being important for the development of the counter current concentrating mechanism [125].

In addition to this constitutive reabsorption mechanism, body water homeostasis is tightly regulated. Dehydration or excess of sodium results in the sensation of thirst and subsequent water uptake. Furthermore, a mechanism to retain water within the body is activated. This is triggered by a release of AVP from the pituitary. Via the blood stream, AVP reaches the principle cells of the cortical and medullary collecting duct, there activating an intracellular signaling cascade and leading to increased reabsorption of water. When isotonicity is restored, a reduction of the AVP level occurs [14].

A reduced or elevated water excretion is a common symptom of kidney disorders such as nephrogenic diabetes insipidus (NDI). In NDI the excretion of up to 20 L urine per day has been observed [125], thereby illustrating the importance of a well functioning regulatory system.

1.1.2 The water channel Aquaporin-2

Before 1992 it was not proven that water can cross cell membranes via specific channels. The discovery of the water channel aquaporin-1 (AQP1, originally known as CHIP28 [1, 104]) led to the Nobel Prize

for Agre and coworkers in 2003. Nowadays it is known that the aquaglyceroporin family consists of the aquaporins (only permeated by water) and the aquaglyceroporins (permeated by water plus glycerol). This work focuses on AQP2 which is only permeated by water.

AQP2 is expressed in the principal cells of the collecting duct in the kidney. In an unstimulated state it is located mainly in intracellular vesicles. Upon a stimulus by AVP an intracellular signaling cascade is activated, which includes the activation of the vasopressin V2 receptor (V2R) at the basolateral membrane, which is coupled to a trimeric G-protein. This results in an increase in intracellular cyclic AMP (cAMP) by activation of the adenylyl cyclase [132], activation of protein kinase A (PKA) and phosphorylation and subsequent translocation of AQP2 into the apical plasma membrane. This leads to an osmotically driven water flow from the pro-urine into the cell via AQP2 and by the water channels AQP3 and AQP4 in the basolateral membrane into the blood. Suppression of vasopressin reverses this mechanism and AQP2 becomes endocytosed from the membrane [125]. This is an important mechanism in the regulation of body water homeostasis (see Fig. 1.1).

AQP2 trafficking as well as long term AQP2 abundance is regulated by vasopressin. In addition vaso-

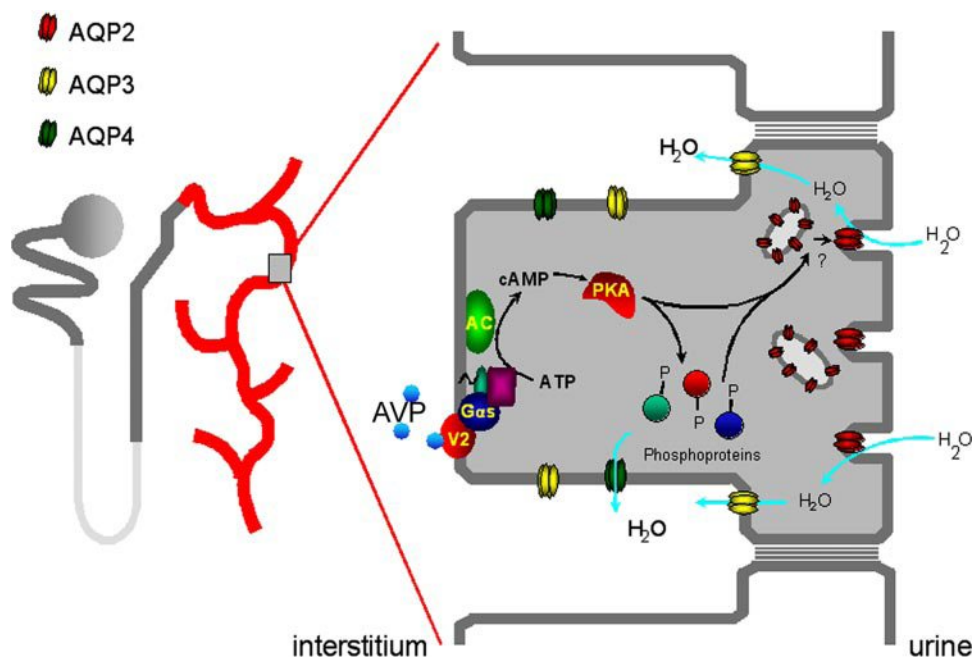


Figure 1.1: Regulation of AQP2 trafficking. Vasopressin (AVP) released from the pituitary gland reaches the collecting duct cells in the kidney via the bloodstream. After activation of the V2 receptor an intracellular signaling cascade is activated, including cAMP production by the adenylyl cyclase (AC), activation of PKA and phosphorylation of AQP2. Upon phosphorylation, AQP2 is translocated from intracellular vesicles to the apical plasma membrane. This leads to reabsorption of water from the pro-urine through the cells into the blood. (The image was reproduced with permission from Robben *et al.*, Am J Physiol Renal Physiol, 2006 [116].)

pressin positively regulates the abundance of AQP3, but not of AQP4 [125]. This work covers mainly the regulation of AQP2 trafficking. Additionally, AQP2 abundance is analyzed *in silico* in form of varying AQP2 concentrations.

1.1.3 Signaling via vasopressin

AQP2 trafficking is regulated by AVP. In the following, the main players of the pathway shall be described in more detail. Those are G-protein coupled receptors (GPCR), to which the V2R receptor belongs, as well as the cAMP-PKA pathway, which is assumed to be the main regulatory pathway for AQP2 trafficking. Furthermore, desensitization of GPCRs is described, which plays a role in the kinetics of the pathway.

- **Signaling through G-protein coupled receptors**

Signaling through GPCRs is generally used by all eukaryotes [2] and about 50% of all known drugs work on GPCRs or their downstream signaling pathways. Analyses of the human genome predict the existence of more than 1,000 GPCRs [57].

GPCRs act through trimeric GTP-binding proteins (G-proteins). In case the G-proteins are bound to GDP, they form trimers composed of α , β and γ subunits (see Fig. 1.2). The G-protein can be physically attached to the GPCR also in the inactive state or it gets recruited after ligand binding. Ligand binding further results in the release of the bound GDP from the α subunit, so that GTP can bind, therefore it acts like a guanine nucleotide exchange factor (GEF). This triggers the detachment of the G-protein from the receptor as well as a conformational change of the G-protein. During this process previously covered surface of the subunits becomes exposed so that membrane localized enzymes or ion channels can bind. In most of the cases this results in a dissociation of the α from the β/γ subunit. Both subunits are able to influence specific target proteins. One target protein of the α subunit of the stimulatory G-protein (G_S) is the adenylate cyclase [2, 78].

The α subunit acts as a GTPase. It hydrolyses GTP to GDP, which results in reassembly and inactivation of the G-protein. Binding of the α subunit to other proteins including the target proteins enhances the GTPase function, leading to faster inactivation of the protein.

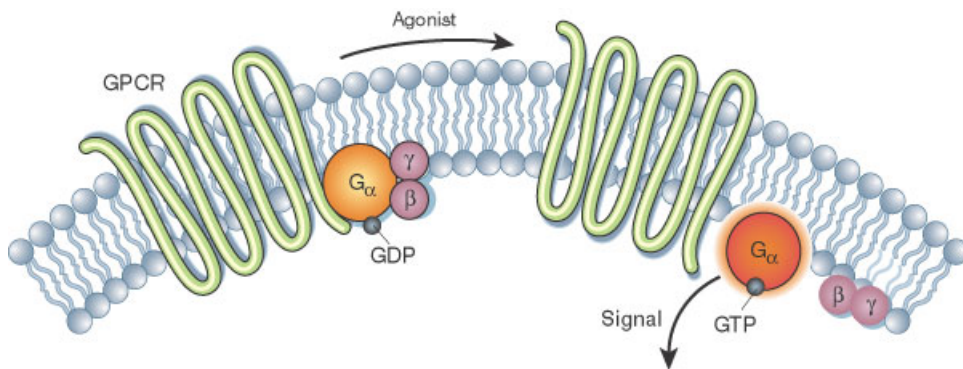


Figure 1.2: Activation of a G-protein coupled receptor. After activation by an agonist the GPCR gets activated. GDP bound to the G-protein gets replaced by GTP resulting in the detachment of the α and β/γ subunits from the receptor. The α or β/γ subunits transmit the signal further. (Reprinted by permission from Macmillan Publishers Ltd: Nature, Li *et al.*, ©2002 [76].)

- **Signaling via cAMP**

cAMP is synthesized from adenosine triphosphate (ATP) by the adenylate cyclase. The only way to degrade it is via cAMP phosphodiesterases to adenosine 5'-monophosphate (see Fig. 1.3) [2, 44]. Both processes are very fast. The basal cAMP concentration lies at approximately 10^{-7} M, but it can increase more than 20-fold after addition of an extracellular signal [2].

AC is a large transmembrane protein with its catalytic domain on the cytosolic side of the plasma membrane. There are at least 10 isoforms in mammals (nine membrane-bound and one soluble [102]) which are regulated e.g. by G-proteins and Ca^{2+} . Rieg *et al.* [111] showed that the AC involved in the regulation of AQP2 trafficking is most likely AC6. Recent reviews focus on the aspect of ACs as potential drug targets [98, 102].

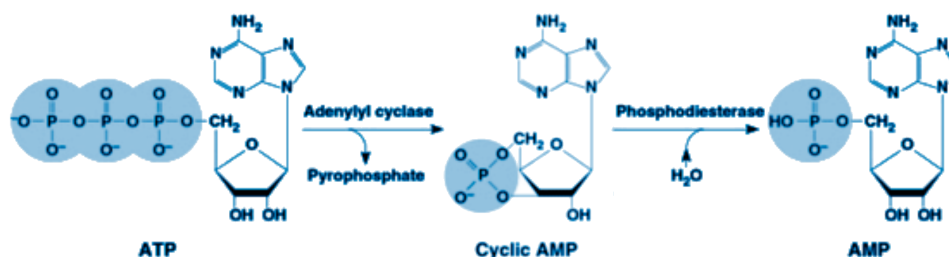


Figure 1.3: cAMP synthesis and degradation. cAMP synthesis via the adenylyl cyclase and degradation via phosphodiesterases (image reproduced from [45]).

- **Signaling via PKA**

One of the major response proteins of cAMP is the PKA. It consists of two regulatory and two catalytic subunits. The regulatory subunits can bind two molecules of cAMP each. After binding of four cAMP molecules the two catalytic subunits get detached and can phosphorylate target proteins throughout the cell (see Fig. 1.4).

AQP2 is phosphorylated by PKA at serine 256, which is part of a PKA consensus sequence and was shown to be phosphorylated by PKA *in vitro* [42]. Furthermore, PKA can phosphorylate and activate phosphodiesterases¹, thus establishing a negative feedback loop by degradation of cAMP. Special A-kinase anchoring proteins are important for the spatial localization of PKA. They bind to the regulatory subunit of PKA and also to AQP2 containing vesicles, therefore bringing both molecules in close proximity [2, 133]. Phosphodiesterases can be included in this functional module, which can affect the kinetics so that a long, weak PKA response can be converted into a strong, transient, local PKA response.

- **Desensitization of GPCRs**

GPCRs can be desensitized after a strong stimulus either via alteration of the receptor structure (G-proteins cannot bind to it any more), receptor sequestration (which means temporarily internalization of the receptor), or receptor internalization followed by degradation of the receptor. Receptor internalization does not necessarily mean a termination of the signal. Receptors can be stored in recycling vesicles and transported back to the plasma membrane, if needed. Degradation of the receptor results in the termination of the signal.

Robben *et al.* [115] have shown that in case of MDCK cells stably transfected with V2R-GFP, higher doses of the vasopressin analogon (deamino-Cys1, D-arg8)-vasopressin (desmopressin,

¹According to recent publications, substrate specificity, activation by PKA, and expression of the protein in IMCD, likely candidates are PDE3A and PDE4D [46, 92, 133].

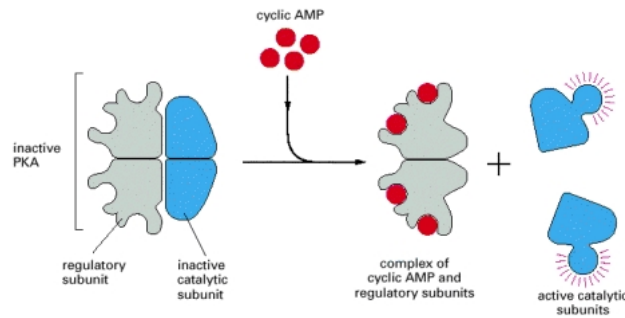


Figure 1.4: Activation of PKA by cAMP. The binding of two cAMP molecules to each of the regulatory subunits leads to the release of the catalytic subunits. (Copyright 2002 from *Molecular Biology of the Cell*, Fourth Edition by Alberts *et al.* Reproduced by permission of Garland Science/Taylor & Francis LLC.)

dDAVP) lead to V2 receptor internalization, which is stronger at higher dDAVP levels. Furthermore, they showed that after 1 h of stimulation with 100 nM dDAVP, 80.2% of the receptors end up in lysosomes to be degraded. They did not observe V2R recycling, however, there is evidence that this might be cell line specific and dependent on the stimulating agent [48, 115]. Furthermore, Robben *et al.* [117] have also shown that agonists can activate V2R intracellularly.

1.1.4 AQP2: regulation via phosphorylation/dephosphorylation

The membrane transporter AQP2 can be phosphorylated at different amino acids at its C-terminus. Known phosphorylation sites are serine 256, serine 261, serine 265, and serine 269 (see Fig. 1.5). Depending on the phosphorylation state of these amino acids, AQP2 can be found at different locations within the cell. Originally it was thought that a phosphorylation of S256 (S for serine) is sufficient for a translocation of AQP2 to the apical plasma membrane [143]. Kamsteeg *et al.* have shown in *Xenopus* oocytes transfected with AQP2-S256A and AQP2-S256D (mimicking non-phosphorylated and phosphorylated AQP2, respectively) that AQP2 is translocated to the apical membrane as soon as 3 of the 4 monomers in one AQP2 tetramer are phosphorylated [55]. More recently it has been shown that also the other residues are of great importance. Hoffert *et al.* [42] discovered that AQP2 phosphorylated at S269 seems to be located exclusively at the apical plasma membrane and not in internal vesicles. The phosphorylation of S256 seems to be preceding the phosphorylation at S269. Furthermore, phosphorylation at S261, which decreases after a vasopressin stimulus, may stabilize AQP2 ubiquitination and intracellular localization [87, 140]. In this work the phosphorylation at S261 after different concentrations of vasopressin was analyzed experimentally.

1.2 Previous model approaches

Knepper and Nielsen proposed the first mathematical model of the AQP2 trafficking [67]. They started with a 3-state model including activated, inactivated, and reserve AQP2 (also called by them transporters) and irreversible transition reactions between the states. Assuming that the transition between the inactivated and the reserve state is very fast, this resulted in a two state model including only activated (membrane located) and inactivated (intracellular) transporters as well as a transition from the inactivated to the activated state (exocytosis) and vice versa (endocytosis).

They fitted their model to data from osmotic water permeability (Pf) measurements in rat inner medulla

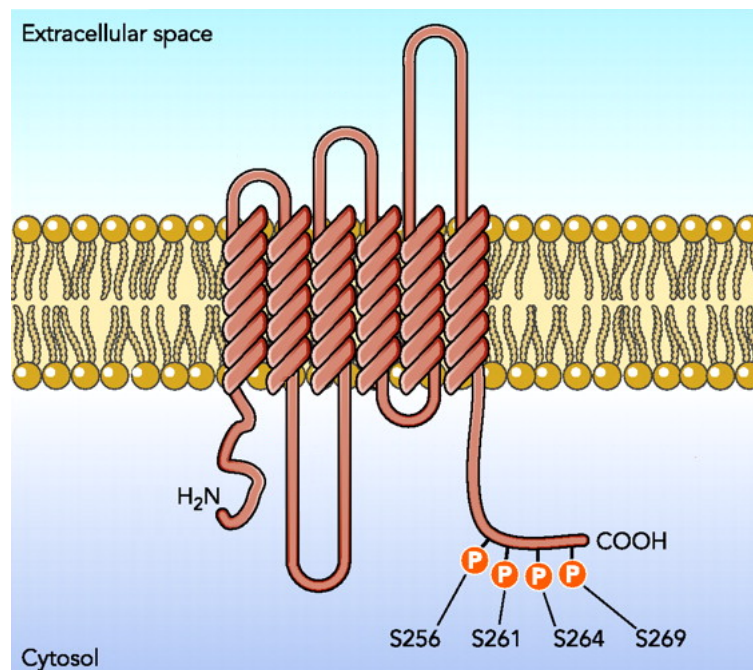


Figure 1.5: Different phosphorylation sites at the C-terminus of AQP2. Four different phosphorylation sites at the C-terminus of AQP2 are known. They are either phosphorylated (S256, S264, and S269) or dephosphorylated (S261) upon a stimulus by vasopressin (image adapted from [103]).

collecting duct (IMCD) after AVP addition and washout. Thereupon, they proposed that the optimal fit results from a scenario where both, the exocytosis as well as the endocytosis of AQP2, is regulated by vasopressin [67, 90].

Despite its usefulness their model was very much simplified and lacking the network of signaling pathways upstream of AQP2 translocation, which most likely involves the cAMP-PKA pathway. Moreover, effects of positive or negative feedback loops in the system were not considered. Those aspects were included in the models from this thesis. Thus, they can be used to analyze specific regulatory aspects of the intracellular signaling cascade, e.g. perturbations in cAMP activation or receptor internalization, and their effects on AQP2 trafficking. This was not possible with the model proposed by Knepper and Nielsen.

1.3 Literature-based data sets

For kinetic modeling it is crucial to have time resolved, quantitative or at least semi-quantitative and in itself consistent data sets. For this work it was decided to build two different models for AQP2 trafficking. The first model is based on a data set from Deen *et al.* [20] derived from experiments performed with MDCK cells. This data set consists of data for cAMP and Pf after stimulation with dDAVP. Furthermore, Pf was measured over time after a stimulus followed by washout of dDAVP. The data are presented in Fig. 1.6.

The second model is based on a data set by Stefan *et al.* [133] derived from experiments performed with primary cultured rat IMCD cells. Stefan *et al.* measured PKA activation, intracellular cAMP content and AQP2 at the membrane over time after a stimulus by vasopressin or forskolin with or without inhibition

of phosphodiesterases. The time courses used in this work are shown in Fig. 1.7.

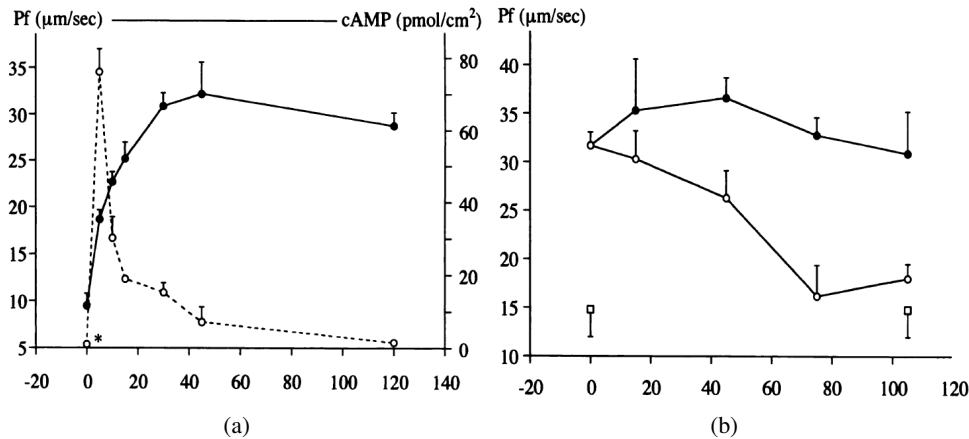


Figure 1.6: Data set from Deen *et al.* [20] based on experiments performed with MDCK cells. a) Stimulus by 10^{-8} M dDAVP at time point 0 s. The dotted line represents intracellular cAMP, the solid line osmotic water permeability (Pf). **b)** Open circles represent measurement of osmotic water permeability starting after 30 min of pretreatment with dDAVP followed by washout at time point 0. Closed circles represent the same pretreatment, but at time point 0 fresh dDAVP was added. The open squares represent the negative control, where no dDAVP was added. (Reprinted by permission from the American Society of Nephrology, Deen *et al.*, JASN, ©2007.)

1.4 Clinical disorders in body water homeostasis

To underline the importance of studying AQP2 trafficking and body water homeostasis, some examples of their clinical relevance are listed below. It is shortly mentioned how the models proposed within the present thesis can be used to address them.

- Hyponatremia and hypernatremia - The sodium concentrations in the serum are lower or higher than normal. This is most often caused by disorders of water balance [96, 125]. Hyponatremia usually occurs when the relative amount of total body water is higher compared to total body solute, which most often derives from an inability to maximally suppress the hormone AVP. Hypernatremia arises often from water deficiency of the organism due to a malfunctioning thirst reflex, if sufficient drinking is impossible or during NDI.
- Primary polydipsia or compulsive water drinking - Often occur in patients with psychiatric disorders or as side effects from medication resulting in the dryness of the oral mucosa [16, 125]. Individuals who drink up to 12 litres per day can have normal plasma osmolality. If additional factors play a role, like disturbance of the kidney, heart or liver function, this may lead to severe water intoxication. There exist regulatory mechanisms of the body to reduce the damage. For example, 10 days of increased water intake can lead to a form of AVP-resistant NDI. In this case AQP2 protein expression in the outer and inner medulla gets suppressed and the AQP2 abundance in the apical membrane is decreased.
- Pregnancy - Although not being a disorder, water retention, edema, and a decrease in plasma osmolality are very common during pregnancy. At plasma osmolalities that would normally suppress AVP release, it can still be detected. Furthermore, there is an increase in thirst and fluid intake at

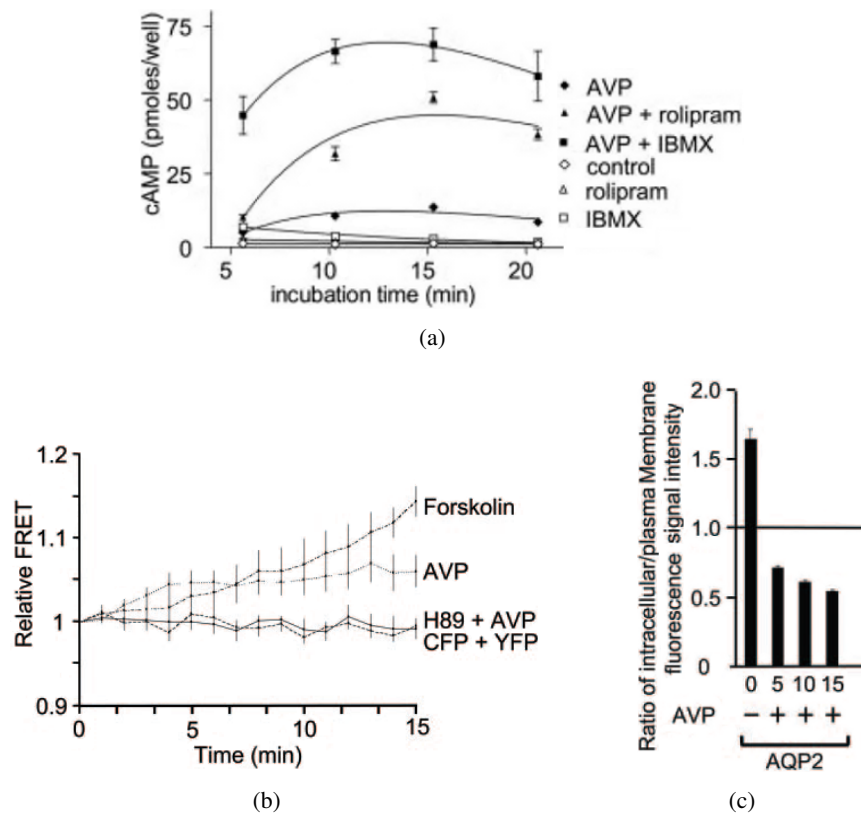


Figure 1.7: Data set from Stefan *et al.* [133] based on experiments performed with primary rat IMCD cells. a) intracellular cAMP at different conditions as indicated, b) relative PKA activity, c) intracellular/plasma membrane fluorescence intensity ratios for AQP2 before as well as 5, 10 and 15 min after a stimulus by AVP. (Reprinted by permission from the American Society of Nephrology, Stefan *et al.*, JASN, ©2007.)

low plasma osmolality, that would normally suppress thirst. It has been shown in rat experiments that AQP2 mRNA as well as membrane localized AQP2 is upregulated [125].

- Heart failure - Water retention and hyponatremia are common symptoms of advanced heart failure. It has been shown in patients with heart failure, that plasma AVP can still be detected, even though the observed hypoosmolality would suppress AVP release in healthy individuals. Furthermore, AVP mRNA in the hypothalamus was significantly elevated indicating increased AVP synthesis. Experiments in rats revealed that AQP2 trafficking and gene expression are increased. Experiments with human patients pointed out that V2 receptor antagonists lead to increased plasma sodium concentration and urine output, and decreased urinary AQP2 and osmolality, thus suggesting a decrease of membrane located AQP2 (see [125] and reference therein).
- Central diabetic insipidus (CDI) - In CDI the production of AVP is impaired, mostly resulting from a destruction of the AVP producing neurons in the neurohypophysis. Hence, only a reduced amount of AVP is released into the blood, leading to insufficient activation of the water reabsorption in the collecting duct. CDI appears in three forms, autosomal dominant, autosomal recessive and X-linked. The autosomal dominant case is most frequent, resulting from mutations in the AVP precursor. This in turn cannot fold and dimerize properly, leading to the accumulation of misfolded precursors and to death of the AVP producing neurons (see Babey *et al.* [5] and references therein). In the autosomal recessive case the AVP gene is mutated, leading to reduced biological activity of AVP. In the X-linked recessive case a not yet identified gene is involved. In most cases, water reabsorption can be restored by treatment with dDAVP.
- Nephrogenic diabetes insipidus (NDI) - In NDI the kidneys are unable to respond properly to AVP. As a result, the patients lose an enormous amount of water and are in danger of dehydration. NDI can be either congenital or acquired. Congenital NDI results in most cases from mutations of either the V2R or AQP2. Approximately 90% of patients with congenital NDI suffer from mutations in the V2R. In most cases the V2R is retained in the ER, thus the intracellular signaling cascade including cAMP, PKA activation and AQP2 trafficking does not get activated. Since this kind of NDI is X-linked, males are mostly affected and they may excrete up to 20 L of urine per day [125]. Without appropriate treatment, dehydration and mental retardation frequently occur. There exist different strategies to reactivate those trapped V2R. One is by using V2R antagonists acting as chaperones [10, 30], another one is to rescue the V2R by using non-peptide agonists [117]. 10% of the families with congenital NDI have mutations in the AQP2 gene [125]. In the autosomal recessive case the AQP2 mutant proteins are misfolded and retain in the endoplasmatic reticulum (ER) whereas in the autosomal dominant case mutations of the C-terminus are involved, which is of high importance for regulated AQP2 trafficking (see Sec. 1.1.4). NDI can also be acquired through lithium treatment (often used as a therapy for bipolar disorder) during which downregulation of AQP2 expression and trafficking could be observed. Furthermore, special diets (e.g. potassium-deficient diet) as well as acute or chronic renal failure can result in NDI. Usually, acquired NDI is less severe than congenital NDI [125].

The models proposed in this part of the thesis can assist in identifying how these problems can be investigated at the kidney level. They can be used to identify relevant mechanisms, for example how membrane localized AQP2 can be kept low despite elevated AVP levels (as it appears in heart failure or pregnancy). Within the present thesis, the models were used to predict potential treatments in situations with reduced amount of active AVP (as in CDI) and AQP2 (as in NDI).

1.5 Aims and structure of this thesis part

Within the last years a lot of knowledge has been achieved concerning the regulation of AQP2. The aim of the present thesis is to include this knowledge and build more detailed and predictive mathematical models. With these models, questions can be answered through *in silico* experiments, such as:

- Which intracellular reactions have the most influence on the abundance of AQP2 at the membrane and on water reabsorption?
- How do initial differences in the AQP2 abundance influence the water reabsorption?
- Which reactions are possible drug targets to inhibit or stimulate water reabsorption in case of a disease?
- What can be learned from different biological model systems?

In Sec. 3 and Sec. 4 mathematical models of the AQP2 trafficking will be proposed, based on data from MDCK and IMCD cells, respectively. Both models were analyzed by ranking of different model variants (Sec. 3.3 and Sec. 4.3). The models were analyzed with sensitivity analysis (Sec. 3.4 and Sec. 4.4) and time-dependent sensitivity analysis (Sec. 3.5 and Sec. 4.5). The models were used to make predictions concerning AQP2 membrane localization. Those predictions were compared with newly generated data from MDCK cells (Sec. 3.6 and Sec. 3.7), and from primary rat IMCD cells (Sec. 4.6). A summary and comparison of the results from the two biological systems will be presented in Sec. 4.7.2 and discussed in Sec. 3.9.

2 Methods

The models presented in this thesis are systems of equations and differential equations. They are implemented and analyzed with the systems biology tool COMplex PATHway SIMulator (COPASI) [43], and with Mathematica® [150]. In the following sections, the methods used in this thesis part are described. For the theoretical part a short introduction into differential equations, sensitivity analysis, and time dependent sensitivity analysis is given. Afterwards the conditions for the time course simulation, parameter estimation, and sensitivity analysis used here are described in detail.

For the biological part first a general introduction into cell surface biotinylation is given, followed by an explanation of the detailed experimental setup.

2.1 Computational techniques

Differential equations

In this work the focus lies on the investigation of the development of biological systems, which means here a mathematical model with given start values, over time. The model consists of species and reactions, which are described by a set of equations and ordinary differential equations (ODEs).

In a system containing r reactions and m species, the change of a species S_i over time is given by the formula

$$\frac{dS_i}{dt} = \sum_{j=1}^r n_{ij}v_j \quad \text{for } i = 1, \dots, m \quad (2.1)$$

where n_{ij} is the stoichiometric coefficient for species i and reaction j . v_j is the rate of reaction j , a function of the species vector $\mathbf{S} = (S_1, S_2, \dots, S_m)^T$ and the parameter vector $\mathbf{p} = (p_1, p_2, \dots, p_r)^T$ of the system and it depends on the kinetics of the reactions. An example of such a kinetic is the mass action kinetic, where the rate of the reaction is proportional to the concentration of the reactants to the power of the number in which they are entering the reaction [63, 145]. Also more complicated kinetics are possible, like Michaelis-Menten [84] or Hill [39] kinetics or different forms of activation or inhibition [19, 127].

Simple systems of differential equations can be solved analytically, but for larger biological systems usually numerical solvers are used. During this work, the LSODA method, which is implemented in COPASI, was applied [43]. This method can automatically adapt to stiff differential equation systems, which combine slow and fast processes, and can reduce the numerical effort to solve them [63].

Parameter estimation

The goal of parameter estimation or model fitting is to find the parameter set so that the model can reproduce given biological data best.

A prominent way to estimate the parameters of a model is via the least squares fitting [63]. For this a model including the involved species and reactions is needed as well as biological data for at least one of

the species at steady state or over time. Because in this work time resolved data were used, the description concentrates on the latter.

Based on a given set of start parameters a simulation is performed with the model. The simulation of the species is compared with the biological data and at each experimental data point the difference between the simulation and the biological data is determined. With this differences the sum of squared residuals is calculated which can be used as part of an objective function $R(\mathbf{p})$ that has to be minimized,

$$R(\mathbf{p}) = \sum_{i,j} \omega_j \cdot (x_{i,j} - y_{i,j}(\mathbf{p}))^2 \quad (2.2)$$

$x_{i,j}$ stands for the experimentally derived value of species S_j at time i , $y_{i,j}(\mathbf{p})$ is the value of species S_j at time i simulated by the model given the parameter vector \mathbf{p} .

If applicable, an individual weight function ω_j can be assigned to every data series [43].

An optimization method like the particle swarm algorithm [60] or evolutionary programming [27] can be used to efficiently vary the parameters so that $R(\mathbf{p})$ gets reduced.

Sensitivity analysis

When analyzing signaling pathways one is often interested in the sensitivity coefficients or concentration response coefficients. They give information about the response of a species' concentration to a small perturbation in a parameter p (see Fig. 2.1). In classical metabolic control analysis (MCA) [38, 53] the response of a steady state concentration S^{SS} is analyzed. The unscaled concentration response coefficients \check{R}_p^{SS} are given by the derivative

$$\check{R}_p^{SS} = \frac{dS^{SS}}{dp} \quad (2.3)$$

and the scaled response coefficients R_p^{SS} by

$$R_p^{SS} = \frac{p}{S^{SS}} \cdot \frac{dS^{SS}}{dp}. \quad (2.4)$$

The latter take into account that the magnitude of the species concentrations and parameters might be very different. By multiplication of $\frac{p}{S^{SS}}$ the response coefficient becomes independent of units. It represents the percentage of a change in the species' steady state concentration as a result of a change of the parameter value by 1%.

By knowing for which parameters and therefore reactions a species of interest is most sensitive, one can identify the reactions which might be suitable drug targets.

Time dependent sensitivity analysis

Since signaling pathways are systems with the function to react on temporal changes, one is often not only interested in the response of the species at the steady state, but also during the whole time course. Ingalls and Sauro [47] proposed the time dependent response coefficients $R_p^S(t)$. Small changes of the

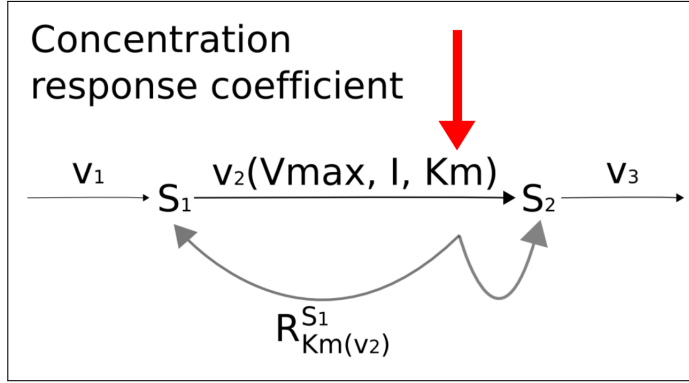


Figure 2.1: Concentration response coefficient. The concentration response coefficient R_p^{SS} is a measure of the effect of minor changes of a parameter p on species S in steady state, in this example a minor change of parameter Km of reaction 2 on species S_1 . (Adapted with permission from Wiley-VCH Verlag GmbH & Co. KGaA., Klipp *et al.*, SystemsBiology: A Textbook, page 53, ©2009 [63].)

parameters (at the starting point of the simulation) and their effect on the species of the system are given by

$$R_q^S(t) := \frac{\partial S(t, q)}{\partial q} \Big|_{q=q_0} = \lim_{\Delta q \rightarrow 0} \frac{S(t, q_0 + \Delta q) - S(t, q_0)}{\Delta q} \quad (2.5)$$

Ingalls and Sauro further proposed a computationally efficient calculation method by calculating in parallel $\frac{\partial S_i}{\partial t}$ and $\frac{\partial}{\partial t} \frac{\partial S_i(t)}{\partial q}$. The calculation requires the reduced stoichiometric matrix N_R , which is achieved by ordering the stoichiometric matrix N with row rank n_0 in such a way that the first n_0 rows are independent. Taking only the first n_0 rows of the reordered N results in N_R .

Furthermore the link matrix $L = \begin{bmatrix} I_{n_0} \\ L_0 \end{bmatrix}$ and the unscaled elasticity coefficients $\frac{\partial v(t)}{\partial S}$, $\frac{\partial v(t)}{\partial q}$ and $\frac{\partial v(t)}{\partial S_d}$ are used for efficient calculation of the response coefficients. This results in the following formula

$$\frac{\partial}{\partial t} \frac{\partial S_i(t)}{\partial q} = N_R \left[\frac{\partial v(t)}{\partial S} L \frac{\partial S_i(t)}{\partial q} + \frac{\partial v(t)}{\partial S_d} \frac{\partial T}{\partial q} + \frac{\partial v(t)}{\partial q} \right] \quad (2.6)$$

The vector q includes the parameters p of the system as well as the initial concentrations of the species. T is a vector defined in terms of the initial conditions as $T = S_d(0) - L_0 S_i(0)$.

Time course simulation, parameter estimation and sensitivity analysis - details

Time course simulation and parameter estimation were performed with the systems biology tool COPASI [43].

Parameter estimation for the MDCK cell model was performed by running evolutionary programming [27] in COPASI 1000 times with 200 generations, a population size of 20, random number generator Mersenne Twister [83] and a random seed. A Python script was used to run the algorithm with random initial parameter values as well as random upper and lower parameter bounds.

The best parameter set from the 1000 runs was taken, in case a parameter was located at a boundary, this boundary was extended by a factor of 100, and a subsequent parameter estimation was performed using the algorithm particle swarm [60] with iteration limit 2000, swarm size 50, standard deviation $1e^{-6}$, random number generator Mersenne Twister and random seed.

Parameter estimation for the IMCD cell model was performed by running evolutionary programming

3000 times with random initial parameter values as well as random upper and lower parameter bounds (700 generations, population size 70, Mersenne Twister and random seed). The best parameter set from the 1000 runs was taken, in case a parameter was located at a boundary, this boundary was extended by a factor of 100, and a subsequent parameter estimation was performed (evolutionary programming, 700 generations, population size 70, Mersenne Twister and random seed).

For all parameter estimation tasks performed in this thesis, the mean function in COPASI $w_j = \frac{1}{\langle x_j \rangle^2}$ was chosen as weight, and calculated manually so that it holds for the whole data set and not only within the individual experiments.

The time course simulation was solved with the deterministic LSODA method, which is part of the ODE-PACK library [41, 100].

Time dependent sensitivity analysis was performed using the algorithm proposed by Ingalls and Sauro [47] which was implemented in Mathematica7.0 [150].

2.2 Experimental approaches

2.2.1 Cell surface biotinylation

Cell surface biotinylation - background

As mentioned in Sec. 1.1.2 an increase in water reabsorption occurs when more AQP2 is located at the apical plasma membrane. Therefore, the relative amount of AQP2 at the membrane was investigated and how it changes over time after a stimulus by vasopressin. There exist different methods how that can be monitored. In an ideal world, AQP2 would be labeled with a fluorescent protein (e.g. GFP) and its localization over time would be monitored and analyzed with image analysis tools. Unfortunately this is not feasible, yet. Another method would be to perform immunocytochemistry. In this microscopic approach, cells would be stimulated, AQP2 would be labeled with antibodies, and images could be taken and analyzed. A further method would be to perform ultracentrifugation to separate the AQP2 vesicle fraction from the membrane fraction and to semiquantify and compare both fractions by western blot analysis.

For this work, a different method was chosen, which is cell surface biotinylation (see Fig. 2.2). With this method it is possible to distinguish between AQP2 located at the apical and the basolateral part of the cell.

The workflow for cell surface biotinylation is as follows. After stimulation of the cells with the desired substance (here, vasopressin was used), the cells are transferred to ice to stop any further AQP2 translocation. Afterwards the cells get biotinylated on the apical cell membrane (here, sulfo-NHS-SS-biotin was used; the N-hydroxysulfosuccinimide ester group on this reagent binds to the epsilon-amine of lysine residues and generates a stable product). After stopping the biotinylation reaction (quenching) the cells are lysed. Afterwards, the proteins from the apical membrane (labeled with biotin) are separated from the proteins from the cytoplasm, the intracellular membranes, and the basolateral membrane (all not labeled with biotin). This is done by isolating the biotin labeled proteins with streptavidin beads (streptavidin binds extremely strong to biotin with an affinity of 10^{15} M^{-1} [148] and is often used as a sensor for biotin). The biotin labeled proteins are eluded with Laemmli buffer [72], which cuts the disulfide bridge between the biotin and the protein.

The proteins from the apical membrane as well as the total lysate which serves as a control are analyzed

and semiquantified by western blot analysis.

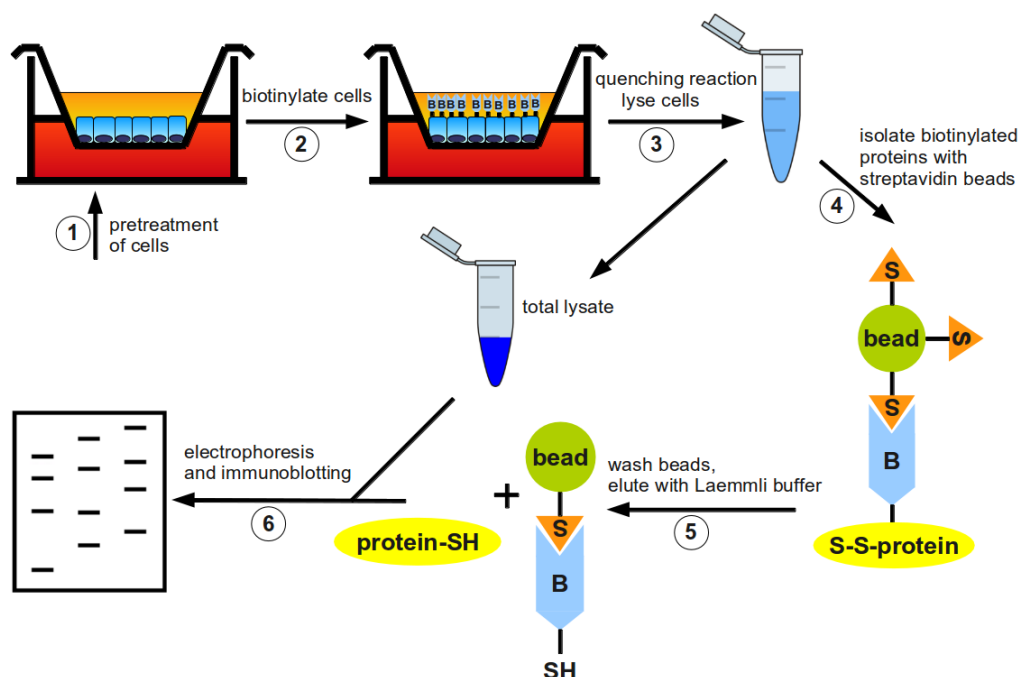


Figure 2.2: Workflow: cell surface biotinylation. 1. pretreatment of the cells as desired, 2. biotinylation of the cell surface proteins (here: at the apical cell membrane), 3. stopping (quenching) the biotinylation reaction and cell lysis, separation in test sample and control sample (total lysate) 4. use streptavidin beads to separate biotinylated proteins from others, 5. elute biotin labeled proteins with Laemmli buffer [72], 6. analyze eluded proteins as well as total lysate by western blot analysis.

Cell surface biotinylation - experiment

For this work Madin-Darby canine kidney cells (MDCK-hAQP2-T269S) were seeded at a density of $2.7 \cdot 10^5$ cells/cm² on semipermeable 4.7 cm² filters (Transwell®, 0.4 μm pore size, Corning Costar, Cambridge, MA, USA). The cells grew at 37°C for two days, then the medium was changed and $5 \cdot 10^{-5}$ M indomethacin was added for 1 more day to lower intracellular cAMP levels. After 3 days of seeding, the basolateral side of the cells was exposed to medium with (deamino-Cys1, D-arg8)-vasopressin (dDAVP, Sigma, St. Louis, MO, USA). Different concentrations of dDAVP were used (10^{-6} M and 10^{-8} M) for durations of 0, 2, 5, 10, 20, 30 and 90 min. Apical cell surface biotinylation was performed as in [21]. The samples were denaturated for 30 min at 37°C. Samples from total lysate were sonicated for 20 s. After SDS-PAGE on a 12% acrylamide gel the proteins were immunoblotted as in [21]. Incubation with the primary antibody against the C-tail of AQP2 (750 K5007, 1:100,000 dilution, kindly provided by Dr. M. Knepper, NIH, Bethesda) took place overnight at 4°C. The signal was amplified by 1:10,000-diluted biotinylated anti-rabbit IgGs and 1:8,000-diluted streptavidin-peroxidase (HRP; Sigma, St. Louis, MO, U.S.A.). Semi-quantification was performed with an Epson Expression 1640 XL (300dpi) using the software AIDA - Advanced Image Data Analyzer (V4.10.020; raytest Isotopemessgeräte GmbH). The experiment was done twice in duplicates.

3 Modeling of AQP2 trafficking in MDCK cells

To understand measured dynamics of AQP2 regulation and trafficking and to get a tool for rationale drug target prediction, a mathematical model was constructed based on knowledge from MDCK cells. In the first section of this chapter the model building and data fitting process is described.

After generation, the MDCK cell model was analyzed by

- generating and ranking model variants,
- sensitivity analysis,
- time dependent sensitivity analysis,
- model predictions and comparison with newly generated data.

At the end of this chapter the results of the different analyses are discussed.

3.1 A mathematical model of AQP2 trafficking in MDCK cells

A mathematical model was generated based on prior knowledge from MDCK cells to acquire new information about AQP2 trafficking. The currently available data are mainly qualitative and rarely quantitative and time course data are not available for most model components. In accordance with the availability of data it was decided to generate a more general and less detailed model. The model consists of the species vasopressin, cyclic AMP, inactive and active PKA, and AQP2 in internal vesicles as well as in the apical membrane. The concentration dynamics of the involved components are represented as a system of ordinary differential equations using mass action kinetics. The complete model version contains nine reactions: increase of cAMP via vasopressin, activation and inactivation of PKA, and endo- and exocytosis of AQP2. cAMP can be degraded via negative feedback from active PKA on cAMP, which represents the decrease of cAMP by phosphodiesterases as well as via a PKA independent mechanism. Since it has been shown that treatment of MDCK cells with vasopressin leads to internalization of the V2 receptor [115], the decrease of the stimulus was included into the model. Robben *et al.* [115] reported that the percentage of internalized receptors increases at a stronger stimulus of dDAVP. Hence, second order kinetics were used to implement that reaction. Furthermore, it was assumed that starting with a basal level of membrane located AQP2, this level does not change without any vasopressin stimulus. To achieve this, a constitutive exocytosis reaction was added to maintain a basal level of exocytosis and endocytosis.

The model does not include the regulation of endocytosis via vasopressin as proposed by Knepper and Nielsen in rat terminal IMCD [67]. Using the model by Knepper and Nielsen and MDCK cell data [20] it was shown that their model can reproduce the data reasonably well, when exclusively the exocytosis of AQP2 is regulated [29].

A graphical representation of the model is shown in Fig. 3.1. The corresponding differential equations

system is given in Table 3.1.

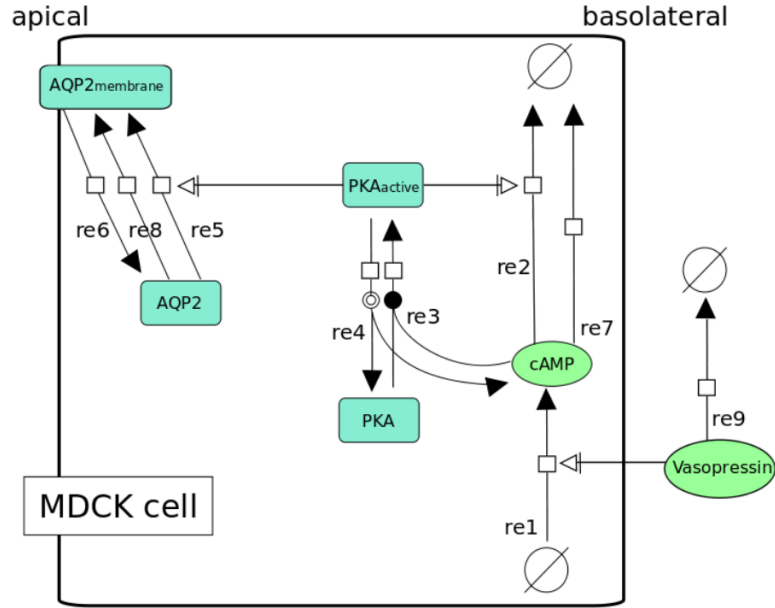


Figure 3.1: The MDCK cell model, using the Systems Biology Graphical Notation (SBGN) [49]. The model consists of 6 different species and 9 reactions. Vasopressin stimulates directly the increase of intracellular cAMP (re1). cAMP can form, together with PKA, in a reversible reaction PKA_{active} (re3), (re4). cAMP can be degraded in a PKA_{active} dependent (re2) and independent (re7) reaction. PKA_{active} stimulates the integration of AQP2 into the apical membrane (re5) which is assumed to occur also via a PKA_{active} independent reaction (re8). Endocytosis is assumed to depend only on the concentration of $AQP2_{membrane}$ (re6). The stimulus by vasopressin can decrease over time, which represents the internalization and desensitization of the V2 receptor (re9).

$\frac{d[PKA]}{dt}$	$= -(k3 \cdot [PKA] \cdot [cAMP]) + (k4 \cdot [PKA_{active}])$
$\frac{d[PKA_{active}]}{dt}$	$= (k3 \cdot [PKA] \cdot [cAMP]) - (k4 \cdot [PKA_{active}])$
$\frac{d[cAMP]}{dt}$	$= (k1 \cdot [AVP]) - (k2 \cdot [cAMP] \cdot [PKA_{active}]) - (k3 \cdot [PKA] \cdot [cAMP])$ $+ (k4 \cdot [PKA_{active}]) - k7 \cdot [cAMP]$
$\frac{d[AQP2]}{dt}$	$= -(k5 \cdot [AQP2] \cdot [PKA_{active}]) + (k6 \cdot [AQP2_{membrane}]) - (k8 \cdot [AQP2])$
$\frac{d[AQP2_{membrane}]}{dt}$	$= (k5 \cdot [AQP2] \cdot [PKA_{active}]) - (k6 \cdot [AQP2_{membrane}]) + (k8 \cdot [AQP2])$
$\frac{d[AVP]}{dt}$	$= -(k9 \cdot [AVP]^2)$
$k8$	$= k6 \cdot \frac{[AQP2_{membrane}][0]}{[AQP2][0]}$
$k1, \dots, k7, k9$	were estimated

Table 3.1: Algebraic and differential equations describing the model for MDCK cells. The model includes differential equations for the input stimulus vasopressin (AVP), cAMP, PKA and PKA_{active} as well as AQP2 and $AQP2_{membrane}$. Parameter $k8$ is calculated so that a basal amount of $AQP2_{membrane}$ is secured and the parameters $k1$ to $k7$ and $k9$ are estimated with COPASI.

3.2 Time course simulation and parameter estimation

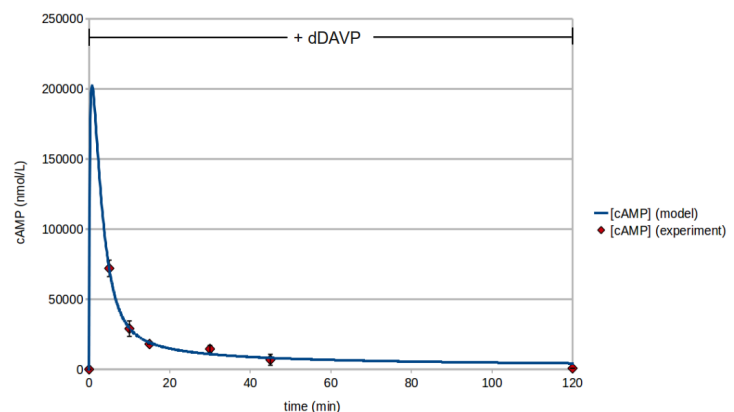
The model parameters were estimated to fit the experimental data taken from Deen *et al.* [20]. They measured the increase in osmotic water permeability (Pf) and the peak in [cAMP] after a stimulus by dDAVP as well as the decrease in Pf after dDAVP washout. Furthermore, information was taken from Xie *et al.* [152] to assign a range of the values for $[AQP2_{membrane}]$ between $114 \mu\text{M}$ and $255 \mu\text{M}$ with a total concentration of AQP2 ($[AQP2_{total}]$) of $1000 \mu\text{M}$. In the model it was assumed that, while starting with a basal AQP2 level of $114 \mu\text{M}$, this value should not change without any stimulus by vasopressin. A total PKA concentration of 500 nM was taken which is in consistency with published data [70, 130]. The absolute values for [cAMP] were taken from Deen *et al.* [20] and translated to nM. Parameter estimation was performed as described in materials and methods (see Sec. 2.1). The estimated model parameters are presented in Tab. 3.2 and the resulting data fits in Fig. 3.2.

Parameter name	Value	Units
k_1	$2.94e^{+5}$	1/min
k_2	$1.02e^{-3}$	l/(nmol · min)
k_3	$3.21e^{-4}$	l/(nmol · min)
k_4	$4.04e^{-0}$	1/min
k_5	$2.59e^{-5}$	l/(nmol · min)
k_6	$2.15e^{-2}$	1/min
k_7	$3.04e^{-2}$	1/min
k_8	$2.76e^{-3}$	1/min
k_9	$3.74e^{-0}$	l/(nmol · min)

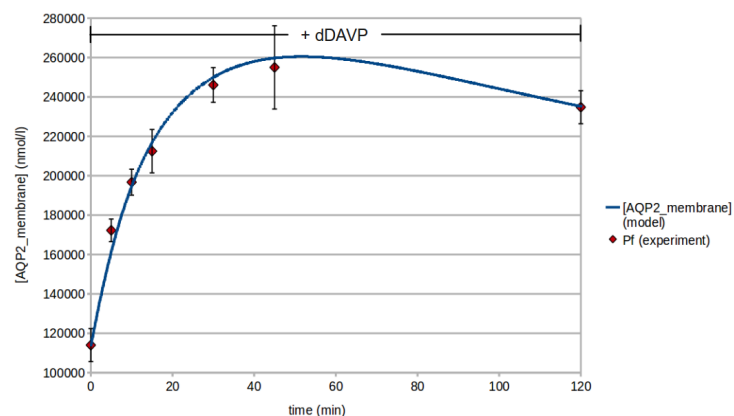
Table 3.2: Estimated model parameters for the complete MDCK model. The parameters for the model shown in Fig. 3.1 with the differential equations given in Tab. 3.1 were estimated to reproduce the biological data (see Fig. 1.6) best. The parameters were estimated with COPASI.

3.3 Model variations and ranking - To reproduce the data either a negative feedback or degradation of the stimulus has to be included

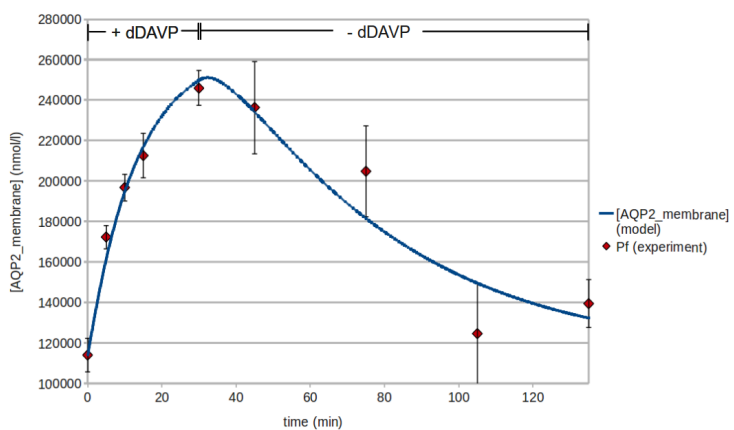
It was tested whether the data set from Deen *et al.* [20] could also be reproduced with a simpler variant of the model to get an impression, which parts of the model are essential. Therefore, different model variants were generated excluding either the negative feedback by phosphodiesterases (-re2), the reduction of the signal representing internalization of the receptor (-re9) or both (-re2 -re9) (see Fig. 3.3). Parameter estimation was performed for all model variants as described in Sec. 2.1. They were ranked according to their objective function (see Fig. 3.4, the calculation of the objective function is described in Sec. 2.1). The models including either the vasopressin receptor internalization or the negative feedback had a better fit than the minimal model, which was not able to reproduce the peak of intracellular cAMP. The models including vasopressin receptor internalization were able to reproduce the data best.



(a)



(b)



(c)

Figure 3.2: Parameter estimation with the old and the new data set using COPASI. Fitting of intracellular cAMP time course (a) and membrane localized AQP2 (b) after a stimulus with 10^{-8} M vasopressin, c) Fitting of membrane localized AQP2 after addition of 10^{-8} M vasopressin for 30 min followed by washout of vasopressin.

3.3 Model variations and ranking - To reproduce the data either a negative feedback or degradation of the stimulus has to be included

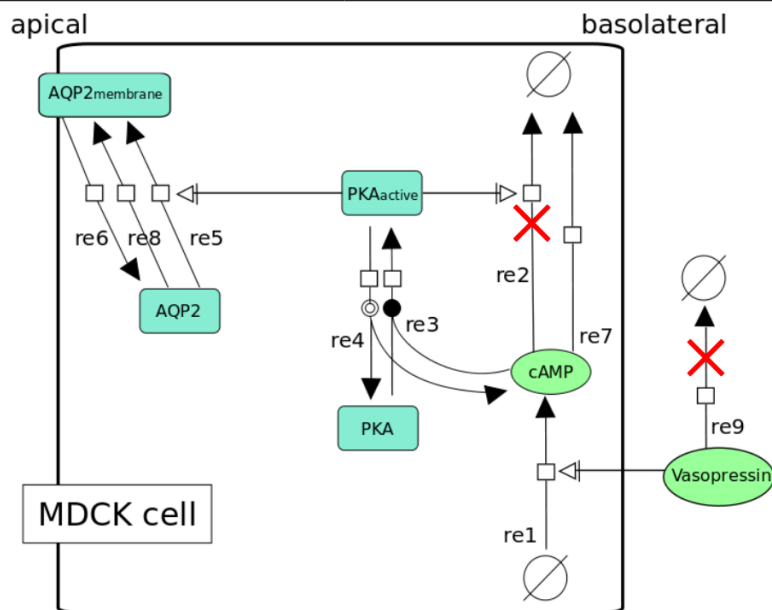


Figure 3.3: Generating of variants of the MDCK cell model. Generation of different model variants by deleting the labeled reactions. The model variants are later referred to as: Complete: model version as shown in Fig. 3.1; -re2: complete model reduced by reaction re2 representing negative feedback via phosphodiesterases; -re9: complete model reduced by reaction re9, which represents the internalization and degradation of the receptor; -re2 -re9: reduced by both reactions re2 and re9.

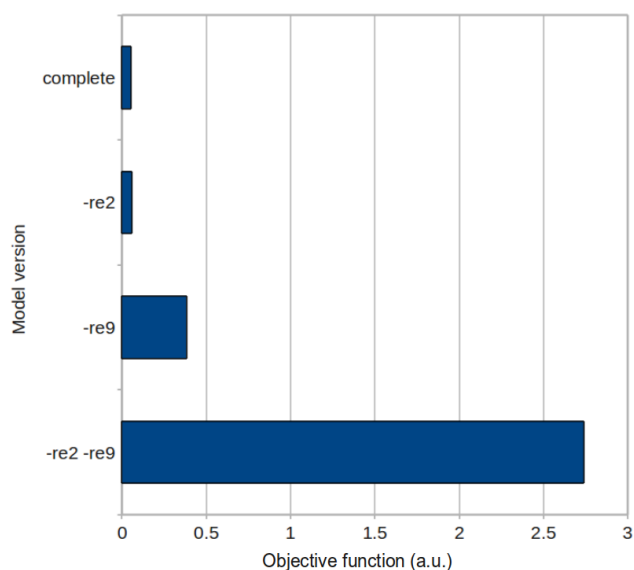


Figure 3.4: Ranking of variants of the MDCK cell model. Ranking of the model variants presented in Fig. 3.3 by their objective function. Complete: model version as shown in Fig. 3.1; -re2: complete model reduced by reaction re2 representing negative feedback via phosphodiesterases; -re9: complete model reduced by reaction re9, which represents the internalization and degradation of the receptor; -re2 -re9: reduced by both reactions re2 and re9.

3.4 Sensitivity analysis reveals importance of AQP2 endocytosis

It was investigated how sensitive the model species cAMP and AQP2 at the membrane react to minor perturbations in the parameter values. To get a first impression, the effect on the model species was analyzed with the sensitivity analysis task in COPASI after a simulation of 120 min (the longest duration for which experimental data was available, delta factor: 0.0001, delta minimum: 1e-12).

Fig. 3.5 shows that cAMP was highly sensitive to the parameters k_1 , k_2 and k_9 , which represent the activation of cAMP by vasopressin, the negative feedback loop, and decrease of vasopressin by reaction re9, which represents the internalization of the receptor. Shortly after followed the parameters k_3 and k_4 , representing the binding of cAMP to PKA as well as the detachment of cAMP from PKA. k_7 , the PKA independent cAMP degradation, has only minor effect.

$AQP2_{membrane}$ was highly sensitive to parameter k_6 , which characterizes the internalization of AQP2. Furthermore k_5 and k_8 had high effects on $AQP2_{membrane}$, which are the PKA depend and PKA independent translocation of AQP2 to the membrane.

The hypothesis which could be drawn from this analysis was that if one wants to suppress or increase the amount of $AQP2_{membrane}$ at the conditions present in the model simulation, the most effective way would be to target the processes responsible for AQP2 internalization.

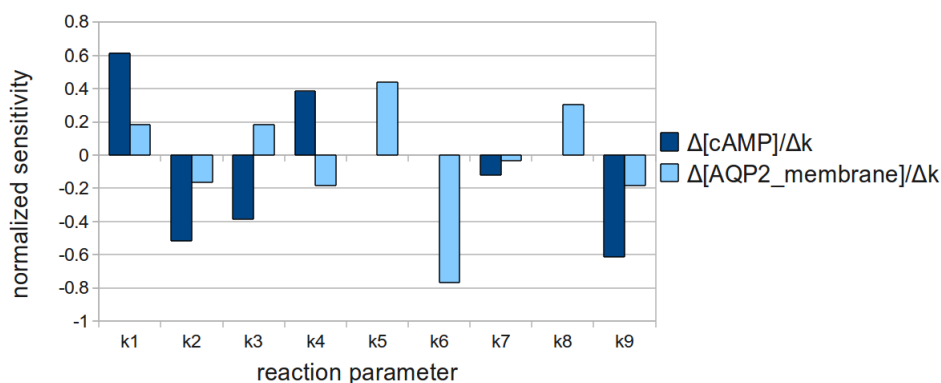


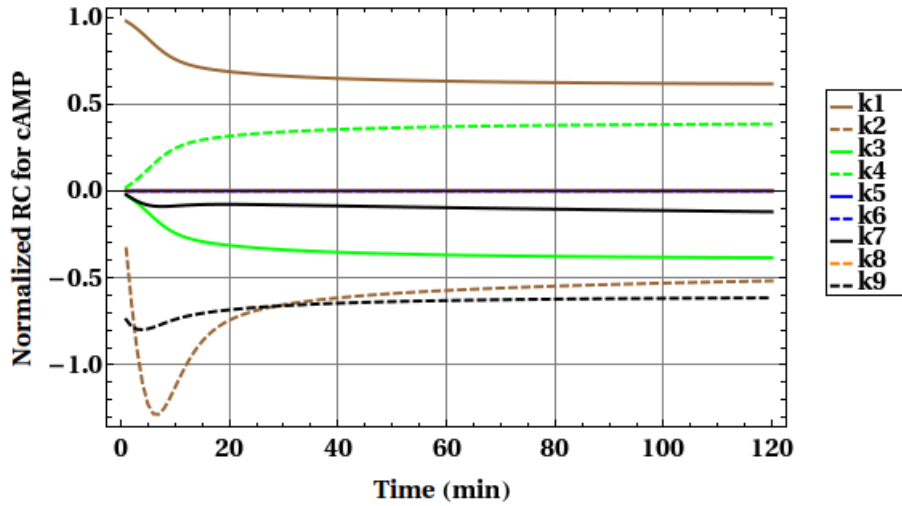
Figure 3.5: Sensitivity analysis of the MDCK cell model. Effect of small perturbations in the parameters on the model species at time point 120 min. The normalized sensitivities were taken. The analysis was performed with COPASI.

3.5 Time-dependent sensitivity analysis

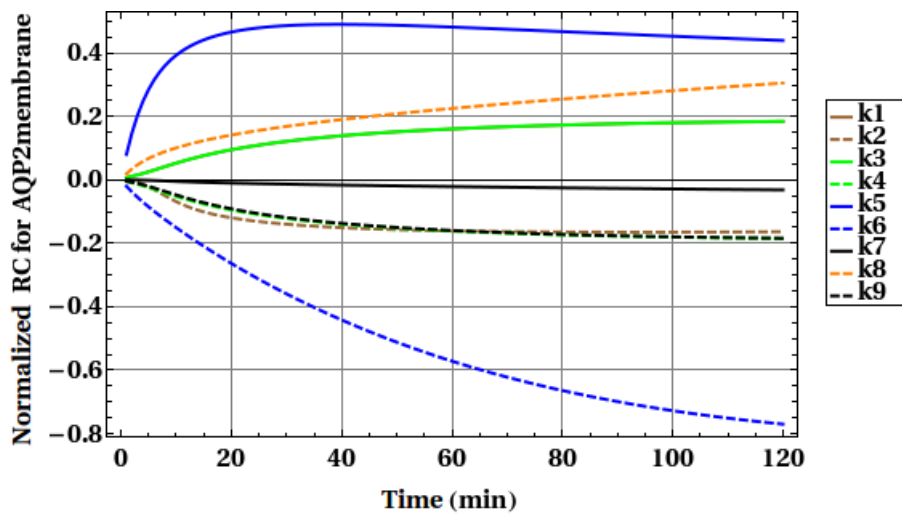
While looking at signaling cascades, i.e. systems with the function to react on temporal changes, one is mainly interested in the behavior over time and not only at the system at steady state or at one specific time point. Therefore, in addition to the analysis performed in the previous section, time-dependent sensitivity analysis was used to analyze the model [47].

It was analyzed how sensitive the model species cAMP and $AQP2_{membrane}$ react to minor changes in the model parameter values (Fig. 3.6).

The analysis was applied on the complete model with the optimal set of parameters found in Sec. 3.2. cAMP was highly sensitive to the parameters k_1 , k_2 and k_9 , which represent the activation of cAMP by



(a)



(b)

Figure 3.6: Time-dependent sensitivity analysis. Time-dependent sensitivity analysis performed with the complete MDCK cell model as shown in Fig. 3.1 with the optimal set of parameters found. **a)** Time-dependent normalized response coefficients (RC) for all parameters in respect to cAMP. **b)** Time-dependent normalized response coefficients (RC) for all parameters in respect to AQP2 in the membrane.

vasopressin, the negative feedback loop, and the decrease of vasopressin by reaction re9, corresponding to the internalization of the receptor. While calculating the sensitivities over time, a change in $k1$ had the strongest (positive) effect when cAMP got accumulated at the beginning of the stimulation, while $k9$ and $k2$ affected cAMP mostly around the time when the peak started and finished decreasing, respectively. $AQP2_{membrane}$ was highly sensitive to parameters $k5$ and $k6$, which characterize AQP2 translocation to the membrane as well as its internalization. The effect of a small change in $k5$ was not as strong as a change in $k6$, but it appeared earlier after the begin of the stimulus.

3.6 AQP2 translocation after dDAVP stimulation

After AQP2 is phosphorylated at S256 it is translocated to the apical plasma membrane [3]. Cell surface biotinylation as described in Sec. 2.2.1 was performed to monitor the amount of AQP2 at the membrane over time after a stimulus by dDAVP (see Fig. 3.7). The experiments were performed by myself in the laboratory of Prof. Deen (Radboud University Nijmegen Medical Centre, Nijmegen, the Netherlands).

As can be seen in Fig. 3.8(a) and 3.8(b), there is an increase in AQP2 at the membrane over time after treatment with 10^{-6} M and 10^{-8} M dDAVP, respectively. There appear two bands at approximately 28 and 29 kD (indicated by arrows), which seem to be AQP2 specific and are changing over time. In the total lysate, only one band can be detected (see Figure 3.7). This might be a hint that AQP2 in internal vesicles occurs mainly in one form, whereas AQP2 at the membrane occurs in two major forms that might be phosphorylated and unphosphorylated or otherwise modified. Fig. 3.8(a) reveals an increase in AQP2 at the apical plasma membrane after a stimulus with 10^{-6} M dDAVP. Fig. 3.8(b) shows the time curve after a stimulus by 10^{-8} M dDAVP. For these plots the intensity of the bands of the membrane fraction (upper and lower band were added) were taken, first normalized with the intensity of the total lysate and than normalized to one. At 10^{-6} M dDAVP, the curve shows an increase until it reaches its maximum after 30 min. Then it drops slightly at 90 min. The curve with 10^{-8} M dDAVP treatment looks more staggered. It increases first, decreases then slightly, increases again sharply till the maximum is reached after 20 min. Then it starts decreasing again and after 90 min a value below 50% of the maximum is reached.

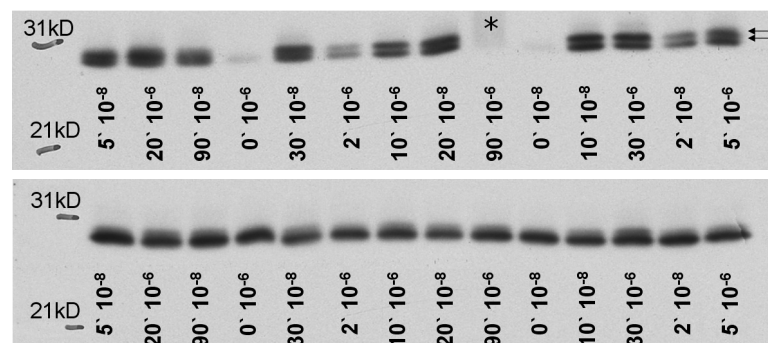


Figure 3.7: Cell surface biotinylation, monitoring AQP2 translocation over time. Membrane fraction (upper panel) and total lysate (lower panel) of cells treated with 10^{-6} M dDAVP and 10^{-8} M dDAVP for durations of 0, 2, 5, 10, 20, 30 and 90 min, loaded in random order. The sample labeled with * was left out from the calculation shown in Fig. 3.8.

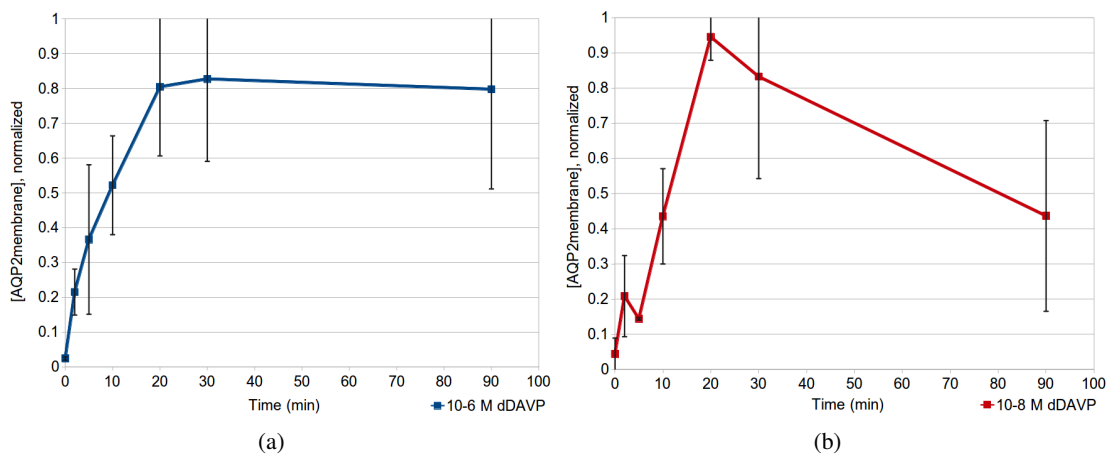


Figure 3.8: Cell surface biotinylation performed on MDCK cells. a) Amount of AQP2 at the membrane after treatment with 10^{-6} M dDAVP. **b)** Amount of AQP2 at the membrane after treatment with 10^{-8} M dDAVP. (The experiments were done twice in duplicates.)

3.7 Model predictions and comparison with recent data

An interesting analysis to perform with the model was how the system reacts to different input stimuli. Important for the clinical analysis is here to study the amount of AQP2 at the membrane, because this should be directly related to the amount of water being reabsorbed. Also interesting was how the intracellular pathway behaves. Since data for cAMP was already available for one dDAVP concentration and therefore at least one time course was fixed, it was decided to test also this model species in additional *in silico* experiments.

The most reasonable model version from Sec. 3.3 together with the best set of model parameters found in Sec. 3.2 was used to perform the experiments *in silico*.

3.7.1 Prediction of the dose response of vasopressin on AQP2 in the membrane

The change of $AQP2_{membrane}$ in response to a variation in the input stimulus dDAVP was simulated. The dDAVP concentration which was used for the model fitting process in Sec. 3.2 was 10^{-8} M. The change of $AQP2_{membrane}$ was predicted after addition of 10^{-6} M to 10^{-14} M dDAVP as well as after stimulation with dDAVP for 30 min followed by washout of dDAVP (see Fig. 3.9(a) and (b), respectively).

The model indicates that $AQP2_{membrane}$ is already saturated at a concentration of 10^{-9} M dDAVP, which explains why no higher value of $AQP2_{membrane}$ was observed at 10^{-6} M in comparison to 10^{-8} M dDAVP (see Fig. 3.8). This would also be reinforced by experiments performed by myself on the dephosphorylation of S261, which occurs during dDAVP stimulation. As with the membrane localization of $AQP2_{membrane}$ also the dephosphorylation of S261 seems to be saturated at concentrations above 10^{-8} M dDAVP (see Sec. 2 in the Appendix).

What could not be observed during the simulation was a difference between the sustained and transient response of the system at concentrations of 10^{-6} M and 10^{-8} M dDAVP. At both concentrations $AQP2_{membrane}$ was rather similar over time, reached a maximum at around 50 min and decreased slowly afterwards.

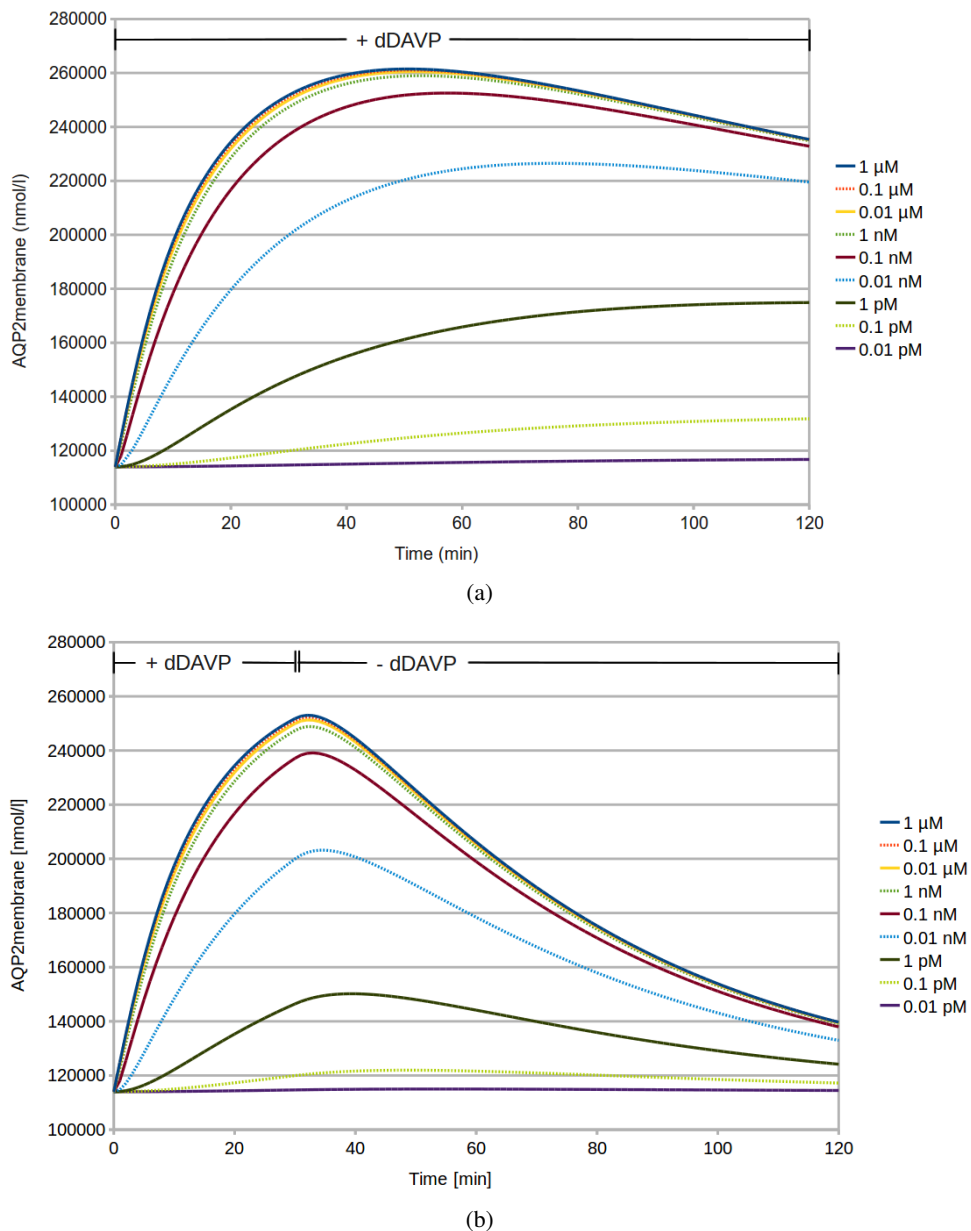


Figure 3.9: Prediction of $AQP2_{membrane}$ over time at different dDAVP concentrations using the MDCK cell model. dDAVP concentration in log scale from 10^{-6} M to 10^{-14} M. **a)** Time course after stimulus with dDAVP at 0 min. **b)** Time course after stimulus with dDAVP at 0 min and washout of dDAVP at 30 min.

3.7.2 Prediction of the dose response of vasopressin on cAMP

Since for this model system only the time course for cAMP at one concentration of dDAVP (10^{-8} M) was available and could be used for parameter estimation, the complete model with the best set of parameters found (see Fig. 3.1 and Tab. 3.2) was used to estimate the cAMP time courses at other dDAVP concentrations. In Fig. 3.10 the estimated time courses for the dDAVP concentrations from 10^{-8} M to 10^{-13} M are presented. The inset shows a detailed version of the dDAVP concentrations corresponding to AVP in a more physiological range from 10^{-11} M to 10^{-13} M.

It can be seen that the cAMP peak in the beginning of the time course, which is very pronounced at high dDAVP concentrations, vanishes at low dDAVP concentrations. One can still see a cAMP increase, but no peak anymore. This supports the hypothesis that it is important to look at lower, more physiological conditions, because here the whole kinetic behavior of the system might be different.

Furthermore, if looking at high dDAVP concentrations, it would be of significant importance to determine the cAMP level within the first 5 min to verify or falsify the model hypothesis and, if necessary, to use the newly generated data to improve the model.

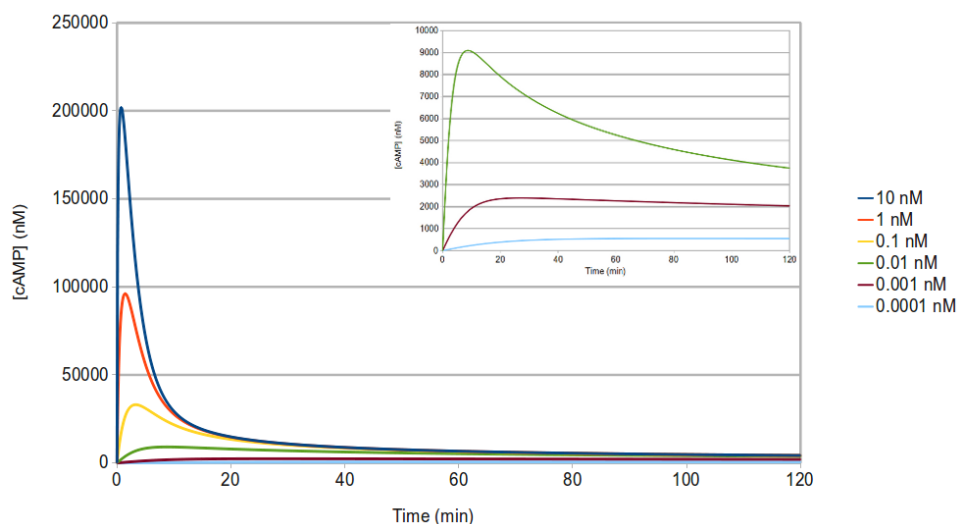


Figure 3.10: Prediction of cAMP concentration over time at different dDAVP concentrations using the MDCK cell model. The predictions were performed by using the complete model with the best set of parameters found (see Fig. 3.1 and Tab. 3.2). Time course of [cAMP] after stimulus with dDAVP. dDAVP concentration in log scale from 10^{-8} M to 10^{-13} M. The figure inset on the upper right is a magnification of the y-axis and shows [cAMP] over time at the three smallest dDAVP concentrations tested. dDAVP concentration in log scale from 10^{-11} M to 10^{-13} M.

3.8 Prediction of potential drug targets with TIdE

Using the carefully parameterized model, it was investigated which reactions are suitable targets in case of medically relevant perturbations. Therefore, the software TIdE [126] was used to analyze the effect of potential activators and inhibitors on $AQP2_{membrane}$. TIdE can automatically substitute individual model reactions by corresponding modifier kinetics (e.g. non-competitive inhibition or non-essential activation). For a reaction with the velocity $v(S, p)$ the software generates a potential non-competitive inhibition with

the velocity

$$v_{inh}(\mathbf{S}, \mathbf{p}, Inh, K_i) = v(\mathbf{S}, \mathbf{p}) \cdot \left(\frac{1}{1 + \frac{Inh}{K_i}} \right)$$

and a non-essential activation reaction with the velocity

$$v_{act}(\mathbf{S}, \mathbf{p}, Act, K_a) = v(\mathbf{S}, \mathbf{p}) \cdot \left(1 + \frac{Act}{K_a} \right).$$

\mathbf{S} are the concentrations of the involved species, \mathbf{p} the parameters of the original reaction, Inh the inhibitor concentration, Act the activator concentration, and K_a and K_i the dissociation constant of the activator and the inhibitor, respectively. To evaluate the quality of the different drug treatments, an objective function (usually a formula containing substance concentrations or fluxes) can be defined by the user. Furthermore, synergism analysis can be performed to identify synergistic or antagonistic effects, i.e. drug combinations that, when taken together, increase or decrease each other's effectiveness, respectively.

Applying the software to the model of AQP2 trafficking one can investigate for example, how one can perturb the amount of $AQP2_{membrane}$ at or over a given time with activators and inhibitors. For this *in silico* experiment once again the complete model with the best set of parameters found (see Fig. 3.1 and Tab. 3.2) was used.

Two medically relevant use cases were analyzed in more detail:

Medical case 1:

- the gene expression of AQP2 is impaired and the concentration of $AQP2_{total}$ is reduced by 50%
- all other species remain unaffected
- the model reactions 5 and 8 (PKA dependent and independent AQP2 translocation to the membrane) are affected by the same inhibitor or activator.

Medical case 2:

- the vasopressin abundance is impaired. In the current setup this means that, instead of 10 nM, there is only a stimulus by 10 fM, 1 pM or 10 pM dDAVP.
- all other species remain unaffected
- the model reactions 5 and 8 (PKA dependent and independent AQP2 translocation to the membrane) are affected by the same inhibitor or activator.

For both medical cases Tlde was used to solve the following question:

- How can one influence the pathway to reach the same concentration of $AQP2_{membrane}$ as in the "healthy" state?

Analysis of medical case 1:

By running the model with different concentrations of $AQP2_{total}$ it turned out that the amount of $AQP2_{membrane}$ is predicted to be proportional to the amount of total AQP2 (see Fig. 1 in the Appendix). Therefore a reduction of $[AQP2_{total}]$ by 50% reduced also $[AQP2_{membrane}]$ by 50%.

Hence, for the scenario of medical case 1, $[AQP2_{total}]$ was set to $500 \mu\text{M}$ instead of $1000 \mu\text{M}$. The maximal concentration of $AQP2_{membrane}$ during the 120 min simulation with the original concentration of $AQP2_{total}$ was $260 \mu\text{M}$ at 52 min. By allowing some divergence from this value still to be classified as "healthy", the objective function was set to $\frac{250 \mu\text{M}}{AQP2_{membrane}[52 \text{ min}]}$. An inhibitor or activator concentration leading to an objective function value of 1 or smaller was assumed to restore the "healthy" state.

Individual drugs First, all inhibitors and activators were analyzed individually with 1st line search (lower and upper boundaries of 0.1 nM and $10 \mu\text{M}$, respectively, increased in 50 steps logarithmically). In Fig. 3.11 D the dose response relationship for all drugs are shown for which a value of $250 \mu\text{M}$ $AQP2_{membrane}$ at 52 min was reached somewhere within the applied concentration range. For medical case 1 only one potential drug was able to reach an objective value below 1, individually. This was activator_{re5,re8}, which acts as an activator of the PKA dependent and independent translocation of AQP2 to the membrane.

Drug combinations Next, it was investigated which concentrations of potential drugs are in combination sufficient to reach $250 \mu\text{M}$ of $AQP2_{membrane}$ and whether there exist potential synergistic or antagonistic effects. Therefore, synergism analysis was performed with lower and upper boundaries of 0.1 nM and $10 \mu\text{M}$, respectively, increased in 50 steps logarithmically.

The most efficient drug combination was activator_{re5,re8} and inhibitor_{re6}. In Fig. 3.12 (blue squares) minimal concentrations for the combination activator_{re5,re8} and inhibitor_{re6} are shown, which were found with the used step sizes. Whereas a treatment with activator_{re5,re8} alone was able to restore the "healthy" state at a concentration of 2.36 nM , as soon as the concentration of activator_{re5,re8} was decreased, inhibitor_{re6} had to be increased strongly.

Simulations with varying dosage for this drug combination are given in 3.13. At a combination of high activator_{re5,re8} and low inhibitor_{re6} concentration, $AQP2_{membrane}$ increased up to $250 \mu\text{M}$ and decreased slightly afterwards (see Fig. 3.13 A and B), which would be similar to the original data.

Instead, by using a combination of low activator_{re5,re8} and high inhibitor_{re6} concentration, higher doses of the drugs were necessary and $AQP2_{membrane}$ kept increasing after 52 min. In the long run, the amount of water being reabsorbed might be too high (see Fig. 3.13 C and D).

For activator_{re5,re8} and inhibitor_{re6} no synergism or antagonism was observed in the relevant concentration range.

Analysis of medical case 2:

In medical case 2 it was assumed that the concentration of vasopressin is reduced, as it would be the case for central diabetes insipidus (CDI). Instead of 10 nM the system was stimulated by 10 fM , 1 pM or 10 pM dDAVP. All other species were kept unchanged. As before it was assumed that the reactions re5 and re8 (PKA dependent and independent AQP2 translocation to the membrane) are affected by the same inhibitor or activator.

As in medical case 1, Tlde was used to analyze potential individual drugs and drug combinations that are able to rescue the concentration of $AQP2_{membrane}$. Also here the desired goal was to reach $250 \mu\text{M}$ $AQP2_{membrane}$ after 52 min dDAVP stimulation.

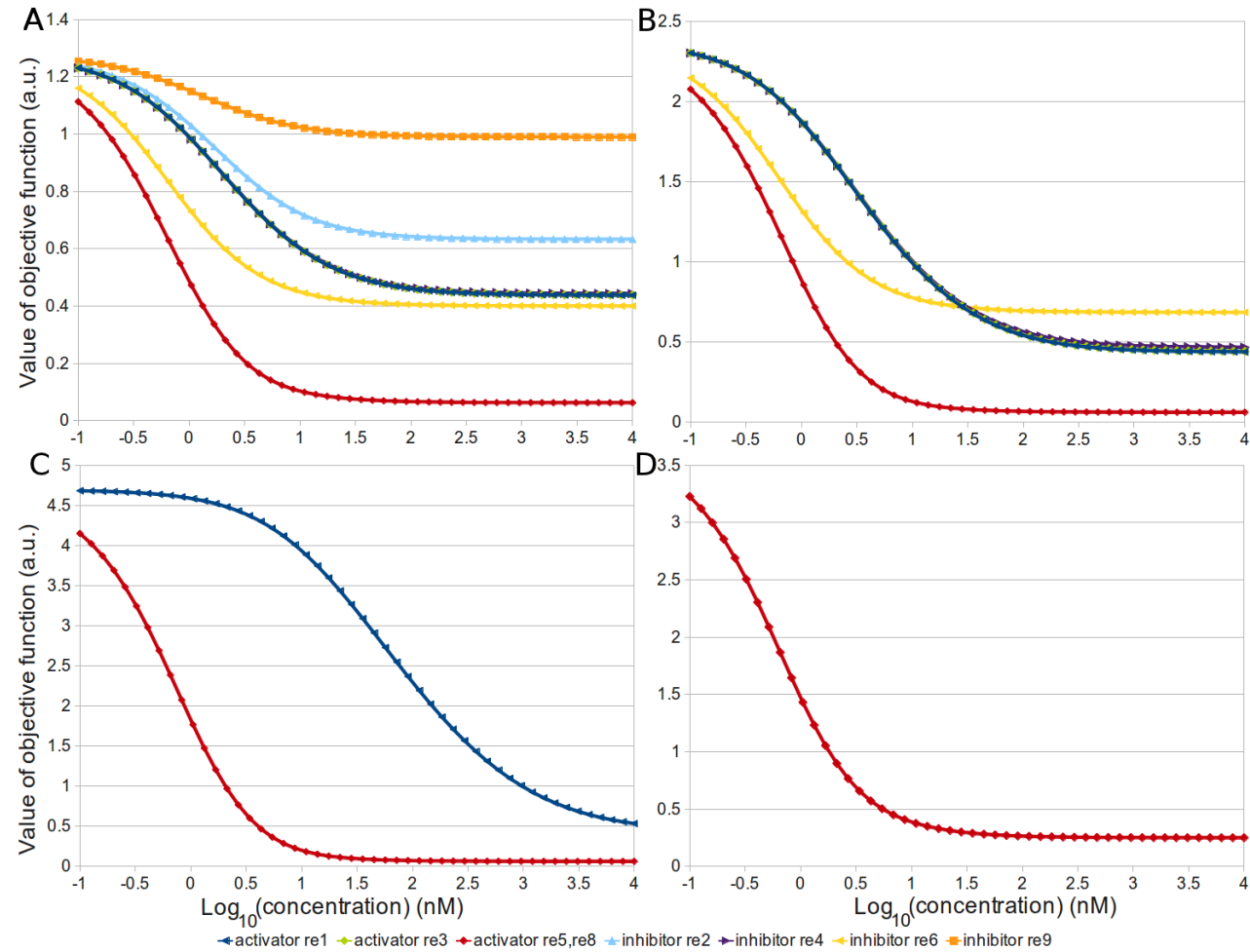


Figure 3.11: Identification of potential drug targets with Tide. It was analyzed with 1st line search how the application of individual inhibitors or activators can influence the concentration of $\text{AQP2}_{membrane}$ during medical case 1 and 2. An objective function value of 1 indicates that exactly $250 \mu\text{M}$ $\text{AQP2}_{membrane}$ were reached at the given concentration of the inhibitor or activator. Objective function values smaller than 1 represent that $\text{AQP2}_{membrane}$ concentrations above $250 \mu\text{M}$ $\text{AQP2}_{membrane}$ were reached. **A)** 10 pM dDAVP **B)** 1 pM dDAVP **C)** 10 fM dDAVP **D)** 50% reduction in AQP2_{total} .

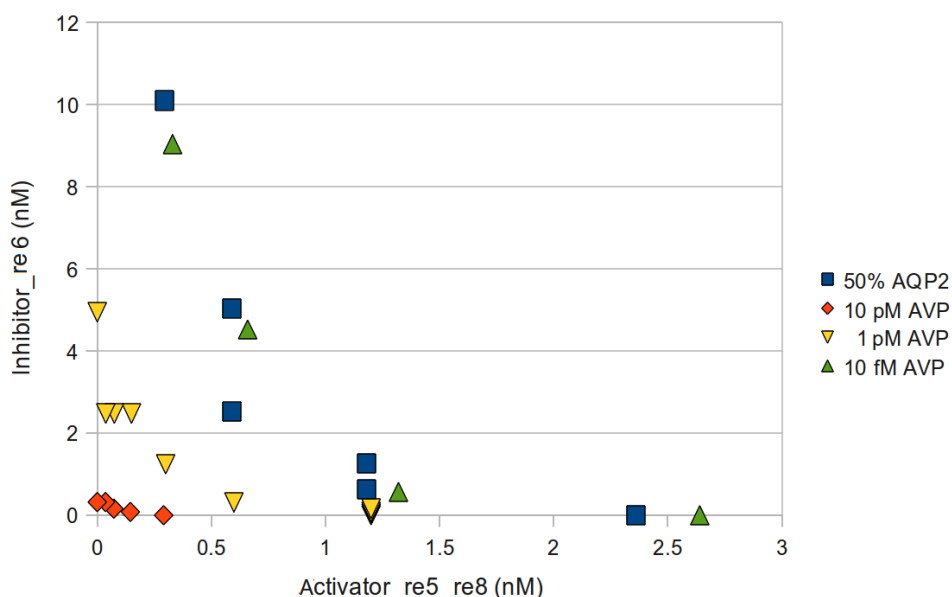


Figure 3.12: Analysis of drug combinations for medical case 1 and 2. Minimal drug combinations of activator_{re5,re8} and inhibitor_{re6} that were able to reach the desired state during stimulation with 10 fM, 1 pM, and 10 pM dDAVP. For comparison, the combination necessary to bring medical case 1 into the desired range is also presented here.

Individual drugs 1st line search was applied to analyze all inhibitors and activators individually (lower and upper boundaries of 0.1 nM and 10 μ M, respectively, increased in 50 steps logarithmically). In Fig. 3.11 A-C the dose response relationships for all drugs are shown for which a value of at least 250 μ M AQP2_{membrane} at time point 52 min was reached at any drug concentration within the applied range during application of A) 10 pM dDAVP, B) 1 pM dDAVP, and C) 10 fM dDAVP. It was observed that with decreasing concentration of dDAVP the selection of possible drugs able to rescue the concentration of AQP2_{membrane} gets reduced. By application of 10 pM dDAVP, 7 drugs were able to reach the desired concentration of AQP2_{membrane}; by application of 1 pM and 10 fM dDAVP this was the case for 5 and 2 drugs, respectively.

The most effective drug was in all cases activator_{re5,re8} (affecting PKA dependent and independent AQP2 translocation to the membrane). The concentration which was necessary to reach a concentration of AQP2_{membrane} above 250 μ M increased with decreasing dDAVP concentration (0.2 nM for 10 pM dDAVP, 0.83 nM for 1 pM dDAVP, 2.12 nM for 10 fM dDAVP).

The second most effective drug was at 10 pM dDAVP inhibitor_{re6}, the inhibitor of the AQP2 internalization reaction. This was the same for 1 pM dDAVP, if one focused at the lowest concentration necessary to reach AQP2_{membrane} concentrations above 250 μ M. If the desired goal was to reach the highest AQP2_{membrane} concentration possible, also activator_{re1}, activator_{re3} and inhibitor_{re4} became important (activators of the cAMP production, PKA activation and inactivation).

For the lowest AVP concentration tested *in silico*, 10 fM dDAVP, activator_{re1} (activator of the cAMP production) was the only drug besides activator_{re5,re8} that reached AQP2_{membrane} concentrations above 250 μ M in the tested concentration ranges, although much higher concentrations would be necessary.

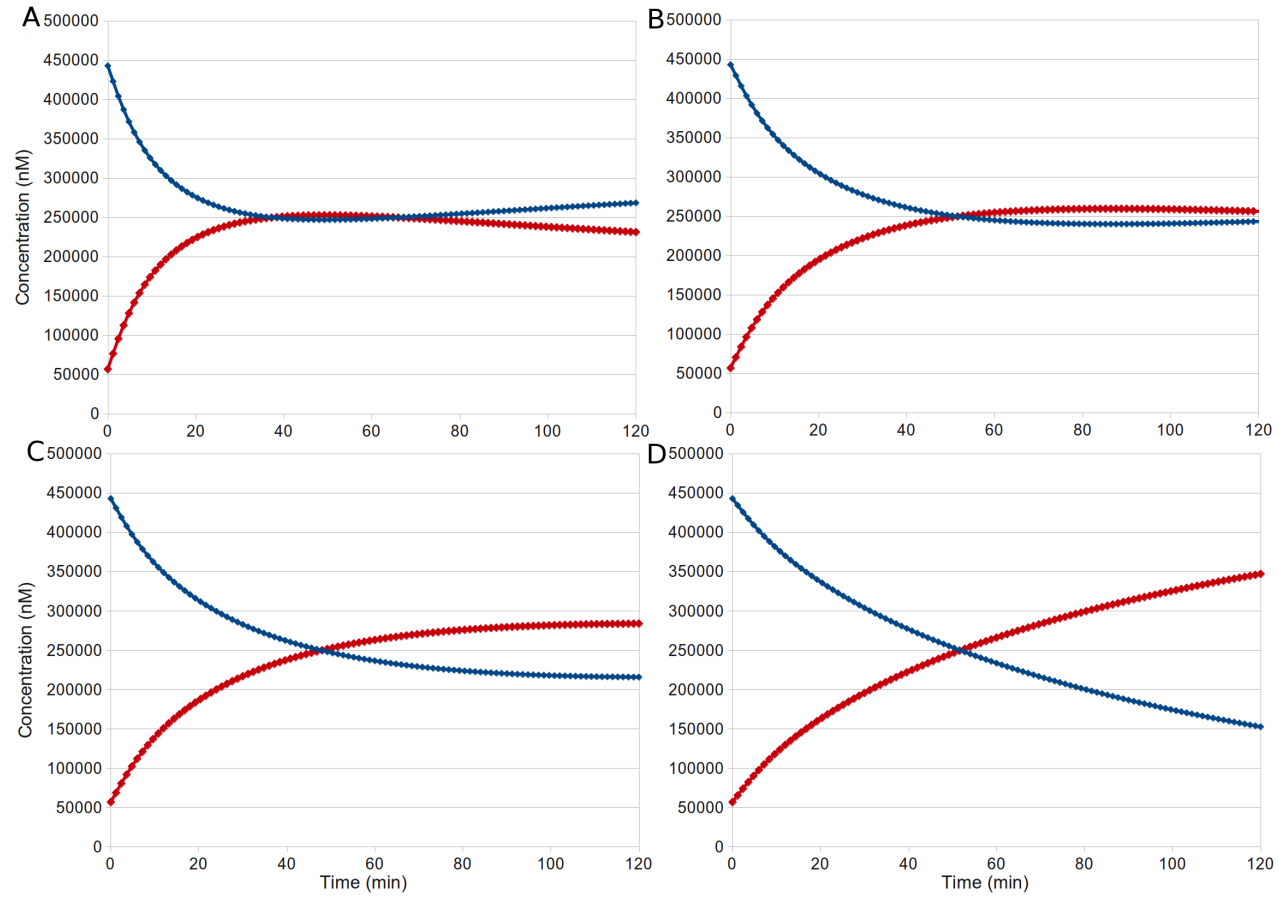


Figure 3.13: Analysis of drug combinations for medical case 1. Exemplary combinations of activator_{*re5, re8*} and inhibitor_{*re6*} are shown. Those combinations are along the curve for the minimal necessary concentrations to reach more than $250 \mu\text{M}$ AQP2_{*membrane*}, which was defined as healthy in this use case. **A:** activator_{*re5, re8*} 1.87 nM, inhibitor_{*re6*} 0 nM **B:** activator_{*re5, re8*} 0.93 nM, inhibitor_{*re6*} 0.83 nM, **C:** activator_{*re5, re8*} 0.66 nM, inhibitor_{*re6*} 1.87 nM, **D:** activator_{*re5, re8*} 0.13 nM, inhibitor_{*re6*} 110 nM

Drug combinations The effect of drug combinations and their synergistic effects were tested with synergism analysis (lower and upper boundaries of 0.1 nM and 10 μ M, respectively, increased in 50 steps logarithmically). The most prominent drug combination was, same as with medical case 1, the activator_{re5,re8} and inhibitor_{re6}. Except for the lowest dDAVP concentration (10 fM) this combination was ranked as most efficient. Fig. 3.12 shows minimal combinations of activator_{re5,re8} and inhibitor_{re6} for the three dDAVP concentrations that were able to reach the desired state. It was observed that the lower the dDAVP concentration, the higher dosage of drugs had to be used.

At 10 fM dDAVP the combination of activator_{re5,re8} and activator_{re1} were marked as most efficient, which is in agreement with the results from 1st line search (Fig. 3.11 C).

3.9 Discussion

The aim of this chapter was to propose a mathematical model for AQP2 trafficking in MDCK cells, which can be used to analyze the dynamic behavior of the system after dDAVP stimulation. The proposed model includes the widely accepted pathway via intracellular cAMP and PKA. The parameters of the model were estimated using data from Deen *et al.* [20].

The model was used to analyze the presence of a negative feedback representing phosphodiesterases as well as a reduction of the signal representing internalization of the V2 receptor. cAMP and AQP2_{membrane} concentrations over time were predicted, the latter was compared with newly generated data. Sensitivity as well as time-dependent sensitivity analysis were performed. Finally, potential drug treatments were analyzed for different medical use cases.

To conclude the major results from this chapter:

- The proposed model was able to reproduce the biological data.
- Ranking of model variants showed that either internalization of the V2 receptor or the negative feedback by phosphodiesterases has to be present to reproduce the biological data. Internalization of the receptor seemed to be more important.
- Sensitivity analyses showed that AQP2_{membrane} is highly sensitive to AQP2 internalization, which might be a potential drug target.
- The model predicted that AQP2_{membrane} has already reached its maximum value at AVP concentrations of 1 nM. This was supported by newly generated data.
- The drug target identification tool TId identified the reactions directly involved in AQP2 trafficking as feasible drug targets. Optimal single and combinatorial treatments with potential inhibitors and activators of those reactions were proposed.

In the following, those results as well as the major aspects of the model shall be discussed.

MDCK cell model Due to the sparse amount of time resolved data available for the different species involved in AQP2 trafficking, the model was restricted to the main players of the pathway (vasopressin, cAMP, PKA, AQP2). The activation of the G-protein coupled receptor, the detachment of the subunits and the activation of the adenylate cyclase were summarized in one reaction, the activation of cAMP production by vasopressin. Due to the same reason, simple kinetics were chosen for the PKA activation,

which were already able to describe the kinetics of the available data.

Another possibility would have been to reuse a model for the cAMP/PKA pathway (e.g. from the model of beta-adrenergic signaling in cardiac myocytes by Saucerman *et al.* [123]) and refit the parameters to the MDCK cell data. Although first steps were made into this direction (data not shown), it was decided to use a simplified model instead to avoid overparameterization.

In contrast to the proposed model by Knepper and Nielsen [90] based on work with isolated tubules, vasopressin dependent regulation of endocytosis was not included in the MDCK cell model. Applying their 2-state model to data from MDCK cells [20] led to the conclusion that this regulation would be irrelevant in MDCK cells (see supplementary material in [29]).

During parameter estimation, the peak in cAMP was allowed to be higher than observed in the experimental data, because the information about the cAMP concentration between 0 and 5 min was lacking. The data from Deen *et al.* [20] is based on a whole population of MDCK cells. It remains to be verified whether the peak of cAMP exists also in individual cells and if cell-to-cell variation exists. Also possible would be that single cells exhibit damped cAMP oscillations which are synchronized shortly after dDAVP stimulation and desynchronized on the longer run, therefore resulting in a peak if averaged over the whole population.

Ranking of model variants To reproduce the experimental data for intracellular cAMP [20] either the negative feedback representing phosphodiesterases or the reduction of the vasopressin signal is required. Using mass action kinetics, the model version including the internalization of the receptor performed better than the model which includes only the negative feedback. This might be a hint that in MDCK cells the internalization of the V2 receptor is more important for the kinetic behavior of AQP2 trafficking than the negative feedback by phosphodiesterases.

Sensitivity and time dependent sensitivity analysis Time dependent sensitivity analysis revealed that cAMP is most sensitive to parameter k_2 (influencing the rate of the PKA dependent cAMP degradation thereby representing phosphodiesterase activity). This was most prominent during the first 15 min after dDAVP addition and could not be captured by the sensitivity analysis performed with COPASI at 120 min after the stimulus. The effect of a change in the parameters during the longer run of the simulation was less pronounced. One may conclude from this that if one wants to analyze the system in more detail, to focus on changes of reaction re2 should be promising. One possibility would be to apply different inhibitor concentrations of phosphodiesterases and focus in particular on the first 15 min after dDAVP addition.

By including the pathway prior of AQP2 in the model, increase and decrease of membrane located AQP2 could be reproduced reasonably well even without including vasopressin regulated endocytosis of AQP2 into the model. Nevertheless, both, sensitivity and time dependent sensitivity analysis revealed that changing the parameter for the endocytosis reaction has the highest impact on AQP2 in the membrane. This means that, even if a regulation of this reaction by vasopressin is not needed to fit the model to the data, it might be useful to integrate in future versions of the model and analyze it in more detail. One can include also information from Kamsteeg *et al.* [56], who proposed regulated endocytosis of AQP2 via short-chain ubiquitination after washout of a stimulus. Nevertheless, one has to be careful with combining those data sets. Kamsteeg *et al.* [56] used forskolin to stimulate the cells instead of dDAVP, which directly activates the adenylate cyclase. Furthermore, they did not incubate the cells with the cyclo-oxygenase inhibitor indomethacin prior the stimulation with forskolin, which was used in the present study and in Deen *et*

al. [20] to reduce basal cAMP levels. This might alter the cellular response significantly.

Prediction of intracellular cAMP concentration over time By using the model to simulate cAMP over time it has been observed that the initial peak in cAMP is less pronounced at lower dDAVP concentrations. This supports the hypothesis, that it is important to look at lower, more physiological conditions, because there the whole kinetic behavior of the system might be different.

Furthermore, if looking at high dDAVP concentrations, it would be of significant importance to determine the cAMP level within the first 5 min to verify or falsify the model hypothesis and, if necessary, to use the newly generated data to improve the model.

AQP2 translocation after dDAVP stimulation - simulation and experiments The model was used to simulate the time course of AQP2 at the membrane at different concentrations. The model indicates that AQP2 at the membrane gets saturated already at a concentration of 10^{-9} M dDAVP. To investigate whether $AQP2_{membrane}$ is consistent with the Pf measured by Deen *et al.* [20] and to verify the model's predictions, cell surface biotinylation was performed on MDCK cells after a given stimulus of dDAVP and the change of AQP2 at the membrane was monitored over time. There was no difference in the maximal amount of AQP2 at the membrane at the concentrations 10^{-8} M and 10^{-6} M dDAVP, which supports the hypothesis that $AQP2_{membrane}$ is already saturated at those concentrations. At a concentration of 10^{-8} M dDAVP a transient response could be observed, whereas at a concentration of 10^{-6} M the response was sustained. That slightly disagrees with the model's predictions, because there a difference between the two concentrations could not be observed.

It is not completely clear why different concentrations of dDAVP shall affect only the form and not the amplitude of the curve. One possibility might be that at the time point of 90 min, which is relevant for the difference between the two concentrations, additional effects have taken place on a transcriptional or metabolic level, affecting the cell and influencing $AQP2_{membrane}$. The integration of further mechanisms might be of interest for future work, like AQP2 production, cell volume changes or growth.

Prediction of potential drug treatments with TIde The model was used to predict drug treatments for medical use cases in which either vasopressin or AQP2 abundance was impaired. Analyses with the drug target identification tool TIde identified the reactions directly involved in AQP2 trafficking as feasible drug targets. Furthermore, a reduction in dDAVP could be balanced by the application of activators or inhibitors more easily than a reduction in AQP2 abundance. This result holds true as long as there is still sufficient AQP2 present despite a reduction in vasopressin. In the long run, a reduction of vasopressin might also reduce AQP2 abundance, leading to even more severe impairment not considered in the current study.

While choosing the optimal drug or drug combination dosage, it is not only important to achieve the maximal effect. To avoid or reduce side effects it is favored to identify the minimal drug dosage still showing the desired effect. As shown in Fig. 3.13 the exact amount of each component of a fixed-combination drug can influence highly the kinetics of the system. In all four combinations of activator_{re5,re8} and inhibitor₆ the desired goal to rescue $AQP2_{membrane}$ was reached, but the response of the system is still different. Drug dosages with high inhibitor₆ and low activator_{re5,re8} were leading to an overshoot of $AQP2_{membrane}$ on the long run, which might most likely result in a higher reabsorption of water than desired. Therefore, if possible, it might be better and more physiological to apply a treatment with high activator_{re5,re8} and low inhibitor₆ concentrations.

At the current stage the model predicts the importance for the AQP2 translocating mechanisms, but leaves it open how exactly they can be regulated. It is known that AQP2 is inhibited by mutations in dynamin and internalized via the clathrin pathway [136]. Furthermore, it is known that besides PKA, also calcyclin, myosin Va, and proteins from the Rab small GTP-binding protein family [103] are involved in AQP2 localization, although specific information about the interactions and kinetics are still lacking. Presumably, the phosphatases and kinases affecting the different AQP2 phosphorylation sites might be excellent drug targets, and may even be specific for this signaling pathway, therefore reducing drug side effects.

4 Modeling of AQP2 trafficking in rat IMCD primary cells

Primary cultures of IMCD cells express AQP2 endogenously [81] and do not need to be transfected prior to the measurement. Therefore, they might be a good model for systems biological studies.

In Ch. 3 a model of the AQP2 regulation in MDCK cells was generated and analyzed. By using the MDCK cell model it had been discovered that the kinetic behavior of the system can only be preserved *in silico*, if the negative feedback by phosphodiesterases or the internalization of the V2 receptor are present, with a slight preference for the latter. Furthermore, potential drug targets for increasing $AQP2_{membrane}$ can most likely be found in the proximity of AQP2 by directly regulating its exo- or endocytosis. In the current chapter, it was analyzed whether those results also hold true for primary rat IMCD cells and whether the model can be used to identify potential species-specific differences.

To model AQP2 trafficking in primary rat IMCD cells the model from MDCK cells was reused and adjusted accordingly (see Sec. 1.3 and Stefan *et al.* [133]). As with the MDCK cell model also the primary rat IMCD cell model was analyzed by

- generating and ranking model variants,
- sensitivity analysis,
- time dependent sensitivity analysis,
- model predictions and comparison with newly generated data.

The results for MDCK and primary rat IMCD cells will be compared in section 4.7.2.

4.1 A mathematical model of AQP2 trafficking in IMCD cells

To model AQP2 trafficking in rat IMCD primary cells the model from MDCK cells was adjusted to data and knowledge from Stefan *et al.* [133] as follows. Since they did not use indomethacin to keep the basal cAMP concentration low, a constitutive adenylate cyclase activity was assumed. This results in a basal PKA activity and thus in basal PKA driven AQP2 exocytosis. For the IMCD cell model it was assumed that this is the only mechanism to achieve a basal amount of membrane-localized AQP2 and that PKA independent AQP2 exocytosis does not occur. This resulted in modifications of the model as follows:

1. Reaction re8 was deleted from the model.
2. A new re8 was added to represent basal, vasopressin independent adenylate cyclase activity and hence cAMP production.

3. The model was adjusted to guarantee the steady state conditions of cAMP, PKA and AQP2. This resulted in dependencies between parameters according to the steady state conditions and had the benefit that not all model parameters had to be estimated. The parameters k_4 , k_6 , k_8 can be calculated from the other model parameters and the species initial conditions as shown in Tab. 4.1.
4. AVP can inhibit the endocytosis of AQP2 (re6). This was motivated by results from Knepper and Nielsen [67], demonstrating the importance of regulated endocytosis in rat IMCD, and by analysis results derived with the MDCK cell model in the previous chapter (see Sec. 3.4 and 3.5). Time dependent sensitivity analysis had led to the suggestion that the regulation of AQP2 endocytosis can have a substantial effect on the kinetic behavior of the system.

The complete model for primary rat IMCD cells is presented in Fig. 4.1, the corresponding algebraic and differential equations are provided in Tab. 4.1.

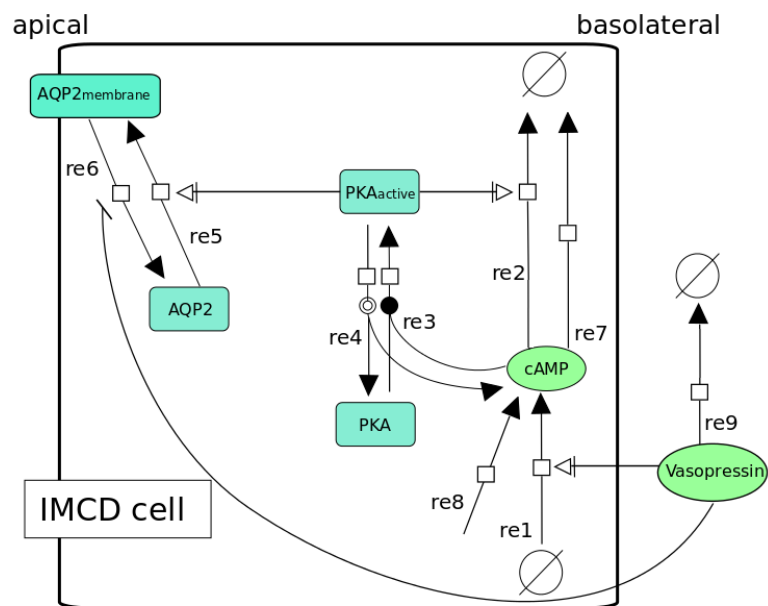


Figure 4.1: IMCD cell model. Complete model for primary rat IMCD cells after adjustment of the MDCK cell model to IMCD cells. Instead of a basal AQP2 endocytosis a basal cAMP generation was included (re8), thereby securing a basal level of cAMP, PKA_{active} and AQP2_{membrane}. In addition, an inhibition of the AQP2 endocytosis by vasopressin was included.

4.2 Time course simulation and parameter estimation

The remaining model parameters were estimated using COPASI and the experimental data from Stefan *et al.* [133] for intracellular cAMP concentration, PKA activity and AQP2 plasma membrane abundance. The cAMP concentrations could be utilized directly for the parameter estimation task. For PKA_{active} over time only relative changes from FRET analysis were available. In the same publication PKA activity was measured by a commercial assay (Upstate/Biomol, Hamburg, Germany) showing that PKA activity increases 1.76 fold after 15 min of AVP stimulation. The time resolved curve of PKA_{active} was scaled to this values and an initial concentration of 250 nM was chosen (values of 10 and 100 nM had failed

$\frac{d[PKA]}{dt}$	$= -(k3 \cdot [PKA] \cdot [cAMP]) + (k4 \cdot [PKA_{active}])$
$\frac{d[PKA_{active}]}{dt}$	$= (k3 \cdot [PKA] \cdot [cAMP]) - (k4 \cdot [PKA_{active}])$
$\frac{d[cAMP]}{dt}$	$= (k1 \cdot [AVP]) - (k2 \cdot rolipram \cdot [cAMP] \cdot [PKA_{active}]) -$ $-(k3 \cdot [PKA] \cdot [cAMP]) + (k4 \cdot [PKA_{active}]) -$ $-(k7 \cdot [cAMP]) + k8$
$\frac{d[AQP2]}{dt}$	$= -(k5 \cdot [AQP2] \cdot [PKA_{active}]) + \frac{k6 \cdot [AQP2_{membrane}]}{1 + \frac{AVP}{Ki6}}$
$\frac{d[AQP2_{membrane}]}{dt}$	$= (k5 \cdot [AQP2] \cdot [PKA_{active}]) - \frac{k6 \cdot [AQP2_{membrane}]}{1 + \frac{AVP}{Ki6}}$
$\frac{d[AVP]}{dt}$	$= -(k9 \cdot [AVP]^2)$
$k4$	$= \frac{k3 \cdot [PKA][0] \cdot [cAMP][0]}{[PKA_{active}][0]}$
$k6$	$= \frac{k5 \cdot [AQP2][0] \cdot [PKA_{active}][0]}{[AQP2_{membrane}][0]}$
$k8$	$= k2 \cdot [PKA_{active}][0] + k7 \cdot [cAMP][0]$
$k1, k2, k3, k5, k7, k9, Ki6$	were estimated

Table 4.1: Algebraic and differential equations describing the model for primary rat IMCD cells. The model includes differential equations for AVP, cAMP, PKA and PKA_{active} as well as AQP2 and $AQP2_{membrane}$. $rolipram = 0$ ($rolipram = 1$) mean rolipram was present (not present) in the experiment. The parameters $k4$, $k6$ and $k8$ were calculated so that a basal amount of cAMP, PKA_{active} and $AQP2_{membrane}$ was secured and the parameters $k1$, $k2$, $k3$, $k5$, $k7$, $k9$ and $Ki6$ were estimated with COPASI.

to reproduce the PKA activity data in foregoing analysis, data not shown). $AQP2_{membrane}$ was calculated from the ratio of intracellular/plasma membrane located AQP2 and assuming 1000 μM $AQP2_{total}$ (as calculated for the MDCK cell model based on information from Xie *et al.* [152]).

Parameter estimation was performed as described in Sec. 2.1. The resulting best fit for cAMP, active PKA and $AQP2_{membrane}$ can be seen in Fig. 4.2. The corresponding set of parameters is presented in Tab. 4.2.

4.3 Model Variations and Ranking indicate only moderate importance of negative feedback

Different model variants were generated by removing either the negative feedback by phosphodiesterases (-re2), the reduction of the signal representing internalization of the receptor (-re9) or both (-re2 -re9). Parameter estimation was performed for all model variants as described in Sec. 2.1. They were ranked according to their objective function (Fig. 4.3(a)).

The ranking of IMCD model variants did not show a difference between the complete model and the model with a deletion of re9, whereas deletion of re2 shows an effect. The effect of deleting either re2, re9 or both had a minor effect in primary rat IMCD cells compared to MDCK cells. The double-deletion resulted in a 1.4-fold increase in the objective function compared to the complete model (instead of a 48-fold increase in the MDCK cell model).

Both the single deletion -re2 and the double deletion -re2-re9 exhibited a similar increase in the objective function. The fits for the model without the negative feedback are described in Sec. 3 in the Appendix.

As a control it was tested whether a deletion of the non-competitive inhibition of re6 followed by addi-

4 Modeling of AQP2 trafficking in rat IMCD primary cells

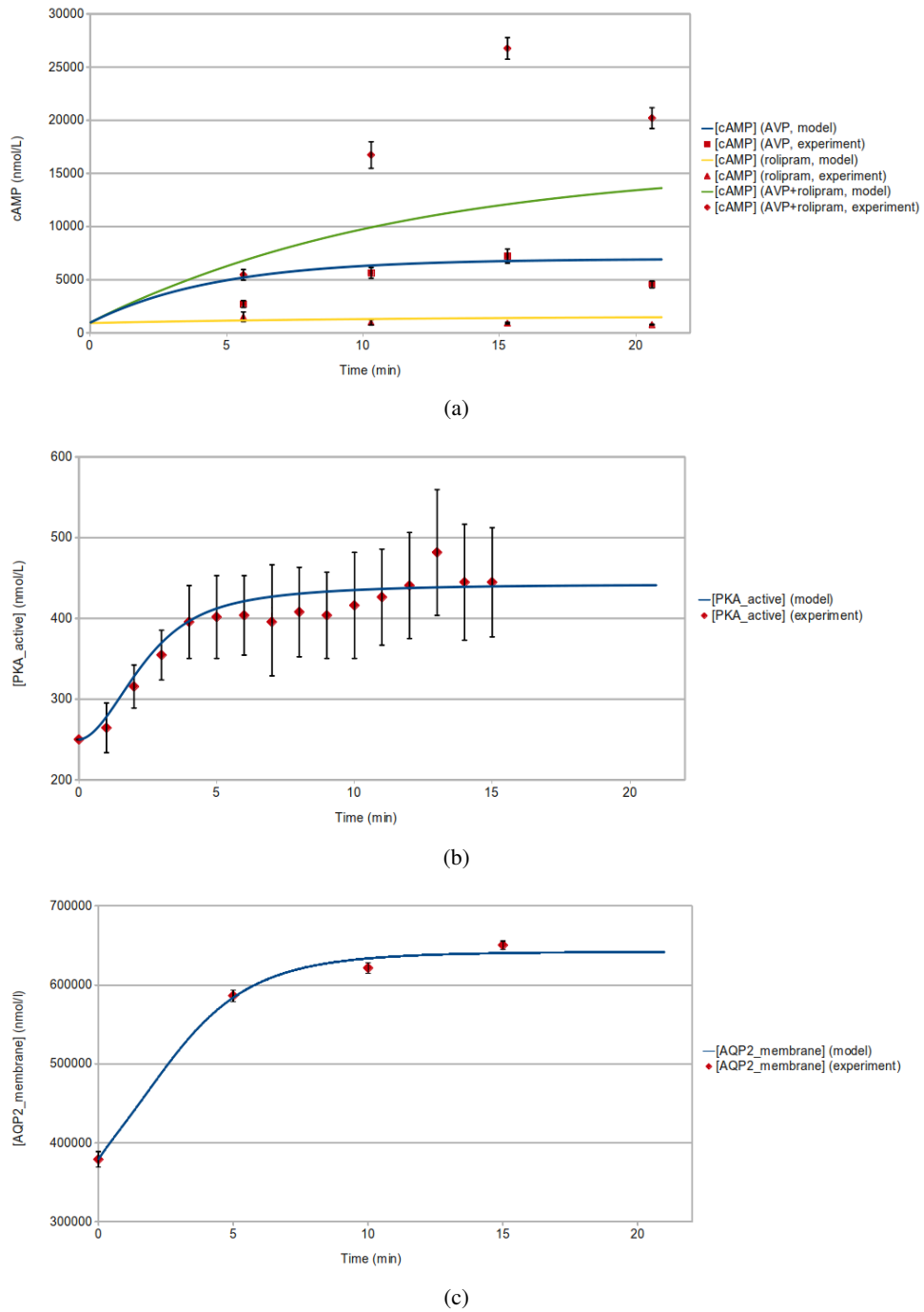


Figure 4.2: Parameter estimation with COPASI: primary rat IMCD cells. a) Fitting of the intracellular cAMP time courses. The cells were treated with AVP (100 nM), rolipram, or a combination of both for the indicated time points. b) Reproduction of the PKA activity and c) fitting of the membrane localized AQP2 after treatment with 100 nM AVP. The experimental data were taken from Stefan *et al.* [133]. cAMP could be directly used for comparison, PKA_{active} was assumed to have an initial value of 250 nM and AQP2_{membrane} was calculated from the ratio of intracellular/plasma membrane located AQP2 and assuming 1000 μ M AQP2_{total}.

Parameter name	Value	Units	Source
k_1	12.98	1/min	estimation
k_2	$2.635e^{-4}$	l/(nmol · min)	estimation
k_3	$2.1497e^{-4}$	l/(nmol · min)	estimation
k_4	0.198	1/min	calculation
k_5	$8.421e^{-4}$	l/(nmol · min)	estimation
k_6	0.345	1/min	calculation
k_7	$9.069e^{-2}$	1/min	estimation
k_8	144.4	nmol/(l · min)	calculation
k_9	$1e^{-12}$	1/min	estimation
Ki_6	150.4	nmol/l	estimation

Table 4.2: Parameters for primary rat IMCD cell model. The parameters for the model presented in Fig. 4.1 were estimated with COPASI. k_4 , k_6 , and k_8 were calculated with the equations in Tab. 4.1.

tional parameter estimation shows any difference to the original model (Fig. 4.3(b)). The model including re6 without the inhibition by AVP was able to reproduce the biological data only 3.4% worse than the original model.

4.4 Sensitivity analysis reveals importance of both AQP2 exo- and endocytosis

The effect of small perturbations of the initial parameter values on the amount of cAMP and $AQP2_{membrane}$ was analyzed 21 min after starting the simulation (the longest duration for which experimental data was available). The parameters with the strongest effect on cAMP was k_1 (affecting the AVP dependent activation of cAMP), followed by k_2 and k_7 (affecting PKA dependent and independent degradation of cAMP). Changes in k_9 (the decrease of the stimulus representing the degradation of the vasopressin V2 receptor) showed only a minor effect.

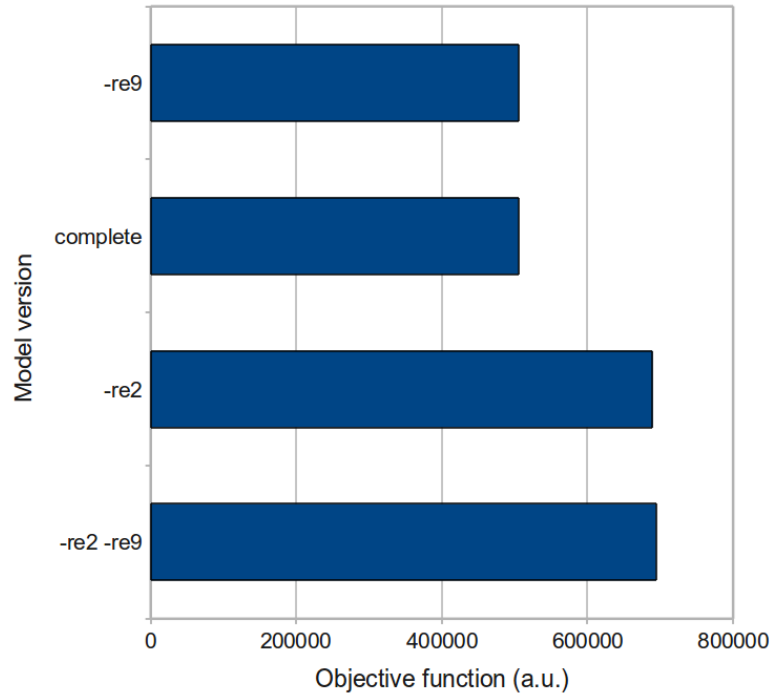
The major parameters affecting the abundance of AQP2 at the membrane were k_5 and k_6 (AQP2 exo- and endocytosis, respectively) to similar amounts. The effect of a perturbation in the inhibitory constant Ki_6 was less than half as strong as a change in the kinetic constants k_5 and k_6 .

4.5 Time-dependent sensitivity analysis

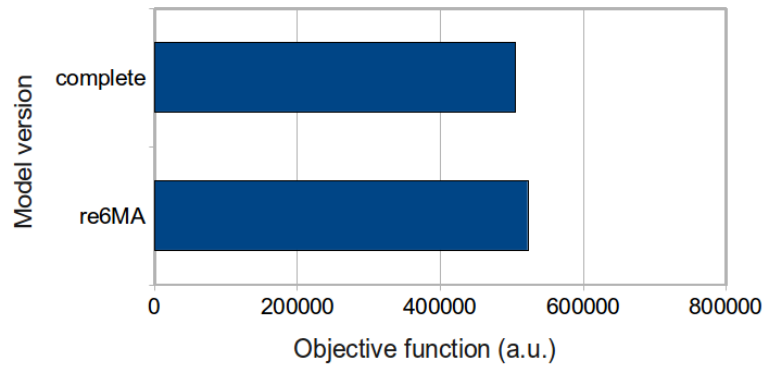
In accordance with the analysis of the MDCK cell model, time dependent sensitivity analysis was performed in Mathematica®. Again, the effect of small perturbations of the model parameters on cAMP and $AQP2_{membrane}$ was analyzed (see Fig. 4.5).

In consistency with the sensitivity analysis performed in COPASI for time point 21 min, cAMP was highly depending on k_1 (affecting the AVP dependent activation of cAMP), followed by k_2 and k_7 (affecting PKA dependent and independent cAMP degradation). A change in k_1 affected the time course instantaneously whereas for the parameters k_2 or k_7 the effect increased over time.

The change in the amount of $AQP2_{membrane}$ depended highly on k_5 (affecting AQP2 exocytosis) at around 4 min. On the long run this effect decreased slightly and got equal to k_6 (affecting AQP2 endocytosis) at approximately 12 min. A perturbation in the inhibition constant Ki_6 (k_{10}) showed some importance



(a)



(b)

Figure 4.3: Ranking of model variants. Different model variants were generated. For each model variant the parameters were estimated individually. Afterwards they were ranked according to their objective function. **a)** Complete: model version as shown in Fig. 4.1; -re2: complete model reduced by reaction re2 representing negative feedback via phosphodiesterases; -re9: complete model reduced by reaction re9, which represents the internalization and degradation of the receptor; -re2 -re9: reduced by both reactions re2 and re9. **b)** Complete: model version as shown in Fig. 4.1, reaction re6 is inhibited by AVP. re6MA: the inhibition of re6 was deleted, instead normal mass action kinetics were used.

4.6 Model predictions and comparison with newly generated data indicate that regulated endocytosis might have a minor effect in primary rat IMCD cells

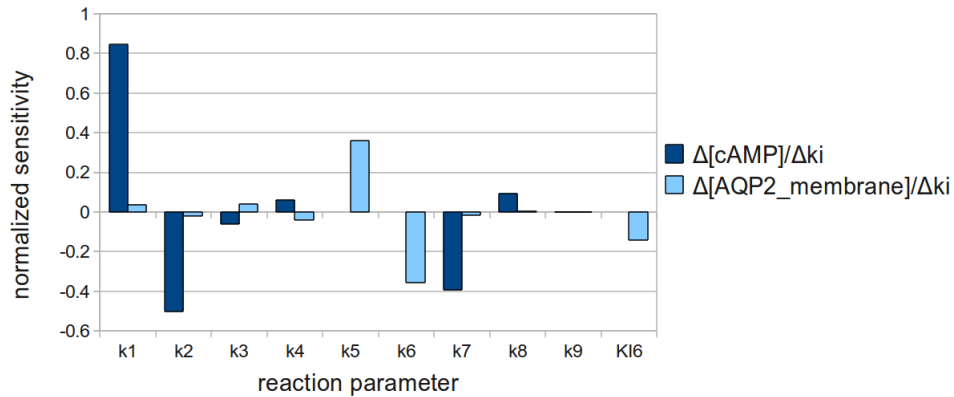


Figure 4.4: Sensitivity analysis of the primary rat IMCD cell model. Effect of small changes in the parameters on the model species at time point 21 min. The normalized sensitivities were taken. The analysis was performed with COPASI.

but much less than a change in the kinetic constant k_6 . During the first 10 min also changes in k_1 , k_3 , k_4 (affecting cAMP generation, PKA activation and deactivation) had an effect on the amount of AQP2 at the membrane. The long term impact of minor changes of those parameters seemed to be neglectable.

4.6 Model predictions and comparison with newly generated data indicate that regulated endocytosis might have a minor effect in primary rat IMCD cells

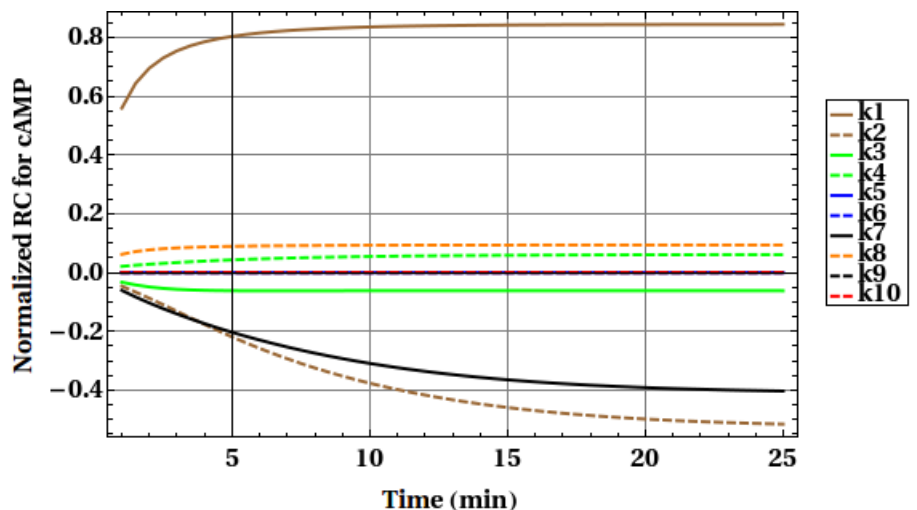
The model proposed in Sec. 4.1 with the best set of parameters found in Sec. 4.2 was employed to make *in silico* predictions. According to the analysis of the MDCK cell model $\text{AQP2}_{\text{membrane}}$ was simulated over time at different concentrations of the stimulating hormone, here AVP. AVP concentrations from 0.1 nM to 1 mM were applied. The results are presented in Fig. 4.6. The brown line shows the concentration to which the model was fitted (100 nM). The maximal amount of $\text{AQP2}_{\text{membrane}}$ was reached at an AVP concentration of 0.01 - 0.1 mM.

The simulation results were compared with newly generated data from immunofluorescence measurements performed by Klussmann *et al.* (see Fig. 4.7). Primary rat IMCD cells were treated with

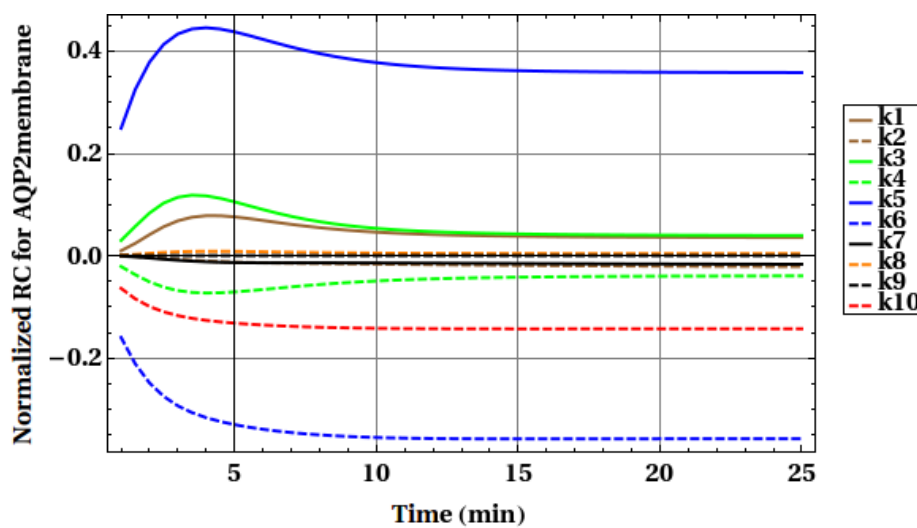
1. different amounts of AVP for 30 min (0.1, 1, 10, 50 and 100 nM AVP),
2. 100 nM AVP over different durations (0, 2, 5, 10, 20, 30 and 90 min).

A comparison of the new dose response measurement with the model predictions is presented in Fig. 4.8. For this purpose the initial condition of $\text{AQP2}_{\text{membrane}}$ was calculated from the new dose response measurement.

The model could predict the dose response of the new experimental data rather well. Yet, there were some discrepancies. In the model prediction the increase at AVP concentrations below 10 nM was less intense than in the experimental data, being most prominent there at the step between 0 and 0.1 nM AVP. At concentrations higher than 10 nM the $\text{AQP2}_{\text{membrane}}$ increased more slowly in the experiment, but still strongly in the model. The experiment left it open whether $\text{AQP2}_{\text{membrane}}$ had reached a plateau at



(a)



(b)

Figure 4.5: Time-dependent sensitivity analysis performed with IMCD cell model. Time-dependent sensitivity analysis was performed with the complete IMCD cell model as shown in Fig. 4.1 with the optimal set of parameters found. **a)** Time-dependent normalized response coefficients (RC) for all parameters in respect to cAMP, **b)** Time-dependent normalized response coefficients (RC) for all parameters in respect to AQP2 in the membrane. k_{10} is handled as a synonym for $Ki6$ in this figure.

4.6 Model predictions and comparison with newly generated data indicate that regulated endocytosis might have a minor effect in primary rat IMCD cells

100 nM AVP. Although the slope of the curve was decreasing at higher AVP concentrations. Instead, the model predicted an increase of $AQP2_{membrane}$ up to 100% at higher AVP concentrations.

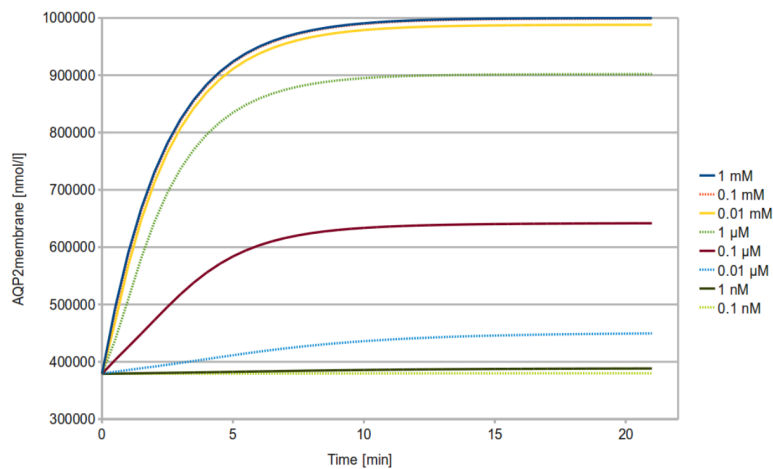


Figure 4.6: Prediction of $AQP2_{membrane}$ over time at varying AVP concentrations using the IMCD cell model. AVP was added at 0 min in log scale from 0.1 nM to 1 mM.

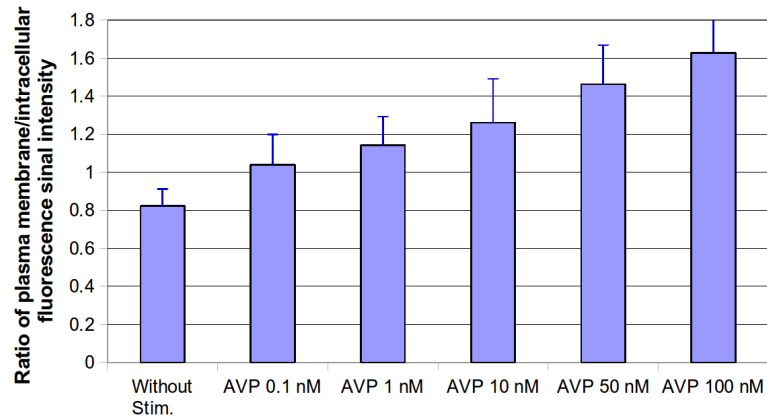
Fig. 4.9 shows $AQP2_{membrane}$ over time in the old as well as in the new data set compared with the model prediction. Two distinct *in silico* simulations are presented, either starting with a value for $AQP2_{membrane}$ calculated from the Stefan *et al.* data set or from the new data set from Klussmann *et al.*

The comparison of both the old and the new data set revealed that the two measurements show a slightly different behavior. The range in which $AQP2_{membrane}$ varied was narrower in the new than in the Stefan *et al.* data set. Furthermore, the kinetic behavior seemed to be slightly different. In the new data set $AQP2_{membrane}$ increased rather slowly with a half-maximum value around 13 min. In the Stefan *et al.* data $AQP2_{membrane}$ increased the most in the first 5 min. Unfortunately, data between 0 and 5 min and longer than 15 min were missing, therefore it was not known, whether the curve increased directly after stimulation and whether the maximal value was already reached at 15 min. The same counted for the time between 30 and 90 min in the new data set by Klussmann *et al.*

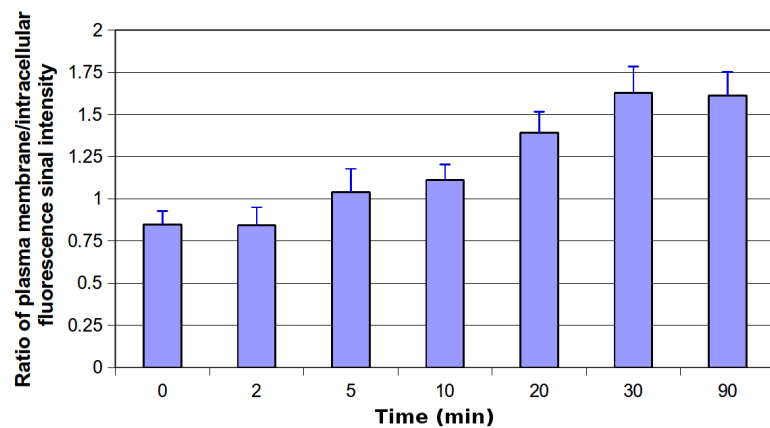
Due to the fact that the model was fitted to the Stefan *et al.* data set, in which $AQP2_{membrane}$ was increasing faster, the simulation fitted nicely to the old, but not to the new data set. If the 0 min value of the Stefan *et al.* data set was used as start value for the simulation, the differences were most prominent during the first 20 min, where the simulation first underestimated (0 min) and then overestimated the actual data. If the 0 min value of the new data set was used as start value for the simulation, the simulation highly overestimated $AQP2_{membrane}$ at all following time points.

To analyze how the model characteristics change by fitting the model to the new $AQP2_{membrane}$ data, an additional parameter estimation was performed with the previously estimated parameters as start values. The results for the dose response measurements are shown in Fig. 4.10 (a) and (c). The comparison for the time resolved measurements are presented in Fig. 4.11(a).

Although the model was now able to reproduce the 50 and 100 nM better, there were still discrepancies at lower concentrations. The model predicted that after 30 min stimulation with 100 μ M AVP 92% of the



(a)



(b)

Figure 4.7: Ratio of AQP2 plasma membrane/intracellular fluorescence signal intensity in primary rat IMCD cells. **a)** The cells were stimulated with the indicated concentrations of AVP. The AQP2 plasma membrane/intracellular fluorescence signal intensity ratio was determined 30 min after the start of the stimulation ($n \geq 57$ cells for each condition). **b)** The cells were stimulated with 100 nM AVP. The AQP2 plasma membrane/intracellular fluorescence signal intensity ratio was determined at the indicated time points ($n \geq 23$ cells for each time point). The experimental setup was as described in [133]. The measurements were performed by Klusmann, Geelhaar *et al.* (Max Delbrück Center, Berlin-Buch, Germany).

4.6 Model predictions and comparison with newly generated data indicate that regulated endocytosis might have a minor effect in primary rat IMCD cells

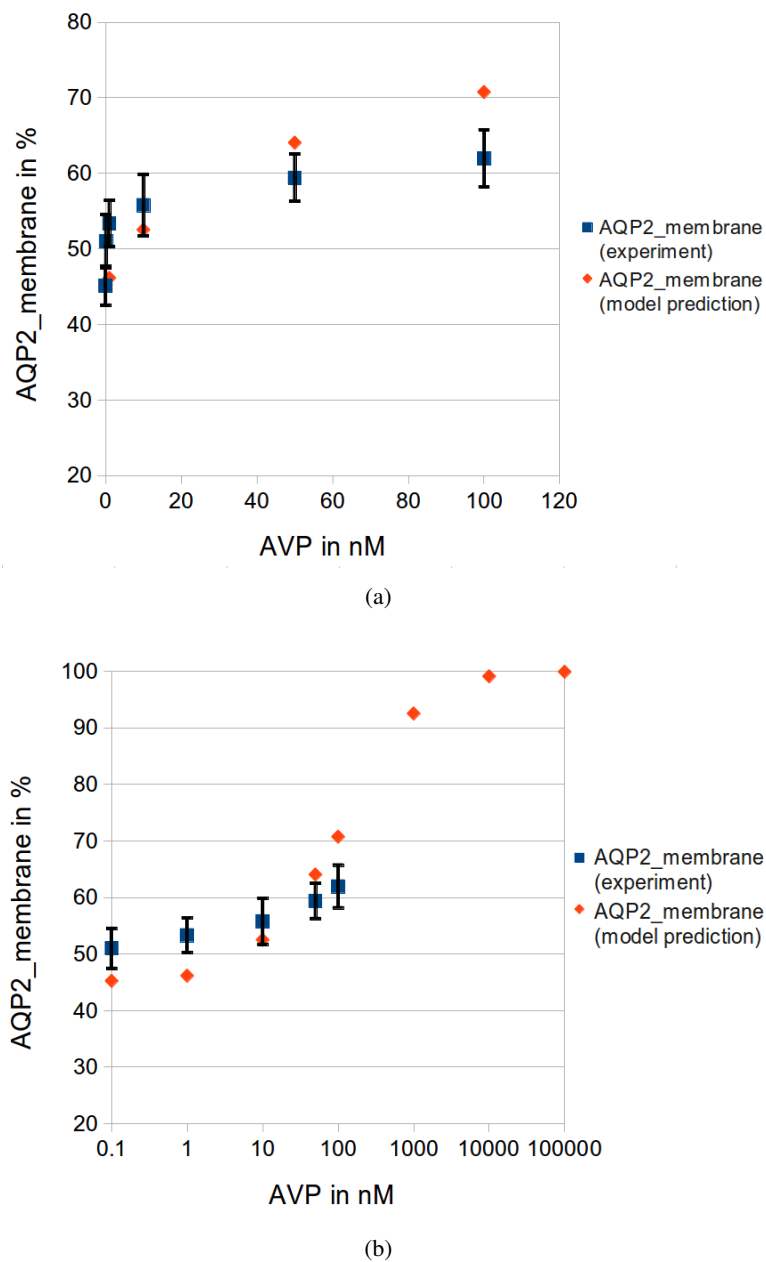


Figure 4.8: Comparison of model and experiment for AQP2 localization in IMCD cells. Blue: experimental data, orange: model prediction. **a)** AVP concentrations in linear scale, **b)** AVP concentrations in logarithmic scale. $AQP2_{membrane}$ in % was calculated from the AQP2 plasma membrane/intracellular fluorescence signal intensity ratio as determined 30 min after the start of the stimulation. Additional model predictions for 1, 10 and 100 μ M were included.

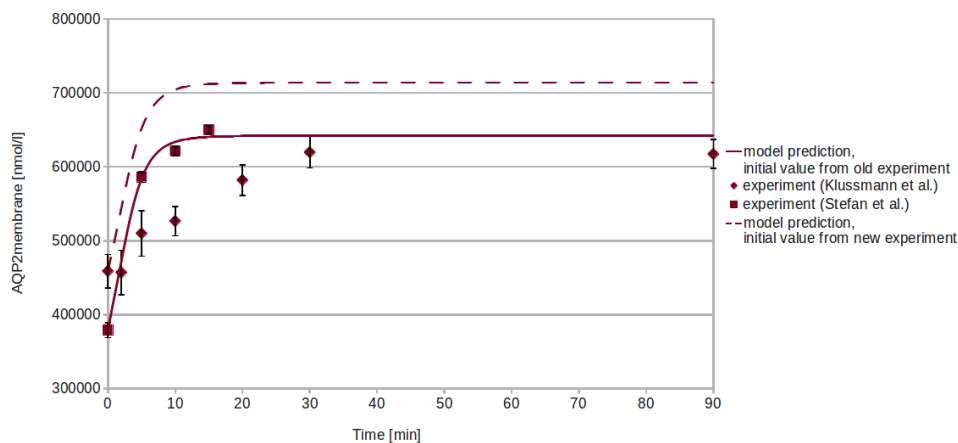


Figure 4.9: Simulation of $AQP2_{membrane}$ in primary rat IMCD cells and comparison between the Stefan *et al.* and the new data set. Squared symbols represent the data by Stefan *et al.*, diamond-shaped symbols the newly generated data from Klussmann *et al.*. The solid line shows the model simulation with the value for $AQP2_{membrane}$ at time point 0 min calculated from the data by Stefan *et al.* whereas for the dashed line the value at time point 0 min was calculated from the new data set.

AQP2 is located at the membrane.

The model with the newly estimated parameters was able to reproduce the time course of $AQP2_{membrane}$ derived from the new data set reasonably well (see Fig. 4.11(a)). Presented are also model predictions for time resolved $AQP2_{membrane}$ at the concentrations 0.1 nM - 1 mM.

Motivated by the result that in the sensitivity analysis performed in the present chapter the *Ki6* (inhibition of endocytosis by AVP) did not have such a prominent effect, a model variant lacking this regulation was tested. As with the complete model the model variant was fitted to the new data set by using the estimated parameters from the complete model and the Stefan *et al.* data set as start values. Fig. 4.10 b) and d) show the dose response relationships and Fig. 4.11(b) the simulation of $AQP2_{membrane}$ over time for different AVP concentrations (0.1 nM - 1 mM). Without the inhibition of re6 by AVP, $AQP2_{membrane}$ reached its maximal value already at a concentration of 1 μ M.

Due to the fact that the model variants with and without the inhibition of re6 varied the most at AVP concentrations above 1 μ M, it might be useful to have additional experiments for those concentrations, to be able to distinguish between the two model variants.

4.7 Discussion

Within this chapter a model for AQP2 trafficking in primary rat IMCD cells was proposed. The aim was to analyze the kinetic behavior of IMCD cells after stimulation with AVP and to analyze potential species-specific differences. The parameters of the model were estimated using data from Stefan *et al.* [133]. Ranking of model variants, parameter estimation, sensitivity analysis and time dependent sensitivity analysis as well as model predictions and comparison with newly generated data were performed.

To conclude the results from this part of the thesis:

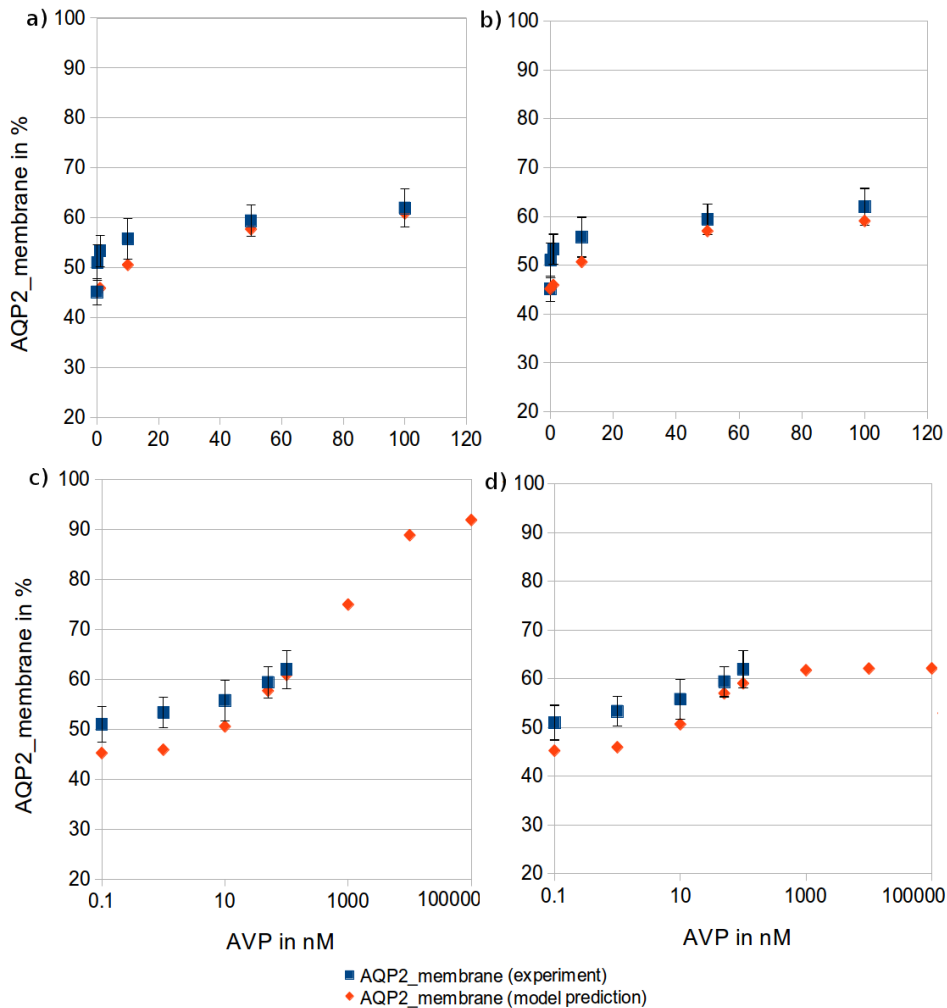
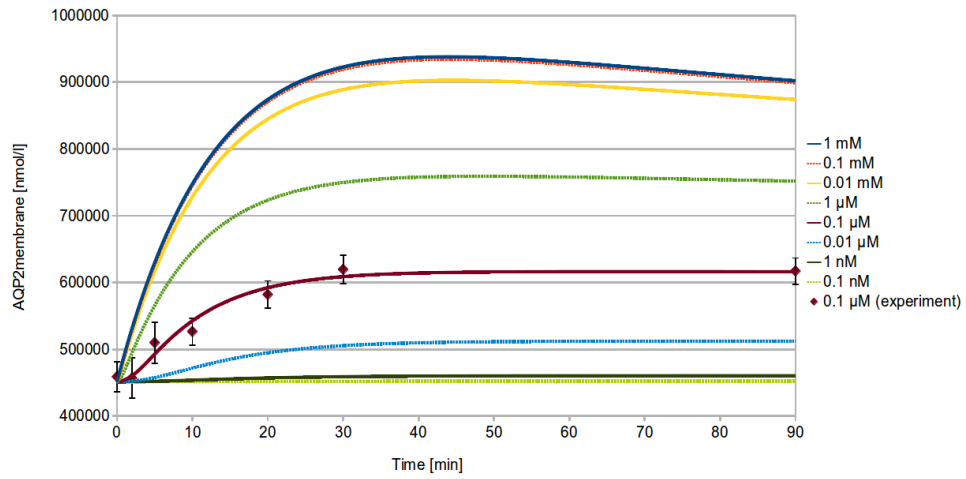
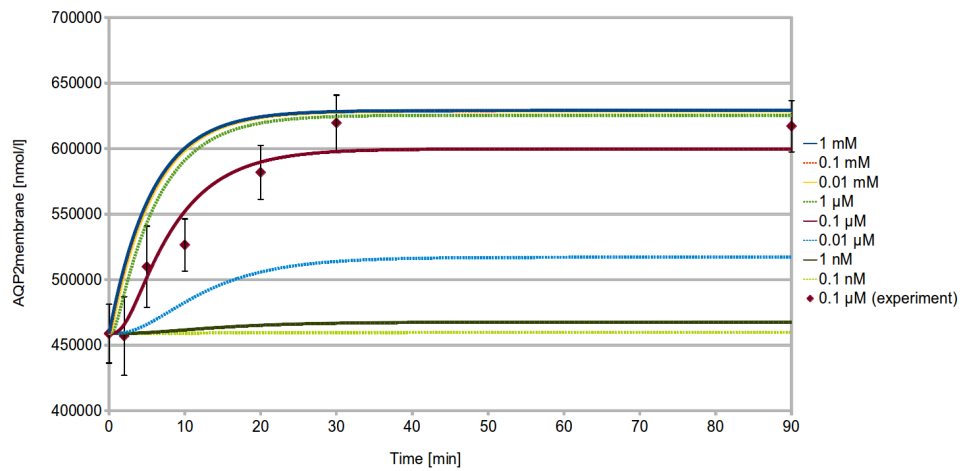


Figure 4.10: Comparison of model and experiment for AQP2 localization in IMCD cells (after additional parameter estimation by using the new data set provided by Klusmann *et al.*). Blue: experimental data, orange: model prediction. **a)** and **c)** model including the inhibition of endocytosis by AVP, **b)** and **d)** model without inhibition of endocytosis by AVP. In **a)** and **b)** the AVP concentration is scaled linearly, in **c)** and **d)** logarithmically, additional model predictions for 1, 10 and 100 μM are shown. $\text{AQP2}_{\text{membrane}}$ in % was calculated from the AQP2 plasma membrane/intracellular fluorescence signal intensity ratio as determined 30 min after the start of the stimulation.



(a)



(b)

Figure 4.11: Simulation of AQP2_{membrane} after estimation of the parameters with the new data set. AQP2_{membrane} was simulated over time at different concentrations of AVP (0.1 nM - 1 mM) as indicated. **a)** Model including the inhibition of endocytosis by AVP. **b)** Model in which the inhibition of endocytosis by AVP was deleted.

- The model was able to reproduce the biological data for cAMP, PKA activity and $AQP2_{membrane}$. Only cAMP after treatment with AVP and rolipram could not be captured perfectly.
- Ranking of model variants suggested that the internalization of the receptor is not important in IMCD cells. The negative feedback via PDEs is slightly important.
- Sensitivity analysis revealed importance of both AQP2 exo- and endocytosis. cAMP was most sensitive to its generation reaction and on the long run on PKA dependent and constitutive degradation via PDEs.
- The model fitted to the Stefan *et al.* data set predicted that the maximal amount of $AQP2_{membrane}$ would be reached at AVP concentrations between of 0.01 - 0.1 mM.
- The model could reproduce the new data from Klussmann *et al.* reasonably well with or without an inhibition of AQP2 endocytosis by AVP. An experimental setup to distinguish between the two variants was proposed.

Those results and different aspects of the model will be discussed in Sec. 4.7.1. The results from MDCK and IMCD cells will be compared and discussed in Sec. 4.7.2.

4.7.1 Primary rat IMCD cell model

Model generation and data usage The model for MDCK cells was adapted to IMCD cells as described in Sec. 4.1. Therefore, some assumptions and simplifications had to be made. The simplifications concerning the model structure have already been discussed for the MDCK cell model in Sec. 3.9.

Some difficulties arose while applying the model to experimental data from IMCD cells. The intracellular cAMP concentration by Stefan *et al.* [133] was in pmoles/well. To convert it into nM, 1.9 cm^2 surface per well was used according to a 24-well plate [36] and a cell height of $10 \text{ }\mu\text{m}$ was assumed. According to the measurements of apical, basal and lateral cell surface areas of IMCD cells by Flamion and Spring [26] the assumption of $10 \text{ }\mu\text{m}$ should be reasonable.

With the PKA activity data by Stefan *et al.* [133] it was more challenging. The time resolved data from FRET experiments were only relative, and no absolute values or percentages were available. In the same publication PKA activity was measured by a commercial assay showing that PKA activity increases 1.76 fold after 15 min of AVP stimulation. The time resolved curve of PKA_{active} was scaled to this values and an initial concentration of 250 nM was assumed. It might be possible that this value has been overestimated, although previous parameter estimations using lower concentrations (10 nM, 100 nM) were not able to reproduce PKA_{active} sufficiently. This points out once more the need for quantitative measurements, e.g. of absolute concentrations of free catalytic subunits. $AQP2_{membrane}$ was calculated from the ratio of intracellular/plasma membrane located AQP2. The calculation of the percentage of membrane located AQP2 was quite convenient by using simple mathematics. From the percentage the concentration could be calculated by assuming a cell size of $1000 \text{ }\mu\text{m}^3$ (based on Flamion and Spring [26]) and a concentration of $1000 \text{ }\mu\text{M}$ $AQP2_{total}$. This was already applied in the MDCK cell model and based on calculations by Xie *et al.* (see supplementary material in [152]) showing that there are around $4.4 - 6.7 \cdot 10^8$ copies of AQP2 per cell. However, this cannot completely make up for measurements of absolute AQP2 concentrations in IMCD cells.

Furthermore, one more uncertainty was added by using the PKA reporter AKAR1 for the measurement. As stated by Zhang *et al.* [155] one cannot detect transient behavior with this reporter system. So even

if the PKA would peak in this cell system, one would not be able to detect it. For future experiments, AKAR2 or its successors should be used instead.

In the IMCD cell model, one exception was that the kinetics for the rolipram and AVP treated cells could only be fitted moderately. Once more data becomes available for this inhibitor in IMCD cells, e.g. different concentrations of the inhibitor, it might make sense to model this inhibition in more detail.

In the complete model, which includes the vasopressin degradation reaction, the kinetic parameter for this reaction was estimated much lower than in the MDCK cell model. One reason for this might be that in the primary rat IMCD cell data set intracellular cAMP increases and more important decreases only moderately. Therefore, internalization of the V2 receptor seems not to be necessary for the observed behavior. Nevertheless, this only holds if cAMP has the shape as observed in Stefan *et al.* [133]. If somehow cAMP peaks already in the first 5 min this would show a completely different behavior. In that case the parameters might be more similar to those estimated from MDCK cell data.

Ranking of model variants Model variants were generated by removing either the negative feedback by phosphodiesterases (-re2), the reduction of the signal representing internalization of the receptor (-re9) or both (-re2 -re9). Deletion of the negative feedback had a stronger effect on the objective function than deletion of the degradation of the vasopressin signal. A reason for this might be that already in the complete model this reaction seemed to be of minor importance.

The effect of deleting either AVP degradation, the negative feedback or both had a minor effect in primary rat IMCD cells compared to MDCK cells. Even the double-deletion resulted only in a 1.4-fold increase in the objective function instead of a 48-fold increase in the MDCK cell model. The reason for this should be again the missing sharp peak in the cAMP data, which was observed in MDCK cells, but not in IMCD cells (compare Fig. 1.6 A and 1.7 b).

Deletion of the negative feedback shows approximately the same results as deletion of the negative feedback and AVP degradation, together. Both single and double deletion variants showed an increase in the objective function. This comes due to the fact, that with deletion of re2 (the degradation of cAMP by phosphodiesterases) in the model also the effect of rolipram will fall apart. Since rolipram was modeled to act only on re2 and not re7 (the PKA independent cAMP degradation), no difference between the presence and absence of rolipram could be observed and the rolipram dependent time courses could not be fitted properly.

Furthermore, the ranking of different model variants shows that a model lacking the inhibition of AQP2 endocytosis by AVP can, after parameter estimation, reproduce the data nearly as good as the complete model. This suggests that the inhibition has only a minor effect in primary rat IMCD cells. However, if the parameter set from the complete model was used and the inhibition was deleted, this resulted in reduced $AQP2_{membrane}$ at higher AVP concentrations (data not shown). To investigate this further one idea might be to use specific PKC inhibitors and analyze the effect on $AQP2_{membrane}$.

Sensitivity analyses reveal in the long run equal importance for AQP2 endo- and exocytosis

Sensitivity and time-dependent sensitivity analysis of the IMCD cell model revealed that cAMP is most affected if the parameters for cAMP generation as well as PKA dependent and independent cAMP degradation are disturbed. A small change in the parameter for internalization of the V2 receptor had no effect. This strengthens the hypothesis drawn from the ranking of model variants, that this reaction might be less important for the behavior of the system in IMCD than in MDCK cell. Although, it has to be kept in mind that this analysis holds only for minor changes in the parameters.

The hypothesis arising from sensitivity analysis on the MDCK cell model that the endocytosis of AQP2 has a crucial effect, did not hold completely true in primary rat IMCD cells. At the beginning of the simulation a small modification in the parameter affecting AQP2 exocytosis has a higher effect than a change in endocytosis, with a maximum at around 4 min after AVP addition. After approximately 12 min the changes in exo- and endocytosis have the same effect.

The effect of a tiny change in the inhibitory constant Ki_6 of the endocytosis revealed a moderate effect on AQP2 at the membrane. Ki_6 was estimated with 150.4 nmol/L, so with a concentration of 100 nM AVP, less than 50% of the AQP2 internalization was inhibited.

One can discuss here the simplicity of the model, in which the inhibition acts directly from AVP on the AQP2 endocytosis and was modeled with simple kinetics. In reality this might be an additional pathway via inhibition of PKC [14, 56] and other involved proteins, which might result in a rather complex kinetic behavior. Here, additional experiments have to be performed to secure PKC as the involved kinase. To investigate the interplay of AQP2 exo- and endocytosis in more detail, it might be useful to test different combinations of PKA and PKC inhibitors and to analyze the kinetic behavior of the system in more detail. A crucial time point would be the behavior of the system around 4 min as well as at least one time point above 12 min.

AQP2 translocation after dDAVP stimulation - simulation and experiments In the IMCD cell line, this section incorporated

1. predictions with the model fitted to the Stefan *et al.* data set [133],
2. comparison of the predictions with the new data set provided by Klussmann *et al.*,
3. refit of the model to the new data set performed with 2 different model variants (with or without inhibition of endocytosis by vasopressin).

The model fitted to the Stefan *et al.* data set could predict the newly generated dose response relationship of $AQP2_{membrane}$ on AVP rather well. Yet, the slope of the dose response was slightly different. The prediction of the time resolved data was not that good, increasing too fast and, by starting with the new 0 min value, far too high. Unfortunately, that had to be expected given the fact that also the experimental values differ slightly between the Stefan *et al.* data set and the newly produced data set. In both the dose response and the time resolved measurement the ranges between the minimal and the maximal value of $AQP2_{membrane}$ were different, being more narrow in the new data set. Furthermore, $AQP2_{membrane}$ increased more slowly over time in the new data set, compared to the old one.

The Stefan *et al.* data left it open whether $AQP2_{membrane}$ has reached a plateau at 15 min or whether it continues increasing with higher concentrations. The model fitted to the Stefan *et al.* data set predicted that $AQP2_{membrane}$ has already reached the maximum value at 15 min. Nevertheless, in the new data set $AQP2_{membrane}$ was still increasing after 15 min.

The new data set left it open whether $AQP2_{membrane}$ has reached its maximum at 100 nM or whether it continues increasing with higher concentrations. Comparison between model simulations and newly generated data has underlined the importance to analyze the behavior of the system at AVP concentrations higher than 100 nM.

Two different model variants were used for refitting the model to the new data set (with or without inhibition of endocytosis by vasopressin). Both model variants could be fitted reasonably well to the data. The

model with the inhibition predicted much higher $AQP2_{membrane}$ concentrations than the model without the inhibition. According to the simulations, a way to distinguish between the two model variants would be to apply higher AVP concentrations (e.g. 10-100 μM) and to measure $AQP2_{membrane}$ around 40 min after AVP addition. For better comparison to the data from Klussmann *et al.* and because the effect, according to the simulations, shall still be high enough, a measurement at 30 min would be recommendable.

Possible alternative pathways The model focuses on the regulation of AQP2 trafficking via the cAMP/PKA pathway. Although the regulation via this pathway is widely accepted, there is still some open discussion about alternative or additional pathways. Some publications suggest a responsibility for Ca^{2+} for the AQP2 trafficking instead of the PKA pathway. Ca^{2+} is increased after a stimulus by vasopressin in rat IMCD [18, 132], also Ca^{2+} oscillations were observed [154]. Chou *et al.* [17] proposed that Ca^{2+} might affect non-muscle myosin II via the Ca^{2+} -calmodulin pathway, which activates the myosin light chain kinase.

Klussmann *et al.* [66] showed by application of the PKA inhibitor H89, that PKA activation is necessary for AQP2 trafficking. However, a concentration of 30 μM H89 might have been too high to be PKA specific, since at 50 μM also the increase of intracellular Ca^{2+} gets inhibited [154]. The results from Lorenz *et al.* [79] support the results from Klussmann *et al.* [66] by demonstrating that cAMP is sufficient to trigger the exocytic recruitment of AQP2 in renal primary cells. Ca^{2+} could be clamped at a basal level while AQP2 trafficking was still observed.

Another pathway thought to attenuate AQP2 endocytosis acts via the protein kinase C (PKC). It is currently not known how the attenuation takes place directly. Drugs like 12-tetradecanoylphorbol-13-acetate (TPA) are known to activate PKC and can induce AQP2 ubiquitination, internalization and degradation [56, 88].

Hormones like extracellular purines and dopamine are known to counteract the AVP induced AQP2 translocation via a dual mechanism [15]. Both can activate PKC and increase AQP2 ubiquitination, S261 phosphorylation and degradation. Furthermore, they decrease intracellular cAMP levels. JNK, p38, and CDK5/9 are also potential kinases responsible for S261 phosphorylation [112]. As soon as more detailed knowledge and time resolved data for primary rat IMCD cells is available, the model can be extended and those mechanisms can be analyzed *in silico*.

4.7.2 Comparison between MDCK and primary rat IMCD cells

First the data as well as the experimental setup that was used to obtain them will be compared for both biological model systems. Then a summary of the analysis performed with the models will be presented and how they can, despite those differences, be used to learn something about the biological system.

Comparison between the MDCK and the primary rat IMCD cell data

In the following, the major differences between the MDCK and IMCD cell data and the experimental setup will be pointed out and discussed.

Differences already visible in the data sets What could be seen already by comparing the data from MDCK and primary rat IMCD cells is that both data sets are different when it comes to intracellular cAMP over time. While in MDCK cells a sharp peak in cAMP at approx. 5 min after dDAVP stimulation was observable, this was not the case if primary rat IMCD cells were stimulated with AVP. AQP2 at the

membrane after AVP/dDAVP stimulation changes quite similar qualitatively in both biological systems, although in IMCD cells the translocation seemed to be faster than in MDCK cells. By looking at the data one could not draw a conclusion about the long term behavior of $AQP2_{membrane}$, because data were only available over 15 min. For PKA activity over time data were only available in IMCD cells.

Differences in experimental setup The experiments used in this thesis differ in their experimental setup. The crucial points to discuss here are

- different cell lines,
- different stimuli,
- different pretreatment,
- different measurements.

Different cell lines In Deen *et al.* [20] and in Sec. 3.6 of the present thesis, MDCK cells transfected with AQP2 were used. In Deen *et al.* this were MDCK-hAQP2 and in this work MDCK-hAQP2-T269S cells. The latter were used to compare the results from the present work with results from experiments with an antibody against the ratified, phosphorylated form of serine 269 (data not shown). It can be assumed that both cell lines behave similar upon dDAVP stimulation (personal communication with Prof. Dr. Peter M.T. Deen). Nevertheless it has to be mentioned that in both cases cell cultures were used, that have lost their endogenous AQP2 [20], are transfected with AQP2, and are a slightly artificial system. Furthermore, as with all cell lines, they adapted various mutations.

In contrast, Stefan *et al.* [133] and Klussmann *et al.* (Sec. 4.6 of this thesis) used primary rat IMCD cells for the experiments. Although the cells were removed from the rat and prepared for the experiment, they were freshly harvested and still had their endogenous AQP2. Therefore they might be a better model for systems biological studies.

Different stimuli In the work on MDCK cells within the present thesis and presented by Deen *et al.* [20] the vasopressin analog dDAVP was used to stimulate the cells. However, Stefan *et al.* [133] and Klussmann *et al.* used AVP for the stimulation of the primary rat IMCD cells. This might lead to difficulties while comparing the results from both experiments.

It is known that dDAVP has a three times larger antidiuretic activity than AVP [50]. This might be part of the reason why higher concentrations of AVP are necessary to saturate the system in the IMCD cell experimental setup.

Different pretreatment Furthermore, in the work on MDCK cells indomethacin was added to the cells one day prior the experiment to reduce the level of intracellular cAMP. This was not the case for IMCD cells. This should most presumably be the reason why in MDCK cells the level in osmotic water permeability (Pf) is quite low at the start of the experiment, whereas in IMCD cells $AQP2_{membrane}$ is already at a high level without any stimulus by vasopressin.

This is a quite important point to discuss, because it might also influence future experiments. Stimulating of the cells with indomethacin prior the experiment decreases the amount of intracellular cAMP, upon which a change after the stimulation with AVP/dDAVP is more severe. This is important to increase the signal-to-noise ratio. Nevertheless, if one wants to investigate biological system as close to nature as possible, it might be better to resign the indomethacin and only measure and document the desired

modification. In this case the stimulation with AVP/dDAVP should be the method of choice.

Different measurements Deen *et al.* [20] measured the Pf, in the experimental part of this thesis $AQP2_{membrane}$ was measured via cell surface biotinylation and Stefan *et al.* used immunofluorescence measurements to investigate the plasma membrane/intracellular ratio (M/C ratio) of AQP2. Since from the M/C ratio the percentage of $AQP2_{membrane}$ can be calculated, it was assumed that this is linearly related to the measurement of $AQP2_{membrane}$ from the present study and can be compared.

As in Knepper and Nielsen [67], it was assumed that the measured Pf is proportional to $AQP2_{membrane}$. To verify this it would be necessary to measure the exact Pf/ $AQP2_{membrane}$ relationship in these cells. This might lead to difficulties with the experimental setup used by Deen *et al.* Using their setup, it takes some time to reach the maximal value of $AQP2_{membrane}$. By this time the concentration of the solution might have already changed, which might lead to an underestimation of the Pf. In fact, this could also have been the case during the measurement in [20] and might be a reason for the drop in Pf at 90 min.

Although there are a lot of differences in the experimental setup and the resulting data, one can still learn from both model systems. Especially the usage of different animal models (here the comparison between dog and rat) is useful to identify similarities as well as differences between both model systems. Because in the end, one major goal would be to map the gained information to the human body.

Comparison between the MDCK and the primary rat IMCD cell model

By analyzing the models for MDCK and primary rat IMCD cells the following major results were found and compared (see Table 4.3). Ranking of the model variants showed that deletion of the negative feedback via phosphodiesterases as well as deletion of vasopressin degradation has a higher effect in MDCK than in primary rat IMCD cells. In MDCK cells the internalization of the receptor is slightly more important whereas in IMCD cells it is the negative feedback.

Time dependent sensitivity analysis showed that for cAMP in MDCK cells the negative feedback is very important for the shape of the curve whereas in IMCD cells it is dependent on different factors, which are mainly cAMP generation as well as PKA dependent and independent cAMP degradation. $AQP2_{membrane}$ depends in MDCK cells mainly on the AQP2 internalization, whereas this cannot be stated that clearly in IMCD cells, where it is (at the long term) equally dependent on AQP2 endo- and exocytosis. Both models show clearly that the highest change in the $AQP2_{membrane}$ abundance is reached if reactions directly involved in AQP2 trafficking are perturbed.

The model predictions showed that $AQP2_{membrane}$ in MDCK cells has reached already a maximal level at 10^{-9} M dDAVP. In IMCD cells, using the model fitted to data from Stefan *et al.*, $AQP2_{membrane}$ reaches the maximal amount between 10^{-4} M and 10^{-5} M AVP.

Using the new Klusmann *et al.* data set for model fitting, subsequent analysis revealed that the model including an inhibition of AQP2 endocytosis by AVP would reach its maximum value between 10^{-3} M and 10^{-4} M AVP. Instead, a model not including the inhibition would reach its maximal value already at 10^{-6} M AVP and would result in lower maximal AQP2 concentrations. Future experiments should be able to distinguish between the two regulatory mechanisms.

Analysis	MDCK	IMCD
Ranking of model variants	<ul style="list-style-type: none"> - negative feedback or internalization of V2 receptor are important - internalization of V2 receptor is slightly more important 	<ul style="list-style-type: none"> - both deletions have smaller effects in IMCD than in MDCK cells - negative feedback is more important than internalization of the V2 receptor
Time dependent sensitivity analysis	<ul style="list-style-type: none"> - shape of cAMP peak is highly dependent on PKA dependent cAMP degradation - importance for regulation of AQP2 endocytosis (potential drug target) 	<ul style="list-style-type: none"> - cAMP is highly dependent on cAMP generation, followed by PKA dependent and independent cAMP degradation - importance for both AQP2 exo- and endocytosis
Model predictions	<ul style="list-style-type: none"> - indicates that $AQP2_{membrane}$ gets saturated at 1 nM dDAVP 	<ul style="list-style-type: none"> - indicates that $AQP2_{membrane}$ gets saturated at $\geq 1 \mu M$ AVP

Table 4.3: Comparison between the results from the MDCK and the rat IMCD cell model.

Concluding remarks

The present study demonstrated how the models can be used to interpret the individual biological data sets in terms of relevant reactions, sensible parameters, and potential drug targets. With the help of the models, suggestions could be made to assist the experimentalists in future experiments. For example, the model predictions based on the new Klusmann dataset suggested which concentrations of AVP should be applied and which time point is suitable for the measurement to obtain the highest information content. In all presented data sets, cAMP and AQP2 at the membrane increased after stimulation with AVP. However, the kinetics were slightly different and in turn also the conclusion that could be drawn from the different analyses. A comparison of the results nicely represented similarities as well as differences between both datasets. For example in MDCK cells it seemed to be more important to investigate lower concentrations of the stimulus, whereas in the IMCD cells one might learn more by adding higher stimuli.

However, the optimal setup to clearly analyze the species-specific differences without the influence of other factors would be to use the same setup for both species. For example this might be

- perform experiment on two different species, e.g. rat and canine,
- use primary cell cultures,
- pre-incubation with no indomethacin added,
- stimulate cells with AVP,
- analyze samples from both species with immunofluorescence.

From the present study it is already known that this setup can be applied to primary rat IMCD cells. It has to be clarified, whether the setup would also be applicable to primary canine IMCD cells. If this is the case, the model can be a useful tool to guide experiments in both species.

Part II

Thermodynamic Model of the Cation Homeostasis in Yeast

*The second part of this thesis presents a thermodynamic model of the cation homeostasis in the yeast *Saccharomyces cerevisiae* with its main focus on plasma-membrane transporters for cations, in particular transporters for potassium and protons.*

In contrast to the first part of this thesis, with the signaling pathway that triggers the trafficking of a channel as its major aspect, the emphasis of the following part is on transport proteins that are already located in the plasma membrane. It was monitored, how the flux of ions through the plasma membrane, facilitated by the membrane transport proteins, changes due to different conditions and over time.

In order to model cation homeostasis, a thermodynamic approach based on the theory of linear nonequilibrium thermodynamics [23, 58] was used. With this approach it is possible to model passive ion fluxes driven by the electrochemical potential differences but also primary or secondary active transport processes driven by the interplay of different ions (symport, antiport) or by ATP consumption (ATPases) [108, 146].

In contrast to the frequently used approach to model the transporters in full detail [54, 114], linear non equilibrium thermodynamics can be applied to model net ion fluxes and, thus, is perfectly suitable for the available biological data. These were net proton and potassium fluxes from MIFE and FLISE measurements (non-invasive approaches which were used to calculate transmembrane proton and potassium fluxes).

*The parameters of the model were estimated such that the model was able to reproduce the data from measurements with *S. cerevisiae* wild-type strains being stimulated with different concentrations of KCl followed by addition of glucose.*

*The carefully parameterized model was used to predict additional ion fluxes, and chloride was identified as a potential candidate. Furthermore, the model was used to analyze potential mechanisms for *Trk1,2p* transport dynamics and to make predictions about *Trk1,2p* and *Pma1p* mutations. Finally, the effect of multiple KCl stimuli was predicted showing a reduced activity for cells pretreated with higher KCl stimuli.*

Experimental data from MIFE measurements were provided by Prof. Sergey Shabala and Dr. Svetlana Shabala (University of Tasmania). Data from FLISE measurements were provided by Ludwig et al. (University of Bonn, Germany). An initial version of the model was provided by Dr. Susanne Gerber [32].

5 Introduction

5.1 Yeast as a model organism

In this thesis part the focus is on cation homeostasis in the yeast *Saccharomyces cerevisiae*. *S. cerevisiae*, also named "bakers yeast", "brewers yeast" or "budding yeast" is widely known for its essential role in beer, bread and wine production.

It is one of the best characterized eukaryotic organisms [131] and its genome was the first to be completely sequenced [34]. As a unicellular fungus it is a very simple and easy to handle model system. It grows very quickly and is generally recognized as safe (GRAS). It is able to survive in a haploid state and is easy to manipulate. It is widely used as a model organism to study processes such as osmopressure [64, 124], cell cycle [7, 91], or metabolism [141].

Yeast is similar to higher eukaryotes regarding cell structure and physiological processes. In fact, many homologous proteins are highly conserved in sequence and function between yeast and higher eukaryotes. Thus, many results obtained from experiments on yeast also lead to insights in higher eukaryotes. This makes *S. cerevisiae* an ideal model organism to study complex processes such as cation homeostasis [137].

5.2 Cation homeostasis in *S. cerevisiae*

In natural environment the amount of sodium can be very high whereas the amount of potassium is rather sparse. However, while potassium is essential for cellular processes such as protein synthesis and enzyme activation, sodium is rather toxic if present at high concentrations. Furthermore, the interplay between sodium and potassium is important to maintain the membrane potential. Therefore the amount of these cations within the cells is highly regulated.

Under optimal conditions *S. cerevisiae*'s cellular amount of potassium is in the range of 200 to 300 mM whereas in many environments it lies in the micromolar range [137]. *S. cerevisiae* is able to survive in a very broad range of external potassium concentration (10 μ M - 2.5 M) and up to 1.5 mM of external sodium [3]. To maintain the proper intracellular ion distribution under such varying conditions, different mechanisms are used by the cell. Such are the higher affinity of membrane transport proteins for beneficial ions like potassium, efficient efflux systems for toxic cations like sodium and the sequestration (compartmentalization) of toxic cations in cellular organelles like the vacuole [3, 137]. Diverse ion transport proteins mediate the transport of ions either actively (primary active via ATPases or secondary active via symport or antiport) or passive via ion channels or carriers.

S. cerevisiae, such as most microorganisms and plants, uses the energy from ATP hydrolysis to pump protons out of the cell. The resulting proton gradient can be utilized to transport toxic cations out or beneficial cations into the cell [3].

5.3 Aim and structure of this thesis part

In the following part of this thesis a thermodynamic model of the cation homeostasis in the yeast *Saccharomyces cerevisiae* will be proposed, which is based on an initial model version by Dr. Susanne Gerber. With a linear non-equilibrium thermodynamics approach the ion channels of the cellular plasma membrane are modeled implicitly. The major enhancements introduced here are:

- Decomposition of the model parameters and mapping them to individual transporter types allow for *in silico* mutation and knockout experiments.
- The pump affinities depend not only on the ATP hydrolysis reaction affinity but include back pressure effects due to the involved ions.
- The membrane potential is now calculated as a time derivative of the excess of charges on both sides of the membrane. This can be calculated directly via the flux of ions through the membrane.

In Sec. 5.4 the major cation transporting proteins in the yeast plasma membrane will be introduced, how they are regulated and how they contribute to cation homeostasis. A major premise for active transport events is the availability of energy for the cell. Therefore, short-term energy storage mechanisms important for the processes described in the following will be shortly mentioned.

In Sec. 5.5 the foundation of thermodynamics and non linear thermodynamics will be introduced. Sec. 6 lists the relevant methods applied in this thesis part.

In Sec. 7.1 the thermodynamic model will be presented. The biological data, with which the model was confronted with, will be introduced in Sec. 7.2. This were H^+ and K^+ flux measurements from MIFE as well as FLISE experiments. First, estimation of the Onsager coefficients was performed to reproduce the data from MIFE measurements *in silico* (Sec. 7.3). The resulting outcome concerning the importance of specific parameters (Sec. 7.4), *in silico* knockout and inhibition experiments (Sec. 7.5), the analysis of potential Trk1,2p transport mechanisms (Sec. 7.6), and the prediction of the model's behavior at subsequent KCl stimuli (Sec. 7.7) will be presented. Finally, it was investigated whether the model can also be applied to data from FLISE experiments (Sec. 7.8). The results will be discussed in Ch. 8.

5.4 Biological background

5.4.1 Membrane proteins influencing cation homeostasis

The major cation transport proteins in the yeast plasma membrane are the potassium uptake systems Trk1p and Trk2p, the potassium channel Tok1p, the Na^+/H^+ antiporter Nha1p, the P_i - Na^+ symporter Pho89p, the H^+ -ATPases Pma1p and the Na^+ -ATPase Ena1p [3]. In addition, unspecific cation channels like Nsc1p might exist [12].

The most relevant cation transport proteins in the yeast plasma membrane are shown in Fig. 5.1. Although the model does not include the ion channels explicitly, it is important to understand the functional details in order to interpret the Onsager coefficients (see Sec. 5.5.6) correctly.

Proton ATPase Pma1p

The electrogenic proton ATPase Pma1p is one of the most abundant proteins in the yeast plasma membrane. It uses the hydrolysis of ATP to pump H^+ out of the cell. Therefore it is responsible to generate

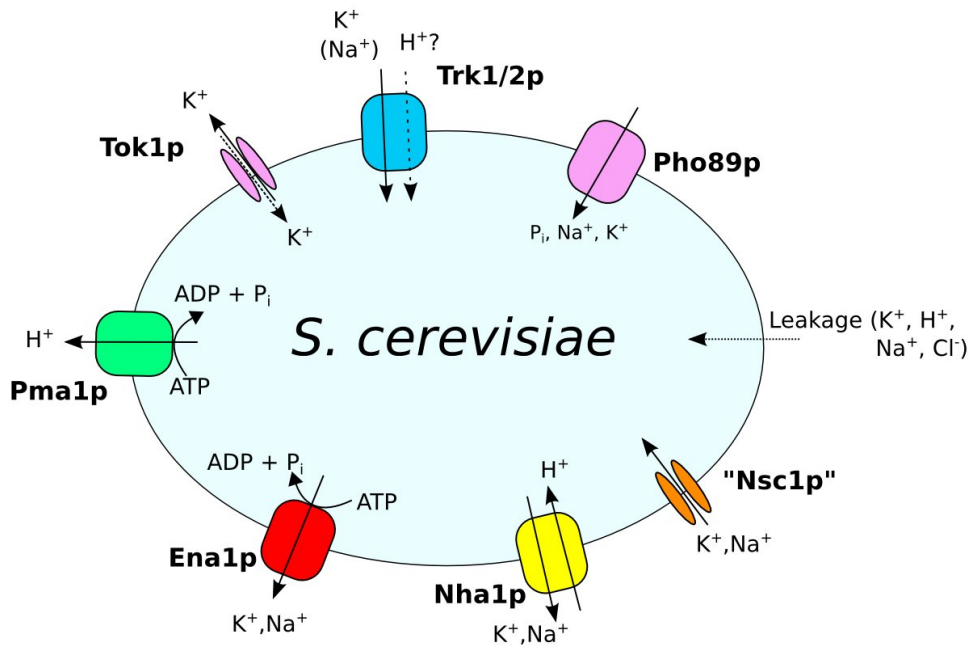


Figure 5.1: Schematic yeast cell including the major cation transport proteins of the cellular plasma membrane.

the proton motive force that is needed to transport ions against their gradients [3, 94].

The Pma1p activity is highly regulated, e.g. positively by a decrease in intracellular pH and increased potassium uptake [3]. Seto-Young and Perlin [129] used a proteoliposome system to analyze the voltage dependency of Pma1p. They discovered that an increase in the membrane potential of the proteoliposome (corresponding to a more negative membrane potential in intact yeast cells) correlates with a decrease in ATP hydrolysis.

It is known that at least 20% of the cellular ATP gets consumed by the Pma1p [3]. The addition of extracellular glucose increases the ATPase activity of purified membranes up to 10-fold [73]. Apparently this process depends not only on the increase of intracellular ATP, but it requires glucose metabolism [128]. Furthermore, Lecchi *et al.* [74] could show by using mass spectrometry methods that stepwise phosphorylation of Ser-911 and Thr-912 is responsible for glucose dependent Pma1p activation.

Perlin *et al.* [99] figured out in 1986 that the stoichiometry of proton pumps in *Neurospora Crassa* is 1 H^+ /ATP. They used membrane vesicles for their measurements and their results are in agreement with previous estimates from electrophysiological measurements on whole cells.

K^+ -channel Tok1p

The K^+ -channel Tok1p shows outward rectification [75], which means that its conductance is voltage dependent (the channel is open at some membrane potentials and closed at others [40]) and it passes K^+ more easily in the outward direction. Unlike other voltage dependent K^+ outward rectifying channels Tok1p is not only dependent on the membrane voltage (V), but also on the K^+ equilibrium potential ($V - E_K$), which has been described for inward rectifying K^+ -channels [75].

Vergani *et al.* [144] verified that positive membrane voltages promote the outward current through Tok1p while external K^+ has an inhibitory effect. At external K^+ concentrations below 1 mM, the Tok1p con-

ductance is insensitive to external K^+ whereas at concentrations above 3 mM the current-voltage curve shifts in parallel with the K^+ equilibrium potential.

Fairman *et al.* [25] supported with patch-clamp analysis on TOK1-hyperexpressing cells lacking Trk1,2p that Tok1p shows an outward current at membrane potentials above the K^+ equilibrium potential. Below the K^+ equilibrium potential he observed a small inward current. This means that under certain conditions, yeast can take up K^+ via Tok1p.

Further characteristics of Tok1p are that it is sensitive to internal, but not external pH (internal acidic pH decreases the Tok1p activity [75]) and that removal of external divalent cations can cause inward currents and a more linear current-voltage relationship [61].

K^+ -carriers Trk1p and Trk2p

The two potassium specific transporters Trk1p and Trk2p use the plasma membrane potential to transport K^+ into the cell [94]. They are homologous proteins and therefore very similar in structure and function [69]. They are often labeled as "Trk1,2p system", although no physical interaction is known between the two proteins [3]. There exist similarities as well as differences between the two transporters.

Trk1p and its high affinity for potassium is the major player for potassium accumulation within the cell [137]. Trk1p can switch its affinity depending on the internal K^+ content from low affinity under K^+ abundance to high affinity under K^+ starvation conditions. Therefore, it enables yeast cells to grow at micromolar concentrations of K^+ [11, 31, 107]. Trk1p is dependent on the internal pH and in turn also influences H^+ homeostasis [153].

Trk2p is also able to transport potassium with high/moderate affinity under K^+ starvation conditions. However, it is very poorly expressed under standard conditions and therefore its effect is not very high [3]. It can still enable a $\Delta trk1$ deletion mutant to grow on medium with less than 10 mM K^+ , which a $\Delta trk1,2$ double mutant is not able to [11]. In contrast to Trk1p, Trk2p seems to be independent of the internal pH [106, 137].

Cells lacking both Trk1p and Trk2p are hypersensitive to acidic pH [85]. Both, the K^+ transport defect and low-pH hypersensitivity of $\Delta trk1,2$ cells, can be overcome by overexpression of either TRK1 or TRK2 [68, 85].

More recently it has been proposed that anions can exit the cell via Trkp transporters in a pH dependent manner [71, 113].

Na^+/H^+ antiporter Nha1p

The Nha1p antiporter plays an important role in sodium tolerance, potassium homeostasis and intracellular pH [6, 138]. It combines H^+ import with Na^+ export and can further mediate the efflux of Li^+ , Rb^+ and K^+ .

NHA1 expression is constitutive and very low. It has the most influence at low extracellular pH [137], when it can use the high H^+ inward gradient to transport toxic or surplus cations out of the cell. It is especially important when the cells are grown under salt stress conditions and low external pH. Under these conditions toxic cations can enter the cells unspecifically via various transport systems and the H^+ gradient can be used for their active extrusion. At high external pH Nha1p fails to export toxic cations even if they accumulate in high concentrations. Under these conditions the Ena1 ATPase becomes activated and exports the cations.

Sodium ATPase Ena1p

The P-type Na⁺-ATPase Ena1p acts as a cellular detoxification system. Primary active transport via ATP hydrolysis is used to export toxic sodium ions against their gradient [137]. It has been shown that Ena1p can, in addition to Na⁺, also export K⁺ and Li⁺. Of those ions it is able to transport K⁺ and Na⁺ with the same efficiency. Therefore, it is not only able to act as a sodium detoxification system but plays also an important role in potassium homeostasis, especially if the medium is alkaline and thus Nha1p cannot export potassium efficiently. Which ion gets exported depends highly on the external cation concentrations. In case of high external sodium it would preferably export this cation [121].

Na⁺/P_i cotransporter Pho89p

The Na⁺/P_i high-affinity cotransporter Pho89p was identified by Martinez and Persson [82]. It uses the Na⁺ gradient across the plasma membrane to transport anorganic P_i into the cell. It is active at high pH and only expressed if P_i is limiting. Pho89p by itself is unable to sense extracellular phosphate levels and is cation-dependent [156]. It is highly specific for Na⁺. It transports Na⁺ twice as efficient as K⁺ or Li⁺ [156]. Its gene expression is upregulated under Mg²⁺ starvation, Ca²⁺ stress, and alkalization [147].

Non-specific cation channel Nsc1p

Although its gene could not be identified, yet, a non-specific cation channel has been proposed and named Nsc1p. This channel is most likely being responsible for the low-affinity K⁺ influx that could be observed in Δ trk1,2 mutants [137].

Experiments showing that Δ trk1,2 mutants are not able to grow at a pH of 3.1 but at 5.8 [11], lead to the conclusion that Nsc1p might be active under the condition of higher pH. Patch-clamp experiments verified that the inward currents can be detected at high external K⁺ and decrease with reduced pH [11, 13].

Furthermore, it has been shown in patch-clamp experiments that Nsc1p is blocked by normal (mM) calcium and other divalent metal ions whereas removal of calcium activates it [12, 13].

5.4.2 Energy storage in cells

Energy can be stored in cells in various ways. Long-term energy storage takes place mainly via glycogen and fat in animal and fungal cells or via amylopectin in plant cells [2, 78]. Prominent variants of short-term energy storage mechanisms are via the phosphate carrier ATP, via the electron carriers NADH and NADPH, and via transmembrane H⁺ gradients [2, 101]. ATP can be hydrolyzed into ADP and P_i. During that process, energy of approximately 50 kJ/mol gets released. Some enzymes use GTP, UTP or CTP instead of ATP, but the resulting energies are equivalent. To avoid death the cell maintains a nonequilibrium concentration of ATP, ADP and P_i [101].

Energy stored in ATP or NADH can be used by pumps to build up H⁺ gradients across the membrane. Those gradients can be used for example for secondary active transport. Nutrients or several ions can be transported in symport or antiport with H⁺ through the membrane, were H⁺ is transported with the electrochemical gradient and the other substance against it.

The energy storage mechanisms via ATP and transmembrane H⁺ gradients are integrated into the model.

5.5 Thermodynamical background

The model proposed here applies the theory of linear non-equilibrium thermodynamics [58] to cation homeostasis in yeast. This approach allows for modeling systems in a general way even though less data and information are available than commonly necessary for building up kinetic or statistical models.

In the following sections, the thermodynamical background will be introduced. To get an overview, the foundation of thermodynamics, its basic characteristics and laws as well as the major differences between equilibrium and nonequilibrium thermodynamics will be briefly outlined. Afterwards, entropy, entropy production and the electrochemical potential will be explained. Thereupon, the basic concepts of linear non-equilibrium thermodynamics will be introduced, i.e. the theory of the dependency between flows and forces as well as Onsager's reciprocal relation. Finally, the calculation of the ATP consumption, the membrane potential, and fluxes due to individual transporter types will be derived, as it was implemented in the model.

5.5.1 Thermodynamic systems

If one wants to study a process thermodynamically, one first has to define the thermodynamic system and its boundaries. Three basic types of thermodynamic systems can be distinguished [58]:

1. adiabatic systems - are enclosed by walls that prevent exchange of heat or matter with the surroundings,
2. closed systems - are surrounded by *diathermal* walls that prevent exchange of matter but allow exchange of heat or thermal energy with the surroundings,
3. open systems - can exchange heat and matter with their surroundings.

The adiabatic and closed systems are the primary objects of classical thermodynamics whereas biological systems fall into the last category.

A thermodynamic system is defined by a set of parameters which can be either *external* or *internal*. External parameters define the interplay between the system with its surroundings, like external pressure or the volume of the system. Internal parameters describe the internal state of the system, like local concentration or pressure differences. In case of equilibrium, the system can be described by using only the external parameters. In non-equilibrium thermodynamics, the internal parameters have to be taken into account, which increases the complexity of the system.

It is also possible to distinguish between *extensive* and *intensive* parameters. Extensive parameters depend on the size of a system as a whole, like the volume or the mass of the system. Whereas intensive parameters have different values at each point in the system, like local concentrations or pressure.

In the model proposed here extensive parameters like the entropy S , the volume V , or the number of particles N in the system will be used as well as intensive parameters like the chemical potential μ , which is independent of the size of the system.

5.5.2 Equilibrium versus nonequilibrium thermodynamics

There exist different branches of thermodynamics and it depends on the task at hand, which one is the best to be applied. In the following, equilibrium and non-equilibrium thermodynamics shall be mentioned

[65]. To understand their field of application, first some more definitions have to be made.

A thermodynamic process can be either reversible or irreversible.

A *reversible* process is always in a state of equilibrium and is thus able to return from every state j to its starting state i without any change in the external environment. In a reversible process the state variables, i.e. the measurable physical quantities by which the state of the system is uniquely defined, are time independent.

An *irreversible* process, as the name suggests, cannot be reversed. This means that a system, leaving a specific state, cannot go back to this state without any change in the external environment. Irreversible processes are necessary if one wants to model instantaneous processes that are far from equilibrium, which is quite often the case in biological systems.

The *equilibrium state* is the state every isolated systems reaches at some point and will not leave afterwards. This state can be described by a small amount of state variables. A *non-equilibrium state* is a state a spatial inhomogeneous and time-dependent system is in until it reaches its equilibrium state.

Equilibrium thermodynamics addresses, which changes are possible for a system (e.g. the difference in entropy). It does not consider the system's properties on its way from the start to the equilibrium state. The process under consideration can be reversible as well as irreversible.

Non-equilibrium thermodynamics enables to monitor systems over space and over time in inhomogeneous systems that are not at equilibrium. Therefore, it is necessary to use state variables which are space and time dependent. Just as equilibrium thermodynamics, non-equilibrium thermodynamics can handle reversible as well as irreversible processes. Due to the fact that it can handle systems that are not in equilibrium, its main benefit lies in the application to irreversible processes.

Linear processes are processes which are close to equilibrium, whereas *non-linear processes* are far from equilibrium. Therefore, *linear non-equilibrium thermodynamics* handles processes, that do not have to be in equilibrium, but are assumed to be close to equilibrium.

5.5.3 The laws of thermodynamics

The zeroth law of thermodynamics The zeroth law of thermodynamics [23, 58, 122] states that in a closed system existing temperature differences will cancel each other out. This can also be applied to a system with multiple subsystems. If subsystem A is in thermal equilibrium with subsystem B , and subsystem B in thermal equilibrium with subsystem C , this implies that also A is in thermal equilibrium with C . The whole system can be described by a single empirical parameter, the temperature T . T is a universal function and depends on the state parameters a_i and the energy of the i th system U_i , $T = f(a_i, U_i)$. When the energy of the whole system increases this means that also the energy of all the subsystems increases and, as a consequence, also its temperature is increasing ($\delta U / \delta T > 0$).

The first law of thermodynamics The first law of thermodynamics [23, 58, 122] is the law of the conservation of energy. Helmholtz formulated it mathematically in 1847 as

$$dU_A = dQ - dW \quad (5.1)$$

where A is a closed system that can exchange heat with a surrounding adiabatic system. The internal energy of the system A , dU_A is given by the heat provided to the system (dQ) and the work performed on

the system (dW). The law states that energy can be transferred from one form to another, but it cannot be produced out of nowhere.

The second law of thermodynamics The second law of thermodynamics [22, 58, 122] is an attempt to describe natural and irreversible processes. As stated before, in reversible processes and in equilibrium the system can be defined completely by the external parameters. If the external parameters are changing so slow that the internal parameters can adjust every instant to the external ones, the temporal process can be divided into a sequence of equilibrium states. Therefore, it is assumed that the laws of equilibrium thermodynamics can, at least on a local scale, also be applied in nonequilibrium systems. This assumption is referred to as the "local thermodynamic equilibrium postulate" and handles so called "quasi-equilibrium processes". It is expected that this postulate holds for systems that are sufficiently close to equilibrium.

Furthermore, the second law provides information about the direction of reactions and the resulting change in energy. It states that during a reversible, cyclic process, the change in work is zero, whereas during natural, irreversible processes, the change in work would be lower than zero.

5.5.4 Entropy and entropy production

The second law of thermodynamics can also be written in terms of a change in the entropy S [23, 58]. For reversible processes it holds that

$$dS = \frac{dQ}{T}. \quad (5.2)$$

The change in the extensive factor S is equal to the change in heat dQ divided by the intensive factor T , the total temperature of the system. The first and the second law of thermodynamics can be summarized by inserting Eq. 5.2 into Eq. 5.1 resulting in

$$dU = TdS - dW \quad (5.3)$$

where TdS is the heat added to the system and dW the work done on the system.

The change in entropy dS is the sum of the entropy produced internally d_iS and the entropy exchanged with the surroundings d_eS

$$dS = d_iS + d_eS. \quad (5.4)$$

If only reversible processes are involved, it holds that $d_iS = 0$ and $d_eS = 0$. If irreversible processes are involved, the change of internal entropy cannot only be explained by the exchange with the surroundings, additional entropy is produced internally and Eq. 5.2 will include the inequality

$$d_iS \geq \frac{dQ}{T} \quad (5.5)$$

This also means, that the entropy is no conserved quantity.

At the macroscopic equilibrium state the entropy reaches its maximum, no internal entropy is produced and therefore $d_iS = 0$.

The internal entropy production is the fundamental property of all irreversible processes. In the following sections some important characteristics of the parameters used in the model will be derived from this property.

Entropy and chemical reactions

In an isothermic and isobaric system the chemical affinity is the driving force for a reaction [58]. The chemical affinity A of a reaction is

$$A = - \sum_{i=1}^k v_i \mu_i \geq 0, \quad (5.6)$$

in which μ_i is the chemical potential and v_i the stoichiometric coefficient of substance i in the reaction. Integrated into the Gibbs equation and written in terms of entropy this leads to

$$dS = \frac{dQ}{T} + \frac{A}{T} d\xi, \quad (5.7)$$

with $d\xi$ the advancement of the reaction. In agreement with Eq. 5.4 this term can be divided into an external and an internal entropy part. The first part $d_e S = \frac{dQ}{T}$ represents the entropy exchanged with the surroundings, whereas the second part $d_i S = \frac{A}{T} d\xi > 0$ stands for the entropy produced internally. As a time differential this yields

$$\frac{d_i S}{dt} = \frac{A}{T} \frac{d\xi}{dt} = \frac{A}{T} J_{ch}, \quad (5.8)$$

with $J_{ch} = \frac{d\xi}{dt}$ the velocity (also termed rate or flow) of the reaction [23, 33, 58, 101]. This means that for a chemical reaction the change in entropy is given by the flow of the system multiplied by its corresponding force, the affinity, divided by the temperature.

This formula will be used later for the description of the ATP dependent term of the flux equations.

In multiple reactions Eq. 5.8 can be written as

$$\frac{d_i S}{dt} = \frac{1}{T} \sum_{j=1}^{n_r} A_j J_{ch_j} \geq 0, \quad (5.9)$$

with the sum over the n_r different reactions. The sum of the products and not each product by itself has to be greater than 0. By coupling different reactions, a reaction can also progress, even if its entropy is decreasing.

Entropy production in irreversible regimes

By assuming local volume quantities, in which temperature T , pressure P and electrochemical potentials $\tilde{\mu}_i$ can assumed to be equal at all points and which are still large enough so that stochastic fluctuations can be neglected, the local entropy production σ can be written as

$$\sigma = \mathbf{J}_q \cdot \text{grad} \frac{1}{T} + \sum_{i=1}^n \mathbf{J}_i \cdot \text{grad} \left(-\frac{\tilde{\mu}_i}{T} \right) + \sum_{j=1}^{n_r} J_{ch_j} \frac{\tilde{A}_j}{T} \quad (5.10)$$

which is a sum of products of flows with their conjugated forces [23, 58]. The first term relates to the flow of heat \mathbf{J}_q driven by the gradient in temperature. The second term is the sum over all ion flows \mathbf{J}_i for

each ion i driven by its electrochemical gradient. The last term is, in accordance with Eq. 5.9, the sum of the change in matter J_{ch_j} due to the n_r chemical reactions within the system. Each J_{ch_j} is driven by the electrochemical affinity \tilde{A}_j of the corresponding reaction j .

From the rules of differentiation it is known that

$$\text{grad} \frac{1}{T} = -\frac{1}{T^2} \cdot \text{grad} T \quad \text{and} \quad \text{grad} \left(-\frac{\tilde{\mu}_i}{T} \right) = -\frac{1}{T} \cdot \text{grad} \tilde{\mu}_i + \frac{\tilde{\mu}_i}{T^2} \cdot \text{grad} T.$$

Applying this to the first and second term of Eq. 5.10 results in

$$\sigma = \left(\frac{J_q - \sum_{i=1}^n \tilde{\mu}_i J_i}{T^2} \cdot \text{grad}(-T) + \sum_{i=1}^n \frac{J_i}{T} \cdot \text{grad}(-\tilde{\mu}_i) + \sum_{j=1}^{n_r} J_{ch_j} \frac{\tilde{A}_j}{T} \right) \geq 0. \quad (5.11)$$

Substitution of $\frac{J_q - \sum_{i=1}^n \tilde{\mu}_i J_i}{T}$ with the flow of entropy J_S and subsequent multiplication by T results in the dissipation function

$$\Psi = T\sigma = \left(J_S \cdot \text{grad}(-T) + \sum_{i=1}^n J_i \cdot \text{grad}(-\tilde{\mu}_i) + \sum_{j=1}^{n_r} J_{ch_j} \tilde{A}_j \right) \geq 0. \quad (5.12)$$

For the proposed model, some simplifications could be made. During the experiment, the temperature is assumed to be identical inside and outside the membrane and constant over time. Therefore $\text{grad}(-T)$ is zero and the first term disappears. Furthermore, only one chemical reaction is included, which is the hydrolysis of ATP. For this reaction the electrochemical affinity \tilde{A} can be simplified to the chemical affinity A . One more simplification that can be made while looking at transmembrane transport, is to model it as a discontinuous system. Assuming a membrane with thickness x , instead of calculating Ψ for every point in the membrane, one can integrate Ψ across the membrane [58]. This leads to $\Psi = \int_0^{\Delta x} \Psi$, with Ψ the dissipation function for the membrane. Therefore, Eq. 5.12 can be reduced to

$$\Psi = \left(-\sum_{i=1}^n J_i \cdot \Delta \tilde{\mu}_i + J_{ch} A \right) \geq 0 \quad (5.13)$$

with $\Delta \tilde{\mu}_i$ the difference in the electrochemical potential of ion i on both sides of the membrane.

5.5.5 The electrochemical potential

Diffusion of particles is caused by concentration differences, whereas drift of ions is caused by potential differences [51]. Fick's law of diffusion states that

$$J = -D \frac{\partial [C]}{\partial x} \quad (5.14)$$

where J is the diffusion flux, D the diffusion coefficient, and $[C]$ the concentration of an ion. The negative sign indicates that the ions flow from high to low concentration. Diffusion is directly proportional to the magnitude of the gradient.

Charged particles experience an additional force according to

$$J_{drift} = \partial_{el} E = -\mu_{qz}[C] \frac{\partial \phi}{\partial x} \quad (5.15)$$

which is the drift flux [51]. σ_{el} is the electrical conductivity and a measure of the materials ability to accommodate the movement of an electric charge. E is the electric field with $E = -\frac{\partial\phi}{\partial x}$, ϕ the electric potential, μ_q the electrical mobility, z the valence, and $[C]$ the concentration of the ion. If positively charged ions are within an electrical field, they will flow down the electrical potential gradient.

As shown by Einstein in 1905 the frictional resistance by the fluid medium is the same for diffusion and for drift. D and μ_q can be related by the equation

$$D = \frac{kT}{q} \mu_q \quad (5.16)$$

where k is the Boltzmann constant ($\frac{1.38 \cdot 10^{-23} \text{ joule}}{K}$), T the absolute temperature and q the charge of the ion in Coulomb. This relation shows that diffusional and drift processes are additive.

The additivity of the diffusional and the drift processes leads to the combined ion flux

$$J_{ion} = J_{diff} + J_{drift} = -D \frac{\partial[C]}{\partial x} - \mu_q z [C] \frac{\partial\phi}{\partial x}. \quad (5.17)$$

Einstein's relation can be used to simplify the equation by substitution of the diffusion coefficient. This leads to the Nernst-Planck equation, which is

$$J_{ion} = -\left(\frac{\mu_q k T}{q} \frac{\partial[C]}{\partial x} + \mu_q z [C] \frac{\partial\phi}{\partial x}\right). \quad (5.18)$$

Substitution of the electrical mobility μ_q with the generalized mobility μ_{gen} via $\mu_{gen} = \mu_q/q$ leads to

$$J_{ion} = -\left(\mu_{gen} k T \frac{\partial[C]}{\partial x} + \mu_{gen} \cdot q z [C] \frac{\partial\phi}{\partial x}\right). \quad (5.19)$$

Division of μ_{gen} by Avogadro's number leads to the Nernst-Planck equation in molar form

$$J = -\left(u R T \frac{\partial[C]}{\partial x} + u z F [C] \frac{\partial\phi}{\partial x}\right) \quad (5.20)$$

where u is the molar mobility, R the universal gas constant and F Faraday's constant.

Applying $L = [C]u$ and the derivation rule $(\ln f)' = f'/f$ results in

$$J = -\left(L R T \frac{\partial \ln[C]}{\partial x} + L z F \frac{\partial\phi}{\partial x}\right). \quad (5.21)$$

For the application to membrane transport and in accordance with Eq. 5.13, Eq. 5.21 can be integrated over the membrane leading to

$$J = -\left(L R T \Delta \ln[C] + L z F \Delta\phi\right) \quad (5.22)$$

with $\Delta \ln[C]$ the difference in $\ln[C]$ across the membrane and $\Delta\phi$ the membrane potential (see also Sec. 5.5.7). Eq. 5.22 will be used in the following to model the fluxes due to electrochemical potential differences.

There exist different kinds of biological ion channels and it has to be mentioned that the Nernst-Planck equation holds only for those who allow for ion movement that is proportional to the ion's concentration gradient. If there exist energy barriers or blocking sites within the channel, the use of the Nernst-Planck equation might be incorrect [51].

5.5.6 Linear non-equilibrium thermodynamics

Flows and forces

Linear non-equilibrium thermodynamics is based on the fact that in all diffusion processes a linear relationship exists between flows and their conjugated forces. The first relation between flows and forces was obtained by Fourier in 1811. He showed that the flow of heat is linearly related to the gradient of temperature. In the 19th century, Ohm showed that the electric current is proportional to the electromotive force and Fick showed that the rate of diffusion of matter depends on the negative gradient of concentration [101].

The dissipation function given in Eq. 5.13 characterizes the fluxes and forces which are important for the system considered here. In a more general way the linear relationship between a flow and its corresponding force can be written as

$$J_i = L_{i,i}X_i, \quad (5.23)$$

with the flux J_i , the corresponding force X_i and the phenomenological or so called Onsager coefficient $L_{i,i}$. If a system consists of several flows and forces coupling of forces is possible, which was first studied by Kelvin in 1854. In such a system, every flow can depend on every force in a complicated non-linear manner. Close to equilibrium one can simplify this system of non-linear flow-force relationships by expanding it in a Taylor series

$$J_i = J_{i,eq}(X_i = 0) + \sum_{j=1}^n \left(\frac{\partial J_i}{\partial X_j} \right)_{eq} X_j + \frac{1}{2!} \sum_{j=1}^n \left(\frac{\partial^2 J_i}{\partial X_j^2} \right)_{eq} X_j^2 + \dots \quad (5.24)$$

with the n standing for the amount of different species in the system.

The first term $J_{i,eq}(X_i = 0)$ disappears, since the flux $J_{i,eq}$ becomes 0 as soon as its corresponding force disappears. One can now neglect the higher order non-linear terms and substitute the partial of the flux J_i and force X_j at equilibrium $\left(\frac{\partial J_i}{\partial X_j} \right)_{eq}$ with $L_{i,j}$. This results in the phenomenological equations proposed by Onsager which show the linear relationship between multiple thermodynamical flows and forces

$$\begin{aligned} J_1 &= L_{1,1}X_1 + L_{1,2}X_2 + \dots + L_{1,n}X_n \\ J_2 &= L_{2,1}X_1 + L_{2,2}X_2 + \dots + L_{2,n}X_n \\ &\vdots \\ J_n &= L_{n,1}X_1 + L_{n,2}X_2 + \dots + L_{n,n}X_n \end{aligned} \quad (5.25)$$

or

$$J_i = \sum_{j=1}^n L_{i,j}X_j. \quad (5.26)$$

The physical meaning of this equation system is, that each flux J_i of an ion i depends in a linear relationship on its conjugated force X_i via the "straight coefficient" $L_{i,i}$. Whether or not a force is conjugated to a flux presupposes that the product J_iX_i has the dimensions of entropy production or decrease in free energy with time [58].

Furthermore, a coupling is given with the other species of the system and their forces also in a linear relation via the "coupling coefficients" $L_{i,j}$. A flow J_i depends on a force X_j as soon as the coupling

coefficients $L_{i,j} \neq 0$.

Onsager's law

One of the cornerstones of non-equilibrium thermodynamics was laid by Lars Onsager in 1931 [93]. He showed that the matrix of phenomenological coefficients is symmetric so that

$$L_{i,j} = L_{j,i}. \quad (5.27)$$

He derived from statistical considerations that Eq. 5.27 holds as long as the flows and forces of the phenomenological equations have the form

$$\sigma = \sum_{i=1}^n J_i X_i. \quad (5.28)$$

This reduces the amount of coefficients to be estimated from n^2 to $\frac{n \cdot (n+1)}{2}$

From the fact that the entropy production density has to be positive-semidefinite, one can deduce important requirements for the Ls. Insertion of the flux equations from 5.26 into Eq. 5.28 results in

$$\sigma = \sum_{i=1}^n L_{i,i} X_i^2 + \sum_{i=1}^{n-1} \sum_{j=i+1}^n (L_{i,j} + L_{j,i}) X_i X_j \geq 0. \quad (5.29)$$

In case of all except of one X_i vanish (which is theoretically possible) a resulting negative $L_{i,i}$ would violate the positive semidefiniteness of σ . Herefrom, one may deduce that the straight coefficients have to be non-negative [65]:

$$L_{i,i} \geq 0 (i = 1, \dots, n). \quad (5.30)$$

In addition Eq. 5.29 will be positive-semidefinite only if the determinant of the matrix of phenomenological coefficients is non-negative [58]. In general this means

$$\begin{vmatrix} L_{1,1} & L_{1,2} & \dots & L_{1,n} \\ L_{2,1} & L_{2,2} & \dots & L_{2,n} \\ \vdots & & & \vdots \\ L_{n,1} & L_{n,2} & \dots & L_{n,n} \end{vmatrix} \geq 0 \quad (5.31)$$

and it has to hold that

$$L_{i,i} L_{j,j} \geq L_{i,j}^2. \quad (5.32)$$

Thermodynamical description of the ATP consumption

Transmembrane ATPases like Pma1p or Ena1p (see Sec. 5.4.1) use the consumption of ATP to pump ions through the membrane. The thermodynamic flux of ions defines also the spatial direction of the ion fluxes

over the cell membrane, whereas in case of ATP only the intracellular concentration will be considered in the following modeling approach.

The overall reaction of the ATP consumption is



By assuming that H_2O and P_i are in excess and do not influence the kinetics of the reaction, the consumption of ATP was modeled as a chemical reaction system of only the two substances ATP and ADP [32]¹,



The flux of J_{ATP} represents the change of the internal ATP concentration as

$$J_{ATP} = \frac{d}{dt} [\text{ATP}]_i. \quad (5.35)$$

As it is usual for thermodynamic fluxes of chemical reactions and already mentioned in paragraph 5.5.4, the consumption of ATP is driven by the affinity A of their reaction

$$A = - \sum_i v_i \mu_i = \mu_{ATP} - \mu_{ADP} \quad (5.36)$$

where the v_i are the stoichiometric coefficients and μ_i the chemical potentials of the substances of interest. Let $\bar{\mu}_i$ denote the chemical potential of substance i at equilibrium. It holds that for a system of two substances at equilibrium $\bar{\mu}_1 = \bar{\mu}_2$ which can be applied to ATP consumption leading to

$$\bar{\mu}_{ATP} = \bar{\mu}_{ADP}. \quad (5.37)$$

The flux of ATP should be proportional to the force, here the affinity, so that

$$J_{ATP} = LA = L(\mu_{ATP} - \mu_{ADP}). \quad (5.38)$$

If \bar{c}_{ATP} and \bar{c}_{ADP} are the equilibrium concentrations of ATP and ADP, then one can define α_{ATP} and α_{ADP} as the deviations of the current concentrations from their equilibrium such as

$$\begin{aligned} \alpha_{ATP} &= c_{ATP} - \bar{c}_{ATP} \\ \alpha_{ADP} &= c_{ADP} - \bar{c}_{ADP}. \end{aligned} \quad (5.39)$$

By assuming the conditions of constant temperature and pressure, the equation for the chemical potential is

$$\mu_i = \mu_i^0 + RT \ln c_i. \quad (5.40)$$

¹This on Katchalsky and Curran [58] based derivation was in similar form already presented by Gerber [32]. For the present study it was adjusted and is included here for completeness.

Using this together with Eq. 5.38 and 5.39 the equation for the affinity is

$$A = \mu_{ATP}^0 + RT \ln \bar{c}_{ATP} + RT \ln \left(1 + \frac{\alpha_{ATP}}{\bar{c}_{ATP}} \right) - \mu_{ADP}^0 - RT \ln \bar{c}_{ADP} - RT \ln \left(1 + \frac{\alpha_{ADP}}{\bar{c}_{ADP}} \right). \quad (5.41)$$

By applying the equality 5.37 for chemical equilibrium this can be transferred into

$$A = RT \left[\ln \left(1 + \frac{\alpha_{ATP}}{\bar{c}_{ATP}} \right) - \ln \left(1 + \frac{\alpha_{ADP}}{\bar{c}_{ADP}} \right) \right]. \quad (5.42)$$

By assuming that $\alpha_{ATP}/\bar{c}_{ATP}$ and $\alpha_{ADP}/\bar{c}_{ADP}$ are much smaller than 1, the logarithms can be expanded in series and the term can be simplified to

$$A = RT \left(\frac{\alpha_{ATP}}{\bar{c}_{ATP}} - \frac{\alpha_{ADP}}{\bar{c}_{ADP}} \right) = RT \frac{\alpha_{ATP}}{\bar{c}_{ATP}} (1 + K), \quad \text{with} \quad K = \frac{\bar{c}_{ATP}}{\bar{c}_{ADP}} \quad (5.43)$$

Together with equation 5.38 one ends up with

$$J_{ATP} = L \cdot \left(\frac{RT}{\bar{c}_{ATP}} \alpha_{ATP} (1 + K) \right). \quad (5.44)$$

In the here presented model of cation homeostasis the L will be substituted by $L_{1,4}$ and $L_{2,4}$ in the equations for the ion fluxes and by $L_{4,4}$ in the equation for the flux of ATP.

If ATP gets consumed within the cell, the flux of the reaction is defined here as positive. However, if ions leave the cell their flux is defined to be negative in order to be in agreement with the biological data.

5.5.7 The membrane potential

In most parts of the living body, the total charges of anions are *approximately* equal to the total charges of cations, which is called space-charge neutrality. The only exception is the separation of charges through biological membranes (e.g. cell membrane or mitochondrial inner membrane). The amount of uncompensated ions required to charge the membrane is very small and even in very small cells, more than 99.9% of the ions are compensated by ions of the opposite charge [51].

Due to the selectively permeable cell membrane different ion concentrations can accumulate inside and outside of the cell. The flow of the ions through the membrane is driven by their electrochemical potential gradients on both sides of the membrane. In the following, two different methods to calculate the potential difference over the membrane will be described and discussed, which are the Goldman-Hodgkin-Katz equation [35] and the calculation via the excess of charge [59].

With the Goldman-Hodgkin-Katz equation the reversal potential $\Delta\phi_{rev}$ is calculated. The reversal potential is the membrane potential which equilibrates when the membrane is at rest and no net ion fluxes exist. It builds up when starting with given inside and outside concentrations for each ion and assuming that at the beginning of the simulation, no membrane potential exists. The reversal potential is calculated by

$$\Delta\phi_{rev} = \frac{RT}{F} \ln \frac{\sum_{Anions} P_i c_i^{in} + \sum_{Cations} P_j c_j^{out}}{\sum_{Anions} P_i c_i^{out} + \sum_{Cations} P_j c_j^{in}} \quad (5.45)$$

with the inside and outside concentrations of the anions (c_i^{in} and c_i^{out}), the cations (c_j^{in} and c_j^{out}), their specific membrane permeability (P_i and P_j), and R , T , F having their usual meaning. The ion with the highest permeability P_i will have the highest influence on the membrane potential. It will diffuse through the membrane and thereby build up the membrane potential. The process will reach a steady state, if the force due to the electrical potential will reach the same level as the force due to the chemical potential. The voltage measured then is called the reversal or resting potential.

In the model of cation homeostasis by Gerber [32] the Goldman-Hodgkin-Katz equation was used to calculate the membrane potential and it was assumed that the membrane potential adapts so fast, that it is always in a state of quasi equilibrium in comparison to the slower ion transport processes. There, the ions K^+ and Cl^- were used for the calculation. Due to the experimental setup, in which the cells were starved in Milli-Q water prior to the experiment, it was assumed that the internal Na^+ could be neglected during the simulation. Given that also the measurement buffer was lacking Na^+ , it was completely excluded from the calculation.

One general hypothesis is, that the active pumping of protons by the Pma1p plays a major role in the generation of a membrane potential and that this potential drives than potassium ions into the cell [3]. Therefore, H^+ ions were integrated into the Goldman-Hodgkin-Katz equation. This led to the final equation for the reversal potential

$$\Delta\phi_{rev} = \frac{RT}{F} \ln \frac{P_{K^+} \cdot [K_{out}^+] + P_{Cl^-} \cdot [Cl_{in}^-] + P_{H^+} \cdot [H_{out}^+]}{P_{K^+} \cdot [K_{in}^+] + P_{Cl^-} \cdot [Cl_{out}^-] + P_{H^+} \cdot [H_{in}^+]} \quad (5.46)$$

which was used in the model of Gerber.

Due to the fact that the Goldman-Hodgkin-Katz equation is only valid at thermodynamic equilibrium, its applicability to living cells is limited. The membrane potential of a living cell is either a diffusion potential or it is generated by electrogenic pumps. Only those ions that are transported solely by passive diffusion are actually in equilibrium [33]. Another drawback is, that with the Goldman-Hodgkin-Katz equation it is assumed that the ions are independent from each other. This is a contradiction if coupling between ions exists, for example via symport or antiport mechanisms. Furthermore, the Goldman-Hodgkin-Katz equation is based on the assumption of a constant electric field through the membrane, which might also not be conformable with the existence of more structurally complicated membrane transport proteins. Therefore, a second approach was tested, which is the calculation of the membrane potential $\Delta\phi$ via the excess of positive and negative charges across the membrane [59]

$$\Delta\phi = \frac{F}{Cm \cdot S} \cdot (V_{in} \cdot ([H_{in}^+]_{ub} + [K_{in}^+] + [Na_{in}^+] - [Cl_{in}^-]) - V_{out} \cdot ([H_{out}^+] + [K_{out}^+] + [Na_{out}^+] - [Cl_{out}^-]) - X). \quad (5.47)$$

With this approach the membrane voltage is calculated by the molar amounts of species at each side of the membrane (for this purpose the volumes of the internal (V_{in}) and external (V_{out}) compartment as well as the molar concentrations of the involved species are taken into account). $[H_{in}^+]_{ub}$ stands for the unbuffered H_{in}^+ concentration. This is the H^+ concentration which would accumulate in case no intracellular buffering of H^+ ions exists (details of H^+ buffering are presented in Sec. 7.1). X is the amount of large, intracellular molecules that are unable to cross the cell membrane, e.g. negatively charged proteins. The charge on each side of the membrane is integrated by multiplication of the right side of the equation with Faraday's

constant F . By using the membrane capacitance Cm and the surface area of the cells S the voltage build up by the access of ions on either side of the membrane is calculated.

In the model proposed here, instead of calculating $d\Delta\phi$ directly (which would lead to difficulties due to the buffering of internal H^+), the derivative of $d\Delta\phi$ over time was used

$$\begin{aligned} \frac{d\Delta\phi}{dt} = \frac{d}{dt} \frac{F}{Cm \cdot S} \cdot (V_{in} \cdot ([H_{in}^+]_{ub} + [K_{in}^+] + [Na_{in}^+] - [Cl_{in}^-]) - \\ - V_{out} \cdot ([H_{out}^+] + [K_{out}^+] + [Na_{out}^+] - [Cl_{out}^-]) - X). \end{aligned} \quad (5.48)$$

Rearranging the equation and assuming that V_{in} and V_{out} and X are constant during the simulation leads to

$$\begin{aligned} \frac{d\Delta\phi}{dt} = \frac{F}{Cm \cdot S} \cdot (V_{in} \cdot \frac{d}{dt} [H_{in}^+]_{ub} - V_{out} \cdot \frac{d}{dt} [H_{out}^+] + V_{in} \cdot \frac{d}{dt} [K_{in}^+] - V_{out} \cdot \frac{d}{dt} [K_{out}^+] + \\ + V_{in} \cdot \frac{d}{dt} [Na_{in}^+] - V_{out} \cdot \frac{d}{dt} [Na_{out}^+] - V_{in} \cdot \frac{d}{dt} [Cl_{in}^-] + V_{out} \cdot \frac{d}{dt} [Cl_{out}^-]). \end{aligned} \quad (5.49)$$

Representing the time derivatives of the ions with their flux expressions results in

$$\begin{aligned} \frac{d\Delta\phi}{dt} = \frac{F}{Cm \cdot S} \cdot (V_{in} \cdot \frac{J_H \cdot S}{V_{in}} - V_{out} \cdot \frac{-J_H \cdot S}{V_{out}} + V_{in} \cdot \frac{J_K \cdot S}{V_{in}} - V_{out} \cdot \frac{-J_K \cdot S}{V_{out}} + \\ + V_{in} \cdot \frac{J_{Na} \cdot S}{V_{in}} - V_{out} \cdot \frac{-J_{Na} \cdot S}{V_{out}} - V_{in} \cdot \frac{J_{Cl} \cdot S}{V_{in}} + V_{out} \cdot \frac{-J_{Cl} \cdot S}{V_{out}}) \end{aligned} \quad (5.50)$$

where $\frac{d\Delta\phi}{dt}$ depends only on fluxes and not on concentrations. Rearranging and reducing the equation leads to

$$\frac{d\Delta\phi}{dt} = \frac{F}{Cm} \cdot (J_H - (-J_H) + J_K - (-J_K) + J_{Na} - (-J_{Na}) - J_{Cl} + (-J_{Cl})). \quad (5.51)$$

Reducing further results in

$$\frac{d\Delta\phi}{dt} = \frac{F}{Cm} \cdot (2 \cdot J_H + 2 \cdot J_K + 2 \cdot J_{Na} - 2 \cdot J_{Cl}) \quad (5.52)$$

which was implemented in the model proposed in this thesis.

It has to be noted, that all of the before mentioned attempts to model the membrane potential are approximations. In reality, the membrane potential depends highly on those membrane transport proteins which are membrane localized and open at that particular moment. The membrane potential is mostly influenced by the ion for which the membrane is most permeable. Due to the fact that some ion channels are voltage dependent or dependent on the internal or external ion concentrations, these conditions can change over time. This is neither integrated in the Goldman-Hodgkin-Katz equation, if the permeabilities or the conductivity are kept constant over time, nor in the calculation via the excess of charges.

5.5.8 Representation of the different transporter types

The approach applied here aims to build a representable model without modeling each transporter in full detail. Nevertheless, the phenomenological coefficients cannot be chosen completely independently. As was shown in Eq. 5.27, 5.30, and 5.32, there exist restrictions on the coefficients. Furthermore, if knock-out experiments are performed *in silico* it is necessary to know the influence on a specific transporter or

type of transporter on the coefficient. Hence, a level of intermediate complexity was chosen.

The transporters were separated into different groups: ion pumps, symporters or antiporters, and uniporters or fluxes due to leakage. Additionally, the stoichiometry of the transporters needs to be included. In the following, this will be described for the different transporter types. The superscript S will be used for ion importing pumps and symporters, A for ion exporting pumps and antiporters, and L for uniporters, channels and leakage.

At the end of this chapter a small example for a system composed of multiple transporter types will be given.

ATPases The overall reaction for a H^+ -ATPase is



with n_{HP}^A the amount of H^+ ions pumped per n_{PH}^A molecules of ATP.

The affinity A_P or $-\Delta G_P$ of the H^+ -ATPase is

$$A_P = -\Delta G_P = -n_{HP}^A \cdot \Delta \tilde{\mu}_H + n_{PH}^A \cdot (\mu_{ATP} + \mu_{H_2O} - \mu_{ADP} - \mu_{P_i}) \quad (5.54)$$

with $\Delta \tilde{\mu}_H = \tilde{\mu}_{H_{out}} - \tilde{\mu}_{H_{in}}$ acting as a back pressure effect on the pump, making it slower at increasing external H^+ (negative pH) or at decreasing membrane potential [108]. It was assumed that $\Delta \mu_P = \mu_{ATP} + \mu_{H_2O} - \mu_{ADP} - \mu_{P_i}$ can be approximated as Eq. 5.43.

Assuming that n_{HP}^A H^+ ions are pumped per n_{PH}^A molecules of ATP, the equation system for the pump can be written as

$$J_{H,ATP}^A = -\frac{n_{HP}^A}{n_{PH}^A} \cdot J_{ATP,H}^A \quad (5.55)$$

$$J_{ATP,H}^A = -n_{PH}^A \cdot L_{HP}^A \cdot (n_{HP}^A \cdot \Delta \tilde{\mu}_H + n_{PH}^A \cdot \Delta \mu_P). \quad (5.56)$$

Inserting Eq. 5.56 into Eq. 5.55 and separation into individual forces leads to

$$J_{H,ATP}^A = n_{HP}^A{}^2 \cdot L_{HP}^A \cdot \Delta \tilde{\mu}_H - n_{HP}^A \cdot n_{PH}^A \cdot L_{HP}^A \cdot \Delta \mu_P \quad (5.57)$$

$$J_{ATP,H}^A = -n_{HP}^A \cdot n_{PH}^A \cdot L_{HP}^A \cdot \Delta \tilde{\mu}_H + n_{PH}^A{}^2 \cdot L_{HP}^A \cdot \Delta \mu_P. \quad (5.58)$$

substitution of $\Delta \tilde{\mu}_H$ and $\Delta \mu_P$ according to Eq. 5.22 and Eq. 5.44 leads to

$$J_{H,ATP}^A = n_{HP}^A{}^2 \cdot L_{HP}^A \cdot \left[RT \ln \frac{c_H^{out}}{c_H^{in}} - zF\Delta\phi \right] - n_{HP}^A \cdot n_{PH}^A \cdot L_{HP}^A \cdot \left(\frac{RT}{\bar{c}_{ATP}} \alpha_{ATP} (1 + K) \right) \quad (5.59)$$

$$J_{ATP,H}^A = -n_{HP}^A \cdot n_{PH}^A \cdot L_{HP}^A \cdot \left[RT \ln \frac{c_H^{out}}{c_H^{in}} - zF\Delta\phi \right] + n_{PH}^A{}^2 \cdot L_{HP}^A \cdot \left(\frac{RT}{\bar{c}_{ATP}} \alpha_{ATP} (1 + K) \right). \quad (5.60)$$

Symporters and Antiporters In the case of symporters and antiporters secondary active transport is considered, which means that the ATP dependent term can be left out of the calculation. As an example the ions H^+ and K^+ shall be considered. Application of the approach used for the ATPase to symport and

antiport leads to

$$J_{H,K}^S = n_{HK}^S \cdot L_{HK}^S \cdot (n_{HK}^S \cdot \Delta\tilde{\mu}_H + n_{KH}^S \cdot \Delta\tilde{\mu}_K) \quad (5.61)$$

$$J_{K,H}^S = \frac{n_{KH}^S}{n_{HK}^S} \cdot J_{H,K}^S \quad (5.62)$$

for symport and

$$J_{H,K}^A = n_{HK}^A \cdot L_{HK}^A \cdot (n_{HK}^A \cdot \Delta\tilde{\mu}_H + n_{KH}^A \cdot \Delta\tilde{\mu}_K) \quad (5.63)$$

$$J_{K,H}^A = -\frac{n_{KH}^A}{n_{HK}^A} \cdot J_{H,K}^A \quad (5.64)$$

for antiport. Substitution of J_H in the equations for J_K and of $\Delta\tilde{\mu}_H$ and $\Delta\tilde{\mu}_K$ according to Eq. 5.22 results in

$$J_{H,K}^S = n_{HK}^{S^2} \cdot L_{HK}^S \cdot \left[RT \ln \frac{c_H^{out}}{c_H^{in}} - zF\Delta\phi \right] + n_{HK}^S \cdot n_{KH}^S \cdot L_{HK}^S \cdot \left[RT \ln \frac{c_K^{out}}{c_K^{in}} - zF\Delta\phi \right] \quad (5.65)$$

$$J_{K,H}^S = n_{HK}^S \cdot n_{KH}^S \cdot L_{HK}^S \cdot \left[RT \ln \frac{c_H^{out}}{c_H^{in}} - zF\Delta\phi \right] + n_{KH}^{S^2} \cdot L_{HK}^S \cdot \left[RT \ln \frac{c_K^{out}}{c_K^{in}} - zF\Delta\phi \right]$$

for symport and

$$J_{H,K}^A = n_{HK}^{A^2} \cdot L_{HK}^A \cdot \left[RT \ln \frac{c_H^{out}}{c_H^{in}} - zF\Delta\phi \right] - n_{HK}^A \cdot n_{KH}^A \cdot L_{HK}^A \cdot \left[RT \ln \frac{c_K^{out}}{c_K^{in}} - zF\Delta\phi \right] \quad (5.66)$$

$$J_{K,H}^A = -n_{HK}^A \cdot n_{KH}^A \cdot L_{HK}^A \cdot \left[RT \ln \frac{c_H^{out}}{c_H^{in}} - zF\Delta\phi \right] + n_{KH}^{A^2} \cdot L_{HK}^A \cdot \left[RT \ln \frac{c_K^{out}}{c_K^{in}} - zF\Delta\phi \right]$$

for antiport.

Note here the sign preceding the phenomenological coefficient $L_{HK}^{S/A}$, which is always positive for symport and at the terms involved in coupling negative for antiport.

Passive transport and leakage of ions This includes passive transport due to uniporters, channels or leakage, where the transport of ions is assumed to be only dependent on their own electrochemical potential differences. For H^+ as an example this leads to

$$J_H^L = L_{HH}^L \cdot \left[RT \ln \frac{c_H^{out}}{c_H^{in}} - zF\Delta\phi \right]. \quad (5.67)$$

Remember that, according to Eq. 5.30, the straight coefficients are always positive. Here, this means that the sign preceding the straight coefficients is always positive.

System composed of multiple transporter types If a system is composed of multiple transporters, the fluxes of the individual transporters add up to the net flux J_{H^+} .

To illustrate how a system composed of multiple transporters would look like, J_{H^+} for a cell including a H^+ -ATPase, a H^+/K^+ symporter and H^+ uniport/leakage would be calculated like this

$$J_{H^+} = J_H^L + J_{H,K}^S + J_{H,ATP}^A. \quad (5.68)$$

Inserting Eq. 5.59, 5.65 and 5.67 in Eq. 5.68 and reorganization leads to

$$\begin{aligned}
 J_{H^+} = & (L_{HH}^L + n_{HK}^S \cdot L_{HK}^S + n_{HP}^A \cdot L_{HP}^A) \cdot \left[RT \ln \frac{c_H^{out}}{c_H^{in}} - zF\Delta\phi \right] + \\
 & + n_{HK}^S \cdot n_{KH}^S \cdot L_{HK}^S \cdot \left[RT \ln \frac{c_K^{out}}{c_K^{in}} - zF\Delta\phi \right] - n_{HP}^A \cdot n_{PH}^A \cdot L_{HP}^A \left(\frac{RT}{\bar{c}_{ATP}} \alpha_{ATP} (1 + K) \right)
 \end{aligned} \tag{5.69}$$

with

$$\begin{aligned}
 L_{H,H} &= L_{HH}^L + n_{HK}^S \cdot L_{HK}^S + n_{HP}^A \cdot L_{HP}^A \\
 L_{H,K} &= n_{HK}^S \cdot n_{KH}^S \cdot L_{HK}^S \\
 L_{H,ATP} &= -n_{HP}^A \cdot n_{PH}^A \cdot L_{HP}^A
 \end{aligned} \tag{5.70}$$

The complete equation system for the Ls used in the model will be presented in Sec. 7.1.

6 Methods

In this part of the thesis, a thermodynamic model of cation homeostasis will be proposed (see Sec. 7). The model's parameters were estimated based on biological data from MIFE and FLISE experiments (non-invasive techniques to measure transmembrane ion fluxes). 1000 replications of the parameter estimation task were performed, the 50 best parameter sets were stored. Those top 50 parameter sets resulted still in a variety of different simulation results. To get a better overview about the generated parameter sets, it was chosen to not evaluate them solely via the best objective functions, but group the resulting simulations first. Therefore, k -means clustering was applied to group the parameter sets according to their simulation results. The cluster with the best objective function was further analyzed regarding simulation output and parameter distribution.

In Sec. 6.1.1 the theory behind k -means clustering is described. In Sec. 6.1.2 the details of the computational methods as applied for this thesis part are provided. A general introduction into differential equations can be found in Sec. 2 in Part I of this thesis.

6.1 Computational techniques

6.1.1 k -means clustering

The term k -means was introduced by MacQueen in 1967 [80]. The k -means clustering is a method to sort multidimensional items into specific groups. Different variants, modifications and similar algorithms with slightly different implementation and purpose exist, e.g. the design of vector quantizers [77] or the method from Forgy [28] and Jennrich for obtaining partitions.

Due to the fact that all those algorithms are slightly different, the focus shall be here on the algorithm that is actually implemented in MATLAB. The algorithm is divided into two phases. In phase 1 the user defines the amount of groups k as well as how to choose the initial k centroids (e.g. select k samples from the set of items randomly). Then the following two phases are performed iteratively:

In phase 1, each step is performed on all items of the set at once:

- assign each item to its closest centroid,
- recalculate the cluster centroids.

In phase 2 the algorithm starts with the centroids calculated in phase 1. For each item individually do

- assign the item to the centroid which is closest to it,
- recalculate the coordinates of the centroid.

Phase 2 guarantees that when the algorithm terminates, each change of an item to another cluster would increase the total sum of all item to centroid distances.

If squared Euclidean distance is chosen as a distance measure, the distance d is calculated as

$$d = \sum_{i=1}^k \sum_{n \in S_i} (x_n - \mu_i)^2 \quad (6.1)$$

In the current application the different model simulations are the different items and each time point represents a new dimension. A graphical example for classical k -means clustering is given in Fig. 6.1(a) and an example for clustering of time courses in Fig. 6.1(b).

It has to be mentioned here, that the algorithm originally named k -means by MacQueen [80] does only consider the addition of new items individually to clusters and subsequently recalculation of the centroids afterwards. It does not consist of additional iteration steps.

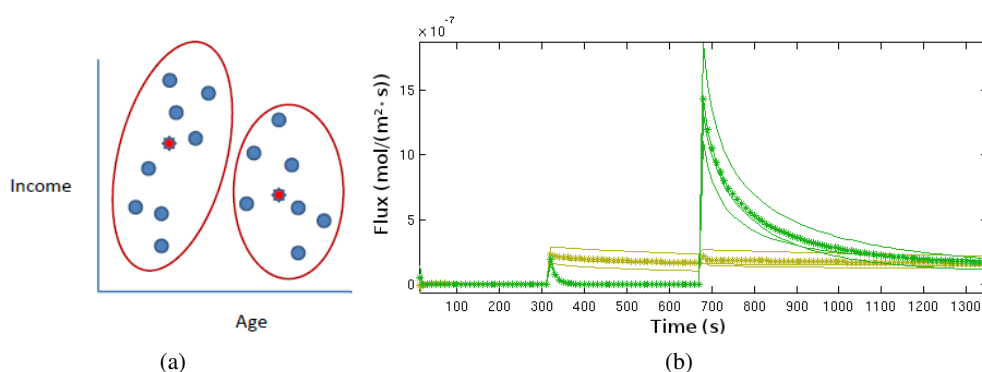


Figure 6.1: k -means clustering. Examples of clustering of data with the k -means algorithm: **a)** data with 2 dimensions (age and income). Image reproduced with permission from http://chem-eng.utoronto.ca/~datamining/dmc/clustering_kmeans.htm, **b)** time course data, each time point in the data set represents one dimension.

6.1.2 Parameter estimation and k -means clustering - details

Parameter estimation was performed in COPASI. As algorithm particle swarm [60] was used with iteration limit 400, swarm size 40, standard deviation $1e^{-6}$, random number generator Mersenne Twister and random seed. A Python script was used to run the algorithm 1000 times with random initial parameter values as well as random upper and lower parameter bounds.

The simulation results of the model using the top 50 parameter sets were clustered with the k -means algorithm. The `kmeans(X,k)` function available in MATLAB was used with squared Euclidean distance, 70 replications and a total of 6 clusters. During each run, the fluxes of K^+ and H^+ for all four KCl stimuli were clustered simultaneously.

7 Results

In this chapter, first the implementation of the model of cation homeostasis will be described by application of the building blocks introduced in Sec. 5.5. This is followed by the presentation of the biological data that were used for parameter estimation. The carefully parameterized model was employed to

- predict additional ion fluxes,
- identify the minimal set of parameters necessary to reproduce the biological data,
- perform predictions of mutations in Trk1,2p and Pma1p,
- analyze different aspects of Trk1,2p dynamics,
- predict the response of the system to a second KCl stimulus.

7.1 A thermodynamic model of cation homeostasis

In the following, the individual aspects of the model's implementation will be introduced. A summary of all equations and differential equations of the model as it was implemented in COPASI is presented in Tab. 1 in the Appendix.

The model species The model species are the intracellular and extracellular ion concentrations as well as ATP. In the experimental setup this were K^+ and H^+ , for which net flux data were available. The aim of the measurement was to analyze K^+ uptake. H^+ is important in this context because it is assumed to be responsible for K^+ uptake via energization of the cell membrane due to Pma1 pumping. Furthermore, Na^+ was included. Although it can be assumed to be present only in low amounts within the cell, and was not added externally, it might play a role as an additional ion flux to stabilize the membrane within physiological ranges.

Cl^- was included because it was present in high concentrations during the experiment (up to 30 mM). Furthermore, there is evidence that it can enter or exit the cell in symport with H^+ [118], through Trk1,2p [71, 113] or due to leakage.

The fluxes The proposed model contains equations for the fluxes of H^+ , K^+ , Na^+ and Cl^- , as well as for the change in intracellular ATP concentration. The ion fluxes and the flux of ATP are dependent on the electrochemical potentials of the involved ions and on the reaction affinity for the ATP consumption as derived in Sec. 5.5.6.

In case all possible coupling combinations are included the matrix notation of the model (see Eq. 5.26),

linking ion fluxes J to differences in electrochemical potentials by the phenomenological coefficients L_{ij} , can be written as

$$\begin{pmatrix} J_{H^+} \\ J_{K^+} \\ J_{Na^+} \\ J_{Cl^-} \\ J_{ATP} \end{pmatrix} = \begin{pmatrix} L_{H,H} & L_{H,K} & L_{H,Na} & L_{H,Cl} & L_{H,ATP} \\ L_{K,H} & L_{K,K} & L_{K,Na} & L_{K,Cl} & L_{K,ATP} \\ L_{Na,H} & L_{Na,K} & L_{Na,Na} & L_{Na,Cl} & L_{Na,ATP} \\ L_{Cl,H} & L_{Cl,K} & L_{Cl,Na} & L_{Cl,Cl} & L_{Cl,ATP} \\ L_{ATP,H} & L_{ATP,K} & L_{ATP,Na} & L_{ATP,Cl} & L_{ATP,ATP} \end{pmatrix} \begin{pmatrix} \Delta\tilde{\mu}_H \\ \Delta\tilde{\mu}_K \\ \Delta\tilde{\mu}_{Na} \\ \Delta\tilde{\mu}_{Cl} \\ \Delta\mu_P \end{pmatrix}. \quad (7.1)$$

The $\Delta\tilde{\mu}_i$ are the electrochemical potentials of the involved ions. $\Delta\mu_P$ denotes the affinity of the ATP consumption ¹ and can be approximated according to Eq. 5.44.

Due to the specific experimental conditions and information on available transporters, a number of assumptions was made restricting the values of the L_{ij} . Specifically, it was assumed that H^+ might be coupled to K^+ , Na^+ , Cl^- and ATP (most likely via Nha1p, Trk1,2p, a potential H^+/Cl^- symporter and the Pma1p). Na^+ and Cl^- were assumed to be only coupled to H^+ , presumably via Nha1p and a potential H^+/Cl^- symporter. It can be assumed that ENA1, which is upregulated upon salt and pH stress, is not expressed at the current experimental conditions [3], thus no Na^+/ATP coupling was considered. K^+ was assumed to be coupled to H^+ and in one model version also to ATP (via Nha1p, Trk1,2p and a potential K^+ -ATPase).

Application of those assumptions and rearranging of the flux equations according to Gerber [32] resulted in the reduced equation system

$$\begin{aligned} J_{H^+} &= RT \left[L_{H,H} \ln \frac{c_H^{out}}{c_H^{in}} + L_{H,K} \ln \frac{c_K^{out}}{c_K^{in}} + L_{H,Na} \ln \frac{c_{Na}^{out}}{c_{Na}^{in}} + L_{H,Cl} \ln \frac{c_{Cl}^{out}}{c_{Cl}^{in}} \right] - \\ &\quad - F \Delta\phi [L_{H,H} + L_{H,K} + L_{H,Na} - L_{H,Cl}] + L_{H,ATP} \left(\frac{RT}{\bar{c}_{ATP}} \alpha_{ATP} (1 + K) \right) \\ J_{K^+} &= RT \left[L_{H,K} \ln \frac{c_H^{out}}{c_H^{in}} + L_{K,K} \ln \frac{c_K^{out}}{c_K^{in}} \right] - \\ &\quad - F \Delta\phi [L_{H,K} + L_{K,K}] + L_{K,ATP} \left(\frac{RT}{\bar{c}_{ATP}} \alpha_{ATP} (1 + K) \right) \\ J_{Na^+} &= RT \left[L_{H,Na} \ln \frac{c_H^{out}}{c_H^{in}} + L_{Na,Na} \ln \frac{c_{Na}^{out}}{c_{Na}^{in}} \right] - F \Delta\phi [L_{H,Na} + L_{Na,Na}] \\ J_{Cl^-} &= RT \left[L_{H,Cl} \ln \frac{c_H^{out}}{c_H^{in}} + L_{Cl,Cl} \ln \frac{c_{Cl}^{out}}{c_{Cl}^{in}} \right] - F \Delta\phi [L_{H,Cl} - L_{Cl,Cl}] \end{aligned} \quad (7.2)$$

A description of the ATP flux as implemented in this thesis will follow in the course of this section.

¹The complete affinity of the pump A_p includes the affinity for the ATP consumption as well as back pressure effects resulting from the involved ions. Reordering the equation as described in Sec. 5.5.8 results in the here presented matrix.

Onsager coefficients and individual transporter types Each net flux of the model is a composition of the fluxes of the individual transporters or, as presented in Sec. 5.5.8, of the individual transporter types. Furthermore, the Onsager coefficients $L_{i,j}$ do not represent the L s of single ion transporters, channels or pumps, but are composed of them. The composition of the $L_{i,j}$ from the L_{ij}^k for the transporter types results in the following equation system.

$$\begin{aligned}
 L_{H,H} &= L_{HH}^L + n_{HK}^S{}^2 \cdot L_{HK}^S + n_{HK}^A{}^2 \cdot L_{HK}^A + n_{HN}^S{}^2 \cdot L_{HN}^S + n_{HN}^A{}^2 \cdot L_{HN}^A + \\
 &\quad + n_{HP}^S{}^2 \cdot L_{HP}^S + n_{HP}^A{}^2 \cdot L_{HP}^A + n_{HC}^S{}^2 \cdot L_{HC}^S + n_{HC}^A{}^2 \cdot L_{HC}^A \\
 L_{H,K} &= n_{HK}^S \cdot n_{KH}^S \cdot L_{HK}^S - n_{HK}^A \cdot n_{KH}^A \cdot L_{HK}^A \\
 L_{H,Na} &= n_{HN}^S \cdot n_{NH}^S \cdot L_{HN}^S - n_{HN}^A \cdot n_{NH}^A \cdot L_{HN}^A \\
 L_{H,ATP} &= n_{HP}^S \cdot n_{PH}^S \cdot L_{HP}^S - n_{HP}^A \cdot n_{PH}^A \cdot L_{HP}^A \\
 L_{H,Cl} &= n_{HC}^S \cdot n_{CH}^S \cdot L_{HC}^S - n_{HC}^A \cdot n_{CH}^A \cdot L_{HC}^A \\
 L_{K,K} &= L_{KK}^L + n_{KH}^S{}^2 \cdot L_{HK}^S + n_{KH}^A{}^2 \cdot L_{HK}^A \\
 L_{Na,Na} &= L_{NN}^L + n_{NH}^S{}^2 \cdot L_{HN}^S + n_{NH}^A{}^2 \cdot L_{HN}^A \\
 L_{Cl,Cl} &= L_{CC}^L + n_{CH}^S{}^2 \cdot L_{HC}^S + n_{CH}^A{}^2 \cdot L_{HC}^A
 \end{aligned} \tag{7.3}$$

In Tab. 7.1 the potential contribution of each transporter or transporter type to the Onsager coefficient is presented. Flux measurements for strains where specific transporters have been knocked out and subsequent parameter fitting can further enlighten these combinations.

Phenomenological Coefficients	Potential contribution of the transporters
$L_{H,H}$	Pma1p, Trk1,2p, Nha1p, leakage
$L_{H,K}$	Nha1p, Trk1,2p (if H ⁺ /K ⁺ symport)
$L_{H,Na}$	Nha1p, Trk1,2p (if H ⁺ /Na ⁺ symport)
$L_{H,ATP}$	Pma1p
$L_{H,Cl}$	H ⁺ /Cl ⁻ symporter?
$L_{K,K}$	Tok1p, Trk1,2p, Pho89p, Nsc1p, leakage
$L_{K,ATP}$	inward directed K ⁺ -ATPase?
$L_{Na,Na}$	Trk1,2p, Nsc1p, Pho89p, leakage
$L_{Cl,Cl}$	Cl ⁻ leakage, Trk1,2p?, H ⁺ /Cl ⁻ symporter?

Table 7.1: Connection between the L s and the proteins

Concentration changes The change in internal and external ion concentrations was calculated with differential equations that include the ion flux through the membrane as well as the surface of the membrane (*Surface*) and the size of either the intracellular (V_{in}) or extracellular compartment (V_{out}).

$$\begin{aligned} \frac{d}{dt} [K^+]_{in} &= \frac{J_{K^+} \cdot Surface}{V_{in}} & \frac{d}{dt} [H^+]_{out} &= \frac{-J_{H^+} \cdot Surface}{V_{out}} \\ \frac{d}{dt} [Na^+]_{in} &= \frac{J_{Na^+} \cdot Surface}{V_{in}} & \frac{d}{dt} [K^+]_{out} &= \frac{-J_{K^+} \cdot Surface}{V_{out}} \\ \frac{d}{dt} [Cl^-]_{in} &= \frac{J_{Cl^-} \cdot Surface}{V_{in}} & \frac{d}{dt} [Na^+]_{out} &= \frac{-J_{Na^+} \cdot Surface}{V_{out}} \\ & & \frac{d}{dt} [Cl^-]_{out} &= \frac{-J_{Cl^-} \cdot Surface}{V_{out}} \end{aligned}$$

To obtain a value for *Surface*, the surface of an individual cell (which was assumed to be $63.6 \mu\text{m}^2$ based on a round cell with a diameter of $4.5 \mu\text{m}$) was multiplied with the total amount of cells (obtained from the optical density of the suspension). V_{in} was calculated accordingly. By using the summation over all cells, the ratios $\frac{Surface}{V_{in}}$ and $\frac{Surface}{V_{out}}$ were equal in the model and in the experiment.

Internal pH The amount of H^+ that was extruded by the cell during the whole experiment was larger than the total amount of intracellular protons freely available initially (based on the measurement of an internal pH between 5 and 7 at time point zero (Ludwig *et al.*, unpublished results)). Kahm [54] identified by comparing flux and pH change data that a change of the internal pH by 1 represents approximately a change of 200 mM of the internal H^+ concentration. Therefore, a cellular pH buffer capacity $pb_c = \frac{200 \text{ mM}}{\text{pH}}$ was assumed in the model.

Instead of calculating $\frac{d}{dt} [H^+]_{in}$ directly, the change in internal pH was calculated from the flux J_{H^+} by the use of pb_c . The internal H^+ concentration in turn was derived from the internal pH (with the use of a conversion factor $cf = 1000 \text{ mM/M}$ to obtain the proper units)

$$\begin{aligned} \frac{d \text{pH}_{in}}{dt} &= \frac{-J_{H^+} \cdot Surface}{V_{in} \cdot pb_c} \\ [H^+]_{in} &= 10^{-\text{pH}_{in}} \cdot cf. \end{aligned}$$

The membrane potential The membrane potential $\Delta\phi$ was calculated via the change in the excess of charge on both sides of the membrane as introduced in Sec. 5.5.7

$$\frac{d\Delta\phi}{dt} = \frac{F}{Cm} \cdot (2 \cdot J_H + 2 \cdot J_K + 2 \cdot J_{Na} - 2 \cdot J_{Cl}). \quad (7.4)$$

ATP production and consumption In the model of Gerber [32] the ATP consumption was modeled to be dependent on the affinity for the pump multiplied by the straight coefficient $L_{ATP,ATP}$ (there named L_{44}). This resulted in a predicted decrease in the ATP concentration after glucose addition. For some experiments on batch cultures this has also been reported [95, 142]. Nevertheless, preliminary data

from Ludwig *et al.* on cells starved in water show an immediate increase in the ATP concentration after glucose addition (unpublished result).

A first attempt for the model of this thesis was to use the complete flux equation

$$J_{ATP} = RT \left[L_{ATP,H} \ln \frac{c_H^{out}}{c_H^{in}} + L_{ATP,K} \ln \frac{c_K^{out}}{c_K^{in}} \right] - F \Delta \varphi [L_{ATP,H} + L_{ATP,K}] + L_{ATP,ATP} \left(\frac{RT}{\bar{c}_{ATP}} \alpha_{ATP} (1 + K) \right)$$

with $L_{ATP,K}$ being zero in the model not including a K^+ -ATPase.

Nevertheless, by assuming a reasonable stoichiometry for the pumps in a range of 0.3-3 ions per ATP, this would result in the consumption of much more ATP than is actually present (assuming that ATP exists in a concentration of 2.5 mM (according to Özalp *et al.* [95]), whereas the internal unbuffered H^+ concentration changes up to 200 mM (based on calculations with MIFE data)).

Therefore, two assumptions were made

- ATP starts with an initial concentration between zero and 2.5 mM. The exact value was estimated together with the $L_{i,j}$.
- ATP increases after glucose stimulation with a rate according to the following equation

$$\frac{d}{dt} ATP = k_{ATP_{incr}} - k_{ATP_{decr}} \cdot ATP \quad (7.5)$$

with

$$k_{ATP_{decr}} = \frac{k_{ATP_{incr}}}{ATP_{max}} \quad (7.6)$$

and ATP_{max} being the maximal concentration of ATP during the experiment.

According to the preliminary data from Ludwig *et al.* this approach seemed to be reasonable. As soon as there will be more information available on ATP concentration changes within the current experimental setup, this can be adjusted.

Post-transcriptional modifications The aim of this project was to model ion fluxes without modeling each transporter in full detail. Nevertheless, during model building it became obvious, that it is not possible to reproduce the biological data, if all phenomenological coefficients $L_{i,j}$ are kept constant over time. Due to the fact that the affinity of the ATPases change after glucose addition (for the Pma1p see [73, 74]), a modification of the ATPase-related L_s (L_{iP}^A for outward and L_{iP}^S for inward directed ATPases, with $i \in \{H^+, K^+\}$) was included in the model. First, a step function was tested for the change in the L_s , being zero before and nonzero after glucose addition. In case the ATPase was already "activated", but the ATP level was still low, the ions were able to reverse the ATPase flux while being driven by their electrochemical potentials. Furthermore, the application of the step function resulted in very steep fluxes after glucose addition. To overcome this, the L_s were changed more slowly and the kinetics of the change were estimated. For the H^+ exporting ATPase this was calculated as

$$\frac{d}{dt} L_{HP}^A = k_{incr} - k_{decr} \cdot L_{HP}^A \quad (7.7)$$

with k_{incr} and k_{decr} being the parameters for the increase and the decrease of the value for L_{HP}^A and

$$k_{decr} = k_{incr} / L_{HP_{aG}}^A \quad (7.8)$$

The other ATPase-related Ls were changed accordingly.

KCl stimuli The stimulation of the cells with KCl and glucose was modeled in COPASI by using events. The KCl stimulus during the MIFE experiment was modeled as $K_{out} = K_{out} + KCl_{stimulus}$ and $Cl_{out} = Cl_{out} + KCl_{stimulus}$. The value of $KCl_{stimulus}$ was dependent on the experiment and either 0.01, 0.1, 1 or 10 mM.

7.2 Application of the model to cellular cation transport

The data sets that were used in order to estimate the model parameters were taken from MIFE and FLISE measurements². The common experimental setup was as such, that the cells were starved for 4 h or overnight in Milli-Q water prior to the measurement to achieve the maximal affinity for K⁺ transport [120]. Afterwards, they were transferred to the measurement buffer. During the measurement different concentrations of KCl were added to each sample, followed by addition of glucose. The extracellular H⁺ and K⁺ concentrations were measured over time and the H⁺ and K⁺ fluxes through the cell membrane were calculated. The resulting fluxes from MIFE experiments are presented in Fig. 7.1(a).

A second rather similar data set was used to test whether the model can also be applied to data from different sources. The experimental setup was similar to the one described before, in such a way that also here starved cells were stimulated with KCl followed by the addition of glucose. In this case the FLISE technique was used to measure changes in H⁺ and K⁺ concentrations in the medium. The resulting fluxes are presented in Fig. 7.1(b).

The data used as orientation for the initial model concentrations were provided by Navarrete *et al.* [86], Petrezsélyová *et al.* (unpublished result) and Gelis *et al.* (unpublished result) (intracellular K⁺ and Na⁺ concentrations after 5 h of K⁺ and Na⁺ starvation and intracellular K⁺ concentrations after overnight starvation in Milli-Q water). The MIFE experimental setup (extracellular pH, K⁺, V_{in} , V_{out}) was provided by Lichtenberg-Fraté *et al.*. The FLISE experimental setup (extracellular K⁺, H⁺ concentrations, V_{in} , V_{out}) was provided by Ludwig *et al.* (unpublished result).

7.3 The model fitted to experimental data predicts chloride influx

The initial focus was on data from MIFE experiments and the data set from Shabala *et al.* (Fig. 7.1(a)) was used for model fitting.

The model proposed in Sec. 7.1 was used and estimation of the Ls, the stoichiometric coefficients, the

²Flux-estimations using Ion Selective Electrodes (FLISE; Ludwig *et al.*, University of Bonn, Germany) and Microelectrode ion flux measuring technique (MIFE; University of Tasmania, Hobart, Australia) as summarized in Newman [89] are methods using ion selective electrodes that enable measurements of real time ion fluxes across the plasma membrane. FLISE calculates net fluxes from extracellular concentration changes using cell suspensions. MIFE periodically measures the concentration difference of a given ion at two different distances from immobilized cells to calculate the net flux. Within the present thesis, data sets for H⁺ and K⁺ fluxes from MIFE and FLISE experiments were utilized.

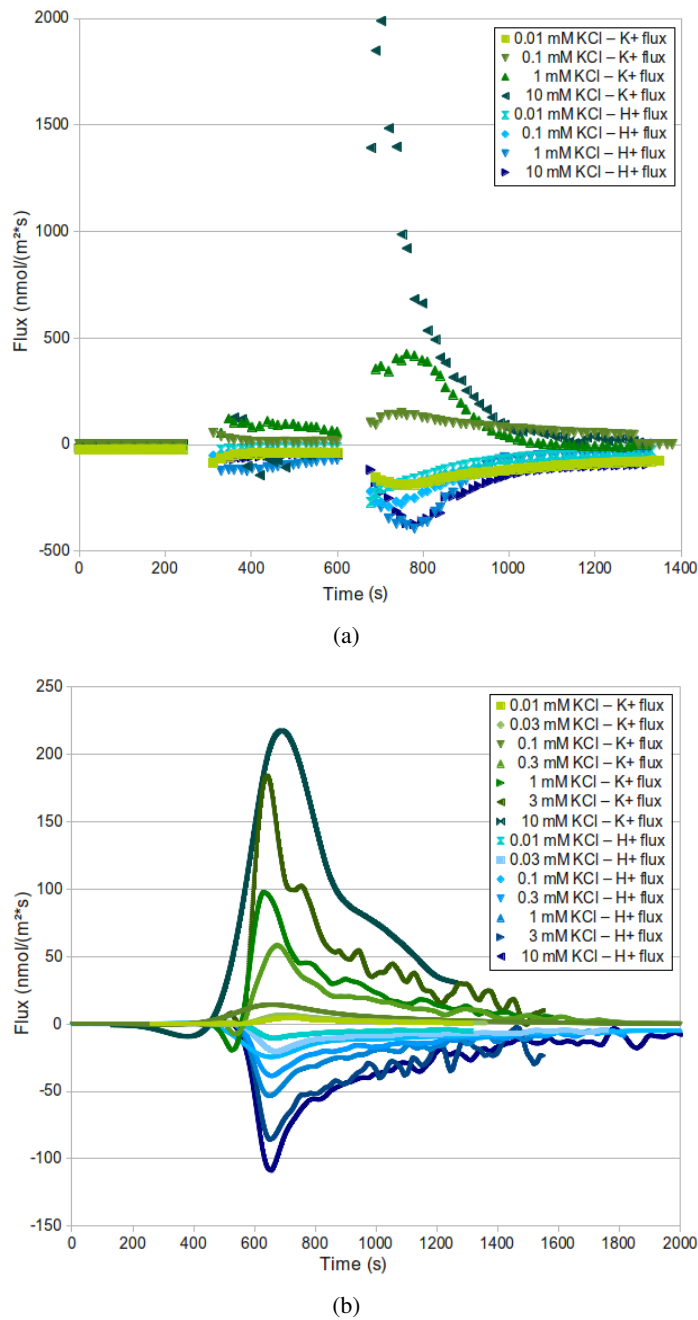


Figure 7.1: Data resulting from MIFE and FLISE experiments on *S. cerevisiae* wild-type. **a)** Data resulting from microelectrode ion flux measurements (MIFE) of potassium fluxes (green) and proton fluxes (blue) in the *S. cerevisiae* wild-type strain PLY232 [11] due to four different stimuli with KCl (0.01 mM, 0.1 mM, 1 mM, 10 mM) followed by addition of glucose. **b)** Data resulting from flux estimations using ion selective electrodes (FLISE) experiments of potassium fluxes (green) and proton fluxes (blue) in the *S. cerevisiae* wild-type strain BY4741 due to seven different stimuli with KCl (0.01 mM, 0.03 mM, 0.1 mM, 0.3 mM, 1 mM, 3 mM, 10 mM) prior to the start of the experiment followed by addition of glucose.

ATP and ATPase kinetics and the initial conditions was performed with COPASI (1000 replications, Particle Swarm algorithm, iteration limit 400, swarm size 40, standard deviation $1e^{-6}$, Mersenne Twister with seed 0). A python script was used to run the parameter estimation algorithm efficiently. The 50 best results were used for subsequent analysis. The k -means algorithm as described in Sec. 6.1.1 was applied to cluster the simulation results of the corresponding models. The simulations of all 4 KCl stimuli were clustered simultaneously.

The model that was able to reproduce the data best contained a K^+ -importing ATPase. The data reproduction using the cluster with the best result as well as predictions performed with the model is presented in Sec. 6 in the Appendix. Although this model showed the best result, it was assumed to be artificial. First, the membrane potential obtained positive values after glucose addition (see Fig. 7(d) in the Appendix). Second, in this case the K^+ influx and H^+ efflux would be completely independent of the Pma1, instead H^+ would be driven out of the cell depending on the preceding active transport of K^+ into the cells. Furthermore, a K^+ -importing ATPase has not been identified in the plasma membrane of *S. cerevisiae*, yet. Although, the existence of such an ATPase cannot completely be ruled out, the mechanism resulting from those model parameters cannot be assumed to be very realistic (personal communication with Ludwig *et al.*).

Thereupon, the model was fitted to the Shabala data with the restriction that no K^+ -ATPase exists ($L_{KP}^S = 0$). The resulting best fit can be seen in Fig. 7.2(a). The fluxes of the lower KCl concentrations can be reproduced reasonably well, only the peak at the highest KCl concentration could not be captured perfectly.

Furthermore, the model was used to simulate the flux of Na^+ and Cl^- , for which no experimental data were available. At the applied initial conditions (internal Na^+ concentration lower than 30 mM) no Na^+ fluxes could be observed (data not shown). Instead, the model predicted an influx of Cl^- ions, which was maximally pronounced at KCl stimuli of 10 mM (see Fig. 7.2(b)).

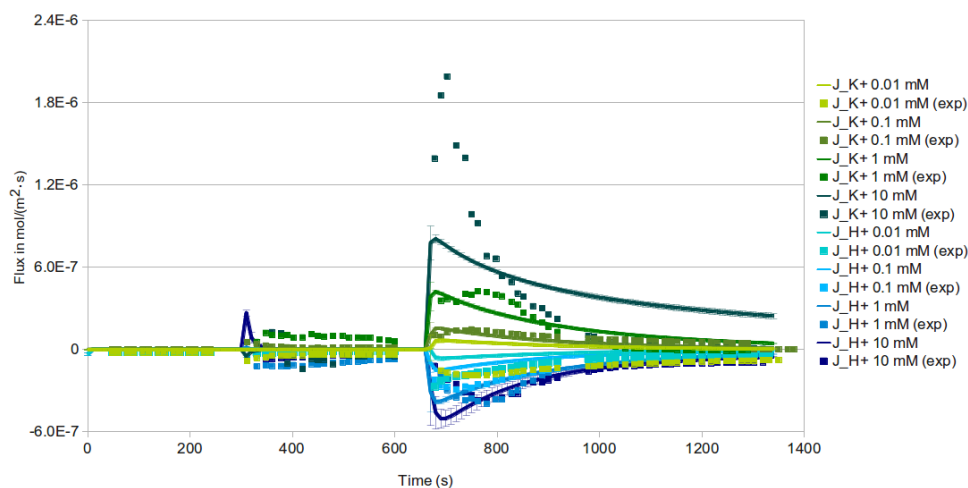
7.4 A minimal set of membrane transport proteins is sufficient to reproduce the biological data

The best cluster from the model excluding a K^+ -ATPase (see previous section) was analyzed in more detail. In Fig. 7.3(a) the average and standard deviation of the parameters for the individual transporter types are presented. $L_{HP_{aG}}^A$ is most prominent and tightly clustered, followed by L_{HC}^S . L_{KK}^L can reach very high values, still it is broadly scattered, because in one of the estimates, $L_{HK_{aG}}^S$ had a large value instead, with a stoichiometry of 3 K^+ per 1.3 H^+ . $L_{KP_{aG}}^S$ and $L_{KP_{aG}}^A$ were 0 by definition.

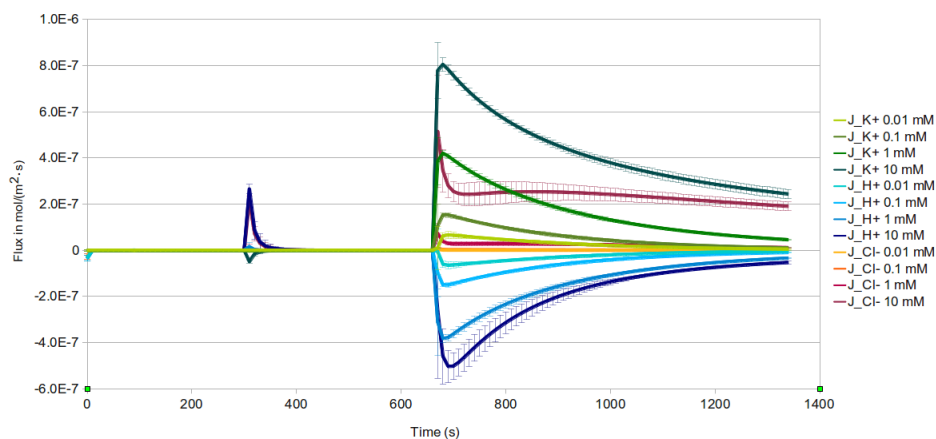
Fig. 7.3(b) and Fig. 7.3(c) show the composed parameters (for details of the calculation see Eqs. 7.3) before and after glucose addition, respectively. The most prominent phenomenological coefficients before glucose are $L_{H,H}$, $L_{H,Cl}$, $L_{K,K}$ $L_{Cl,Cl}$ and $L_{H,K}$. The first ones are unambiguous, whereas $L_{H,K}$ appeared in a high positive and a low negative variant, being unimportant in two samples of the cluster and relevant in one sample.

The most prominent phenomenological coefficients after glucose addition are $L_{H,H}$ and $L_{H,ATP}$, affected by the change in activity of the Pma1 (L_{HP}^A). The K^+ flux after glucose is affected mainly passively via

7.4 A minimal set of membrane transport proteins is sufficient to reproduce the biological data



(a)



(b)

Figure 7.2: Simulation with model fitted to MIFE data. The model was used to reproduce the data from Shabala et al. (Fig. 7.1(a)). **a)** model simulation (solid line) and data (squares), **b)** model simulation including predicted Cl^- fluxes. The K^+ flux is labeled in green, H^+ flux in blue. Cl^- flux (predicted by the model) is shown in red. Darker colors represent higher KCl concentrations used for the KCl stimulus at time point 300 s. Glucose was added in this experiment at time point 660 s.

$L_{K,K}$, although in one sample also via $L_{H,K}$ caused by the high L_{HKaG}^S value representing coupling with H^+ .

The overall behavior of the system could be reproduced by only four Onsager coefficients, L_{HPaG}^A , L_{HC}^S and either L_{KK}^L or L_{HK}^S , of which the estimated values are presented in Tab. 2 and Tab. 3 in the Appendix. The remaining parameters could be set to 0 after the estimation, without affecting the goodness of fit.

7.5 Prediction of the effect of knocking out PMA1p and coupled or uncoupled potassium transport

The model was used to predict the effect of a change in the Ls for specific transporter types. The aim was to predict the effect of a knockout or inhibition of the transporters, which were assumed to contribute the most to the respective L (e.g. Pma1p to L_{HP}^A). Furthermore, it was investigated whether this approach can be applied to distinguish between the model with an estimated high L_{KK}^L value and the model with an estimated high L_{HK}^S value. A clear difference between the effect of mutations in both cases might help to clarify whether Trk1,2p transport solely K^+ (assumed to contribute to a high L_{KK}^L value) or K^+ in symport with H^+ (assumed to result in a high L_{HK}^S value).

First, the effect of setting L_{KK}^L to 0 was analyzed, which would represent a knockout or inhibition of the whole solely K^+ dependent K^+ transport. This would include Tok1p, unspecific K^+ transporters and leakage as well as Trk1p and Trk2p, assuming that the latter work only as uniporters and not as symporters. For the model including an estimated high L_{KK}^L value, setting L_{KK}^L to zero resulted in a complete disappearance of the K^+ flux (Fig. 7.4(a)). Nevertheless, a transient inward directed H^+ flux could be observed after KCl addition and after glucose addition. For the model including an estimated high L_{HK}^S value, setting L_{KK}^L to zero had no effect (Fig. 7.4(b)).

Furthermore, the model was used to predict the effect of setting L_{HK}^S to zero. It was assumed that this would represent a complete inhibition of Trk1p and Trk2p in case they would act as symporters. For the model including an estimated high L_{KK}^L value, setting L_{HK}^S to zero had no effect on the H^+ and K^+ fluxes (Fig. 7.4(c)). Instead, setting L_{12}^S to zero in the model with a high L_{HK}^S value resulted in the disappearance of the K^+ flux and a transient inwards directed H^+ flux (Fig. 7.4(d)).

Finally, the effect of knocking out the PMA1 by setting L_{HP}^A to 0 over the whole time course was analyzed using the parameter set exhibiting an estimated high L_{KK}^L value (Fig. 7.4(e)) and an estimated high L_{HK}^S value (Fig. 7.4(f)), respectively. In both cases, it can be observed that, due to lacking activation of L_{HP}^A , the addition of glucose does not result in an increase of the fluxes.

The results demonstrate that the model can be used to perform predictions of knocking out Pma1p, assuming it contributes mostly to L_{HP}^A . Furthermore, the model produced reasonable predictions about a $\Delta trk1,2$ mutant strain, assuming Trk1,2p contributes the most to L_{KK}^L or L_{HK}^S , whenever this was estimated high. However, it was not able to solve the question, whether Trk1,2p acts in symport with H^+ or not.

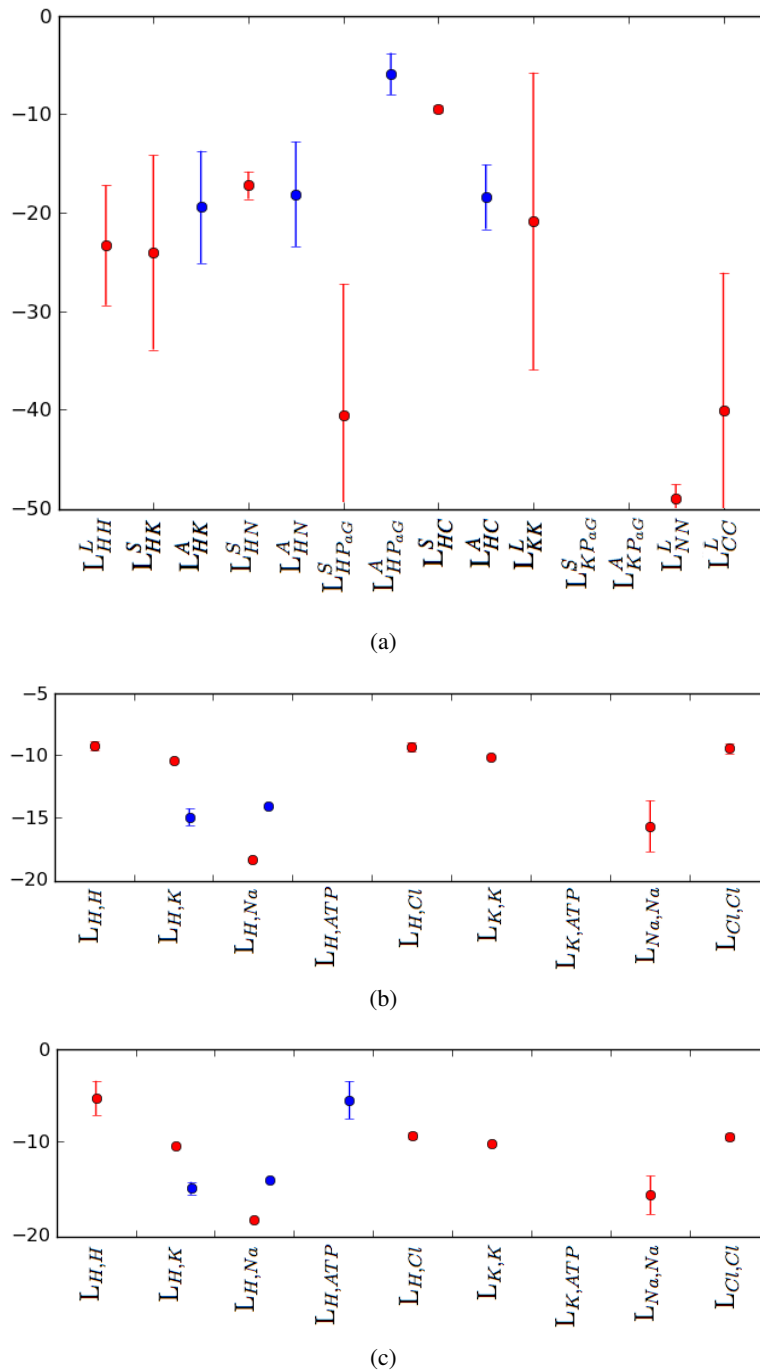


Figure 7.3: Clustering and parameter analysis. The parameters of the model excluding a K^+ -ATPase were estimated. Parameters involved in primary active transport were allowed to change after the addition of glucose (L_{HP}^S , L_{HP}^A). $L_{KP_{aG}}^S$ and $L_{KP_{aG}}^A$ were zero by definition. Clustering with the k -means algorithm was performed as described in Sec. 6.1.1. The simulations of all four KCl stimuli were clustered simultaneously. The 50 best of 1000 estimations were used for clustering. **a)** shows the distribution of the Ls for the individual transporters, **b)** shows the resulting composed Ls before and **c)** after glucose addition. The \log_{10} of the parameters is plotted. Mean and standard deviation of the parameters were calculated after separating them into positive and negative values. Positive values, symporters or inward directed pumps are colored in red, negative values, antiporters or outward directed pumps in blue.

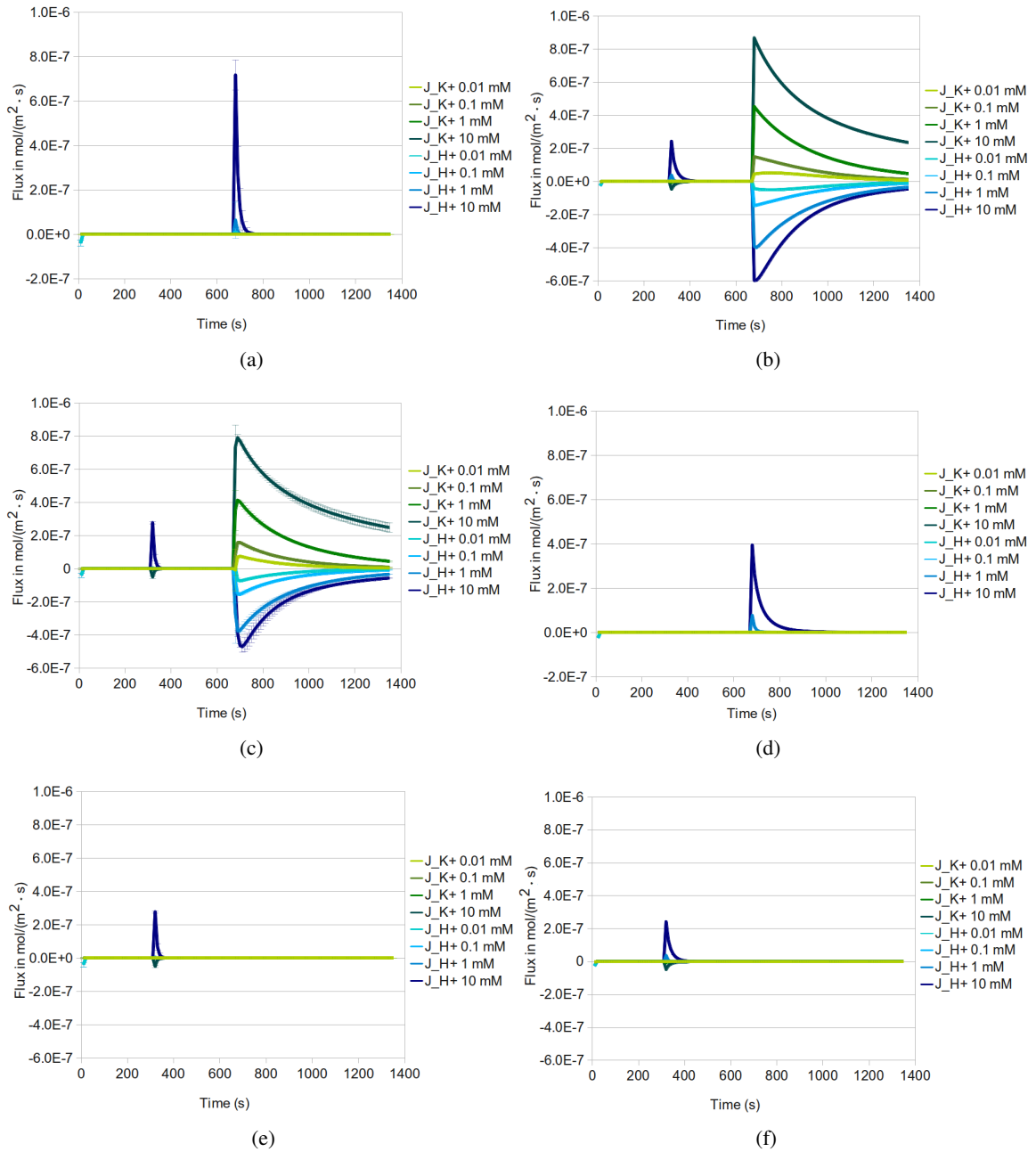


Figure 7.4: *In silico* predictions using the model fitted to the Shabala data. **a)** Inhibition of K uniport and leakage ($L_{KK}^L = 0$), **c)** knockout of a potential H-K symporter ($L_{HK}^S = 0$), and **e)** knockout of the Pma1 ($L_{HP}^A = 0$) for the models with estimated high L_{KK}^S value ($n=2$). **b)** $L_{KK}^L = 0$, **d)** $L_{HK}^S = 0$, and **f)** $L_{HP}^A = 0$ for the model with an estimated high L_{HK}^S value ($n=1$). The K^+ flux is labeled in green, H^+ flux in blue.

7.6 Analysis of potential mechanisms for Trk1,2 transport

One result of the previous chapters was that the K^+ flux after glucose is affected either passively via L_{KK}^L or via coupling with H^+ and thereby contributing to L_{HK}^S , although with low stoichiometry. This indicates that Trk1,2 either act as K^+ uniporters or K^+/H^+ symporters (with transporting more K^+ than H^+ into the cell). Unfortunately, further additional *in silico* experiments have not been able to rule out either of those two transport mechanisms (see Sec. 7.5). Nevertheless, additional analyses were able to identify the major mechanisms both transport variants have in common with respect to K^+ transport as well as some of the differences.

First, the net flux J_{K^+} was separated into the influence due to the electrochemical potentials of the different ions. As a result of the fact that only coupling between K^+ and H^+ was considered, this left over the H^+ dependent part

$$J_{K^+_{Hdep}} = L_{K,H} \cdot \left(RT \ln \frac{c_H^{out}}{c_H^{in}} - F \Delta \phi \right) \quad (7.9)$$

and the K^+ dependent part

$$J_{K^+_{Kdep}} = L_{K,K} \cdot \left(RT \ln \frac{c_K^{out}}{c_K^{in}} - F \Delta \phi \right) \quad (7.10)$$

with $J_{K^+} = J_{K^+_{Hdep}} + J_{K^+_{Kdep}}$. Fig. 7.5(a) shows $J_{K^+_{Hdep}}$ and $J_{K^+_{Kdep}}$ for the models with the parameter sets including high L_{KK}^L . It can be observed that, in this case, J_{K^+} is exclusively dependent on its own electrochemical potential. In the model using the parameter set with high L_{HK}^S (Fig. 7.5(b)) and therefore predicting a K^+/H^+ symporter to be involved, the force due to K^+ and H^+ equal each other out before the KCl stimulus and also more or less after, although with different intensities dependent on the different KCl stimuli. After glucose addition, the shape of the K^+ dependent part is similar to Fig. 7.5(a), but much lower and would even result in K^+ efflux. Coupling to H^+ is necessary for the K^+ fluxes observed in the experiment. The flux due to H^+ stays constant over time, whereas the flux due to K^+ decreases over time again. The closer the K^+ dependent flux gets to the additive inverse of the H^+ dependent flux, the lower gets the net flux J_{K^+} (for comparison see Fig. 7.2).

Next, the dependency of J_{K^+} on the force due to the chemical and the electrical potentials of the ions was analyzed by separating the net flux into a part depending on the chemical potentials

$$J_{K^+_{CP}} = RT \left(L_{K,H} \ln \frac{c_H^{out}}{c_H^{in}} + L_{K,K} \ln \frac{c_K^{out}}{c_K^{in}} \right) \quad (7.11)$$

and a part depending on the electrical potentials

$$J_{K^+_{EP}} = -(L_{K,H} + L_{K,K}) F \Delta \phi \quad (7.12)$$

with $J_{K^+} = J_{K^+_{CP}} + J_{K^+_{EP}}$.

It was observed that, although the model variants with either high L_{HK}^S or L_{KK}^L values exhibit distinct ion dependency, they show a similar dependency on the chemical and the electrical potentials. Fig. 7.5(c) shows $J_{K^+_{CP}}$ and $J_{K^+_{EP}}$ and Fig. 7.5(d) the quotient $J_{K^+_{EP}}/J_{K^+_{CP}}$. It was observed that the fluxes before and after the KCl stimulus equal each other out, resulting in a close to zero net flux (for comparison see

Fig. 7.2). After the addition of glucose, K^+ efflux driven by the chemical potential is slowly increasing, but influx due to the electrical potential is dominating. Directly after the stimulus, approximately three times more K^+ gets transported into the cell driven by the electrical potential than exerts the cell due to chemical potential, resulting in net influx of K^+ . During the long run, $J_{K^+_{CP}}$ and $J_{K^+_{EP}}$ get again closer to each other's additive inverse, thereby approaching a new steady state.

Fig. 7.5(e) shows a prediction of the membrane potential from the models exhibiting K^+ uniport, Fig. 7.5(f) of the model exhibiting K^+/H^+ symport. In case of K^+ uniport (only K^+ dependent K^+ transport) the membrane potential would possess a lower value and changes after addition of KCl and glucose would be more extreme.

7.7 Prediction of the effect of multiple KCl stimuli with the model

Another interesting question would be, whether and how the yeast cells handle successive salt stresses. Do they still react if a second KCl stimulus takes place? Do they react with the same intensity?

To simulate this *in silico* the model with the estimated parameters was used to predict the effect of a second KCl stimulus of 10 mM at time point 1000 s. The resulting time courses for the H^+ and K^+ fluxes are presented in Fig. 7.6.

Under all tested conditions (the four different KCl concentrations for the primary stimulus) it was observed that the cells do also react to a second KCl stimulus. Although the second KCl stimulus was 10 mM in all experiments, the cells with different primary KCl stimuli reacted differently to it. It could be observed that higher KCl stimuli led to more extreme fluxes after glucose addition and to less extreme fluxes after the second KCl stimulus. At the two highest KCl stimuli a transient H^+ influx was observed shortly after the second KCl addition.

7.8 Application of the model to experimental data from FLISE experiments

To analyze whether the model can also be applied to data from multiple sources, the FLISE data set (see Fig. 7.1(b)) was used for parameter estimation. For reproduction of the FLISE experiments, some of the model conditions had to be changed. Not only V_{out} was available but also V_{in} and *Surface* were calculated for each flux measurement from the exact OD of the cell solution. Therefore, this knowledge could be included into the parameter estimation process. Furthermore, the external concentrations in the overall solution were documented and could be included. From the same source the initial concentrations for the external H^+ and K^+ concentrations were known. For the FLISE experiment the simulation started after addition of KCl, in consistency with the available data. The different K^+ and Cl^- concentrations were included in the start conditions. The remaining initial conditions were estimated within reasonable ranges together with the Ls. This resulted in the initial model conditions as can be seen in Tab. 4 in the Appendix.

The same combination of parameters (L_{HP}^A , L_{HC}^S , and L_{KK}^L), which was able to reproduce the MIFE data, was also able to reproduce the data from FLISE experiments (see Fig. 7.7). However, an adjustment of the parameter values was necessary. The estimated Ls as well as the initial conditions are presented in Tab. 4 in the Appendix. It was observed that the value of L_{KK}^L is higher than after fitting to MIFE data.

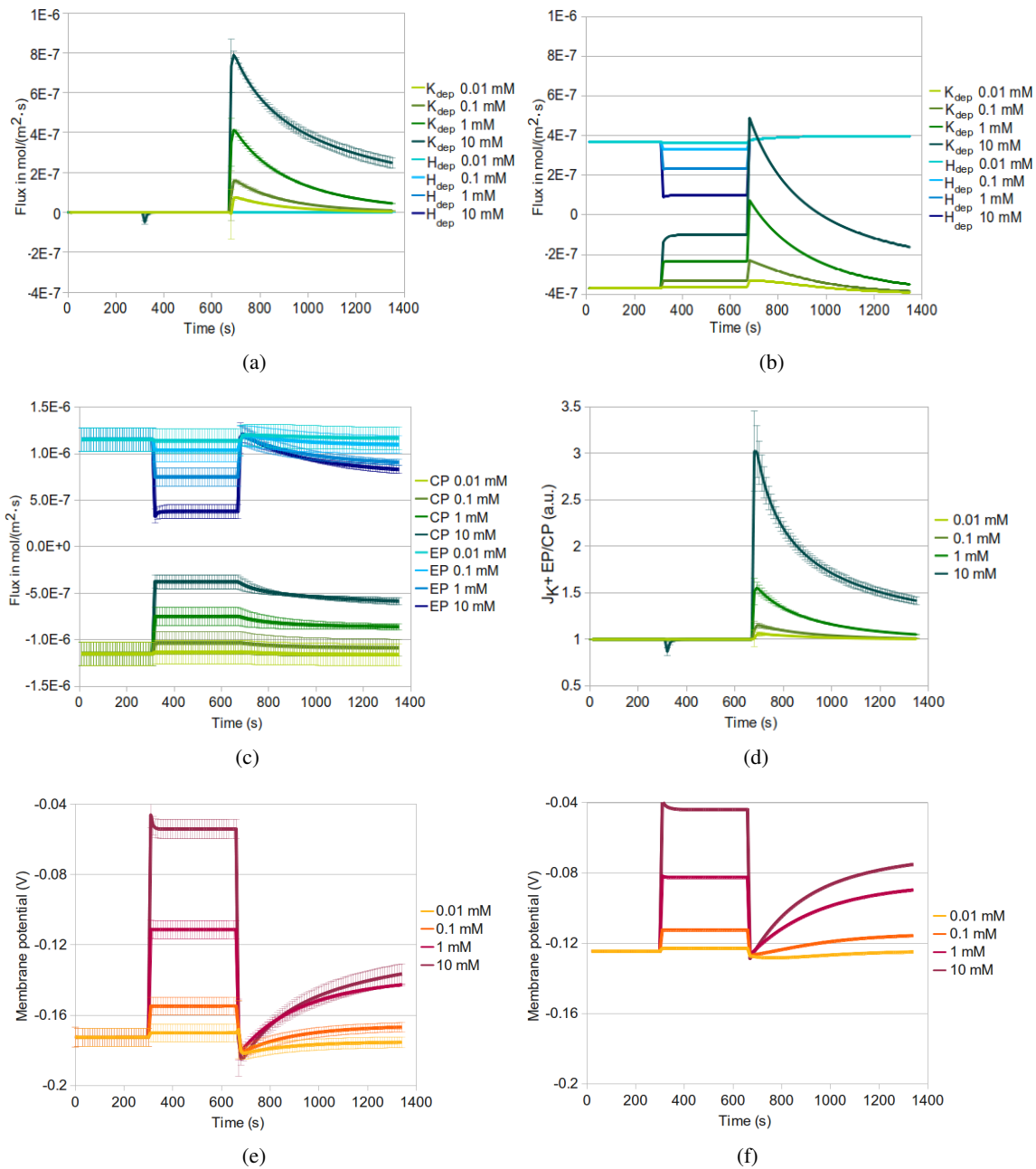


Figure 7.5: Analysis of individual forces. Separation of J_K into a K^+ (green) and a H^+ (blue) dependent part for simulations with parameter sets including **a)** high L_{KK}^L values ($n=2$) and **b)** high L_{HK}^S values ($n=1$). **c)** Separation of J_K into a chemical (green) and a electrical (blue) potential dependent part ($n=3$). **Fig. d)** shows the quotient of the electrical and the chemical potential dependent part of J_K ($n=3$). Simulation of the membrane potential with the parameter sets including **e)** high L_{KK}^L values ($n=2$) and **f)** high L_{HK}^S values ($n=1$).

7 Results

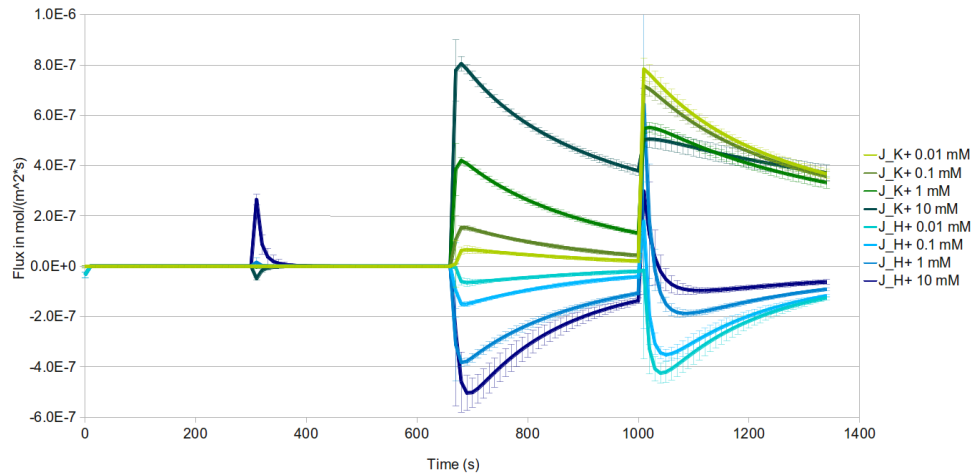
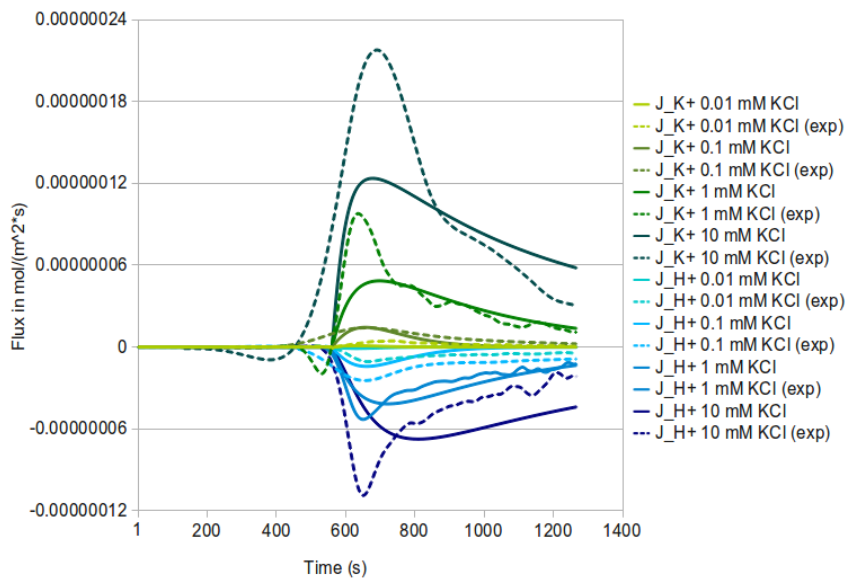
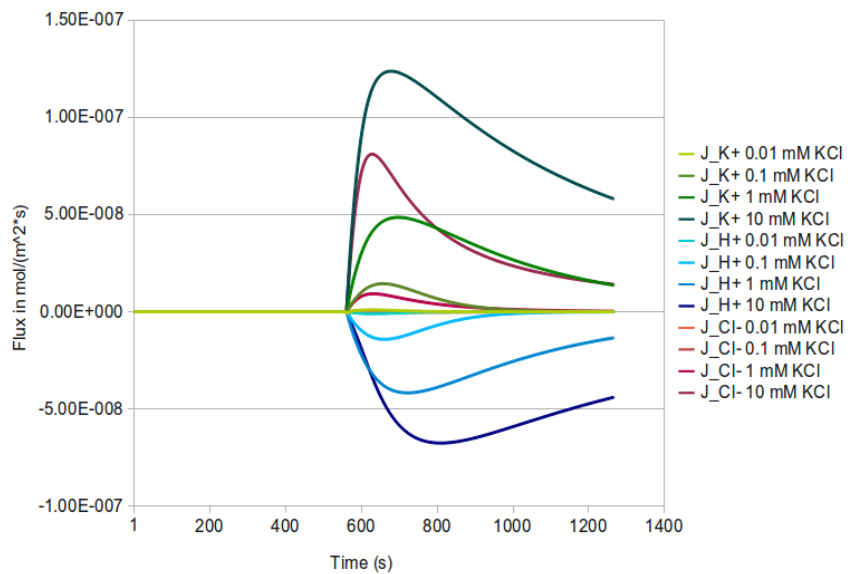


Figure 7.6: Prediction of second KCl stimulus. The model was used to predict the reaction of the system to a second KCl stimulus following the glucose stimulus. As first stimulus the KCl concentrations 0.01, 0.1, 1 and 10 mM were used, in consistency with the data used for model fitting. The second stimulus was modeled as additional 10 mM KCl in all cases. The K^+ flux is labeled in green, H^+ flux in blue. Darker colors represent higher KCl concentrations used for the first KCl stimulus (applied to the system prior to time point 300 s). Glucose was added in this experiment at time point 660 s, the second KCl stimulus was at 1000 s.

Furthermore, the change in L_{HP}^A after glucose was estimated to be more delayed, being consistent with a slower increase in the fluxes after glucose addition. A sharp change in the fluxes was observed within the first second after KCl addition, which occurred in the model at time point 0 s (data not shown). This might be a hint that there additional regulatory processes might exist.



(a)



(b)

Figure 7.7: Simulation with model fitted to FLISE data. The model was fitted to the FLISE data set. It was assumed that no K^+ -ATPase exists. **a)** Data (dotted line), simulation (solid line). **b)** Model simulation including predicted Cl^- fluxes. The K^+ flux is labeled in green, H^+ flux in blue. Cl^- flux (predicted by the model) is shown in red. Darker colors represent higher KCl concentrations used for the KCl stimulus (applied to the system prior to time point 0). Glucose was added in this experiment at time point 560 s. Time points between 0 and 1 s were removed due to transiently high fluxes.

8 Conclusion and discussion

The thermodynamic approach applied here focuses on the effect of the different forces (chemical potential, electrical potential and reaction affinity) on the transmembrane fluxes. With this approach net ion fluxes can be modeled. This makes it perfectly suitable for the available biological data, which were net transmembrane K^+ and H^+ fluxes. Due to fragmentation of the Onsager coefficients into the individual transporter types, a moderately detailed approach was used which allowed for *in silico* knockout and inhibition experiments, while needing only reduced amount of prior knowledge. Another possible and often used approach is to model the ion channels explicitly, as for example done in Kahm *et al.* [54] and Rivetta *et al.* [114]. This detailed approach would rise the complexity of the model. Many parameters would have to be estimated or taken from other sources, which might not be comparable with the experimental conditions applied here. By using the thermodynamic approach the information can be reduced and is included in the Onsager coefficients. With increasing availability of data and rising complexity, the predictions from both model approaches should be more and more similar to each other.

To conclude the results from this part of the thesis:

- The proposed model was able to reproduce K^+ and H^+ flux data from MIFE experiments.
- The model predicts the existence of Cl^- fluxes, predominantly at 10 mM KCl.
- The parameters L_{HP}^A , L_{HC}^S and either L_{KK}^L or L_{HK}^S are sufficient to reproduce the biological data.
- Predictions of mutations in L_{HP}^A (assumed to be Pma1p) and L_{KK}^L/L_{HK}^S (Trk1,2p) result in vanishing K^+ fluxes. However, existing transient H^+ fluxes (partly in the reversed reaction) might hint to not yet captured regulatory mechanisms.
- The model was not able to solve the exact mechanism of Trk1,2 dynamics. However, possible mechanisms were analyzed and a difference in the membrane potential has been observed.
- Application of multiple KCl stimuli *in silico* show that the cells do still react to a second KCl stimulus, but with reversed intensity.
- The model can also be transferred to data from different sources, here to data from FLISE experiments.

In the following, different aspects of the model shall be discussed.

Calculation of the membrane potential

For the computation of the membrane potential the calculation via the excess of charge was chosen, which is common practice in thermodynamic modeling [8, 54, 59]. In the model, the ions K^+ , H^+ , Na^+ and Cl^- can affect the membrane potential. It is known that Pma1p pumps proton out of the cell after a glucose stimulus and it is assumed that this leads to a secondary active transport of other cations [3, 94], most

likely via energization of the cellular plasma membrane. Cl^- was included in the model because the cells were stimulated with KCl and the chloride counteracts with its negative charge the positive charge of the K^+ in the external medium. Due to the fact that also CaCl_2 was added to the solution to inhibit Nsc1, the external amount of Cl^- is quite large (up to 30 mM) and potential Cl^- fluxes can affect the membrane potential. Ca^{2+} was assumed not to be able to cross the plasma membrane at the conditions applied here. However, experiments are currently made by collaborators to rule out this possibility. Na^+ was included because there is low but still measurable Na^+ inside the cells after potassium and sodium starvation conditions (Navarrete, unpublished result), which can affect the membrane potential while flowing out of the cells. According to the results obtained from the model, no Na^+ fluxes can be observed at the current experimental setup. However, it is also possible that other ions can affect the membrane potential, which are not yet included in the model (e.g. HCO_3^-). In principle, it would be better to measure the membrane potential instead of calculating it. Unfortunately, there is currently no method known to measure absolute values for the membrane potential in yeast. Experimentally derived information for membrane potential changes during our experimental setup would be a major advantage to improve the model.

Potassium and proton flux not sufficient to explain the data

During the examination of the data from FLISE and MIFE experiments it became obvious that there are discrepancies between H^+ efflux and K^+ influx. At KCl concentrations of or below 0.1 mM the net H^+ efflux is larger than the net K^+ influx, whereas at KCl concentrations higher than 0.1 mM it is the other way around. If only H^+ and K^+ were transported, this would lead to very high, unphysiological membrane potentials. It is necessary that some additional ions move into or out of the cell. In the model proposed by Gerber [32] this problem was evaded by application of the Goldman-Hodgkin-Katz equation for calculation of the membrane potential, and estimating the permeabilities of the ions independent of the Ls. This allowed to reach membrane potentials at a reasonable range while still allowing the H^+ and K^+ fluxes to be as observed in the experiment. Anyhow, this approach was a first approximation and contained a variety of simplifications. On a closer look, the permeabilities cannot be chosen independently from the Ls but are related [4]. Furthermore, the Goldman-Hodgkin-Katz equation calculates the reversal potential, assumes only passive diffusion and does not take coupling of ions into account. Therefore, in the present study, the calculation via the excess of charges [59] was used instead. However, using this on the one hand more appropriate and correct approach resulted in other difficulties. Using the calculation via the excess of charge in principle one has to include all potential ion fluxes, which is not possible within the current experimental setup. However, Na^+ and Cl^- fluxes were assumed to be most reasonable given the experimental setup. By including additional ions it was possible to reproduce the asymmetric H^+ and K^+ fluxes (e.g. Fig. 7.7 in the main text and Fig. 7(a) in the Appendix). The model predicted Cl^- influx after glucose addition. This might be reasonable, because low affinity H^+/Cl^- co-transport has been reported in patch clamp experiments [118]. Furthermore, chloride fluxes were observed in preliminary data from MIFE experiments (data not shown). Nevertheless, Cl^- electrodes are very unspecific. Currently, algorithms are implemented by Klipp *et al.* to overcome this limitation.

Osmotic shock and volume changes

Addition of KCl to yeast cells can result in hyper-osmotic shock and cell shrinkage. Many eukaryotic cells evolved mitogen-activated protein (MAP) kinase pathways to transmit the signal to the nucleus, were

the gene expression can be rapidly adapted to the stress. In *S. cerevisiae* this is performed by the high osmolarity glycerol (HOG) pathway [110, 139]. However, in Rep *et al.* [109, 110] and Wuytswinkel *et al.* [151] 0.4-0.5 M NaCl were considered as mild osmotic shock, leading only to a transient translocation of double phosphorylated HOG1. In the present study, KCl was added in concentrations of not more than 0.01 M. According to B. Nordlander (unpublished data) and Schaber *et al.* [124] this should not result in significant shrinkage and activation of the HOG pathway. B. Nordlander showed that at 0.05 M NaCl only 10% of the maximal possible HOG activation can be seen. In Schaber *et al.* an addition of 0.1 M NaCl led to a cell shrinkage of 2 - 5%.

Wuytswinkel *et al.* [151] showed by the application of 1.4 M NaCl or 1.4 M KCl that the application of severe stress is osmospecific and not sodium specific. Therefore, it was assumed that the addition of the same amount of KCl instead of NaCl has no significantly higher effect.

In case that higher salt stresses are applied, it might be necessary to include cell volume changes and gene regulatory effects into the model. However, the addition of higher salt stresses would lead the system farther away from equilibrium, which might in turn also affect Onsager coefficients and Onsager symmetry.

Starvation in water

Some aspects should be kept in mind if this model is applied to other systems, e.g. cells in non-starved conditions. As already pointed out by Haro and Rodríguez-Navarro [37], K^+ starved cells are good study objects because they show higher K^+ affinity transport than cells grown in potassium containing medium. Furthermore, yeast cells which are starved in Milli-Q water have a higher K_m value for K^+ and Rb^+ than K^+ starved cells in medium [37, 120]. The change from a medium to a high affinity TRK1 takes 3 h to be completed in a wild type strain [37]. In the experimental setup used here, the cells were starved for 4 h, which means Trk1p should be working with high affinity. Also other processes might be different and the addition of glucose might activate further metabolic changes affecting the whole cell behavior. As a consequence, the model of the present study should only be used for analyses with starved cells. If applied to non-starved cells, the Onsager coefficients might have to be adjusted.

Internal pH and proton buffer capacitance

With both the MIFE and the FLISE data sets one can make the following observation: while assuming an internal pH between 5 and 7 and calculating the amount of change in internal H^+ concentration from the H^+ flux data, more H^+ ions would flow out of the cell than are actually inside it. Therefore, either H^+ is produced inside the cells by glycolysis and other metabolic processes, or H^+ which was previously buffered gets released.

Within the present thesis, a proton buffer capacity of 200 mM unbuffered H^+ per unit pH change was used according to the comparison between H^+ fluxes and pH measurements ([54], Ludwig *et al.*, unpublished results).

In future model versions it might be an option to integrate a more flexible proton buffer capacitance that changes with the current pH of the cell or with the current protein and metabolite composition.

Additional regulatory mechanisms

Data and knowledge of the exact transporter mechanisms involved in cation homeostasis is still sparse. Therefore, within the present thesis, the aim was to model cation homeostasis without modeling every transporter in full detail. Furthermore, with the application of linear non-equilibrium thermodynamics it was possible to model cation homeostasis without using pre-assumptions on the relative contribution of the individual transporters. This information resulted here from parameter estimation.

The model was able to reproduce biological data from MIFE and FLISE experiments. However, some mechanisms were observed that do not completely capture the experimental observations. The model fitted to MIFE data simulated transient H^+ and K^+ fluxes directly after KCl and in knockout experiments after glucose addition, whereas the model fitted to the FLISE data simulated steep transient fluxes directly after KCl addition. The model predicted a strong change in the membrane potential after KCl and glucose addition, which might influence the transporter permeabilities. In future models it might be reasonable to reuse the approach of modeling net ion fluxes, while still including more information for individual transporters, for which it is already known (e.g. voltage gating of Tok1p or pH dependence of Trk1p). Experiments with strains where individual transporters have been knocked out, knocked down or overexpressed might shed more light on the contributions of individual transporters. In addition, measurements of fluxes of other ions (especially Na^+ and Cl^-) would complete the picture. A potential later step is also to include regulation of the transporters (posttranslational modifications, structural changes in different pH, changes of transporter numbers through gene expression or regulated degradation).

Existence of a K^+ -importing ATPase in yeast?

Parameter estimation performed with the model fitted to the Shabala data set revealed that the model can reproduce the data best if the existence of a K^+ -importing ATPase is assumed. However, in this case the model exhibited a K^+ transport mechanism mainly independent of the Pma1. Furthermore, the membrane potential was observed to be increase after glucose addition (data not shown). Although this is in general possible given the thermodynamic forces present at the membrane, it is unlikely given the currently available literature-based knowledge of *S. cerevisiae*. However, ATPases mediating potassium transport have already been found in other fungi [9].

In addition, there might be other possibilities how *S. cerevisiae* can exhibit ATP dependent K^+ transport. Haro and Rodríguez-Navarro [37] identified an active K^+ transporting component in *S. cerevisiae*, which was still existing if 80 μM of the uncoupler CCCP (carbonylcyanide m-chlorophenylhydrazone) was used. Ramirez *et al.* [105] discovered by using PMA1 mutant strains the existence of K^+ channels able to be activated by intracellular ATP.

The investigation of primary active K^+ transport mechanisms can be one aspect of further research.

9 Outlook

The model proposed in this work includes H^+ , K^+ , Na^+ and Cl^- fluxes. In the experimental setup the cells were starved in Milli-Q water prior the experiment. Throughout this process they lost internal K^+ and Na^+ . During the experiment, K^+ was added in form of KCl. Future experiments might focus more on Na^+ fluxes and different Na^+ stimuli.

It would also be of interest to analyze combinations of salt stimuli, e.g. Na^+ in the presence or absence of K^+ . If K^+ is limiting, Na^+ can be used to restore the cell volume, pH and growth, whereas K^+ would be used instead if it is not limited [119]. Therefore, the kinetics for K^+ and Na^+ transport might be different under those conditions.

The observed fluxes in the FLISE data set were lower than in the MIFE data set. As a result, although the same combination of parameters could be used, their respective values had to be adjusted. This might be a hint for different potassium transport properties in the two wild type strains. However, it has to be validated, whether this is caused by the different strains (MIFE: PLY232, FLISE: BY4741), by the different treatments (addition of $CaCl_2$ in FLISE to inhibit unspecific K^+ flux) or by differences in the measurement (e.g. immobilized cells in MIFE, cell solutions in FLISE). Currently, Ludwig *et al.*, who provided the FLISE data for this work, are establishing a MIFE system. This will allow for direct comparison of the two experimental setups. Furthermore, the influence of $CaCl_2$ on the fluxes at the different KCl concentrations will be analyzed.

The current model does not include water flux or volume changes. This can be justified because at concentrations below 0.1 M salt no significant volume changes occur [124]. Nevertheless, if higher salt concentrations are used, the resulting osmotic stress might also lead to water fluxes into or out of the cell. This might also lead to a change of the cellular volume, which will then again affect the internal ion concentrations. For future work under different stress conditions it might therefore be necessary to include water fluxes into the model.

In the current model version it was assumed that the ions are homogeneously distributed within the cell and in the extracellular volume. Furthermore, the stimulus by glucose addition implied an immediate increase in intracellular ATP concentration. Further model versions could include gradients of ions and ATP in space as well as finer changes in ATP concentration by generation via glycolysis and consumption.

The current model started with a linear approach for the thermodynamical model. This approach was slightly modified by assuming that the ATP-dependent Onsager coefficients were able to change after a glucose stimulus. It is further known that Pma1p and Tok1p are voltage dependent [129, 40] and Trk1p has higher affinity at low than at high outside K^+ concentrations [137]. Also one might include the saturation of ion carriers at high concentrations, which might lead to a Michaelis-Menten-like instead of a linear behavior. Therefore, it might make sense to integrate more complicated terms for the Onsager

coefficients, like saturated or voltage dependent terms.

Although the focus of this work lies exclusively on the transport proteins in the plasma membrane, it should shortly be mentioned that there exist also various transport proteins in the organellar membranes. The knowledge of the existence and kinetic behavior of those transporters is at the moment rather sparse [3], but for further modeling and experimental approaches it might be useful to include e.g. transport into the vacuole as cellular storage and detoxification system.

Experiments on the ion fluxes through the organellar membranes and the change in organellar pH are currently performed by our collaborators.

It has to be investigated, whether Na^+ and Cl^- fluxes can be observed with the current experimental setup. In case of Na^+ , coupling via Nha1p should have biological relevance, although it is not clear, if already at the very low Na^+ concentrations which are to be expected with starved cells. A comparison to cells undergoing NaCl stress might be convenient here.

Another possibility is to include CO_2 production after glucose addition as well as the bicarbonate reaction into the model as done in Kahm *et al.* [54]. Part of the H^+ transported out of the cell via the Pma1p might originate from this reaction. In addition, efflux of HCO_3^- might add to the yet unknown ion fluxes.

Global Discussion and Outlook

Kinetic and thermodynamic modeling are valuable tools to understand crucial aspects of water and ion homeostasis. Within the present thesis, the underlying intracellular signaling processes were analyzed with kinetic modeling, whereas ion fluxes were modeled with a thermodynamic approach. In both projects, first models were generated from current knowledge and literature data. Data prepared by collaborators was used to estimate the model parameters. The models were used for analyses *in silico* such as analysis of mutations, sensitivity analysis and time dependent sensitivity analysis as well as model predictions. The modeling approach essentially contributed to both projects. Furthermore, within both projects, it was used to analyze differences between individual species or strains.

Within the aquaporin project it was used to identify the parts of the signaling system, which are crucial for the kinetic behavior of important species in the system. Time dependent sensitivity analysis as well as application of the target identification tool TIDE pointed out the importance of reactions directly involved in AQP2 trafficking. A detailed analysis of the effect of activators and inhibitors acting on potential drug targets could identify optimal single and combinatorial treatments.

Ranking and sensitivity analyses hint to the conclusion that in MDCK cells the internalization of the vasopressin receptor has a higher effect on the intracellular cAMP kinetics than negative feedback via phosphodiesterases. In primary rat IMCD cells this seems to be reversed. In addition, the overall contribution of those two reactions seems to be less pronounced. If further studies focus on cAMP, the MDCK cell model might be the better option.

The results from time dependent sensitivity analysis are able to contribute in two aspects. On one hand, they identify reactions important for the kinetic behavior of the system. On the other hand, they can be used for model guided experiments by indicating which reactions have to be disturbed and which time points have to be chosen for a measurements, to obtain the highest information content. Part of this work was published as M. Fröhlich, P. M. T. Deen and E. Klipp, *A Systems Biology Approach: Modelling of Aquaporin-2 Trafficking*, *Genome Inform.* 2010;24:42-55.

One major benefit of the model of cation homeostasis was the use of linear non-equilibrium thermodynamics. With this approach it was possible to employ the data of net ion fluxes provided by the experimenters. Typically, individual transporters are modeled, requiring detailed information, which is often unavailable. With linear non-equilibrium thermodynamics, the collectivity of membrane transporter proteins can be modeled in a simplified way based on the forces acting on the system. This enables to move one step further and to cope with yet unknown mechanisms.

The major contributions to the Translucent-2 project were the usage of the model to analyze Pma1 and Trk1,2 transport dynamics. The available data suggested that proton and potassium fluxes alone are not sufficient to explain the observed behavior and that additional ions have to flow to keep the membrane potential within reasonable ranges. Within this thesis, sodium and chloride fluxes were included and their parameters were estimated. By applying the experimental conditions and knowledge from the literature, the model predicts the potential existence of chloride fluxes.

Part of this work will be published as M. Fröhlich, S. Gerber, H. Lichtenberg-Fraté, J. Ludwig, S. Shabala, and E. Klipp, *A basic thermodynamic model of cation homeostasis in the yeast *Saccharomyces cerevisiae**. The model's predictions will be verified by our collaborators. Due to the fact that electrodes for chloride are very unspecific, this pointed out also the need for algorithms that can cope with the uncertainty in the

measured fluxes. They are currently implemented in the Klipp group. Furthermore, it revealed the necessity to obtain more information on the ATP content of the cell during the experiment, which is currently investigated by the collaborators with fluorescent sensors.

In the optimal case, both water and ion transport would have been investigated within one and the same organisms, e.g. either yeast or mammalian cells. However, the central point, and often also the bottleneck of systems biology, is the availability of suitable data and the possibility to verify the model's predictions. Due to the fact that the collaboration with experimenters working on ion homeostasis in yeast was already well established and data were already available, whereas no collaboration was existing with experimenters working on ion transport in mammalian cells, the focus of this thesis was switched to this organism. At the current experimental setup used to obtain the proton and potassium fluxes, water fluxes could have been neglected. In the future, additional experiments will be done to test, model and investigate both ion and water fluxes in yeast. Additionally, the knowledge gained from research in yeast, can also be applied to mammalian cells.

The future work on cation homeostasis in yeast will focus more and more on the analysis of the cation content of specific cellular organelles. Fluorescent markers and microscopic images will play a major role, e.g. pHlourin, which is a reporter for cellular pH. The availability of data with spatial resolution will open more opportunities, especially in direction of spatial modeling. Tools such as the Spatio-Temporal Simulation Environment (STSE, Stoma, Fröhlich *et al.* [134]) can be used to digitize, and analyze data from microscopical images and build a framework for efficient spatio-temporal modeling. Besides the application to the organelles, spatio-temporal modeling can assist the further understanding of the processes at the cell membrane, by including diffusion processes in the external and internal environment.

Appendix

1 *In silico* variation of the amount of AQP2

The complete model with the best set of parameters found (see Fig. 3.1 and Tab. 3.2) was used to analyze $[AQP2_{membrane}]$ dependent on the overall concentration of AQP2 (see Fig. 1). For this analysis it was assumed that the percentage of initial $[AQP2_{membrane}]$ stays the same for each simulation. $[AQP2_{membrane}]$ was analyzed 30 min after AVP addition.

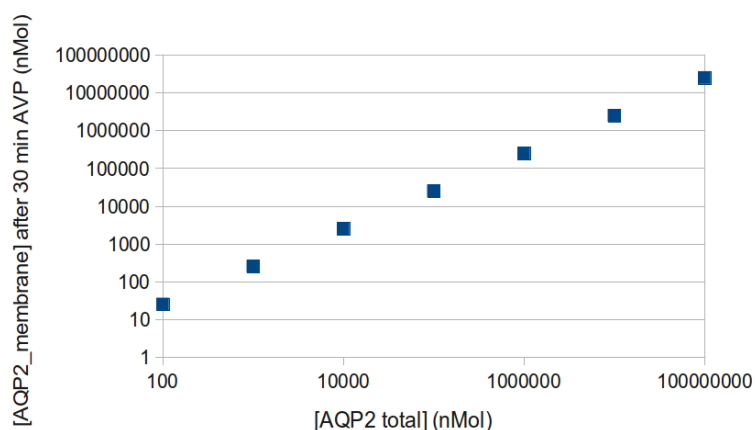


Figure 1: Dependency of $[AQP2_{total}]$ on $[AQP2_{membrane}]$. It was assumed that the percentage of initial $[AQP2_{membrane}]$ stays the same for each simulation. $[AQP2_{membrane}]$ was analyzed 30 min after AVP addition.

2 Dephosphorylation of AQP2 at position S261 in MDCK cells

Experimental setup For this work Madin-Darby canine kidney cells (MDCK-hAQP2-T269S) were seeded at a density of $2.7 \cdot 10^5$ cells/cm² on semipermeable 1.13 cm² filters (Transwell®, 0.4 μm pore size, Corning Costar, Cambridge, MA, USA). The cells grew at 37°C for two days, then the medium was changed and $5 \cdot 10^{-5}$ M indomethacin was added for 1 more day to lower intracellular cAMP levels. After 3 days of seeding, the basolateral side of the cells was exposed to medium with (deamino-Cys1, D-arg8)-vasopressin (dDAVP, Sigma, St. Louis, MO, USA). Different concentrations of dDAVP were used (10^{-6} M, 10^{-7} M, and 10^{-8} M) for durations of 0, 1, 2, 5, 10, 20, 30 and 90 min. The filters were excised and transferred to 1x Laemmli with inhibitors of proteases and phosphatases. The samples were denatured for 30 min at 37°C and sonicated for 20 s. After SDS-PAGE on a 12% acrylamide gel the proteins were immunoblotted as in [21]. Incubation with the primary antibody against AQP2-pS261 (1:2,000-diluted, kindly provided by Dr. M. Knepper, NIH, Bethesda) took place overnight at 4°C. The signal was amplified by 1:10,000-diluted biotinylated anti-rabbit IgGs and 1:8,000-diluted streptavidin-peroxidase (HRP; Sigma, St. Louis, MO, U.S.A.). Semi-quantification was performed with an Epson Expression

1640 XL (300dpi) using the software AIDA - Advanced Image Data Analyzer (V4.10.020; raytest Isotopemessgeräte GmbH). The experiment was done in duplicates.

Results Three different dDAVP concentrations were tested (10^{-6} , 10^{-7} M, and 10^{-8} M, see Fig. 2). The band intensities were quantified, averaged and normalized to 1. All three dDAVP concentrations show a clear decrease in S261 phosphorylation. Fig. 2(a) shows phosphorylated S261 over time after treatment with 10^{-6} M dDAVP. The amount of phosphorylated S261 decreases until a minimum is reached at 30 min. At the concentrations 10^{-7} M and 10^{-8} M dDAVP a slight increase can be detected in the first 2 min. Afterwards the curve is decreasing, although not as smooth as at 10^{-6} M dDAVP. With 10^{-7} M dDAVP a plateau and with 10^{-8} M dDAVP a slight increasing peak can be measured at around 20 min. All three concentrations reach their minimum at 30 min and are slowly increasing afterwards. The experiments were performed by myself in the laboratory of Prof. Deen (Radboud University Nijmegen Medical Centre, Nijmegen, the Netherlands).

3 Model fitting results for the IMCD cell model without negative feedback

The model as shown in Fig. 4.1 was used as a start. The negative feedback reaction representing the existence of phosphodiesterases was deleted and parameter estimation was performed using the data set from Stefan *et al.* [133]. The results are presented in Fig. 3.

4 Sensitivity analysis and time dependent sensitivity analysis applied to the IMCD cell model with the new $AQP2_{membrane}$ dataset produced by Klusmann et al.

After refitting the model for IMCD cells to the new dataset provided by Klusmann et al., the effect of small changes of the initial parameter values on the amount of cAMP and $AQP2_{membrane}$ was investigated 21 min after start of the simulation. The sensitivity coefficients of the parameters affecting cAMP have similar values over time as by using the old dataset (for comparison, see Fig. 4.4 and Fig. 4). By comparing the effect of a change of the parameters on $AQP2_{membrane}$, one can observe that by using the new dataset for model fitting, the sensitivity coefficient for k5 increases and of k6 decreases, slightly. Furthermore and more prominent, the sensitivity coefficient of Ki6 (the inhibition constant for reaction 6) decreases. This indicates that the regulation of the AQP2 endocytosis might have a minor effect in primary IMCD cells.

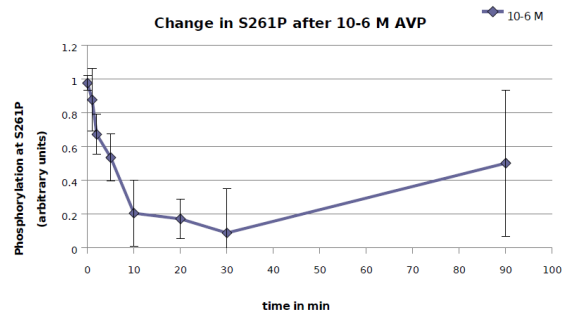
Time dependent sensitivity analysis was performed on the refitted model and the effect of small changes of the model parameters on cAMP and $AQP2_{membrane}$ was analyzed (see Fig. 5).

The sensitivity coefficients of the parameters affecting cAMP have similar values over time as by using the old dataset (compare Fig. 4.5 a) in the main text and Fig. 5 a) in this section)

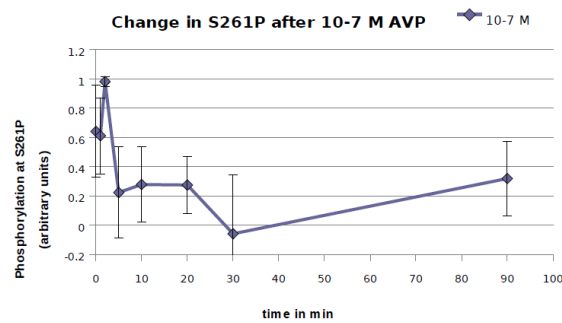
In consistency with the sensitivity analysis performed in COPASI for time point 21 min, one could observe that a change in the Ki6 has only a minor effect.

Due to the fact that $AQP2_{membrane}$ is increasing slower in the new compared to the old dataset, also the

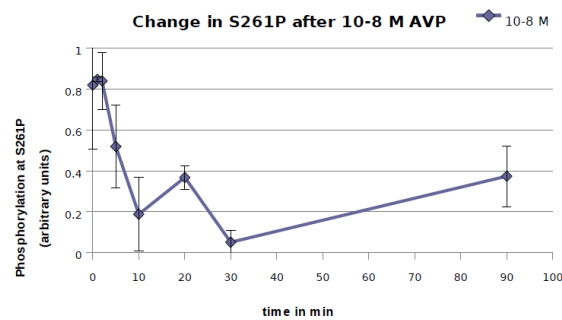
4 Sensitivity analysis and time dependent sensitivity analysis applied to the IMCD cell model
with the new $AQP2_{membrane}$ dataset produced by Klusmann et al.



(a)



(b)



(c)

Figure 2: Dephosphorylation of AQP2 at position S261. The cells were treated with different concentrations of dDAVP for different durations (0, 1, 2, 5, 10, 20, 30, 90 min). The cells were lysed and immunoblotted for AQP2 phosphorylated at S261. a) 10^{-6} M, b) 10^{-7} M, c) 10^{-8} M.

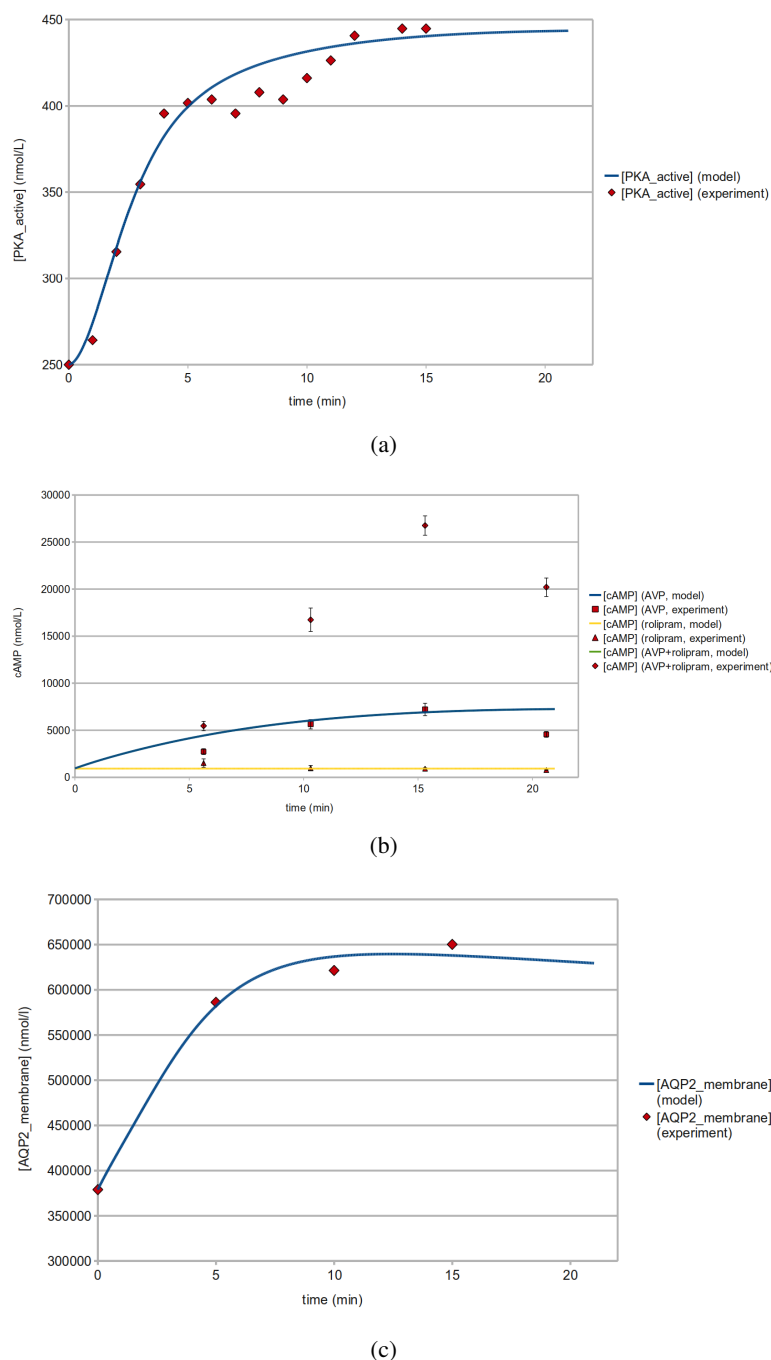


Figure 3: Model Fitting with COPASI: primary rat IMCD cell model without negative feedback (re2). **a)** Fitting of intracellular cAMP time courses. The cells were treated with AVP (100 nM), rolipram, or a combination of both for the indicated time points. **b)** Reproduction of the PKA activity **c)** Fitting of membrane localized AQP2. The experimental data were taken from Stefan et al. [133]. cAMP could be directly used for comparison, PKA_{active} was assumed to have an initial value of 250 nM and AQP2_{membrane} in % was calculated from the ratio of intracellular/plasma membrane located AQP2.

4 Sensitivity analysis and time dependent sensitivity analysis applied to the IMCD cell model with the new $AQP2_{membrane}$ dataset produced by Klussmann et al.

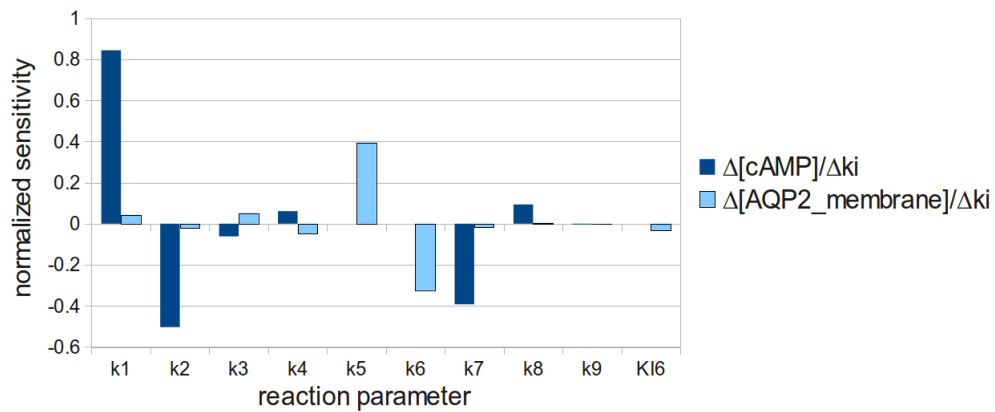
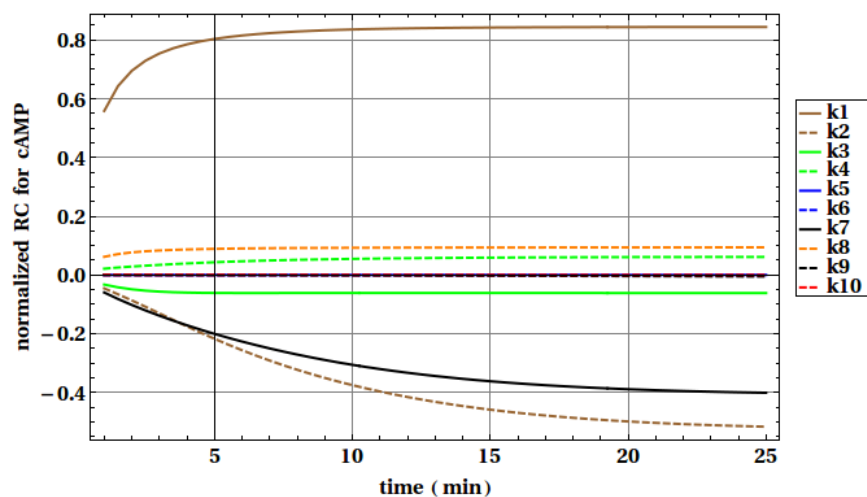
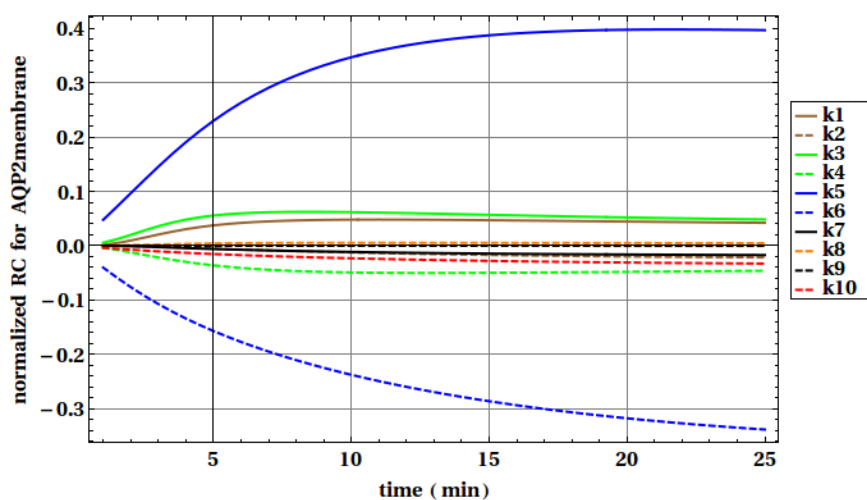


Figure 4: Sensitivity analysis of the primary rat IMCD cell model fitted to the new $AQP2_{membrane}$ dataset produced by Klussmann et al. Effect of small changes in the parameters on the model species at time point 21 min. The normalized sensitivities were taken. The analysis was performed with COPASI.

time dependent sensitivity coefficients are different. By using the new dataset the effect of a change in k_5 and k_6 is less prominent at the beginning of the simulation, but increases over time.



(a)



(b)

Figure 5: Time-dependent sensitivity analysis performed on complete IMCD cell model fitted to the new dataset. Time-dependent sensitivity analysis was performed on the complete IMCD cell model as shown in Fig. 4.1 with the optimal set of parameters found by using the new dataset generated by Klussmann et al. **a)** Time-dependent normalized response coefficients for all parameters in respect to cAMP, **b)** Time-dependent normalized response coefficients for all parameters in respect to AQP2 in the membrane

5 Cation homeostasis model as implemented in COPASI

In Tab. 1 the algebraic and differential equations of the model are presented. The model was fitted to the MIFE data set. The resulting initial conditions and estimated parameters containing an estimated high L_{KK}^L or an estimated high L_{HK}^S value are presented in Tab. 2 and Tab. 3, respectively.

The parameters and initial conditions for the model fitted to the FLISE data are presented in Tab. 4.

6 MIFE - additional results

The model presented in Sec. 7.1 of the main text was fitted to the data from Shabala et al. (Fig. 7.1(a), 1000 replications, Particle Swarm algorithm, iteration limit 400, swarm size 40, standard deviation 1e-06, Mersenne Twister with seed 0). The 50 best results were used for subsequent analysis. The k -means algorithm as described in Sec. 6.1.1 was applied to cluster the simulation results of the corresponding models. Here, no restrictions were made concerning the existence of a K^+ -ATPase. Only the phenomenological coefficients involved in primary active transport ($L_{HP}^S, L_{HP}^A, L_{KP}^S, L_{KP}^A$) were allowed to change after glucose. This model was able to reproduce the data from H^+ and K^+ fluxes best (see Fig. 7(a)) and shows a high importance for a K^+ inward directed pump (L_{KP}^A). The parameter distribution is presented in Fig. 6(b), c) and d). Fig. 7(a) presents a knockout of the PMA1 ($L_{HP}^A = 0$). The K^+ flux is only slightly affected. Instead if $L_{KP} = 0$, representing a knockout of all potential K^+ -ATPases, no K^+ flux can be observed (see Fig. 6(b)). In Fig. 7(c), L_{KK}^L was set to zero, representing $\Delta Trk1,2p$ mutant. This had no effect on the fluxes. The same was observed for $L_{HK}^S = 0$ (data not shown). Therefore, neither a K^+ uniport, nor a K^+/H^+ symporter would play a role in the observed processes. Fig. 7(d) shows a positive membrane potential for the wild-type strain after glucose addition.

Despite its availability to reproduce the experimental data, this model was assumed to be too artificial given the currently available literature-based knowledge.

$$\begin{aligned}
 J_{H^+} &= RT \left[L_{H,H} \ln \frac{c_H^{out}}{c_H^{in}} + L_{H,K} \ln \frac{c_K^{out}}{c_K^{in}} + L_{H,Na} \ln \frac{c_{Na}^{out}}{c_{Na}^{in}} + L_{H,Cl} \ln \frac{c_{Cl}^{out}}{c_{Cl}^{in}} \right] - \\
 &\quad - F \Delta \phi [L_{H,H} + L_{H,K} + L_{H,Na} - L_{H,Cl}] + L_{H,ATP} \left(\frac{RT}{\bar{c}_{ATP}} \alpha_{ATP} (1 + K) \right) \\
 J_{K^+} &= RT \left[L_{H,K} \ln \frac{c_H^{out}}{c_H^{in}} + L_{K,K} \ln \frac{c_K^{out}}{c_K^{in}} \right] - \\
 &\quad - F \Delta \phi [L_{H,K} + L_{K,K}] + L_{K,ATP} \left(\frac{RT}{\bar{c}_{ATP}} \alpha_{ATP} (1 + K) \right) \\
 J_{Na^+} &= RT \left[L_{H,Na} \ln \frac{c_H^{out}}{c_H^{in}} + L_{Na,Na} \ln \frac{c_{Na}^{out}}{c_{Na}^{in}} \right] - F \Delta \phi [L_{H,Na} + L_{Na,Na}] \\
 J_{Cl^-} &= RT \left[L_{H,Cl} \ln \frac{c_H^{out}}{c_H^{in}} + L_{Cl,Cl} \ln \frac{c_{Cl}^{out}}{c_{Cl}^{in}} \right] - F \Delta \phi [L_{H,Cl} - L_{Cl,Cl}] \\
 \\
 \frac{d p H_{in}}{dt} &= \frac{-J_{H^+} \cdot Surface}{V_{in} \cdot pbc} & \frac{d [H^+]_{out}}{dt} &= \frac{-J_{H^+} \cdot Surface}{V_{out}} \\
 \frac{d [K^+]_{in}}{dt} &= \frac{J_{K^+} \cdot Surface}{V_{in}} & \frac{d [K^+]_{out}}{dt} &= \frac{-J_{K^+} \cdot Surface}{V_{out}} \\
 \frac{d [Na^+]_{in}}{dt} &= \frac{J_{Na^+} \cdot Surface}{V_{in}} & \frac{d [Na^+]_{out}}{dt} &= \frac{-J_{Na^+} \cdot Surface}{V_{out}} \\
 \frac{d [Cl^-]_{in}}{dt} &= \frac{J_{Cl^-} \cdot Surface}{V_{in}} & \frac{d [Cl^-]_{out}}{dt} &= \frac{-J_{Cl^-} \cdot Surface}{V_{out}} \\
 \\
 \frac{d[ATP]}{dt} &= k_{ATP_{incr}} - k_{ATP_{decr}} \cdot ATP \\
 k_{ATP_{decr}} &= \frac{k_{ATP_{incr}}}{ATP_{max}} \\
 \frac{d L_{H,P}^{A/S}}{dt} &= k_{incr} - k_{decr} \cdot L_{H,P}^{A/S} \\
 k_{decr}^{A/S} &= \frac{k_{incr}}{L_{H,P_{aG}}^{A/S}} \\
 \alpha_{ATP} &= [ATP] - [\bar{c}ATP] \\
 \\
 [H_{in}] &= 10^{-pH_{in}} \cdot cf \\
 \frac{d \Delta \phi}{dt} &= \frac{F}{Cm} \cdot (2 \cdot J_{H^+} + 2 \cdot J_{K^+} + 2 \cdot J_{Na^+} - 2 \cdot J_{Cl^-}) \\
 \\
 L_{H,H} &= L_{HH}^L + n_{HK}^S \cdot L_{HK}^S + n_{HK}^A \cdot L_{HK}^A + n_{HN}^S \cdot L_{HN}^S + n_{HN}^A \cdot L_{HN}^A \\
 &\quad + n_{HP}^S \cdot L_{HP}^S + n_{HP}^A \cdot L_{HP}^A + n_{HC}^S \cdot L_{HC}^S + n_{HC}^A \cdot L_{HC}^A \\
 L_{H,K} &= n_{HK}^S \cdot n_{KH}^S \cdot L_{HK}^S - n_{HK}^A \cdot n_{KH}^A \cdot L_{HK}^A \\
 L_{H,Na} &= n_{HN}^S \cdot n_{NH}^S \cdot L_{HN}^S - n_{HN}^A \cdot n_{NH}^A \cdot L_{HN}^A \\
 L_{H,ATP} &= n_{HP}^S \cdot n_{PH}^S \cdot L_{HP}^S - n_{HP}^A \cdot n_{PH}^A \cdot L_{HP}^A \\
 L_{H,Cl} &= n_{HC}^S \cdot n_{CH}^S \cdot L_{HC}^S - n_{HC}^A \cdot n_{CH}^A \cdot L_{HC}^A \\
 L_{K,K} &= L_{KK}^L + n_{KH}^S \cdot L_{HK}^S + n_{KH}^A \cdot L_{HK}^A \\
 L_{Na,Na} &= L_{NN}^L + n_{NH}^S \cdot L_{HN}^S + n_{NH}^A \cdot L_{HN}^A \\
 L_{Cl,Cl} &= L_{CC}^L + n_{CH}^S \cdot L_{HC}^S + n_{CH}^A \cdot L_{HC}^A
 \end{aligned}$$

Table 1: Model as implemented in COPASI.

Global quantities and volumes	Value	Source
V_{in}	$1.8 \cdot 10^{-11} \text{ m}^3$	Calculation
V_{out}	$2.85 \cdot 10^{-6} \text{ m}^3$	Exp. condition
T	296 K	Exp. condition
F	96,485 C/mol	Faraday constant
Surface (of all cells)	$2.29 \cdot 10^{-05} \text{ m}^2$	Calculation
Proton buffer capacity (pb_c)	$\frac{200 \text{ mM}}{\text{pH}}$	Experimental observation
conversion factor (cf)	1000 mM/M	
K	$1 \cdot 10^{-6}$	estimated
\bar{c}_{ATP}	0.316 nM	estimated
$\Delta\phi$	-0.168 V	estimated
Initial conditions	Values	Source
H_{out}	$3.162 \cdot 10^{-3}$	Exp. condition (pH 5.5)
K_{out}	0.1	Exp. condition
Cl_{out}	0.1	Exp. condition
ATP	2.48 mM	estimated between 0 and 2.5 mM
$ATP_{stimulus}$	2.5	Özalp <i>et al.</i> [95]
$KCl_{stimulus}$	0.01, 0.1, 1, 10	Exp. condition
pH_{in}	5.51	estimated between 5 and 7
K_{in}	75.5 nM	estimated between 60 and 100 nM
Cl_{in}	0.54 nM	estimated between 0.1 and 10 nM
Na_{in}	30 nM	estimated between 5 and 30 nM
Na_{out}	0.01 nM	estimated between 0.01 and 0.1 nM
Phenomenological and stoichiometric coefficients	Parameter values	Source
L_{KK}^L	$6.37 \cdot 10^{-11} \text{ mol}^2/(\text{J} \cdot \text{m}^2 \cdot \text{s})$	estimated
$L_{HPP_{mit}}^A$	$0 \text{ mol}^2/(\text{J} \cdot \text{m}^2 \cdot \text{s})$	Assumption
$L_{HPP_{aG}}^A$	$0.001 \text{ mol}^2/(\text{J} \cdot \text{m}^2 \cdot \text{s})$	estimated
L_{HC}^S	$1 \cdot 10^{-9} \text{ mol}^2/(\text{J} \cdot \text{m}^2 \cdot \text{s})$	estimated
n_{HP}^A	1.36	estimated
n_{PH}^A	1.4	estimated
n_{HC}^S	1.27	estimated
n_{CH}^S	1.02	estimated
$k_{ATP_{incr}}$	10	estimated
k_{incr}	$1.09 \cdot 10^{-9} \text{ mol}^2/(\text{J} \cdot \text{m}^2 \cdot \text{s}^2)$	estimated

Table 2: Initial concentrations, global quantities and volumes used for fitting the model to data from MIFE experiments resulting in a high L_{KK}^L value. Estimated model parameters for stress with 4 different concentrations of KCl. Parameters for the model exhibiting a high L_{KK}^L are presented. All other Ls and ns could be set to 0 without affecting goodness of fit.

Global quantities and volumes	Value	Source
V_{in}	$1.8 \cdot 10^{-11} \text{ m}^3$	Calculation
V_{out}	$2.85 \cdot 10^{-6} \text{ m}^3$	Exp. condition
T	296 K	Exp. condition
F	96,485 C/mol	Faraday constant
Surface (of all cells)	$2.29 \cdot 10^{-05} \text{ m}^2$	Calculation
Proton buffer capacity (pb_c)	$\frac{200 \text{ mM}}{\text{pH}}$	Experimental observation
conversion factor (cf)	1000 mM/M	
K	0.293899	estimated
\bar{c}_{ATP}	0.298098 nM	estimated
$\Delta\phi$	-0.124 V	estimated
Initial conditions	Values	Source
H_{out}	$3.162 \cdot 10^{-3}$	Exp. condition (pH 5.5)
K_{out}	0.1	Exp. condition
Cl_{out}	0.1	Exp. condition
ATP	2.38 mM	estimated between 0 and 2.5 mM
$ATP_{stimulus}$	2.5	Özalp <i>et al.</i> [95]
$KCl_{stimulus}$	0.01, 0.1, 1, 10	Exp. condition
pH_{in}	5.34	estimated between 5 and 7
K_{in}	99.9 nM	estimated between 60 and 100 nM
Cl_{in}	0.37 nM	estimated between 0.1 and 10 nM
Na_{in}	14.3 nM	estimated between 5 and 30 nM
Na_{out}	0.087 nM	estimated between 0.01 and 0.1 nM
Phenomenological and stoichiometric coefficients	Parameter values	Source
L_{HK}^S	$8.3 \cdot 10^{-12} \text{ mol}^2/(\text{J} \cdot \text{m}^2 \cdot \text{s})$	estimated
$L_{HP_{mi}}^A$	$0 \text{ mol}^2/(\text{J} \cdot \text{m}^2 \cdot \text{s})$	Assumption
$L_{HP_{aG}}^A$	$2.05265 \cdot 10^{-7} \text{ mol}^2/(\text{J} \cdot \text{m}^2 \cdot \text{s})$	estimated
L_{HC}^S	$1 \cdot 10^{-7} \text{ mol}^2/(\text{J} \cdot \text{m}^2 \cdot \text{s})$	estimated
n_{HK}^S	1.3	estimated
n_{KH}^S	2.9	estimated
n_{HP}^A	1.9	estimated
n_{PH}^A	1.0	estimated
n_{HC}^S	1.4	estimated
n_{CH}^S	1.1	estimated
$k_{ATP_{incr}}$	$1.84 \cdot 10^{-2} \text{ mol}/(\text{m}^3 \cdot \text{s})$	estimated
k_{incr}	$1.4 \cdot 10^{-4} \text{ mol}^2/(\text{J} \cdot \text{m}^2 \cdot \text{s}^2)$	estimated

Table 3: Initial concentrations, global quantities and volumes used for fitting the model to data from MIFE experiments resulting in a high L_{HK}^S value. Estimated model parameters for stress with 4 different concentrations of KCl. Parameters for the model exhibiting a high L_{HK}^S are presented. All other Ls and ns could be set to 0 without affecting goodness of fit.

Global quantities and volumes	Value	Source
V_{in}	$1.49 - 4.34 \cdot 10^{-8} \text{ m}^3$	Calculation, dependent on each experiment
V_{out}	$2.12 \cdot 10^{-6} \text{ m}^3$	Exp. condition
T	296 K	Exp. condition
F	96,485 C/mol	Faraday constant
Surface (of all cells)	0.01990 - 0.05789 m^2	Calculation, dependent on each experiment
Proton buffer capacity (pb_c)	$\frac{200 \text{ mM}}{\text{pH}}$	Experimental observation
conversion factor (cf)	1000 mM/M	
K	2.08	estimated
\bar{c}_{ATP}	0.546 mM	estimated
$\Delta\phi$	-0.2, -0.17, -0.08, -0.58 V	dependent on simulation
Initial conditions	Values	Source
H_{out}	$2.76 \cdot 10^{-2}$	Exp. condition (mean)
K_{out}	0.01, 0.1, 1, 10 mM	Exp. condition
Cl_{out}	20 mM + K_{out}	Exp. condition
ATP	1.2	estimated between 0 and 2.5 mM
$ATP_{stimulus}$	2.5	Özalp <i>et al.</i> [95]
pH_{innen}	5.16	estimated between 5 and 7
K_{in}	100 mM	estimated between 60 and 100 nM
Cl_{in}	3.1 mM	estimated between 0.1 and 10 nM
Na_{in}	5.3 mM	estimated between 5 and 30 nM
Na_{out}	0.09 mM	estimated between 0.01 and 0.1 nM
Phenomenological Coefficients	Parameter Values	Source
L_{KK}^L	$4.36 \cdot 10^{-8} \text{ mol}^2/(\text{J} \cdot \text{m}^2 \cdot \text{s})$	estimated
$L_{HP_{mit}}^A$	$0 \text{ mol}^2/(\text{J} \cdot \text{m}^2 \cdot \text{s})$	Assumption
$L_{HP_{aG}}^A$	$1.18 \cdot 10^{-12} \text{ mol}^2/(\text{J} \cdot \text{m}^2 \cdot \text{s})$	estimated
L_{HC}^S	$2.36 \cdot 10^{-8} \text{ mol}^2/(\text{J} \cdot \text{m}^2 \cdot \text{s})$	estimated
n_{HP}^A	2.98	estimated
n_{PH}^A	2.71	estimated
n_{HC}^S	1.04	estimated
n_{CH}^S	2.50	estimated
$k_{ATP_{incr}}$	$1.2 \text{ mol}/(\text{m}^3 \cdot \text{s})$	estimated
k_{incr}	$9.16 \cdot 10^{-8} \text{ mol}^2/(\text{J} \cdot \text{m}^2 \cdot \text{s}^2)$	estimated

Table 4: Initial concentrations, global quantities and volumes, and estimated parameters for model fitted to FLISE data. Estimated model parameters for stress with 4 different concentrations of KCl. All other Ls and ns could be set to 0 without affecting goodness of fit.

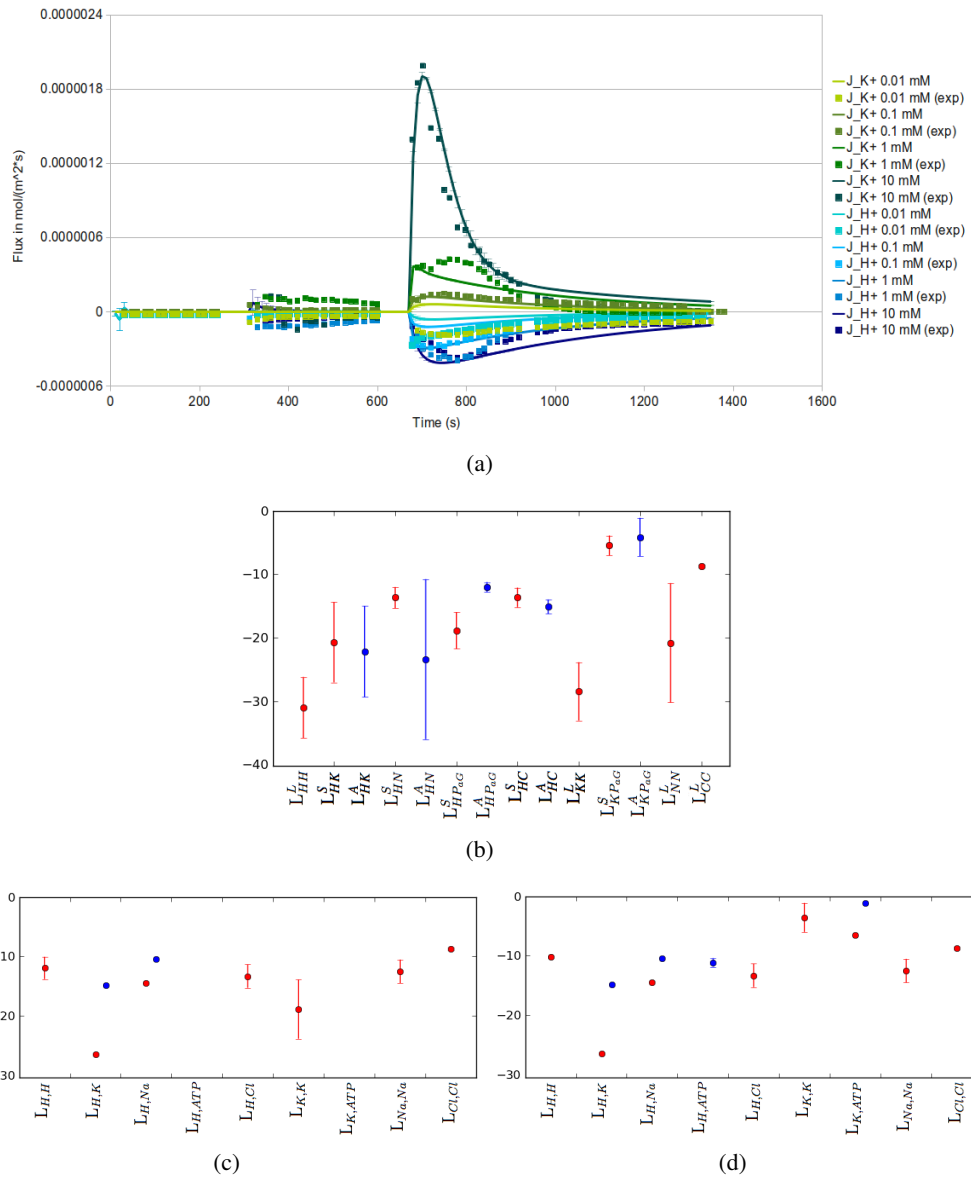


Figure 6: Clustering and parameter analysis with the model including a K^+ -ATPase. The parameters of the model including a K^+ -ATPase were estimated. Furthermore, it was restricted that the parameters do not change after glucose addition, except for those involved in the primary active transport (L_{HP}^S , L_{HP}^A , L_{KP}^S , L_{KP}^A). Clustering with the k -means algorithm was performed as described in Sec. 6.1.1. The simulations of all 4 KCl stimuli were clustered simultaneously. The 50 best of 1000 estimations were used for clustering. **a)** shows the cluster with the best fit, **b)** shows the parameter distribution for the individual transporters, **c)** shows the resulting composed Ls before and **d)** after glucose addition. The log₁₀ of the parameters is plotted. Mean and standard deviation of the parameters were calculated after separating them into positive and negative values. Positive values, symporters or inward directed pumps are colored in red, negative values, antiporters or outward directed pumps in blue.

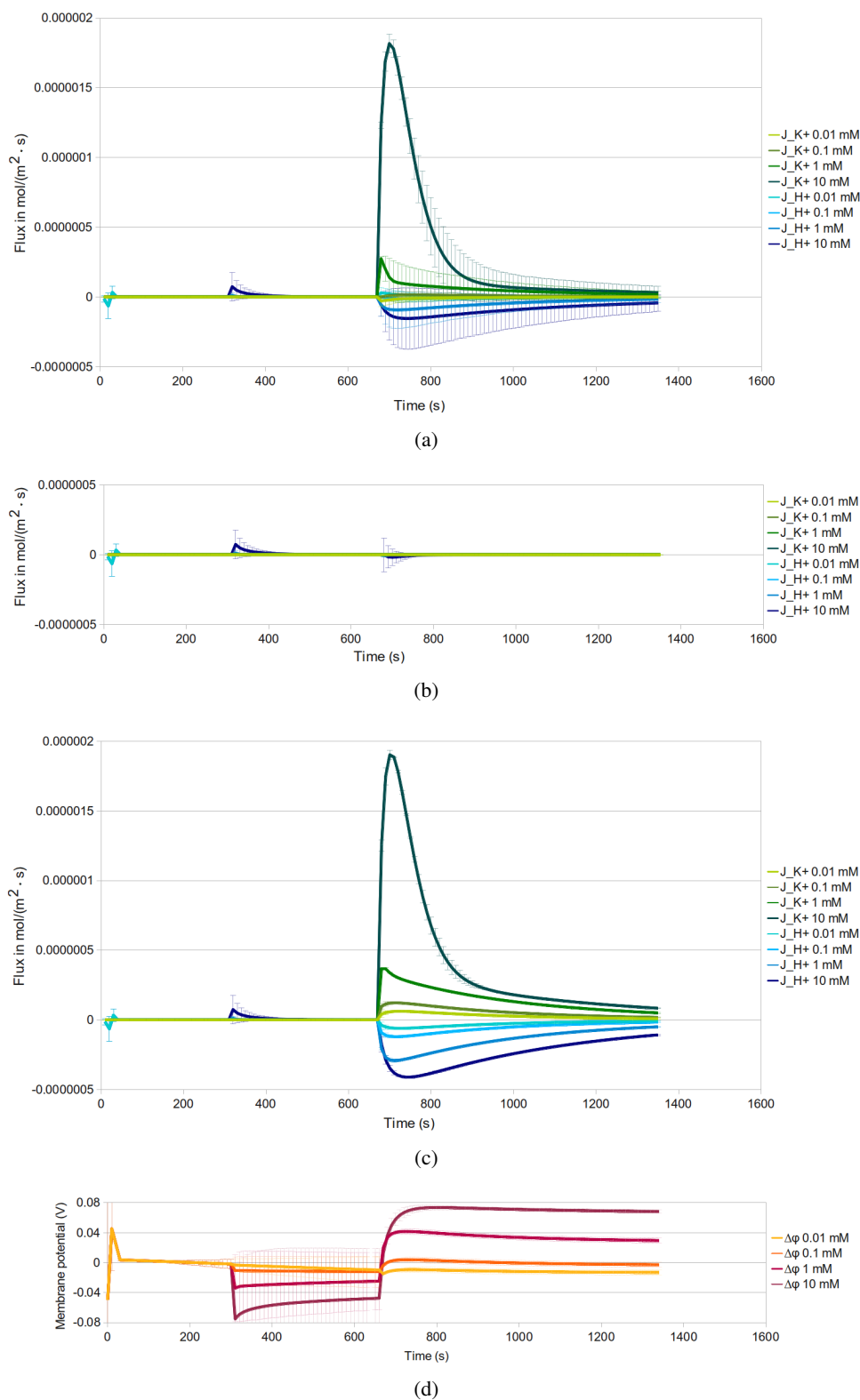


Figure 7: Predictions performed with the model including a K⁺-ATPase. The model including a K⁺-ATPase was used to predict the knockout or inhibition of **a)** the Pma1p ($L_{HP}^A = 0$), **b)** potential K⁺-ATPases ($L_{K,ATP} = 0$), **c)** the K⁺ uniport and leakage ($L_{KK}^L = 0$). **d)** The model was used to predict the membrane potential for the wild-type strain. Shown are the mean and standard deviation of the best cluster (n=2)

Bibliography

- [1] P. Agre, G. M. Preston, B. L. Smith, J. S. Jung, S. Raina, C. Moon, W. B. Guggino, and S. Nielsen. Aquaporin chip: the archetypal molecular water channel. *Am J Physiol*, 265(4 Pt 2):F463–F476, Oct 1993.
- [2] B. Alberts, A. Johnson, J. Lewis, M. Raff, K. Roberts, and P. Walter. *Molecular Biology of the Cell, Fourth Edition*. Garland Science/Taylor & Francis LLC, 2002.
- [3] J. Ariño, J. Ramos, and H. Sychrová. Alkali metal cation transport and homeostasis in yeasts. *Microbiol Mol Biol Rev*, 74(1):95–120, 2010.
- [4] B. Auclair, V. Nikonenko, C. Larchet, M. Métayer, and L. Dammak. Correlation between transport parameters of ion-exchange membranes. *Journal of Membrane Science*, 195(1):89 – 102, 2002.
- [5] M. Babey, P. Kopp, and G. L. Robertson. Familial forms of diabetes insipidus: clinical and molecular characteristics. *Nat Rev Endocrinol*, 7(12):701–714, Dec 2011.
- [6] M. A. Bañuelos, M. C. Ruiz, A. Jimenez, J. L. Souciet, S. Potier, and J. Ramos. Role of the Nha1 antiporter in regulating K(+) influx in *Saccharomyces cerevisiae*. *Yeast*, 19, 2002.
- [7] M. Barberis, E. Klipp, M. Vanoni, and L. Alberghina. Cell size at s phase initiation: an emergent property of the *g1/s* network. *PLoS Comput Biol*, 3(4):e64, Apr 2007.
- [8] D. A. Beard. A biophysical model of the mitochondrial respiratory system and oxidative phosphorylation. *PLoS Comput Biol*, 1(4):e36, Sep 2005.
- [9] B. Benito, B. Garciadeblás, P. Schreier, and A. Rodríguez-Navarro. Novel p-type atpases mediate high-affinity potassium or sodium uptake in fungi. *Eukaryot Cell*, 3(2):359–368, Apr 2004.
- [10] V. Bernier, J.-P. Morello, A. Zarruk, N. Debrand, A. Salahpour, M. Lonergan, M.-F. Arthus, A. Laperrière, R. Brouard, M. Bouvier, and D. G. Bichet. Pharmacologic chaperones as a potential treatment for x-linked nephrogenic diabetes insipidus. *J Am Soc Nephrol*, 17:232–243, 2006.
- [11] A. Bertl, J. Ramos, J. Ludwig, H. Lichtenberg-Fraté, J. Reid, H. Bihler, F. Calero, P. Martínez, and P. O. Ljungdahl. Characterization of potassium transport in wild-type and isogenic yeast strains carrying all combinations of *trk1*, *trk2* and *tok1* null mutations. *Mol Microbiol*, 47(3):767–780, Feb 2003.
- [12] H. Bihler, C. Slayman, and A. Bertl. Nsc1: A novel high-current inward rectifier for cations in the plasma membrane of *saccharomyces cerevisiae*. *Febs Letters*, 432:59–64, 1998.

- [13] H. Bihler, C. L. Slayman, and A. Bertl. Low-affinity potassium uptake by *Saccharomyces cerevisiae* is mediated by nsc1, a calcium-blocked non-specific cation channel. *Biochim Biophys Acta*, 1558(2):109–118, Feb 2002.
- [14] M. Boone and P. M. T. Deen. Physiology and pathophysiology of the vasopressin-regulated renal water reabsorption. *Pflugers Arch*, 456(6):1005–1024, Sep 2008.
- [15] M. Boone, M. L. A. Kortenoeven, J. H. Robben, G. Tamma, and P. M. T. Deen. Counteracting vasopressin-mediated water reabsorption by atp, dopamine, and phorbol esters: mechanisms of action. *Am J Physiol Renal Physiol*, 300(3):F761–F771, Mar 2011.
- [16] M. A. Cadnapaphornchai, S. N. Summer, S. Falk, J. M. Thurman, M. A. Knepper, and R. W. Schrier. Effect of primary polydipsia on aquaporin and sodium transporter abundance. *Am J Physiol Renal Physiol*, 285(5):F965–F971, Nov 2003.
- [17] C.-L. Chou, B. M. Christensen, S. Frische, H. Vorum, R. A. Desai, J. D. Hoffert, P. de Lanerolle, S. Nielsen, and M. A. Knepper. Non-muscle myosin ii and myosin light chain kinase are downstream targets for vasopressin signaling in the renal collecting duct. *J Biol Chem*, 279(47):49026–49035, Nov 2004.
- [18] C. L. Chou, K. P. Yip, L. Michea, K. Kador, J. D. Ferraris, J. B. Wade, and M. A. Knepper. Regulation of aquaporin-2 trafficking by vasopressin in the renal collecting duct. roles of ryanodine-sensitive Ca^{2+} stores and calmodulin. *J Biol Chem*, 275(47):36839–36846, Nov 2000.
- [19] A. Cornish-Bowden. *Fundamentals of Enzyme Kinetics*. Portland Press Limited; Rev Sub edition, 1995.
- [20] P. M. T. Deen, J. P. L. Rijss, S. M. Mulders, R. J. Errington, J. Van Baal, and C. H. Van Os. Aquaporin-2 Transfection of Madin-Darby Canine Kidney Cells Reconstitutes Vasopressin-Regulated Transcellular Osmotic Water Transport. *J. Am. Soc. Nephrol.*, 8:1493–1501, 1997.
- [21] P. M. T. Deen, B. W. Van Balkom, P. J. Savelkoul, E. J. Kamsteeg, M. Van Raak, M. L. Jennings, T. R. Muth, V. Rajendran, and M. J. Caplan. Aquaporin-2: COOH terminus is necessary but not sufficient for routing to the apical membrane. *Am J Physiol Renal Physiol.*, 282:F330–40, 2002.
- [22] S. DeGroot and P. Mazur. *Non-Equilibrium Thermodynamics*. Interscience, New York, 1962.
- [23] Y. Demirel. *Nonequilibrium Thermodynamics, Second Edition: Transport and Rate Processes in Physical, Chemical and Biological Systems*. Elsevier Science, 2007.
- [24] A. A. Eddy and J. A. Barnett. A history of research on yeasts 11. the study of solute transport: the first 90 years, simple and facilitated diffusion(1). *Yeast*, 24(12):1023–1059, Dec 2007.
- [25] C. Fairman, X. Zhou, and C. Kung. Potassium uptake through the tok1 K^{+} channel in the budding yeast. *J Membr Biol*, 168(2):149–157, Mar 1999.
- [26] B. Flamion and K. R. Spring. Water permeability of apical and basolateral cell membranes of rat inner medullary collecting duct. *Am J Physiol*, 259(6 Pt 2):F986–F999, Dec 1990.

- [27] D. B. Fogel, L. J. Fogel, and J. W. Atmar. Meta-evolutionary programming. In *25th Asiloma Conference on Signals, Systems and Computers. IEEE Computer Society, Asilomar*, 540 - 545, 1992.
- [28] E. W. Forgy. Cluster analysis of multivariate data: efficiency vs interpretability of classifications. *Biometrics*, 21:768–769, 1965.
- [29] M. Fröhlich, P. M. T. Deen, and E. Klipp. A systems biology approach: Modelling of aquaporin-2 trafficking. *Genome Inform.*, 24:42–55, 2010.
- [30] T. M. Fujiwara and D. G. Bichet. Molecular biology of hereditary diabetes insipidus. *J Am Soc Nephrol*, 16(10):2836–2846, 2005.
- [31] R. F. Gaber, C. A. Styles, and G. R. Fink. Trk1 encodes a plasma membrane protein required for high-affinity potassium transport in *saccharomyces cerevisiae*. *Mol Cell Biol*, 8(7):2848–2859, Jul 1988.
- [32] S. Gerber. *In Silico Modeling of Cation Homeostasis in Saccharomyces cerevisiae*. PhD thesis, Humboldt-Universität zu Berlin, 2011.
- [33] R. Glaser. *Biophysics*. Springer, 2000.
- [34] A. Goffeau, B. G. Barrell, H. Bussey, R. W. Davis, B. Dujon, H. Feldmann, F. Galibert, J. D. Hoheisel, C. Jacq, M. Johnston, E. J. Louis, H. W. Mewes, Y. Murakami, P. Philippsen, H. Tettelin, and S. G. Oliver. Life with 6000 genes. *Science*, 274(5287):546, 563–546, 567, Oct 1996.
- [35] D. Goldman. Potential, impedance and rectification in membranes. *J Gen Physiol*, 27:37–60, 1943.
- [36] E. Grantcharova, J. Furkert, H. P. Reusch, H.-W. Krell, G. Papsdorf, M. Beyermann, R. Schulein, W. Rosenthal, and A. Oksche. The extracellular n terminus of the endothelin b (etb) receptor is cleaved by a metalloprotease in an agonist-dependent process. *J Biol Chem*, 277(46):43933–43941, Nov 2002.
- [37] R. Haro and A. Rodríguez-Navarro. Molecular analysis of the mechanism of potassium uptake through the trk1 transporter of *saccharomyces cerevisiae*. *Biochim Biophys Acta*, 1564(1):114–122, Aug 2002.
- [38] R. Heinrich and T. A. Rapoport. A linear steady-state treatment of enzymatic chains. General properties, control and effector strength. *European Journal of Biochemistry*, 42:89–95, 1974.
- [39] A. V. Hill. The possible effects of the aggregation of the molecules of haemoglobin on its dissociation curves. *Journal of Physiology*, 40:iv–vii, 1910.
- [40] B. Hille. *Ion Channels of Excitable Membranes*. Sinauer Associates, 3rd edition edition, 2001.
- [41] A. Hindmarsh. Odepack, a systematized collection of ode solvers. *Scientific Computing, R. S. Stepleman et al. (eds.), North-Holland, Amsterdam, IMACS Transactions on Scientific Computation*, 1:55–64, 1983.

- [42] J. D. Hoffert, R. A. Fenton, H. B. Moeller, B. Simons, D. Tchapyjnikov, B. W. McDill, M.-J. Yu, T. Pisitkun, F. Chen, and M. A. Knepper. Vasopressin-stimulated increase in phosphorylation at ser269 potentiates plasma membrane retention of aquaporin-2. *J Biol Chem*, 283(36):24617–24627, Sep 2008.
- [43] S. Hoops, S. Sahle, R. Gauges, C. Lee, J. Pahle, N. Simus, M. Singhal, L. Xu, P. Mendes, and U. Kummer. COPASI - a COMplex PATHway SIMulator. *Bioinformatics*, 83:3067–3074, 2006.
- [44] M. D. Houslay and D. R. Adams. Pde4 camp phosphodiesterases: modular enzymes that orchestrate signalling cross-talk, desensitization and compartmentalization. *Biochem J*, 370(Pt 1):1–18, Feb 2003.
- [45] <http://www.thinkcopdifferently.com>.
- [46] J. Huling, D. Tchapyjnikov, A. N. Sachs, B. Ruttenberg, V. Jacob, G. Ma, J. D. Hoffert, T. Pisitkun, and M. A. Knepper. Database of renal inner medullary collecting duct (imcd) proteins.
- [47] B. Ingalls and H. Sauro. Sensitivity analysis of stoichiometric networks: an extension of metabolic control analysis to non-steady state trajectories. *Journal of Theoretical Biology*, 222(1):23–36, 2003.
- [48] D. A. Jans, P. Jans, H. Luzius, and F. Fahrenholz. Monensin-resistant llc-pk1 cell mutants are affected in recycling of the adenylate cyclase-stimulating vasopressin v2-receptor. *Mol Cell Endocrinol*, 81(1-3):165–174, Oct 1991.
- [49] A. Jansson and M. Jirstrand. Biochemical modeling with Systems Biology Graphical Notation. *Drug Discovery Today*, 2010. doi:10.1016/j.drudis.2010.02.012.
- [50] M. D. Johnson, L. B. Kinter, and R. Beeuwkes. Effects of avp and ddavp on plasma renin activity and electrolyte excretion in conscious dogs. *Am J Physiol*, 236(1):F66–F70, Jan 1979.
- [51] D. Johnston and S. M.-S. Wu. *Foundations of Cellular Neurophysiology*. The MIT Press, 1994.
- [52] D. S. Jones and B. D. Sleeman. *Differential Equations and Mathematical Biology*. Chapman and Hall/CRC, 2003.
- [53] H. Kacser and J. A. Burns. The control of flux. *Symp. Soc. Exp. Biol.*, 27:65–104, 1973.
- [54] M. Kahm, C. Navarrete, V. Llopis-Torregrosa, R. Herrera, L. Barreto, L. Yenush, J. Ariño, J. Ramos, and M. Kschischo. Actuators of yeast potassium homeostasis revealed by mathematical modeling. Manuscript in preparation.
- [55] E. J. Kamsteeg, I. Heijnen, C. H. van Os, and P. M. Deen. The subcellular localization of an aquaporin-2 tetramer depends on the stoichiometry of phosphorylated and nonphosphorylated monomers. *J Cell Biol*, 151(4):919–930, Nov 2000.
- [56] E. J. Kamsteeg, G. Hendriks, M. Boone, I. B. Konings, V. Oorschot, P. van der Sluijs, J. Klumperman, and P. M. T. Deen. Short-chain ubiquitination mediates the regulated endocytosis of the aquaporin-2 water channel. *PNAS*, 103:18344–18349, 2006.

- [57] R. Karchin, K. Karplus, and D. Haussler. Classifying g-protein coupled receptors with support vector machines. *Bioinformatics*, 18(1):147–159, Jan 2002.
- [58] A. Katchalsky and P. Curran. *Nonequilibrium Thermodynamics in Biophysics*. Books in Biophysics, 1. Harvard Univ. Press, 1965.
- [59] J. Keener and J. Sneyd. *Mathematical Physiology*. Springer, 1998.
- [60] J. Kennedy and R. Eberhart. Particle swarm optimization. In *Proc. Conf. IEEE Int Neural Networks*, volume 4, pages 1942–1948, 1995.
- [61] K. A. Ketchum, W. J. Joiner, A. J. Sellers, L. K. Kaczmarek, and S. A. Goldstein. A new family of outwardly rectifying potassium channel proteins with two pore domains in tandem. *Nature*, 376(6542):690–695, Aug 1995.
- [62] H. Kitano. *Foundations of Systems Biology*. The MIT Press, 2009.
- [63] E. Klipp, W. Liebermeister, C. Wierling, A. Kowald, H. Lehrach, and R. Herwig. *Systems Biology: A Textbook*. Wiley-VCH, 2009.
- [64] E. Klipp, B. Nordlander, R. Krüger, P. Gennemark, and S. Hohmann. Integrative model of the response of yeast to osmotic shock. *Nat Biotechnol*, 23(8):975–982, Aug 2005.
- [65] G. Kluge and G. Neugebauer. *Grundlagen der Thermodynamik*. Spektrum Akademischer Verlag, 1994.
- [66] E. Klussmann, K. Maric, B. Wiesner, M. Beyermann, and W. Rosenthal. Protein kinase a anchoring proteins are required for vasopressin-mediated translocation of aquaporin-2 into cell membranes of renal principal cells. *J Biol Chem*, 274(8):4934–4938, Feb 1999.
- [67] M. A. Knepper and S. Nielsen. Kinetic model of water and urea permeability regulation by vasopressin in collecting duct. *Am. J. Physiol.*, 265:F214–F224, 1993.
- [68] C. H. Ko, A. M. Buckley, and R. F. Gaber. Trk2 is required for low affinity k⁺ transport in *saccharomyces cerevisiae*. *Genetics*, 125(2):305–312, Jun 1990.
- [69] C. H. Ko and R. F. Gaber. Trk1 and trk2 encode structurally related k⁺ transporters in *saccharomyces cerevisiae*. *Mol Cell Biol*, 11(8):4266–4273, Aug 1991.
- [70] R. Kopperud, A. E. Christensen, E. Kjarland, K. Viste, H. Kleivdal, and S. O. Doskeland. Formation of Inactive cAMP-saturated Holoenzyme of cAMPdependent Protein Kinase under Physiological Conditions. *J. Biol. Chem.*, 277:13443–13448, 2002.
- [71] T. Kuroda, H. Bihler, E. Bashi, C. L. Slayman, and A. Rivetta. Chloride channel function in the yeast trk-potassium transporters. *J Membr Biol*, 198(3):177–192, Apr 2004.
- [72] U. K. Laemmli. Cleavage of structural proteins during the assembly of the head of bacteriophage t4. *Nature*, 227(5259):680–685, Aug 1970.

- [73] S. Lecchi, K. E. Allen, J. P. Pardo, A. B. Mason, and C. W. Slayman. Conformational changes of yeast plasma membrane h(+)-atpase during activation by glucose: role of threonine-912 in the carboxy-terminal tail. *Biochemistry*, 44(50):16624–16632, Dec 2005.
- [74] S. Lecchi, C. J. Nelson, K. E. Allen, D. L. Swaney, K. L. Thompson, J. J. Coon, M. R. Sussman, and C. W. Slayman. Tandem phosphorylation of ser-911 and thr-912 at the c terminus of yeast plasma membrane h(+)-atpase leads to glucose-dependent activation. *J Biol Chem*, 282(49):35471–35481, Dec 2007.
- [75] F. Lesage, E. Guillemare, M. Fink, F. Duprat, M. Lazdunski, G. Romey, and J. Barhanin. A pH-sensitive yeast outward rectifier k⁺ channel with two pore domains and novel gating properties. *J Biol Chem*, 271(8):4183–4187, Feb 1996.
- [76] J. Li, Y. Ning, W. Hedley, B. Saunders, Y. Chen, N. Tindill, T. Hannay, and S. Subramaniam. The molecule pages database. *Nature*, 420(6916):716–717, Dec 2002.
- [77] Y. Linde, A. Buzo, and R. M. Gray. An algorithm for vector quantizer design. *IEEE Trans. on Communications*, COM-28(1):84–95, Jan. 1980.
- [78] H. Lodish, A. Berk, S. L. Zipursky, P. Matsudaira, B. Baltimore, and J. E. Darnell. *Molekulare Zellbiologie*. Spektrum Akademischer Verlag, 2001.
- [79] D. Lorenz, A. Krylov, D. Hahm, V. Hagen, W. Rosenthal, P. Pohl, and K. Maric. Cyclic amp is sufficient for triggering the exocytic recruitment of aquaporin-2 in renal epithelial cells. *EMBO Rep*, 4(1):88–93, Jan 2003.
- [80] J. MacQueen. Some methods for classification and analysis of multivariate observations. In L. M. LeCam and J. Neyman, editors, *Proc. of the 5th Berkeley Symp. on Mathematics Statistics and Probability*, 1967.
- [81] K. Maric, A. Oksche, and W. Rosenthal. Aquaporin-2 expression in primary cultured rat inner medullary collecting duct cells. *Am J Physiol*, 275(5 Pt 2):F796–F801, Nov 1998.
- [82] P. Martinez and B. L. Persson. Identification, cloning and characterization of a derepressible na⁺-coupled phosphate transporter in *saccharomyces cerevisiae*. *Mol Gen Genet*, 258(6):628–638, Jun 1998.
- [83] M. Matsumoto and T. Nishimura. Mersenne twister: A 623-dimensionally equidistributed uniform pseudorandom number generator. *ACM Transactions on Modeling and Computer Simulation*, 8:3–30, 1998.
- [84] L. Michaelis and M. L. Menten. Die kinetik der invertinwirkung. *Biochem. Z*, 49(333-369):352, 1913.
- [85] B. Michel, C. Lozano, M. Rodríguez, R. Coria, J. Ramírez, and A. Peña. The yeast potassium transporter *trk2* is able to substitute for *trk1* in its biological function under low k and low pH conditions. *Yeast*, 23(8):581–589, Jun 2006.

- [86] C. Navarrete, S. Petrešyová, L. Barreto, J. L. Martínez, J. Zahrádka, J. Ariño, H. Sychrová, and J. Ramos. Lack of main k^+ uptake systems in *saccharomyces cerevisiae* cells affects yeast performance in both potassium-sufficient and potassium-limiting conditions. *FEMS Yeast Res*, 10(5):508–517, Aug 2010.
- [87] P. I. Nedvetsky, V. Tabor, G. Tamma, S. Beulshausen, P. Skroblin, A. Kirschner, K. Mutig, M. Boltzen, O. Petrucci, A. Vossenkämper, B. Wiesner, S. Bachmann, W. Rosenthal, and E. Klussmann. Reciprocal regulation of aquaporin-2 abundance and degradation by protein kinase a and p38-map kinase. *J Am Soc Nephrol*, 21(10):1645–1656, Oct 2010.
- [88] P. I. Nedvetsky, G. Tamma, S. Beulshausen, G. Valenti, W. Rosenthal, and E. Klussman. Regulation of aquaporin-2 trafficking. *Aquaporins, Handbook of Experimental Pharmacology*, 190:133–157, 2009.
- [89] I. A. Newman. Ion transport in roots: measurement of fluxes using ion-selective microelectrodes to characterize transporter function. *Plant Cell Environ*, 24(1):1–14, Jan 2001.
- [90] S. Nielsen and M. A. Knepper. Vasopressin activates collecting duct urea transporters and water channels by distinct physical processes. *Am. J. Physiol.*, 265:F204–F213, 1993.
- [91] B. Novak, J. J. Tyson, B. Györffy, and A. Csikasz-Nagy. Irreversible cell-cycle transitions are due to systems-level feedback. *Nat Cell Biol*, 9(7):724–728, Jul 2007.
- [92] K. Omori and J. Kotera. Overview of pdes and their regulation. *Circ Res*, 100(3):309–327, Feb 2007.
- [93] L. Onsager. Reciprocal relations in irreversible processes i. *Phys. Rev.*, 37(4):405–426, Feb 1931.
- [94] R. Orij, S. Brul, and G. J. Smits. Intracellular ph is a tightly controlled signal in yeast. *Biochim Biophys Acta*, Mar 2011.
- [95] V. Özalp, T. Pedersen, L. Nielsen, and L. Olsen. Time-resolved measurements of intracellular atp in the yeast *saccharomyces cerevisiae* using a new type of nanobiosensor. *J Biol Chem*, 26(285(48)):37579–88, 2010.
- [96] C. Palm, A. Wagner, and P. Gross. [Hypo- and hypernatremia]. *Dtsch. Med. Wochenschr.*, 136:29–33, 2011.
- [97] B. O. Palsson. *Systems Biology Properties of Reconstructed Networks*. Cambridge University Press, 2006.
- [98] B. Pavan, C. Biondi, and A. Dalpiaz. Adenylyl cyclases as innovative therapeutic goals. *Drug Discov. Today*, 14:982–991, 2009.
- [99] D. S. Perlin, M. J. S. Francisco, C. W. Slayman, and B. P. Rosen. H^+ /atp stoichiometry of proton pumps from *neurospora crassa* and *escherichia coli*. *Arch Biochem Biophys*, 248(1):53–61, Jul 1986.
- [100] L. Petzold. Automatic selection of methods for solving stiff and nonstiff systems of ordinary differential equations. *SIAM Journal on Scientific and Statistical Computing*, 4:136–148, 1983.

- [101] R. Phillips, J. Kondev, and J. Theriot. *Physical Biology of the Cell*. Garland Science, 2008.
- [102] S. Pierre, T. Eschenhagen, G. Geisslinger, and K. Scholich. Capturing adenylyl cyclases as potential drug targets. *Nat Rev Drug Discov*, 8:321–335, 2009.
- [103] T. Pisitkun, J. D. Hoffert, M.-J. Yu, and M. A. Knepper. Tandem mass spectrometry in physiology. *Physiology (Bethesda)*, 22:390–400, Dec 2007.
- [104] G. M. Preston, T. P. Carroll, W. B. Guggino, and P. Agre. Appearance of water channels in xenopus oocytes expressing red cell chip28 protein. *Science*, 256(5055):385–387, Apr 1992.
- [105] J. A. Ramirez, V. Vacata, J. H. McCusker, J. E. Haber, R. K. Mortimer, W. G. Owen, and H. Lecar. Atp-sensitive k⁺ channels in a plasma membrane h⁺-atpase mutant of the yeast *saccharomyces cerevisiae*. *Proc Natl Acad Sci U S A*, 86(20):7866–7870, Oct 1989.
- [106] J. Ramos, R. Alijo, R. Haro, and A. Rodríguez-Navarro. Trk2 is not a low-affinity potassium transporter in *saccharomyces cerevisiae*. *J Bacteriol*, 176(1):249–252, Jan 1994.
- [107] J. Ramos, P. Contreras, and A. Rodríguez-Navarro. A potassium transport mutant of *Saccharomyces cerevisiae*. *Archives of Microbiology*, 143:88–93, 1985. 10.1007/BF00414774.
- [108] S. I. Rapoport. The sodium-potassium exchange pump: relation of metabolism to electrical properties of the cell. *Biophysical Journal*, 10:246–259, 1970.
- [109] M. Rep, M. Krantz, J. M. Thevelein, and S. Hohmann. The transcriptional response of *saccharomyces cerevisiae* to osmotic shock. *hot1p* and *msn2p/msn4p* are required for the induction of subsets of high osmolarity glycerol pathway-dependent genes. *J Biol Chem*, 275(12):8290–8300, Mar 2000.
- [110] M. Rep, V. Reiser, U. Gartner, J. M. Thevelein, S. Hohmann, G. Ammerer, and H. Ruis. Osmotic stress-induced gene expression in *saccharomyces cerevisiae* requires *msn1p* and the novel nuclear factor *hot1p*. *Mol Cell Biol*, 19(8):5474–5485, Aug 1999.
- [111] T. Rieg, T. Tang, F. Murray, J. Schroth, P. A. Insel, R. A. Fenton, H. K. Hammond, and V. Vallon. Adenylate cyclase 6 determines cAMP formation and aquaporin-2 phosphorylation and trafficking in inner medulla. *J. Am. Soc. Nephrol.*, 21:2059–2068, 2010.
- [112] M. M. Rinschen, M.-J. Yu, G. Wang, E. S. Boja, J. D. Hoffert, T. Pisitkun, and M. A. Knepper. Quantitative phosphoproteomic analysis reveals vasopressin v2-receptor-dependent signaling pathways in renal collecting duct cells. *Proc Natl Acad Sci U S A*, 107(8):3882–3887, Feb 2010.
- [113] A. Rivetta, T. Kuroda, and C. Slayman. Anion currents in yeast k⁺ transporters (*trk*) characterize a structural homologue of ligand-gated ion channels. *Pflugers Arch*, 462(2):315–330, Aug 2011.
- [114] A. Rivetta, C. Slayman, and T. Kuroda. Quantitative modeling of chloride conductance in yeast *trk* potassium transporters. *Biophys J*, 89(4):2412–2426, Oct 2005.
- [115] J. H. Robben, N. V. A. M. Knoers, and P. M. T. Deen. Regulation of the Vasopressin V2 Receptor by Vasopressin in Polarized Renal Collecting Duct Cells. *Molecular Biology of the Cell*, 15:5693–5699, 2004.

- [116] J. H. Robben, N. V. A. M. Knoers, and P. M. T. Deen. Cell biological aspects of the vasopressin type-2 receptor and aquaporin 2 water channel in nephrogenic diabetes insipidus. *Am J Physiol Renal Physiol*, 291:F257–F270, 2006.
- [117] J. H. Robben, M. L. Kortenoeven, M. Sze, C. Yae, G. Milligan, V. M. Oorschot, J. Klumperman, N. V. Knoers, and P. M. Deen. Intracellular activation of vasopressin V2 receptor mutants in nephrogenic diabetes insipidus by nonpeptide agonists. *Proc. Natl. Acad. Sci. U.S.A.*, 106:12195–12200, 2009.
- [118] S. Roberts, G. Dixon, M. Fischer, and D. Sanders. A novel low-affinity $\text{h}^+\text{-cl}^-$ co-transporter in yeast: Characterization by patch clamp. *Mycologia*, 93(4):636–633, 2001.
- [119] A. Rodríguez-Navarro. Potassium transport in fungi and plants. *Biochim Biophys Acta*, 1469(1):1–30, Mar 2000.
- [120] A. Rodríguez-Navarro and J. Ramos. Dual system for potassium transport in *saccharomyces cerevisiae*. *J Bacteriol*, 159(3):940–945, Sep 1984.
- [121] A. Ruiz and J. Ariño. Function and regulation of the *saccharomyces cerevisiae* ena sodium atpase system. *Eukaryot Cell*, 6(12):2175–2183, Dec 2007.
- [122] E. Sackmann and R. Merkel. *Lehrbuch der Biophysik*. Wiley-VCH, 2010.
- [123] J. J. Saucerman, L. L. Brunton, A. P. Michailova, and A. D. McCulloch. Modeling beta-adrenergic control of cardiac myocyte contractility in silico. *J Biol Chem*, 278(48):47997–48003, Nov 2003.
- [124] J. Schaber, M. A. Adrover, E. Eriksson, S. Pelet, E. Petelenz-Kurdziel, D. Klein, F. Posas, M. Gok-sör, M. Peter, S. Hohmann, and E. Klipp. Biophysical properties of *saccharomyces cerevisiae* and their relationship with hog pathway activation. *Eur Biophys J*, 39(11):1547–1556, Oct 2010.
- [125] R. W. Schrier. Body water homeostasis: clinical disorders of urinary dilution and concentration. *J. Am. Soc. Nephrol.*, 17:1820–1832, 2006.
- [126] M. Schulz, B. M. Bakker, and E. Klipp. Tide: a software for the systematic scanning of drug targets in kinetic network models. *BMC Bioinformatics*, 10:344, 2009.
- [127] I. H. Segel. *Enzyme Kinetics: Behavior and Analysis of Rapid Equilibrium and Steady-State Enzyme Systems*. Wiley-Interscience, 1993.
- [128] R. Serrano. In vivo glucose activation of the yeast plasma membrane atpase. *FEBS Lett*, 156(1):11–14, May 1983.
- [129] D. Seto-Young and D. S. Perlin. Effect of membrane voltage on the plasma membrane $\text{H}(+)\text{-ATPase}$ of *Saccharomyces cerevisiae*. *J. Biol. Chem.*, 266:1383–1389, 1991.
- [130] C. Sette and M. Conti. Phosphorylation and Activation of a cAMP-specific Phosphodiesterase by the cAMP-dependent Protein Kinase. *J. Biol. Chem.*, 271:16526–16534, 1996.
- [131] Smutzer. Yeast: An attractive, yet simple model. *TheScientist*, 15, 2001.

- [132] R. A. Star, H. Nonoguchi, R. Balaban, and M. A. Knepper. Calcium and cyclic adenosine monophosphate as second messengers for vasopressin in the rat inner medullary collecting duct. *J Clin Invest.*, 81:1879–1888, 1988.
- [133] E. Stefan, B. Wiesner, G. S. Baillie, R. Mollajew, V. Henn, D. Lorenz, J. Furkert, K. Santamaria, P. Nedvetsky, C. Hundsrucker, M. Beyermann, E. Krause, P. Pohl, I. Gall, A. N. MacIntyre, S. Bachmann, M. D. Houslay, W. Rosenthal, and E. Klussmann. Compartmentalization of camp-dependent signaling by phosphodiesterase-4d is involved in the regulation of vasopressin-mediated water reabsorption in renal principal cells. *J Am Soc Nephrol*, 18(1):199–212, Jan 2007.
- [134] S. Stoma, M. Fröhlich, S. Gerber, and E. Klipp. Stse: Spatio-temporal simulation environment dedicated to biology. *BMC Bioinformatics*, 12:126, 2011.
- [135] H. H. Stone, L. D. Kolb, C. A. Currie, C. E. Geheber, and J. Z. Cuzzell. Candida sepsis: pathogenesis and principles of treatments. *Ann Surg*, 179(5):697–711, May 1974.
- [136] T.-X. Sun, A. V. Hoek, Y. Huang, R. Bouley, M. McLaughlin, and D. Brown. Aquaporin-2 localization in clathrin-coated pits: inhibition of endocytosis by dominant-negative dynamin. *Am J Physiol Renal Physiol*, 282(6):F998–1011, Jun 2002.
- [137] H. Sychrová. Yeast as a model organism to study transport and homeostasis of alkali metal cations. *Physiol Res*, 53 Suppl 1:S91–S98, 2004.
- [138] H. Sychrová, J. Ramírez, and A. Peña. Involvement of nha1 antiporter in regulation of intracellular ph in saccharomyces cerevisiae. *FEMS Microbiol Lett*, 171(2):167–172, Feb 1999.
- [139] M. J. Tamás, M. Rep, J. M. Thevelein, and S. Hohmann. Stimulation of the yeast high osmolarity glycerol (hog) pathway: evidence for a signal generated by a change in turgor rather than by water stress. *FEBS Lett*, 472(1):159–165, Apr 2000.
- [140] G. Tamma, J. H. Robben, C. Trimpert, M. Boone, and P. M. T. Deen. Regulation of aqp2 localization by s256 and s261 phosphorylation and ubiquitination. *Am J Physiol Cell Physiol*, 300(3):C636–C646, Mar 2011.
- [141] B. Teusink, J. Passarge, C. A. Reijenga, E. Esgalhado, C. C. van der Weijden, M. Schepper, M. C. Walsh, B. M. Bakker, K. van Dam, H. V. Westerhoff, and J. L. Snoep. Can yeast glycolysis be understood in terms of in vitro kinetics of the constituent enzymes? testing biochemistry. *Eur J Biochem*, 267(17):5313–5329, Sep 2000.
- [142] U. Theobald, W. Mailinger, M. Baltés, M. Rizzi, and M. Reuss. In vivo analysis of metabolic dynamics in saccharomyces cerevisiae : I. experimental observations. *Biotechnol Bioeng*, 55(2):305–316, Jul 1997.
- [143] B. W. M. van Balkom, P. J. M. Savelkoul, D. Markovich, E. Hofman, S. Nielsen, P. van der Sluijs, and P. M. T. Deen. The role of putative phosphorylation sites in the targeting and shuttling of the aquaporin-2 water channel. *J Biol Chem*, 277(44):41473–41479, Nov 2002.
- [144] P. Vergani, T. Miosga, S. M. Jarvis, and M. R. Blatt. Extracellular k⁺ and ba²⁺ mediate voltage-dependent inactivation of the outward-rectifying k⁺ channel encoded by the yeast gene tok1. *FEBS Lett*, 405(3):337–344, Apr 1997.

- [145] P. Waage and C. Guldberg. Studies concerning affinity. *Forhandlinger: Videnskabs-Selskabet, Christiana*, page pp 35, 1864.
- [146] A. R. Waldeck, K. van Dam, J. Berden, and P. W. Kuchel. A non-equilibrium thermodynamics model of reconstituted Ca^{2+} -ATPase. *Eur Biophys J*, 27(3):255–262, 1998.
- [147] G. Wiesenberger, K. Steinleitner, R. Malli, W. F. Graier, J. Vormann, R. J. Schweyen, and J. A. Stadler. Mg^{2+} deprivation elicits rapid Ca^{2+} uptake and activates Ca^{2+} /calcineurin signaling in *Saccharomyces cerevisiae*. *Eukaryot Cell*, 6(4):592–599, Apr 2007.
- [148] M. Wilchek and E. A. Bayer. The avidin-biotin complex in bioanalytical applications. *Anal. Biochem.*, 171:1–32, 1988.
- [149] D. J. Wilkinson. *Stochastic Modelling for Systems Biology (second edition)*. CRC Press, 2012.
- [150] Wolfram Research, Inc. *Mathematica 7.0*, 2008.
- [151] O. V. Wuytswinkel, V. Reiser, M. Siderius, M. C. Kelders, G. Ammerer, H. Ruis, and W. H. Mager. Response of *Saccharomyces cerevisiae* to severe osmotic stress: evidence for a novel activation mechanism of the Hog1 kinase pathway. *Mol Microbiol*, 37(2):382–397, Jul 2000.
- [152] L. Xie, J. D. Hoffert, C. L. Chou, M. J. Yu, T. Pisitkun, M. A. Knepper, and R. A. Fenton. Quantitative analysis of aquaporin-2 phosphorylation. *Am J Physiol Renal Physiol.*, 298:F1018–23, 2010.
- [153] L. Yenush, S. Merchan, J. Holmes, and R. Serrano. pH-responsive, posttranslational regulation of the Trk1 potassium transporter by the type 1-related Ppz1 phosphatase. *Mol Cell Biol*, 25(19):8683–8692, Oct 2005.
- [154] K.-P. Yip. Coupling of vasopressin-induced intracellular Ca^{2+} mobilization and apical exocytosis in perfused rat kidney collecting duct. *J Physiol*, 538(Pt 3):891–899, Feb 2002.
- [155] J. Zhang, C. J. Hupfeld, S. S. Taylor, J. M. Olefsky, and R. Y. Tsien. Insulin disrupts beta-adrenergic signalling to protein kinase A in adipocytes. *Nature*, 437(7058):569–573, Sep 2005.
- [156] R. A. Zvyagilskaya, F. Lundh, D. Samyn, J. Pattison-Granberg, J.-M. Mouillon, Y. Popova, J. M. Thevelein, and B. L. Persson. Characterization of the Pho89 phosphate transporter by functional hyperexpression in *Saccharomyces cerevisiae*. *FEMS Yeast Res*, 8(5):685–696, Aug 2008.

List of Figures

1.1	Regulation of AQP2 trafficking.	12
1.2	Activation of a G-protein coupled receptor.	13
1.3	cAMP synthesis and degradation.	14
1.4	Activation of PKA by cAMP	15
1.5	Different phosphorylation sites at the C terminus of AQP2	16
1.6	Data set from Deen <i>et al.</i> [20] based on experiments performed with MDCK cells.	17
1.7	Data set from Stefan <i>et al.</i> [133] based on experiments performed with primary rat IMCD cells.	18
2.1	Concentration response coefficient	23
2.2	Workflow: cell surface biotinylation.	25
3.1	The MDCK cell model, using the Systems Biology Graphical Notation (SBGN).	28
3.2	Parameter estimation with the old and the new data set.	30
3.3	Generating of variants of the MDCK cell model.	31
3.4	Ranking of variants of the MDCK cell model.	31
3.5	Sensitivity analysis of the MDCK cell model.	32
3.6	Time-dependent sensitivity analysis performed with the MDCK cell model.	33
3.7	Cell surface biotinylation on MDCK cells	34
3.8	Cell surface biotinylation performed on MDCK cells	35
3.9	Prediction of $AQP2_{membrane}$ over time at different dDAVP concentrations using the MDCK cell model.	36
3.10	Prediction of cAMP concentration over time at different dDAVP concentrations using the MDCK cell model.	37
3.11	Identification of potential drug targets with TIdr.	40
3.12	Analysis of drug combinations for medical case 1 and 2.	41
3.13	Analysis of drug combinations for medical case 1.	42
4.1	IMCD cell model.	48
4.2	Parameter estimation: primary rat IMCD cells	50
4.3	Ranking of model variants.	52
4.4	Sensitivity analysis of the primary rat IMCD cell model.	53
4.5	Time-dependent sensitivity analysis performed with IMCD cell model.	54
4.6	Prediction of $AQP2_{membrane}$ in primary rat IMCD cells	55
4.7	Ratio of AQP2 plasma membrane/intracellular fluorescence signal intensity in primary rat IMCD cells	56
4.8	Comparison of model and experiment for AQP2 localization in IMCD cells	57

4.9	Simulation of AQP2 _{membrane} in primary rat IMCD cells and comparison between the Stefan <i>et al.</i> and the new data set.	58
4.10	Comparison of model and experiment for AQP2 localization in IMCD cells (after additional parameter estimation by using the new data set provided by Klussmann <i>et al.</i>) . . .	59
4.11	Simulation of AQP2 _{membrane} after estimation of the parameters with the new data set. . .	60
5.1	Schematic yeast cell including the major cation transport proteins of the cellular plasma membrane.	75
6.1	<i>k</i> -means clustering	94
7.1	Data resulting from MIFE and FLISE experiments on <i>S. cerevisiae</i> wild-type.	101
7.2	Simulation with model fitted to MIFE data.	103
7.3	Clustering and parameter analysis.	105
7.4	<i>In silico</i> predictions using the model fitted to the Shabala data.	106
7.5	Analysis of individual forces.	109
7.6	Prediction of second KCl stimulus.	110
7.7	Simulation with model fitted to FLISE data.	111
1	Dependency of AQP2 _{total} on AQP2 _{membrane}	123
2	Dephosphorylation of AQP2 at position S261.	125
3	Model Fitting with COPASI: primary rat IMCD cell model without negative feedback . .	126
4	Sensitivity analysis of the primary rat IMCD cell model with new dataset.	127
5	Time-dependent sensitivity analysis performed on complete IMCD cell model fitted to the new dataset.	128
6	Clustering and parameter analysis with the model including a K ⁺ -ATPase.	134
7	Predictions performed with the model including a K ⁺ -ATPase.	135

List of Tables

3.1	Algebraic and differential equations describing the model for MDCK cells.	28
3.2	Estimated model parameters for the complete MDCK model.	29
4.1	Algebraic and differential equations describing the model for primary rat IMCD cells. . .	49
4.2	Parameters for primary rat IMCD cell model.	51
4.3	Comparison between the results from the MDCK and the rat IMCD cell model.	67
7.1	Connection between the Ls and the proteins	97
1	Model as implemented in COPASI.	130
2	Initial concentrations, global quantities and volumes used for fitting the model to data from MIFE experiments resulting in a high L_{KK}^L value.	131
3	Initial concentrations, global quantities and volumes used for fitting the model to data from MIFE experiments resulting in a high L_{HK}^S value.	132
4	Initial concentrations, global quantities and volumes, and estimated parameters for model fitted to FLISE data.	133

List of publications

Publications

M. Fröhlich, P. M. T. Deen and E. Klipp, *A Systems Biology Approach: Modelling of Aquaporin-2 Trafficking*, *Genome Inform.* 2010;24:42-55.

Szymon Stoma, Martina Fröhlich, Susanne Gerber, Edda Klipp, *STSE: Spatio-Temporal Simulation Environment Dedicated to Biology*, *BMC Bioinformatics*, 2011, 12(1):126

Martina Fröhlich, Susanne Gerber, Hella Lichtenberg-Fraté, Jost Ludwig, Sergey Shabala, and Edda Klipp, *A basic thermodynamic model of cation homeostasis in the yeast *Saccharomyces cerevisiae**, manuscript in preparation.

Talks and presentations

- | | |
|-------------|--|
| 07/2010 | “The Tenth Annual International Workshop on Bioinformatics and Systems Biology”, Kyoto, Japan |
| 09/2009 | “The 10th International Conference on Systems Biology” (Poster), Stanford, USA |
| 07/2009 | “The Ninth Annual International Workshop on Bioinformatics and Systems Biology” (Poster), Boston, USA |
| 09/2008 | “Global Researcher Conference of the NDI Foundation” (Poster), Amelia Island, USA |
| 08/2008 | “The 9th International Conference on Systems Biology” (Poster), Gothenburg, Sweden |
| 05/2008 | “Conference on Systems Biology of Mammalian Cells” (Poster), Dresden, Germany |
| 04/2008 | Seventh Hiddensee Workshop “Genomics and Systems Biology of Molecular Networks”, Hiddensee, Germany |
| 2008 - 2010 | Oral presentations of the ongoing work on the biannual meetings of the Marie Curie Research Training Network in Aquaglyceroporin research and the SysMo (Systems Biology of Microorganisms) ERA-NET project TRANSLUCENT. |

Berlin, May 16, 2012

CURRICULUM VITAE

For reasons of data protection, the Curriculum vitae is not published in the online version.

Zusammenfassung

Membranen sind mehr als einfache Barrieren zwischen Zellen und ihrer Umgebung. Sie dienen sowohl zum Schutz der Zelle, ermöglichen aber auch den Austausch von Substanzen. Für diese Arbeit wurden zwei Aspekte des Membrantransports untersucht, zum einen der Transport von Wasser und zum anderen der Transport von Ionen, insbesondere von Kationen.

Zur Untersuchung des Wassertransports wurden Säugernierenzellen als biologisches Modellsystem herangezogen. Es wurde ein Ansatz angewendet, der biologische Experimente mit der Generierung eines mathematischen Modells kombiniert. Dieser Ansatz wurde dazu verwendet, den intrazellulären Signalweg zu untersuchen, welcher die Menge des Wasserkanals Aquaporin-2 in der Membran der Nierenzellen reguliert. Aus Experimenten an Ratten- und Hundenierenzellen gewonnene Daten wurden zur Schätzung der Modellparameter herangezogen. Dies ermöglichte die Erstellung von spezie-spezifischen Modellen. Die Modelle wurden zur Untersuchung der zeitabhängigen Dynamik des Systems verwendet und wie folgt analysiert. Durch Eliminieren von Reaktionen und anschließender Parameterschätzung wurden verschiedene Modellvarianten generiert. Diese wurden, in Anhängigkeit davon, wie gut sie die biologischen Daten wiedergeben konnten, sortiert. Die Ergebnisse zeigten, dass in Nierenzellen unterschiedlicher Herkunft verschiedene Reaktionen wichtig sind und identifizierten jeweils diejenigen Reaktionen, die für das zeitabhängige Verhalten des Systems entscheidend sind. Eine Sensitivitätsanalyse wurde durchgeführt und zeigte, dass Veränderungen in den direkt am Translokationsmechanismus beteiligten Reaktionen den größten Einfluss auf die zelluläre Verteilung von Aquaporin-2 haben. Basierend auf den Kenntnissen über Funktionsstörungen der Wasserhomöostase wurden medizinische Fallbeispiele erzeugt. Mithilfe des auf Hundenierenzellen basierenden Modells wurde eine für den jeweiligen Fall geeignete Behandlung identifiziert.

Da viele Membrantransportsysteme von Hefe sehr ähnlich zu denen höheren Organismen sind, wurde die Regulierung des Kationentransports in der Hefe *Saccharomyces cerevisiae* untersucht. Die Theorie der linearen Nichtgleichgewichtsthermodynamik wurde dazu verwendet, thermodynamische Modelle der Kationenhomöostase zu erstellen. Dieser Ansatz ermöglichte die Modellierung passiver Ionenflüsse angetrieben durch elektrochemische Potentialdifferenzen sowie primär und sekundär aktive Transportprozesse durch Symport, Antiport oder ATPasen. Biologische Daten für Kalium- und Protonenflüsse aus MIFE- und FLISE-Experimenten (nicht-invasive Techniken zur Messung von transmembranen Ionenflüssen) wurden zur Schätzung der Modellparameter herangezogen. Das Modell wurde dazu verwendet, Vorhersagen über zusätzliche Ionenflüsse zu machen und identifizierte Chloridflüsse als mögliche Kandidaten. Die *Trk1/2p*- und *Pma1p*-Dynamik wurde in Mutations- und Inhibierungs-Experimenten *in silico* untersucht. Des Weiteren wurde das Modell dazu genutzt, das Verhalten der Zellen bei aufeinanderfolgenden Salzstressen zu analysieren und sagte reduzierte Ionenflüsse bei Zellen mit einem höheren primären Stimulus voraus.

Die durchgeführten Untersuchungen verdeutlichen die Anwendbarkeit von mathematischer und thermodynamischer Modellierung auf Membrantransportprozesse. Die Vorhersagen des Modells bieten wertvolle Anhaltspunkte zur Planung und Durchführung zukünftiger Experimente.

Ehrenwörtliche Erklärung

Hiermit erkläre ich, dass ich diese Arbeit selbstständig verfasst und keine anderen als die angegebenen Hilfsmittel und Quellen verwendet habe.

Berlin, 16. Mai 2012

Martina Fröhlich